

## Durham E-Theses

---

### *Experimental fast-ion transport studies on the Mega-Amp Spherical Tokamak*

JONES, OWEN, MATTHEW

#### How to cite:

---

JONES, OWEN, MATTHEW (2015) *Experimental fast-ion transport studies on the Mega-Amp Spherical Tokamak*, Durham theses, Durham University. Available at Durham E-Theses Online: <http://etheses.dur.ac.uk/11221/>

#### Use policy

---

The full-text may be used and/or reproduced, and given to third parties in any format or medium, without prior permission or charge, for personal research or study, educational, or not-for-profit purposes provided that:

- a full bibliographic reference is made to the original source
- a [link](#) is made to the metadata record in Durham E-Theses
- the full-text is not changed in any way

The full-text must not be sold in any format or medium without the formal permission of the copyright holders.

Please consult the [full Durham E-Theses policy](#) for further details.

# Experimental fast-ion transport studies on the Mega-Amp Spherical Tokamak

Owen M. Jones

Thesis presented in fulfilment  
of the requirements of the degree of  
Doctor of Philosophy



Centre for Advanced Instrumentation  
Department of Physics  
University of Durham  
UK

May 2015

# Experimental fast-ion transport studies on the Mega-Amp Spherical Tokamak

Owen M. Jones

## Abstract

Nuclear fusion holds the promise of a sustainable means of electrical power generation. The technical challenge posed by controlled nuclear fusion however is formidable. One key aspect of research into magnetically-confined fusion plasmas is the study of the behaviour of fast ions. Produced by auxiliary heating systems including neutral beam injection (NBI) and ion cyclotron resonance heating, as well as by the fusion reactions themselves, the energies of these particles range from tens of keV to several MeV. Four fast-ion diagnostics on a medium-sized experimental fusion research device, namely the Mega-Amp Spherical Tokamak (MAST), have been used to investigate the transport of NBI-generated fast ions under the influence of various magnetohydrodynamic (MHD) instabilities. These include frequency-chirping fast-ion-driven modes known as toroidal Alfvén eigenmodes (TAE) and fishbones, as well as saturated internal kink modes and sawtooth reconnection events. The frequencies of these modes in the plasma frame ranged from 0 kHz to 150 kHz in MAST. The effects of these modes on the fast ions have been investigated with the use of a fission chamber, a collimated neutron detector, a fast-ion deuterium alpha spectrometer and a charged fusion product detector. Data from each diagnostic are examined and compared for consistency in the presence of each type of instability. Fast-ion transport modelling is coupled with synthetic diagnostics to model the observed signals based on calculated fast-ion distributions. The data reveal a significant enhancement of fast-ion transport due to each of the MHD modes. It is found that the transport of fast ions in the presence of TAE and fishbones, averaged over the chirping mode cycle, is well-represented by assuming anomalous radial diffusion of these ions. A simple model for fast-ion mixing during sawtooth reconnection is found to reproduce partially the observations accompanying such events. The effects of the saturated internal kink mode cannot be modelled in such a simple way, and partial consistency with the measurements requires the use of tailored transport coefficients. Shortcomings and possible enhancements of the diagnostic capability are discussed in the light of these results.

# Declaration

The research described in this thesis was carried out at the Culham Centre for Fusion Energy (CCFE), UK. A large team of collaborators both from the UK and overseas, named in the Acknowledgments, have made contributions to this research effort. Where the results and analysis included in this thesis are not the product solely of my own work, this is explicitly stated in the text. No part of this thesis has been submitted elsewhere for any other degree or qualification.

This research was part-funded by the Engineering and Physical Sciences Research Council, and part-funded by the RCUK Energy Programme under grant EP/I501045.

**Copyright © 2015 by Owen Jones.**

The copyright of this thesis rests with the author. No quotations from it should be published without the author's prior written consent and information derived from it should be acknowledged.

# Acknowledgments

Thanks are due to M. Imran for the diligent preparation and public release of this LaTeX template, and to Scott Silburn for his guidance in its implementation.

This research has been the product of fruitful collaboration with many people at CCFE and further afield. Those currently or formerly at CCFE who deserve special thanks include: Ken McClements for his patience, for looking out for my interests and for providing a guiding hand; Matthew Carr, Neil Conway, Brendan Crowley, Nick Hawkes and Alex Meakins for their invaluable support and camaraderie in all matters related to the practical aspects of spectroscopy on MAST; David Keeling and Clive Challis for coaxing me along the rocky road to becoming a better researcher, and for putting up with my questions about TRANSP; Simon Pinches, Sergei Sharapov and Michael Fitzgerald for correcting my half-baked notions about the behaviour of fast ions and MHD; Rob Akers for being on hand to fix MC<sup>3</sup> every time I broke it; and last but not least Clive Michael for giving me a diagnostic to work with, and for showing me the ropes at the start of my Ph.D. Many others deserve mention for their hard work; I hope they will not take offence if I include them by thanking “the MAST team”.

Turning to look outside CCFE, it must first be acknowledged that none of this would have been possible without the continual support, friendship and patience of Marco Cecconello and Iwona Klimek. I owe them a tremendous debt of gratitude. Werner Boeglin and Ramona Perez are also deserving of my heartfelt thanks, as is Mikhail Turnyanskiy for his participation in many illuminating discussions. Bill Heidbrink has shown me, and many others, the path to follow since he sparked the worldwide interest in FIDA. Through his development of FIDASIM, along with Deyong Liu he also gave us the means to travel this path. Ben Geiger has done a sterling job of rewriting the code in Fortran, as has Luke Stagner of making it available to the masses. Thanks also to Marina Gorelenkova for opening the doors to the citadel of TRANSP.

It would be quite remiss of me not to acknowledge the formidable support provided by all the administrative staff who go above and beyond the call of duty to make everything work so smoothly. Kathy Patton and Ann Maynard at CCFE, Claire Whitehill at Durham and Rachael Stephenson at York each deserve my profound thanks.

For his unwavering support when the going got tough, or when I wasn't sure which way to turn, I am eternally grateful to my supervisor Ray Sharples at Durham.

Life at CCFE, and before that at York, was immeasurably improved by some of the people with whom I shared my time there. Thanks to my fellow students and recent graduates, too numerous to name, each of whom has brightened my days with laughter, companionship and cake. The Friday badminton crew also provided a sociable outlet for my stress, and I always looked forward to seeing them at the end of the week.

Finally, for all their love, support, home-cooked food, encouragement and the belief that I could make it through those difficult times when I most doubted myself, I thank my mum and Gail. Words cannot express how grateful I am for all that you have done for me over the last four years.

# Contents

<b>Abstract</b>	<b>i</b>
<b>Declaration</b>	<b>ii</b>
<b>Acknowledgments</b>	<b>iii</b>
<b>1 Introduction</b>	<b>1</b>
1.1 The energy crisis . . . . .	1
1.2 Nuclear energy . . . . .	2
1.3 Magnetic confinement of fusion plasmas . . . . .	6
1.3.1 Equilibrium in a tokamak . . . . .	8
1.3.2 Conventional and spherical tokamaks . . . . .	11
1.3.3 Alternatives to the tokamak . . . . .	13
1.4 Fusion plasma diagnostics . . . . .	15
1.4.1 Active diagnostics . . . . .	15
1.4.2 Passive diagnostics . . . . .	17
1.5 Thesis outline . . . . .	18
<b>2 Fast ions in tokamaks</b>	<b>20</b>
2.1 Outline . . . . .	20
2.2 Mechanisms of fast-ion production . . . . .	21
2.2.1 Neutral beam injection . . . . .	21
2.2.2 Ion cyclotron resonance heating . . . . .	22
2.2.3 Fusion reactions . . . . .	23
2.3 Dynamics of fast ions in tokamak plasmas . . . . .	23
2.3.1 Particle orbits in a tokamak . . . . .	23
2.3.2 Properties of fast-ion orbits in MAST . . . . .	27
2.3.3 Collisional interactions with thermal species . . . . .	27
2.4 Steady-state fast-ion distributions . . . . .	29
2.5 Loss mechanisms of fast ions . . . . .	33
2.6 Fast-ion research on MAST . . . . .	34
<b>3 Interactions between MHD instabilities and fast ions</b>	<b>35</b>
3.1 Outline . . . . .	35
3.2 MHD modes of a toroidal plasma . . . . .	36
3.2.1 Ideal MHD modes of a cylinder . . . . .	36
3.2.2 Alfvén gap modes . . . . .	38
3.2.3 Internal kink modes . . . . .	39
3.2.4 Damping and dissipative processes . . . . .	42

3.3	Interactions with fast ions . . . . .	43
3.3.1	Resonant energetic-particle drive . . . . .	43
3.3.2	Nonlinear wave-particle interactions . . . . .	45
3.4	MHD activity observed in MAST . . . . .	47
3.4.1	Classification of MHD modes . . . . .	47
3.4.2	Research background . . . . .	55
<b>4</b>	<b>Diagnosing the fast-ion distribution</b>	<b>56</b>
4.1	Outline . . . . .	56
4.2	Fast-ion diagnostics on MAST . . . . .	56
4.2.1	Description of the diagnostics . . . . .	56
4.2.2	Real-space sensitivity . . . . .	60
4.2.3	Velocity-space sensitivity . . . . .	65
4.3	Alternative fast-ion diagnostics . . . . .	67
<b>5</b>	<b>The FIDA diagnostic on MAST</b>	<b>69</b>
5.1	Outline . . . . .	69
5.2	Design considerations . . . . .	69
5.2.1	Optical components . . . . .	71
5.2.2	EMCCD camera . . . . .	73
5.2.3	Mechanical components . . . . .	74
5.3	Calibration procedures . . . . .	75
5.4	Preliminary data . . . . .	78
<b>6</b>	<b>Modelling for fast-ion diagnostics</b>	<b>83</b>
6.1	Outline . . . . .	83
6.2	TRANSP simulations of MAST plasmas . . . . .	84
6.2.1	Equilibrium reconstruction . . . . .	84
6.2.2	Profile mapping . . . . .	86
6.2.3	Calculation of the fast-ion distribution . . . . .	87
6.3	Synthetic fast-ion diagnostics . . . . .	89
6.3.1	Fission chamber . . . . .	90
6.3.2	FIDA diagnostic . . . . .	91
6.3.3	Neutron camera . . . . .	95
<b>7</b>	<b>Effects of resonant MHD instabilities</b>	<b>98</b>
7.1	Outline . . . . .	98
7.2	Plasma scenarios . . . . .	99
7.3	Effects of chirping modes on confined fast ions . . . . .	100
7.3.1	TAE . . . . .	100
7.3.2	Fishbones . . . . .	105
7.4	Fast-ion losses due to resonant MHD instabilities . . . . .	108
7.5	TRANSP modelling of fast-ion redistribution . . . . .	110
7.5.1	Anomalous transport models . . . . .	110
7.5.2	Modelling with anomalous diffusion . . . . .	111
7.5.3	Inclusion of the fishbone model . . . . .	113
7.6	Summary . . . . .	118

---

<b>8</b>	<b>Effects of non-resonant MHD instabilities</b>	<b>120</b>
8.1	Outline . . . . .	120
8.2	Plasma Scenarios . . . . .	121
8.3	LLM-induced redistribution . . . . .	123
8.4	Sawtooth-induced redistribution . . . . .	126
8.5	Effects of RMP and ELMs . . . . .	130
8.6	Summary . . . . .	133
<b>9</b>	<b>Summary and conclusions</b>	<b>135</b>
9.1	Outline . . . . .	135
9.2	Experimental techniques . . . . .	135
9.2.1	Fusion product diagnostics . . . . .	135
9.2.2	The FIDA diagnostic . . . . .	137
9.2.3	The MAST device . . . . .	138
9.3	Analysis tools . . . . .	139
9.3.1	Data preparation . . . . .	139
9.3.2	TRANSP modelling . . . . .	139
9.4	Conclusions and contextual discussion . . . . .	141
	<b>Bibliography</b>	<b>143</b>



# List of Figures

1.1	Binding energy per nucleon as a function of nucleon number . . . . .	2
1.2	Fusion reactivity as a function of ion temperature . . . . .	4
1.3	Historical values of temperature and triple product in tokamaks . . . . .	6
1.4	Schematic drawing of a magnetised torus and a tokamak . . . . .	7
1.5	Diagram of the toroidal geometry of a tokamak . . . . .	9
1.6	Schematic cross-sections of a conventional and a spherical tokamak . . . . .	12
1.7	Colour photograph of a plasma in MAST . . . . .	14
1.8	Schematic illustration of stellarator and RFP geometry . . . . .	15
1.9	Principles of Thomson scattering and charge exchange diagnostics . . . . .	16
1.10	Plasma profiles measured in MAST . . . . .	17
2.1	Sketch of a magnetic mirror field . . . . .	25
2.2	Poloidal projections of trapped and passing orbits in a tokamak . . . . .	26
2.3	Sketch of NBI and ICRH-driven FI distributions . . . . .	31
2.4	Typical TRANSP-calculated FI distribution for MAST . . . . .	32
3.1	Magnetic pick-up coil signal of a fishbone . . . . .	36
3.2	Alfvén wave speed in a magnetised cylinder . . . . .	37
3.3	Alfvén continua in circular cross-section and JET plasmas . . . . .	40
3.4	TAE and internal kink eigenmodes in MAST . . . . .	41
3.5	Sketch of FI transport across a resonant surface . . . . .	44
3.6	Spectrogram of a typical MAST discharge . . . . .	48
3.7	Mirnov coil time trace during a typical MAST shot . . . . .	49
3.8	Soft X-ray line-of-sight geometry on MAST . . . . .	51
3.9	Fluctuations in soft X-ray signal during a fishbone . . . . .	52
3.10	The effect of sawteeth on soft X-ray emission and on $T_e$ . . . . .	54
4.1	MAST fast-ion diagnostic geometry . . . . .	57
4.2	Examples of FI diagnostic time traces . . . . .	61
4.3	TRANSP FI density and neutron emission for shot #29976 . . . . .	64
4.4	D-D fusion reaction cross-section . . . . .	66
4.5	FI distributions and FIDA weight functions . . . . .	67
5.1	Modelled FIDA spectrum . . . . .	70
5.2	Schematic plan of the FIDA spectrometer . . . . .	72
5.3	Raw FIDA and calibration spectra . . . . .	73
5.4	Calibration CCD frames . . . . .	77
5.5	Raw and processed FIDA data . . . . .	79
5.6	Effect of systematic errors on FIDA signal . . . . .	81
5.7	Beam emission contamination of FIDA spectra . . . . .	82

---

6.1	EFIT pressure and current profiles . . . . .	85
6.2	Relative concentration of impurities in MAST plasma . . . . .	87
6.3	Global properties of the FI population . . . . .	89
6.4	TRANSP neutron rate comparison . . . . .	90
6.5	FIDASIM spectrum compared to measurements . . . . .	92
6.6	FIDASIM grid and neutral density . . . . .	93
6.7	Neutron camera field of view projections . . . . .	96
6.8	NC measured and modelled count rate profiles . . . . .	96
7.1	Parameters of discharges with TAE and fishbones . . . . .	100
7.2	Spectrogram of TAE and fishbone discharges . . . . .	101
7.3	NC and FIDA signals with chirping TAE . . . . .	102
7.4	Identification of events in FI diagnostic signals . . . . .	103
7.5	TAE and fishbone identification factors . . . . .	105
7.6	NC and FIDA signals with fishbones . . . . .	106
7.7	Drop in FIDA signal scales with fishbone amplitude . . . . .	107
7.8	$D_\alpha$ spikes coincide with chirping TAE . . . . .	109
7.9	$D_\alpha$ spikes coincide with fishbones . . . . .	109
7.10	Passive FIDA spikes coincide with chirping modes . . . . .	110
7.11	TRANSP modelling with anomalous diffusion . . . . .	112
7.12	Modelling #29976 with anomalous diffusion . . . . .	114
7.13	Neutron rate match with TRANSP fishbone model . . . . .	114
7.14	Measured and modelled NC profiles affected by fishbones . . . . .	116
7.15	Measured and modelled FIDA profiles affected by fishbones . . . . .	117
7.16	Relative changes in FIDA profiles caused by fishbones . . . . .	118
7.17	CFPD time traces during large fishbones . . . . .	119
8.1	Parameters of discharges with LLM and sawteeth . . . . .	122
8.2	Spectrogram and toroidal rotation profiles during LLM . . . . .	122
8.3	Measured and modelled FI diagnostic signals before and during a LLM . . . . .	123
8.4	FI diagnostic signals modelled using tailored transport coefficients . . . . .	125
8.5	Profiles of TS and FI diagnostic signals before and after sawteeth . . . . .	127
8.6	TRANSP-simulated effects of sawteeth on FI diagnostic signals . . . . .	128
8.7	ELM control coil layout in MAST . . . . .	131
8.8	Time traces showing effects of RMP on FI confinement . . . . .	132
8.9	FI diagnostic observations during sawteeth and ELMs . . . . .	133

# List of Tables

1.1	Typical parameters of some tokamak plasmas . . . . .	13
5.1	Noise sources in FIDA measurements . . . . .	75
5.2	Parameters to derive spectral radiance . . . . .	80
7.1	Parameters used in TRANSP fishbone model . . . . .	115

# List of Acronyms

<b>ADAS</b>	Atomic Data and Analysis Structure
<b>ADC</b>	analogue-to-digital converter
<b>ASDEX</b>	Axisymmetric Divertor Experiment
<b>AUG</b>	ASDEX-Upgrade
<b>BAE</b>	beta-induced Alfvén eigenmode
<b>CFPD</b>	charged fusion product detector
<b>CX</b>	charge exchange
<b>CXRS</b>	charge exchange recombination spectroscopy
<b>D<sub>α</sub></b>	deuterium Balmer-alpha (emission)
<b>D-D</b>	deuterium-deuterium
<b>DIID</b>	A tokamak operated by General Atomics, USA
<b>DND</b>	double-null diverted
<b>D-T</b>	deuterium-tritium
<b>EAE</b>	ellipticity-induced Alfvén eigenmode
<b>EI</b>	electron impact (ionisation)
<b>ELM</b>	edge-localised mode
<b>EM</b>	electron multiplication
<b>EMCCD</b>	electron-multiplying charge-coupled device
<b>EPM</b>	energetic-particle mode
<b>FC</b>	fission chamber
<b>FI</b>	fast ions
<b>FIDA</b>	fast-ion deuterium alpha
<b>FILD</b>	fast-ion loss detector
<b>FOV</b>	field of view
<b>GFLDR</b>	generalised fishbone-like dispersion relation
<b>GPU</b>	graphics processing unit
<b>ICRH</b>	ion cyclotron resonance heating
<b>II</b>	ion impact (ionisation)
<b>JET</b>	Joint European Torus
<b>JT-60U</b>	A tokamak operated by JAEA, Japan
<b>KBM</b>	kinetic ballooning mode
<b>LCFS</b>	last closed flux surface

---

<b>LLM</b>	long-lived mode
<b>LOCUST</b>	Larmor Orbit Code for Use in Spherical Tokamaks
<b>LOS</b>	line of sight
<b>MAST</b>	Mega-Amp Spherical Tokamak
<b>MHD</b>	magnetohydrodynamics
<b>MSE</b>	motional Stark effect
<b>NAE</b>	non-circularity-induced Alfvén eigenmode
<b>NBI</b>	neutral beam injection
<b>NC</b>	neutron camera
<b>NEBULA</b>	Neutral-Beam Universal Line-Integrated Analysis
<b>NSTX</b>	National Spherical Torus Experiment
<b>PBX</b>	Princeton Beta Experiment
<b>PDX</b>	Poloidal Divertor Experiment
<b>RFP</b>	reversed field pinch
<b>RMP</b>	resonant magnetic perturbation
<b>RMS</b>	root-mean-square
<b>SND</b>	single-null diverted
<b>SNR</b>	signal-to-noise ratio
<b>SS</b>	south-south (neutral beam)
<b>ST</b>	spherical tokamak
<b>START</b>	Small Tight-Aspect Ratio Tokamak
<b>SW</b>	south-west (neutral beam)
<b>SXR</b>	soft X-ray
<b>TAE</b>	toroidal Alfvén eigenmode
<b>TEXTOR</b>	Tokamak Experiment for Technology-Oriented Research
<b>TFTR</b>	Tokamak Fusion Test Reactor
<b>TS</b>	Thomson scattering
<b>VPH</b>	volume phase holographic

# Chapter 1

## Introduction

### 1.1 The energy crisis

Global electricity demand is predicted to grow by approximately 80% over the period 2012–2040 [1]. Although much of this increased demand will be satisfied by renewable sources under the International Energy Agency’s baseline ‘New Policies Scenario’, the share which will be met with fossil fuels is nonetheless predicted to remain high, at 55% in 2040 compared to 68% in 2012. The share of total electricity generation provided by renewable sources is expected to grow from 21% in 2012 to 33% in 2040. Nuclear power is expected to remain at approximately 12% of the global generating capacity over this time frame. These global statistics hide a substantial shift in the geographical distribution of energy demand, with most of the growth expected to occur in China, India, south-east Asia and the Middle East. Increasing economic development and improving standards of living in these regions strongly weight the increased demand towards electricity generation; *total* global primary energy consumption, by comparison, is predicted to grow by 37% over the same period.

The consequences of continuing dependence on fossil fuels are potentially severe. In order to limit global warming by the year 2100 to less than 2°C above pre-industrial levels, analysis by the Intergovernmental Panel on Climate Change suggests that the global average CO<sub>2</sub> concentration should remain below 480 ppm [2]. Under the forecast discussed above, the entire CO<sub>2</sub> emissions budget allowable within this constraint would be used up by 2040 and the world would be on track for an average global surface temperature increase of 3°C to 4°C by 2100. At the same time, dwindling oil and natural gas resources threaten global economic and political stability, jeopardising the world’s ability to confront the consequences of global warming and to implement miti-

gation strategies. The dominant positions of Russia and the Middle East in the natural gas export market allow the governments of these regions to use their resources for political leverage, as demonstrated recently by the international tensions surrounding the conflict in Ukraine [3]. It is clear therefore that in the interests of environmental protection and geopolitical stability, the world needs to establish a carbon-neutral means of electricity generation using abundant or renewable resources which are distributed relatively evenly across the globe.

## 1.2 Nuclear energy

One way to satisfy the requirement of a carbon-neutral energy source is to release the binding energy from atomic nuclei. Different atomic nuclei have different binding energies per nucleon, as seen in fig. 1.1, hence the possibility exists to release the difference in binding energy between two isotopes via nuclear *fusion* or *fission* reactions. The data points in fig. 1.1 exhibit a maximum corresponding to the nucleus of nickel-62.

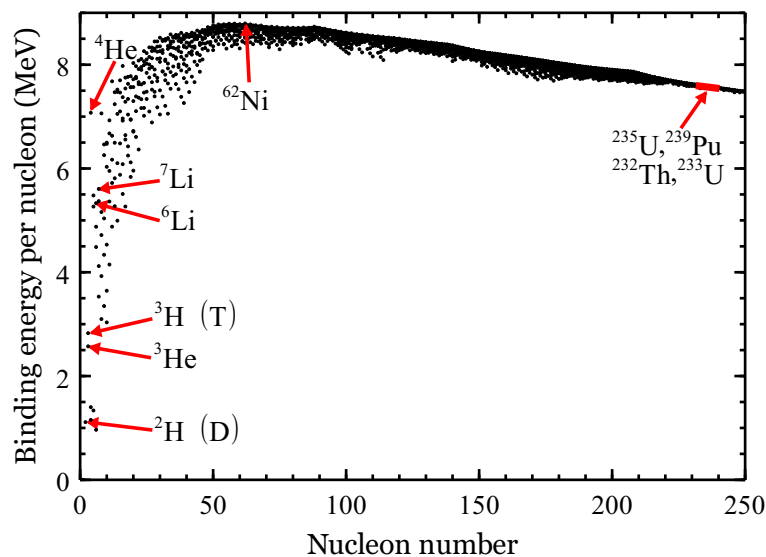
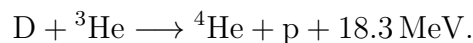
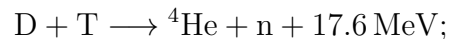


Figure 1.1: The binding energy per nucleon as a function of nucleon number (mass number,  $A$ ) for isotopes of elements with  $A$  from 1 to 250 (which includes isotopes of all elements from hydrogen to fermium). Data points corresponding to some elements of interest in the context of fusion and fission power generation are labelled. Data source: [www.einstein-online.info/spotlights/binding\\_energy-data\\_file/index.txt](http://www.einstein-online.info/spotlights/binding_energy-data_file/index.txt).

Isotopes much heavier than  $^{62}\text{Ni}$  have the potential to release energy when their nuclei are split into lighter products in the process of nuclear fission. Commonly-used fissile or fertile isotopes in this regard are uranium-233 and 235, plutonium-239 and thorium-232. The technological challenges posed by nuclear fission are well-understood, and the process has been used in power plants for more than sixty years. Fission however is problematic as a power source for several reasons: long-lived radioactive waste is

produced which must be stored safely in stable geological repositories, in some cases for hundreds of thousands of years [4], and the possibility of enriched fissile material being used to produce nuclear weapons means that nuclear facilities must be closely monitored on a global scale [4].

Isotopes much lighter than  $^{62}\text{Ni}$  have the potential to release energy when their nuclei are joined together into heavier products in the process of nuclear fusion. For its mass, helium-4 is seen to have an exceptionally high binding energy per nucleon. Exploiting this fact, the fusion of hydrogen-2 and hydrogen-3 (more commonly known as deuterium (D) and tritium (T) respectively), or of deuterium and helium-3 are promising candidates for power generation using nuclear fusion. Neither tritium nor helium-3 occur naturally in large quantities however, which means that they must be produced by neutron bombardment of lithium in the case of tritium, and by the subsequent decay of tritium or by extraction from the lunar regolith in the case of  $^3\text{He}$ . D-T fusion is also problematic because the energetic (14.1 MeV) neutrons produced by this reaction have the potential to activate and also to damage the structural materials in a fusion reactor. In this sense, D- $^3\text{He}$  fusion would be preferable since this reaction is aneutronic. Reactions involving D, T and  $^3\text{He}$  which may plausibly be used for fusion energy generation proceed as follows<sup>1</sup>:



Due to the requirement of momentum conservation, the excess energy is divided between the fusion products in inverse proportion to their mass. The neutron and proton from the above reactions therefore carry most of the energy. In a D-T fusion power plant, the energetic neutron would be used to produce tritium in a lithium-containing blanket surrounding the reactor.

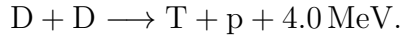
As mentioned above, neither tritium nor helium-3 occur naturally in sufficient quantities to render D-T or D- $^3\text{He}$  fusion viable using existing resources. Fusion research is therefore conducted using mainly deuterium as a fuel, which is abundant in water. The two reactions involving only deuterium are as follows:




---

<sup>1</sup>Reactions not considered here include  $^3\text{He}(^3\text{He}, 2\text{p})^4\text{He}$ ,  $^3\text{He}(\text{T}, \text{n} + \text{p})^4\text{He}$  and  $^3\text{He}(\text{T}, \text{D})^4\text{He}$ , since the reaction rates under current realistically-achievable conditions would be too low for them to be viable [5]. p- $^{11}\text{B}$  fusion, although it has a similar reactivity to D- $^3\text{He}$  at high fuel ion temperatures, requires specialised approaches which are beyond the scope of this work.





Since both these reactions are exothermic but do not produce neutrons with an energy sufficient to cause severe material damage, D-D fusion may at first glance appear ideally suited to energy generation. D-T fusion however is the only viable reaction from a current technological standpoint due to one important factor, namely its cross-section. At centre-of-mass energies up to 200 keV, the cross-section  $\sigma$  for the D-T reaction is at least an order of magnitude larger than that of the other reactions. In the context of a fusion reactor, the figure of merit is the *reactivity*, which is the product of cross-section and relative velocity  $v$  averaged over the velocity distribution of the reactant species, i.e.  $\langle\sigma v\rangle$ . In the case of thermonuclear fusion, the velocity distribution of the reactant ions is a Maxwellian. The resulting reactivity as a function of ion temperature for each of the reactions discussed in this chapter is shown in fig. 1.2. The D-T fusion reactivity

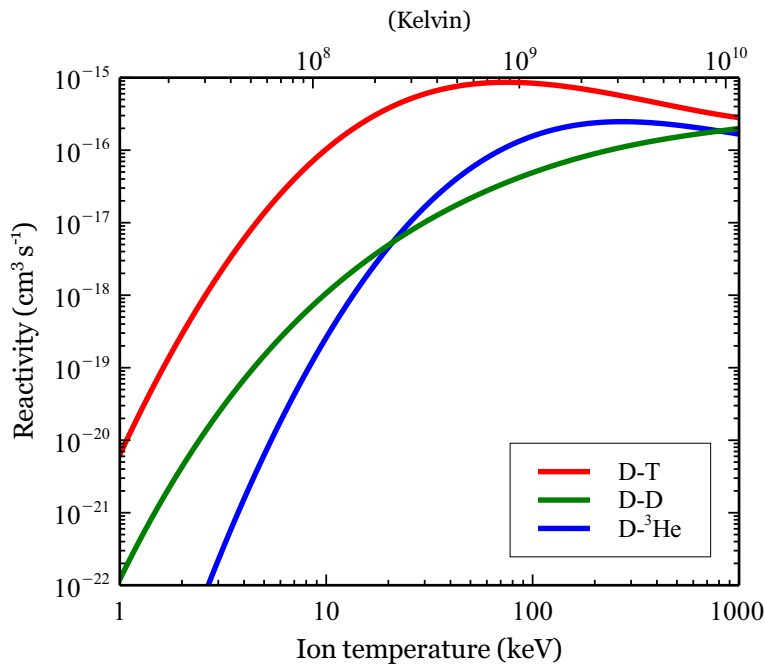


Figure 1.2: Reactivity  $\langle\sigma v\rangle$ , where  $v$  is the relative velocity of the reactant ions,  $\sigma$  is the cross-section of the fusion reaction and the angled brackets indicate averaging over a Maxwellian (thermal) velocity distribution, as a function of the temperature of the reactant ions. Temperature is given in kiloelectronvolts on the lower horizontal axis, and in Kelvin on the upper horizontal axis. Data derived from ref. [6].

is seen to peak at a temperature of approximately 800 MK. At this temperature, the hydrogen isotopes are fully ionised and form a *plasma*; a fourth state of matter which conducts electric currents and responds to magnetic fields due to its composition of free electrons and ions. In plasma physics, temperatures are usually expressed in terms of average energy of the particles in electronvolts; this is seen in the horizontal axis of

fig. 1.2, where the lower and upper axes have the relation  $1 \text{ eV} = 11\,600 \text{ K}$ . Since no material exists which can withstand temperatures of hundreds of millions of Kelvin, the aim of fusion research is to develop schemes whereby a plasma may be contained and heated to fusion-relevant conditions without coming into contact with material surfaces.

A fusion plasma should ideally be sufficiently dense and confined for sufficiently long that the power output from fusion reactions maintains the high temperatures necessary for a self-sustaining thermonuclear burn. In the case of D-T fusion, the  $14.1 \text{ MeV}$  neutron leaves the plasma without interacting with the fuel ions. Heating of the plasma must therefore come from the  $3.5 \text{ MeV}$   ${}^4\text{He}$  nucleus, or alpha particle. Having almost the same charge-to-mass ratio as the deuterium nucleus, confinement schemes developed to contain the D-T plasma should in principle be able to confine the alpha particles while they equilibrate with the fuel ions. The necessary condition for a self-sustaining, or *ignited*, fusion plasma may be expressed through the so-called *triple product*,  $nT\tau_E$ . Here,  $n$  is the number density of fuel ions,  $T$  is the ion temperature and  $\tau_E$  is the *energy confinement time*.  $\tau_E$  expresses the characteristic time over which energy is transported out of the plasma. An analysis of the energy balance in a 50:50 D-T fusion plasma allows the following ignition criterion, known as the *Lawson criterion* [7], to be derived [8]:

$$nT\tau_E \gtrsim 3 \times 10^{21} \text{ keV s m}^{-3}.$$

At this value of the triple product, an idealised fusion reactor with no losses would achieve a *gain*,  $Q$ , of infinity.  $Q$  is defined as the ratio of fusion power produced to total heating power input (including both alpha-particle and auxiliary heating) to the plasma. An ignited plasma would allow all auxiliary heating sources to be switched off, as the fusion burn would be self-sustaining. A more realistic expectation is that some auxiliary heating power would be required in a fusion power plant in order to sustain the necessary conditions, so  $Q$  would be finite. Commercially-viable power generation would require  $Q$  well in excess of unity;  $Q \gtrsim 20$  is considered viable in many conceptual design studies [9]. Currently, the next-step goal in fusion research is to achieve  $Q > 1$  in a D-T plasma. To this end, a large experimental fusion device called ITER is under construction at a site in France. ITER is designed to achieve  $Q = 10$  for at least 400 s of a typical plasma pulse during D-T operation, which is scheduled to commence in 2027 [10]. Figure 1.3 shows the historical progress towards reactor conditions in

fusion experiments of the same type as ITER, known as *tokamaks*. It can clearly be seen that over the last four decades of fusion research, the temperature and value of the triple product has steadily increased thanks to the construction of larger tokamaks with improved confinement and auxiliary heating systems.

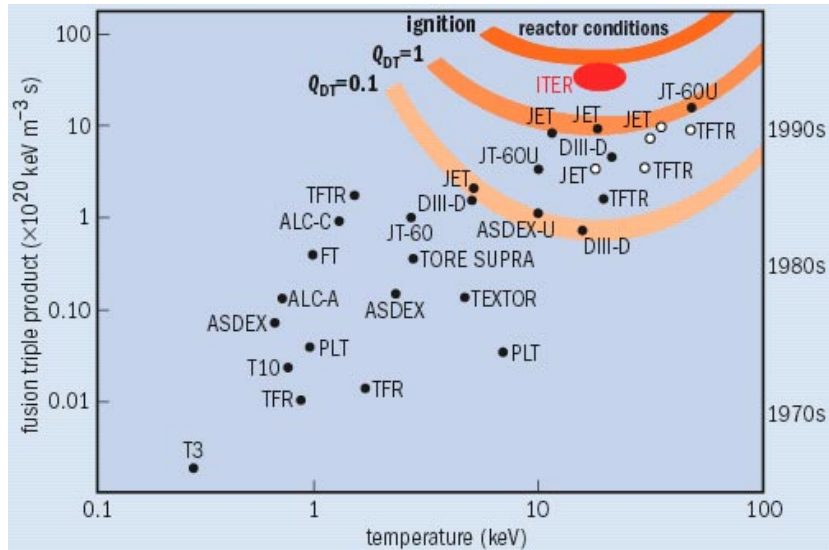


Figure 1.3: Values of the central ion temperature and the triple product achieved in experimental fusion devices of the tokamak type. Black points represent operation with deuterium, white points operation with deuterium and tritium. Only two tokamaks, namely the Joint European Torus (JET, EU) and the Tokamak Fusion Test Reactor (TFTR, USA), have operated with D-T plasmas to date. The projected operational regime of the next-step device, ITER, is also shown. Note that contours of  $Q$ -values are only meaningful for the D-T plasmas in this context. Image from <http://physicsworld.com/cws/article/print/2006/mar/01/fusion-the-way-ahead>.

The remainder of this chapter focuses on methods by which fusion plasmas may be confined and controlled using magnetic fields, starting with the confinement scheme which is pertinent to the tokamak.

### 1.3 Magnetic confinement of fusion plasmas

Since in a plasma the electrons are separated from the ions, one way in which the plasma may be confined is by using magnetic fields. Charged particles move freely along magnetic field lines but, to lowest order, are constrained to move on circular orbits around them. A configuration of closed magnetic field lines would therefore be expected to confine a plasma [11]. One way in which such a configuration may be created is with a set of coils linking a toroidal, or doughnut, shaped chamber. The magnetic field created by these coils runs the ‘long way’ around the torus, as shown in panel (a) of fig. 1.4. Unfortunately, a toroidal magnetic field alone cannot confine

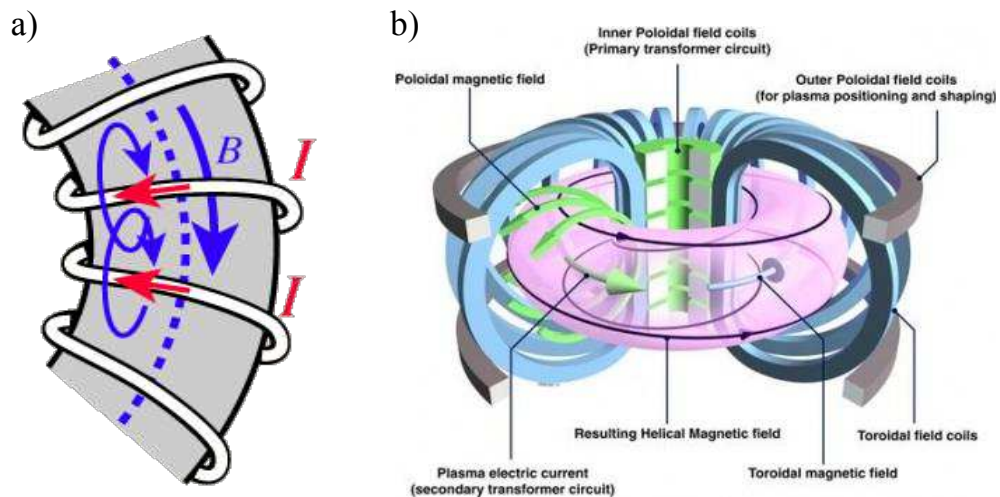


Figure 1.4: a) Plan view of a toroidal magnetic field  $B$  produced by a coil carrying a current  $I$  linking part of a torus. Image from <http://hyperphysics.phy-astr.gsu.edu/hbase/magnetic/toroid.html>. b) Schematic drawing of a plasma confinement scheme based on a set of coils producing a toroidal field (blue) and a toroidal current in the plasma induced by a transformer at the centre of the torus (green). The sum of the toroidal and poloidal fields produces a helical field (black line). Additional coils (grey) modify the poloidal field to provide control over the position and shape of the plasma, which is shown as a pink shaded volume. Image from <http://www.iopblog.org/2010-schools-lecture-part-5/>.

a plasma since the inhomogeneous field produces a higher pressure on the inside than on the outside of the torus [12]. The net force on the plasma in such a configuration causes it to expand radially outward. An additional component of the magnetic field, running the ‘short way’ around the torus, is necessary to allow external actuators to control the position of the plasma and arrest the outward expansion. This poloidal field may be created by inducing a toroidal current in the plasma, as illustrated in panel (b) of fig. 1.4. One of the characteristics of a plasma is that, unlike a normal conductor in which resistivity increases with temperature, the collisionality between particles, and hence electrical resistivity, *decreases* with increasing temperature. At the extreme temperatures of a fusion plasma, there is very little resistance to the flow of current. This makes the induction of a toroidal current an ideal scheme by which a poloidal magnetic field may be created. The magnetic confinement device which utilises this mechanism is called a *tokamak*, from the Russian acronym for **т**ороидальная **к**амера с **м**агнитными **к**атушками, meaning ‘toroidal chamber with magnetic coils’. During the creation of the plasma, when the temperature is low and the resistivity is relatively high, Ohmic heating by the toroidal current also provides a significant part of the total power input to the plasma.

### 1.3.1 Equilibrium in a tokamak

The high conductivity of tokamak plasmas, coupled with the fact that a stable equilibrium evolves on timescales much longer than the time taken to establish thermodynamic equilibrium, means that the simplest applicable description of these plasmas is provided by *ideal magnetohydrodynamics* (MHD). Ideal MHD considers the plasma to be an inviscid, perfectly-conducting fluid. Additional constraints are that the thermal speed of the electrons and the phase speed of perturbations in the plasma be much slower than the speed of light ( $v_{\text{th},e} = (2T_e/m_e)^{1/2} \ll c$ ,  $\omega/k \ll c$ ) [12]. Both of these conditions are easily satisfied in tokamak plasmas.

The equations of ideal MHD are as follows [12]:

$$\begin{aligned} \frac{\partial \rho}{\partial t} + \nabla \cdot (\rho \mathbf{u}) &= 0; \\ \rho \frac{d\mathbf{u}}{dt} &= \mathbf{J} \times \mathbf{B} - \nabla p; \\ \frac{d}{dt} \left( \frac{p}{\rho^\gamma} \right) &= 0; \\ \mathbf{E} + \mathbf{u} \times \mathbf{B} &= 0; \\ \nabla \times \mathbf{E} &= -\frac{\partial \mathbf{B}}{\partial t}; \quad \nabla \times \mathbf{B} = \mu_0 \mathbf{J}; \quad \nabla \cdot \mathbf{B} = 0. \end{aligned}$$

The first three expressions are the continuity equation (expressing conservation of mass), the equation of motion (expressing conservation of momentum) and the energy equation (expressing an adiabatic relationship between pressure and density). The fourth expression is the ideal-MHD form of Ohm's law, in which the RHS is zero because of the aforementioned assumption of perfect conductivity. The last three expressions encapsulate Maxwell's equations; note the absence of an equation for  $\nabla \cdot \mathbf{E}$ . The usual expression for  $\nabla \cdot \mathbf{E}$ , given as one of Maxwell's equations, is inapplicable to plasmas described by ideal MHD since the force between electrons and ions causes the plasma to maintain neutrality ( $n_i = n_e$ ) on spatial scales relevant to the MHD model. This does not however imply that  $\mathbf{E}$  or  $\nabla \cdot \mathbf{E}$  are zero within a plasma, only that the relation between the electric field and the local charge density is not captured by the Poisson equation. Ideal MHD forms a closed set of equations linking properties of the fluid, including the pressure  $p$ , density  $\rho$  and flow velocity  $\mathbf{u}$ , to electromagnetic vector fields of current density  $\mathbf{J}$ , electric field  $\mathbf{E}$  and magnetic field  $\mathbf{B}$ . Solving these equations allows the magnetic field configuration to be determined based on given profiles of, for example, the pressure and current density.

In a tokamak, the toroidal symmetry allows the solution of the ideal-MHD system of equations to be simplified. Figure 1.5 shows a cross-section of a torus with the linear and angular dimensions used to describe tokamak equilibria. The line described

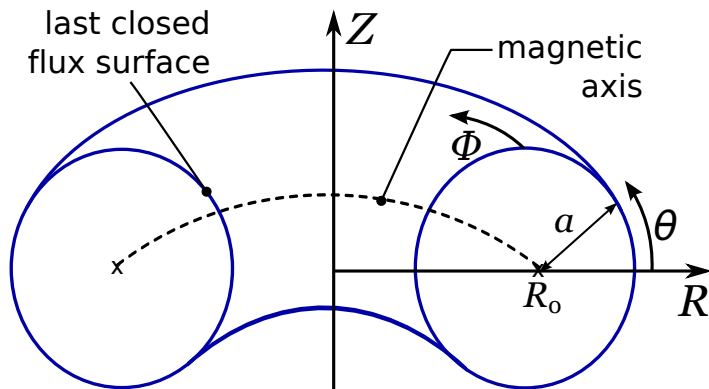


Figure 1.5: Diagram of the toroidal geometry used in the study of tokamak equilibria. The torus, a cross-section of which is shown in blue, is defined by its major radius  $R_0$  and minor radius  $a$ . The ratio of these quantities is known as the *aspect ratio*  $A = R_0/a$ . The  $Z$ -coordinate measures the height above the *midplane*, defined as the plane in which the magnetic axis lies. The region at  $R < R_0$  is often called the *inboard* side, while that at  $R > R_0$  is the *outboard* side. Two angles,  $\phi$  and  $\theta$ , measure the distance around the torus in the toroidal and poloidal directions.

by  $(R, Z) = (R_0, 0)$  is known as the *magnetic axis*; this is the circle on which the equilibrium field is purely toroidal,  $\mathbf{B} = B_0 \hat{\mathbf{e}}_\phi$ .

Starting from the reduced set of ideal-MHD equations for a static, incompressible plasma, an equation may be derived connecting the pressure of the fluid to the magnetic flux in a toroidal, axisymmetric configuration. From the condition that the equilibrium is static, the current and magnetic field are related to the pressure through ideal-MHD force balance,  $\mathbf{J} \times \mathbf{B} = \nabla p$ . It follows that the  $\mathbf{J}$  and  $\mathbf{B}$  field lines lie on surfaces of constant pressure; in other words, current and pressure are both *flux functions*. In an axisymmetric equilibrium it is useful to decompose the field into a poloidal component and a toroidal component,  $\mathbf{B} = \mathbf{B}_\theta + B_\phi \hat{\mathbf{e}}_\phi$ . The field may be expressed as the curl of a vector potential,  $\mathbf{B} = \nabla \times \mathbf{A}$ , so the poloidal component of the field depends on the toroidal component of the vector potential  $A_\phi$ . We introduce the stream function  $\psi = RA_\phi$  to write the poloidal field as

$$B_\theta = \frac{1}{R} \nabla \psi \times \hat{\mathbf{e}}_\phi.$$

$\psi$  is proportional to the total poloidal flux enclosed between the magnetic axis and a given flux surface. Contours of  $\psi$  form a set of nested toroidal flux surfaces within the confined plasma, with helical magnetic field lines lying on each surface. Combining

Ampère's law  $\nabla \times \mathbf{B} = \mu_0 \mathbf{J}$  with the force-balance relation  $\mathbf{J} \times \mathbf{B} = \nabla p$  then allows an equation governing the shape of these flux surfaces to be derived. This is the *Grad-Shafranov equation* [13], given as

$$R \frac{\partial}{\partial R} \left( \frac{1}{R} \frac{\partial \psi}{\partial R} \right) + \frac{\partial^2 \psi}{\partial Z^2} + \mu_0 R^2 \frac{\partial p}{\partial \psi} + F \frac{\partial F}{\partial \psi} = 0.$$

This second-order, nonlinear differential equation describes the force balance of a plasma with a pressure profile  $p(\psi)$  and a toroidal flux function  $F(\psi) = RB_\phi(\psi)$ . For practical purposes, the normalised quantity  $\psi_N = \psi/\psi_a$  is commonly used.  $\psi_N = 0$  at the magnetic axis and  $\psi_N = 1$  at the *last closed flux surface* (LCFS) which forms the boundary of the confined plasma.

A useful quantity in MHD stability analysis is the *safety factor*,  $q$ . This is defined as the number of toroidal transits made by a field line for one poloidal transit, i.e.

$$q = \frac{1}{2\pi} \oint \frac{B_\phi}{RB_\theta} dl_\theta$$

where  $dl_\theta$  represents an element of the poloidal path around a flux surface. A useful approximation in the case of flux surfaces with a near-circular cross-section is

$$q \simeq \frac{rB_\phi}{RB_\theta}$$

where  $r$  is the position in minor radius,  $0 \leq r \leq a$ . The implications of the safety factor for global MHD stability of the plasma will be discussed further in chapter 3.

Bulk plasma flow and non-ideal effects are not encapsulated in the Grad-Shafranov equation; toroidal flow in particular often results in significant modifications to the equilibrium in a real tokamak, and pressures parallel and perpendicular to the magnetic field may differ. The Grad-Shafranov equation nonetheless captures most of the essential features of the equilibrium in an axisymmetric toroidal confinement device. The concepts of the magnetic axis, flux surfaces, flux functions and safety factor will be used extensively throughout this work. One more concept which should be introduced before discussion of the experimental realisation of the tokamak is the *plasma beta*. This is an important measure of performance, and is defined as the ratio of kinetic pressure to magnetic pressure,

$$\beta = \frac{2\mu_0 p}{B^2}.$$

In order to maximise the efficiency of power generation in a fusion reactor,  $\beta$  should be as high as possible. The thresholds for various MHD instabilities however impose stringent limits on the achievable value of  $\beta$ ; for practical purposes,  $\beta < 10\%$  is considered to be achievable [14, 15]. The reason for maximising  $\beta$  is that the pressure

imposed by the magnetic field must be derived either from the toroidal field or from the induced poloidal field; making either the toroidal field coils or the central solenoid larger in order to carry a higher current dramatically increases the construction cost of a tokamak. In addition to the total beta, in which the magnetic pressure is dominated by the toroidal field, the *poloidal beta* is defined as the ratio of kinetic pressure to poloidal field pressure. This quantity is particularly relevant when considering the MHD stability of the plasma.

### 1.3.2 Conventional and spherical tokamaks

Since the first tokamak, T-1, was developed in Russia in 1958 [16], the majority of devices of this type have had an aspect ratio  $A \gtrsim 3$ . As experience with tokamaks developed, it was realised that certain deleterious MHD instabilities, among them the *kink mode* discussed in chapter 3, were mitigated at low aspect ratio. The largest tokamak currently in existence, JET, has a major radius  $R_0 = 2.96$  m and an aspect ratio  $A \approx 2.5$ . In the 1980s however, a branch of tokamak research started to develop the *spherical tokamak* (ST) concept [17]. The ST, which has a typical aspect ratio  $A \approx 1.3$ , benefits from the improved MHD stability of low aspect ratio as well as from the increase in beta which arises due to the much weaker toroidal field permissible in these devices [18]. The first high-temperature ST, the Small Tight-Aspect Ratio Tokamak (START), was developed at CCFE in 1990 and commissioned in 1991. Plasma  $\beta$  of up to  $\sim 40\%$  in plasmas with auxiliary heating was obtained, heralding the success of the ST concept [17].

Figure 1.6 shows a comparison between the typical cross-sections of a conventional and a spherical tokamak. The figure also illustrates a key feature of modern tokamaks, namely the *divertor* configuration. It was established on the Axisymmetric Divertor Experiment (ASDEX) tokamak in Germany that a regime with a transport barrier at the edge of the plasma, leading to greatly improved energy confinement, could be accessed using such a configuration [19]. Previous tokamak research had focused on the *limiter* configuration, in which the radial extent of the plasma was restricted by structures within the vacuum vessel. With the discovery of the so-called *H-mode* (high-confinement mode) in 1982, the focus shifted to the divertor configuration. In this configuration, toroidal coils are used to generate an additional component of the poloidal field at the edge of the plasma. At one or more points in the poloidal plane, the imposed poloidal field may be chosen to exactly cancel the poloidal field induced by the



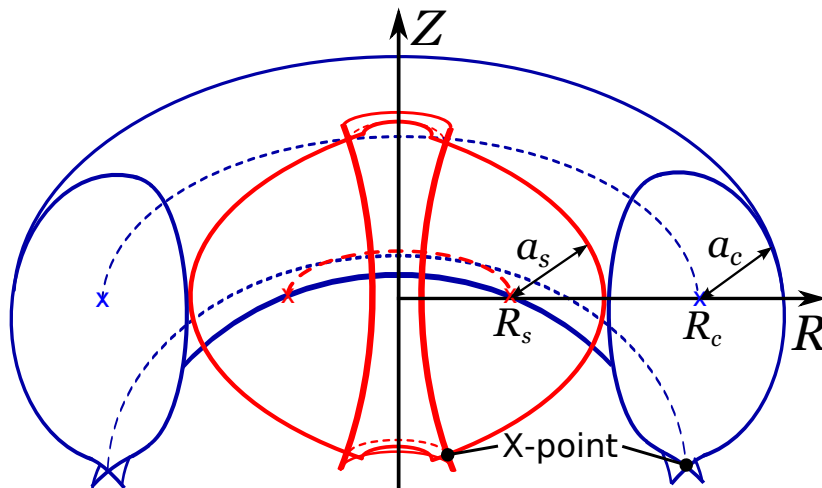


Figure 1.6: Schematic diagram showing the cross-section of a conventional large aspect ratio tokamak with major radius  $R_c$  and minor radius  $a_c$  (blue), and the cross section of a spherical tokamak with a similar minor radius  $a_s$  and a much smaller major radius  $R_s$  (red). The conventional tokamak illustrated here has a single X-point at the bottom of the poloidal plane, while the spherical tokamak has both an upper and a lower X-point. These features are discussed in more detail in the text.

plasma current. At such points, a poloidal field null in the form of an X-point is created. Two of the ‘legs’ extending from this X-point enclose the confined plasma, while the other two extend away from the plasma and eventually reach material surfaces within the vessel. The structure designed to shape the field in the region of the X-point, and to dissipate the heat and particle flux from the plasma which is efficiently transported along open field lines in this region, is known as a divertor. Both conventional and spherical tokamaks today use the divertor configuration, and they may have either one X-point (*single-null diverted*, SND) or two (*double-null diverted*, DND). Tokamaks with a divertor may operate either in H-mode or in L-mode (low-confinement mode) depending on the power input and plasma shaping.

Since the success of experiments on START, two much larger spherical tokamaks have been built to allow ST to explore regimes similar to those accessible to mid-sized conventional tokamaks. These are named the National Spherical Torus Experiment (NSTX, USA), and the Mega-Amp Spherical Tokamak (MAST, UK). Operations on each of these devices commenced in 1999. Recent experiments performed on MAST, and the subsequent numerical modelling of these experiments, are the subject of this dissertation. Both MAST and NSTX are currently in the process of being upgraded, with an advanced divertor configuration, a more flexible auxiliary heating system and a larger central solenoid offering the potential for improved performance and longer pulse lengths in MAST-UpGrade. In table 1.1 are shown some of the key parameters of

typical discharges (pulses) in MAST and JET, along with values foreseen for MAST-Upgrade and ITER. It should be noted that these are not the maximum values which have been achieved or are expected in each device, but rather a set of simultaneously-achievable values for a typical pulse. It is clear that while the step from MAST to

	MAST	MAST-U	JET	ITER
Major radius (m)	0.90	0.90	3.0	6.2
Minor radius (m)	0.50	0.50	1.3	2.1
Plasma volume (m <sup>3</sup> )	8.5	8.5	90	830
Plasma current (MA)	0.9	2.0	3.5	15
Magnetic field on axis (T)	0.55	0.84	3.4	5.3
Pulse length (s)	0.50	4.0	20	650
Aux. heating power (MW)	3.5	5.0	35	50

Table 1.1: Parameters of typical discharges in MAST and JET (achieved) and in MAST-Upgrade and ITER (predicted).

MAST-Upgrade represents a modest improvement in performance, the step from JET to ITER entails an order of magnitude increase in many of the key plasma parameters, in particular the volume of the plasma, the pulse duration and the plasma current. This is thanks in large part to the use of superconducting coils in ITER. These will allow a higher current and toroidal field to be sustained for much longer than in JET, which uses water-cooled copper coils.

Figure 1.7 shows a plasma inside the MAST vessel. Most of the visible light consists of deuterium Balmer-alpha ( $D_\alpha$ ) emission from neutral atoms at the edge of the plasma. Observations in the visible part of the spectrum provide limited information about the behaviour of the core plasma, since the deuterium and most of the impurities in the core are fully ionised. The continuum radiation from the core delivers most of its power in the UV and soft X-ray wavelength ranges. For this reason, diagnosing the properties of the confined plasma poses a technical challenge. Some of the plasma diagnostics commonly used on tokamaks are described in the next section. Before considering these diagnostics however, magnetic confinement schemes being developed as an alternative to the tokamak should be mentioned.

### 1.3.3 Alternatives to the tokamak

Given that it relies on a primary transformer circuit to induce the plasma current, a tokamak is inherently a pulsed device. The duration of each pulse is limited by the maximum flux swing of the transformer. One type of magnetic confinement device developed to overcome this limitation is the *stellarator*. Instead of imposing a purely



Figure 1.7: Colour photograph of a plasma inside the MAST vessel. Deuterium Balmer-alpha ( $D_\alpha$ ) emission at 656.1 nm dominates the visible part of the spectrum. Also visible in the image are in-vessel poloidal field coils (top and bottom) and smaller radial coils (bottom left and bottom right) used to perturb the edge of the plasma to control the MHD stability of the edge region. The bright spot on the centre column marks the location of a gas valve used to fuel the plasma; emission from the injected gas can be seen wrapping around the centre column in the middle of the image as the fuel becomes ionised and starts to flow along the field lines.. Image credit: Dr. Scott Silburn and Dr. James Harrison.

axisymmetric toroidal field, the stellarator uses coils with a complex shape surrounding a helical vessel to impose both a toroidal and a poloidal field on the plasma. Although this overcomes the limitations imposed by the use of a transformer, the cost and complexity of designing and manufacturing extremely complicated coils means that the development of stellarators has historically been neglected in favour of the much simpler tokamak device. Numerous stellarators are however in use, notably in Japan, Germany and Spain. The latest development is the completion of the Wendelstein 7-X stellarator in Germany, which has a poloidal cross-section similar in area to that of a mid-sized tokamak. First plasma on Wendelstein 7-X is expected by the end of 2015 [20].

Another type of magnetic confinement device is the *reversed field pinch* (RFP). The configuration of a RFP is somewhat similar to that of a tokamak, but the applied toroidal field is typically a factor of 10 weaker than that in a tokamak with similar dimensions. A large toroidal current induces a strong poloidal field in the plasma, while a *dynamo effect* causes an equilibrium to form in which the direction of the toroidal field is reversed near the edge of the plasma. In terms of the safety factor  $q$  introduced above, rather than having a  $q$ -profile which increases monotonically with radius as is typically the case in a tokamak, a RFP has a  $q$ -profile which decreases monotonically with radius and which changes sign near the edge of the plasma. This

renders the RFP configuration extremely susceptible to low-order, large-scale MHD instabilities. It was found recently however that RFP plasmas are capable of forming a self-organised helical state dominated by a kink mode of a single toroidal and poloidal mode number [21]. These helical equilibria are also found to form electron transport barriers, improving confinement. The single helical axis (SHAx) state is observed to persist in some cases for times comparable to the current diffusion time, which at several tens of milliseconds is the longest timescale of interest in the system. The scaling of this persistence with plasma current is moreover found to be favourable [21], supporting further investigation of this phenomenon [22].

The reason for discussing these alternatives to the tokamak is that many of the experimental techniques introduced in this work are applicable, either directly or with minor modifications, to the stellarator and the RFP. The diagnostics described in the next section, as well as the methods of plasma heating and the diagnostics of the energetic ion population discussed in later chapters, may all be used on stellarators and RFP even if the modelling codes required to analyse those experiments are somewhat more complex. Figure 1.8 shows schematically the geometry of the magnetic field in the Wendelstein 7-X stellarator and in a circular cross-section RFP.

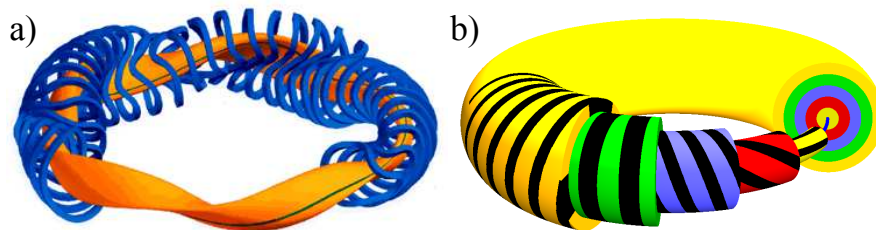


Figure 1.8: a) Diagram of the coil geometry (blue) surrounding part of the Wendelstein 7-X plasma (orange). A single magnetic field line is shown in green. Image from <http://www.ihm.kit.edu/97.php> b) Schematic representation of the magnetic field on concentric flux surfaces in a reversed field pinch. The black striations on each surface show the orientation of the field on that surface. Image credit: Wikimedia Commons.

## 1.4 Fusion plasma diagnostics

### 1.4.1 Active diagnostics

The lack of visible emission from the core of a fusion plasma, and the requirement for spatially-resolved measurements of plasma profiles, means that many diagnostics rely on *active* probing techniques. Active techniques are those which depend on a controlled, externally-driven perturbation to generate a signal. One such example is the Thomson scattering (TS) diagnostic used on most tokamaks to obtain spatially and

temporally-resolved profiles of electron density and temperature. TS diagnostics use a pulsed laser, the light from which scatters off the electrons in the plasma. Measuring the intensity of the scattered light provides information on the electron density along the laser path, while the broadening of the line may be resolved with a spectrometer to obtain measurements of the electron temperature. Another commonly-used active diagnostic is charge exchange recombination spectroscopy (CXRS). A beam of neutral atoms fired into the plasma may exchange electrons with impurity ions, which subsequently emit line radiation characteristic of that element and charge state. Modelling of the collisional and radiative processes using the known electron density and temperature, along with suitable atomic physics data, allows the impurity ion density to be determined. A more common application of CXRS however is to determine the ion temperature and flow velocity by measuring the broadening and Doppler shift of one of the spectral lines. The mechanisms underlying the generation of TS and CXRS signals are illustrated in fig. 1.9.

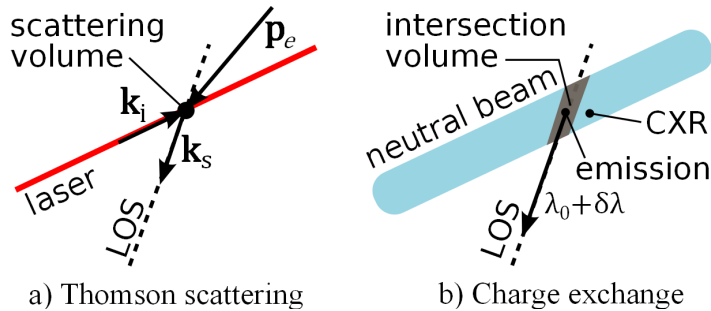


Figure 1.9: a) Schematic diagram of the principle underlying a Thomson scattering diagnostic. An incident photon (wave vector  $\mathbf{k}_i$ ) is scattered by an electron to produce a scattered photon (wave vector  $\mathbf{k}_s$ ) travelling along the LOS of the diagnostic. The difference between the incident and scattered wave vectors is the momentum of the electron prior to scattering ( $\mathbf{p}_e = \hbar(\mathbf{k}_s - \mathbf{k}_i)$ ). b) Schematic diagram of the principle underlying a charge exchange recombination diagnostic. A beam of neutral hydrogen atoms provides a donor for charge exchange (CX) by which an impurity ion gains an electron. The subsequent radiative decay of the impurity ion causes it to emit a photon at wavelength  $\lambda_0$  in the rest frame of the ion. The measured wavelength includes a Doppler shift  $\delta\lambda = \lambda_0(v_i/c)$ , where  $v_i$  is the combination of the thermal and bulk flow velocities of the ion projected onto the LOS.

High-resolution TS and CXRS diagnostics were used on MAST. Figure 1.10 shows profiles of the plasma parameters measured by each of these diagnostics during a typical MAST pulse. ‘Pulses’ or ‘discharges’ are also commonly called *shots*; these terms will be used interchangeably throughout this work.

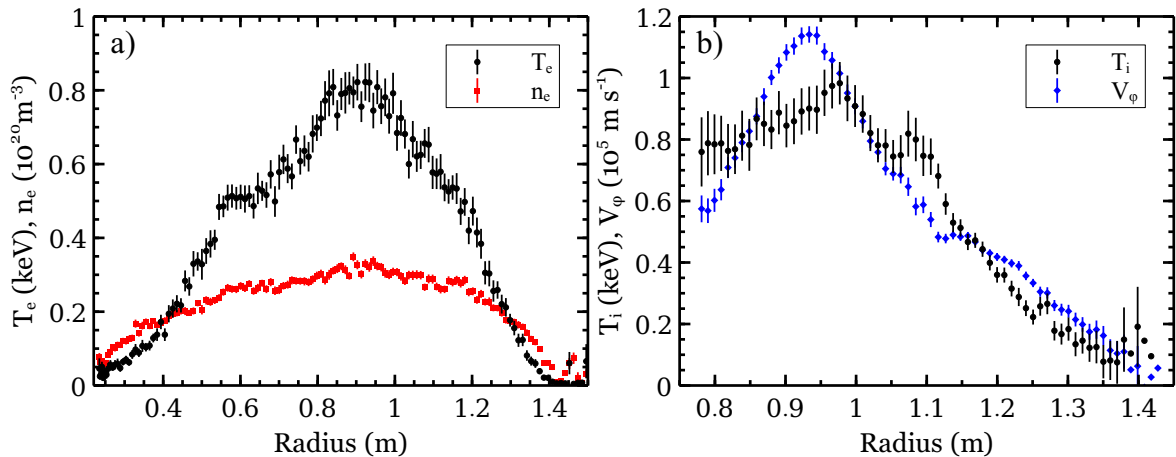


Figure 1.10: a) Profiles of electron temperature and density measured with the 130-point Nd:YAG laser TS diagnostic on MAST. Data were acquired at  $t = 0.205$  s during shot #29034. b) Corresponding profiles of carbon ion temperature and toroidal rotation velocity measured with the CXRS diagnostic on one of MAST’s two neutral beams.

## 1.4.2 Passive diagnostics

Passive diagnostics are those which make use of the naturally-occurring emission from the plasma. A common example is that of soft X-ray (SXR) diagnostics, which have been used since the early days of fusion research [23]. SXR diagnostics make use of the continuum radiation arising from Coulomb collisions between free electrons and ions to infer the density and temperature of the free electrons. The gradient of the continuous spectrum with respect to wavelength allows the electron temperature to be inferred, while the intensity of the emission is proportional to the product of the free electron and ion densities. Since no active probing beam is used, measurements from such diagnostics are inherently line-integrated. If sufficient lines of sight are available, and if the system has rotational symmetry about a particular axis, Abel inversion may however be used to deduce one-dimensional profiles of electron density. This is significantly complicated by uncertainties in the concentration of impurity ion species in the plasma, which is often not straightforward to measure [24]. For this reason, SXR diagnostics on current fusion experiments are more commonly employed to observe perturbations within the plasma caused by various instabilities. This has historically been the primary use of the SXR diagnostic installed on MAST [25, 26]. X-ray spectroscopy may also be used to diagnose the presence of metallic impurities in the plasma. The emission lines of high ionisation states of heavy ions such as iron, tungsten and molybdenum lie in the X-ray range of wavelengths. Impurity ions also increase the *effective charge* of the plasma. This is a normalised measure of the concentration

of non-hydrogenic species, defined as

$$Z_{\text{eff}} = \frac{\sum_i n_i Z_i^2}{n_e}$$

where the sum is over each of the ion species in the plasma. A pure hydrogenic plasma has  $Z_{\text{eff}} = 1.0$ , while a 1% concentration of fully-ionised carbon for instance would increase this to  $Z_{\text{eff}} = 1.3$ . Local SXR emission is proportional to  $Z_{\text{eff}}$ , so these diagnostics can provide an indirect measurement of the concentration even of fully-ionised impurity species.

At the other end of the spectrum of electromagnetic waves which are of interest in fusion plasmas, many low-frequency MHD perturbations are detected with the use of magnetic pick-up coils located inside the vacuum vessel. These are known as *Mirnov coils* [27]. The voltage induced by a changing magnetic flux through the coil is recorded and integrated to provide measurements of the perturbation amplitude. The frequencies of interest typically span the range from a few kilohertz to a few megahertz. The orientation of the coil renders it sensitive to changes in a particular component of the magnetic field; radial, poloidal and toroidal perturbations may evolve differently depending on the nature of the MHD instability. Arrays of Mirnov coils in the MAST vessel were sensitive to perturbations in each of these three axes [28]. The largest set consisted of a toroidal array of vertically-oriented coils close to the outboard midplane, which detected perturbations to the poloidal field. The signatures of many of the MHD instabilities observed in MAST in the data from these coils are illustrated in chapter 3.

Each of the diagnostics described in this section is designed to measure properties of the thermal species in the plasma. There is however another population of particles which often demands a different set of approaches to its detection. These are the *super-thermal* ions. Occurring naturally as a product of fusion reactions, energetic ions are also created by auxiliary heating systems in the manner described in the next chapter. It is with the population of energetic ions in MAST plasmas that the rest of this thesis is concerned. The structure of this work is outlined in the following section.

## 1.5 Thesis outline

The next chapter, as mentioned above, introduces the mechanisms of energetic-ion, or *fast-ion*, production in tokamaks. The interaction of these particles with the background plasma drives numerous MHD instabilities, and the physics of this instability drive and the subsequent transport of fast ions is the subject of chapter 3. Together, these two chapters provide the conceptual background necessary for understanding the

motivation of this work.

Chapter 4 describes the four diagnostics used during the 2013 experimental campaign on MAST to study the fast-ion population. The interpretation of data from these diagnostics forms the basis of the results presented later in this dissertation. One of these diagnostics, namely the fast-ion deuterium alpha (FIDA) spectrometer, is described in greater detail in chapter 5. The exploitation of the FIDA diagnostic was the primary responsibility of this author during the 2013 experimental campaign. Set-up and calibration procedures are described, and the process of data acquisition and processing outlined. The chapters on experimental methodology conclude with a discussion of the ancillary fast-ion and synthetic-diagnostic modelling in chapter 6.

The results of the data analysis, along with the interpretation of these results, are presented in chapters 7 and 8. Those instabilities which interact with the fast ions through a wave-particle resonance are the subject of the first of these chapters. Such instabilities exhibited varied behaviour in MAST, and were observed in the vast majority of discharges with auxiliary heating. The second results chapter concerns those instabilities which are believed to affect the fast ions through means other than a direct resonance. The effects of these instabilities are weaker and harder to resolve than those discussed in the preceding chapter, so different techniques must be adopted in the analysis. In each case, global transport modelling is used to attempt to reproduce the effects of the instabilities on fast ions. The results of this modelling are compared to fast-ion diagnostic data, and reasons for discrepancies are discussed.

Finally, a summary of the main results and conclusions are presented in chapter 9.



# Chapter 2

## Fast ions in tokamaks

### 2.1 Outline

In order to heat a D-T plasma to temperatures sufficient for the generation of useful amounts of fusion power, it is anticipated that auxiliary heating methods will be required in addition to the Ohmic heating and fusion- $\alpha$  heating of the plasma. Systems which fulfil this role include neutral beam injection (NBI) and radio-frequency heating, each of which generates a super-thermal tail on the ion or electron velocity distribution. These energetic particles serve the dual purpose of providing supplementary current drive in cases where they are accelerated parallel to the magnetic field, and providing a source of heating via the process of collisional energy transfer to the bulk plasma. Further to these auxiliary heating mechanisms, fusion reactions themselves generate populations of energetic ions which, in reactor-relevant conditions, also heat the plasma.

Mechanisms by which energetic ions are produced include NBI and ion cyclotron resonance heating (ICRH). Auxiliary heating mechanisms which deposit power in the electron population include electron cyclotron and lower hybrid heating and current drive<sup>1</sup>. The topic of this work is the transport of fast ions (FI), so we restrict consideration to NBI and ICRH as well as energetic ions produced by fusion reactions.

This chapter introduces the principles by which each auxiliary heating system delivers energy to the plasma and focuses particularly on the FI population produced by neutral beam injection, which was used for heating and current drive in MAST plasmas. The confinement, orbit dynamics, velocity distributions and possible loss mechanisms of particles in tokamak plasmas are described. Finally, the relevance of

---

<sup>1</sup>Above a critical electron density, lower hybrid waves may also heat the ions [29,30]. This technique is seldom used in present experiments however [31], and is not discussed here.

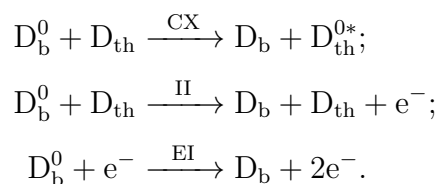
MAST FI research to the development of advanced operating scenarios for ITER is highlighted.

## 2.2 Mechanisms of fast-ion production

### 2.2.1 Neutral beam injection

First employed on tokamaks in the 1970s [32], NBI systems inject neutral atoms into the plasma at a fixed energy set by accelerating ions across a given potential difference before neutralising them in the NBI beamline. Electron and ion impact ionisation and charge exchange with plasma ions then result in the production of FI which respond to the helical magnetic field. FI which are confined in the magnetic field interact with the background plasma, slowing down and undergoing scattering by collisional interactions with bulk electrons and ions [33]. The energy of the injected ions is thus deposited in the plasma, causing electron and ion heating.

Beam species typically used in tokamaks include deuterium [34], tritium [35] and helium [36]. D and T beams serve the dual purpose of fuelling the plasma as well as heating it. Injected He may be used as a minority species for subsequent ICRH [37], via which the helium ions are accelerated from the injection energy of  $\sim 100$  keV up to  $\sim 1$  MeV. Deuterium beam injection into a deuterium plasma was used in MAST. The two beams on MAST, denoted south-south (SS) and south-west (SW), injected up to 2.5 MW each of neutral deuterium at energies up to 75 keV. The NBI power is significantly higher than the Ohmic heating power, with  $P_{\text{OH}} \lesssim 1$  MW. Injection was in the co-current direction under normal operation, centred vertically on the machine midplane and oriented toroidally with tangency radius  $R_{\text{tan}} = 0.7$  m. This geometry allowed the beams to drive current in the plasma as well as delivering electron and ion heating. The main channels for ionisation of deuterium beam neutrals are charge exchange (CX) with thermal deuterons, and ion and electron impact ionisation (II and EI). These proceed according to the following reaction equations:



Here, the subscripts ‘b’ and ‘th’ refer to the beam and thermal ions, with superscripts ‘0’ to denote a neutral atom and ‘\*’ to denote an atom in an excited state. At the energies of the MAST NBI system (45 keV to 75 keV), CX, II and EI are responsible

for approximately 55%, 35% and 10% of the beam ionisation respectively; the exact ratio depends on the beam energy and electron temperature. Collisions with fast ions and impurity ion species make a small additional contribution to CX and II ionisation of beam neutrals. Despite the fact that CX with FI is responsible for ionisation of very few beam neutrals, the Balmer-alpha light from FI which have been reneutralised in the neutral beam is measurable; the measurement of this *fast-ion*  $D_\alpha$  (FIDA) light is the basis of much of the work presented in this thesis.

### 2.2.2 Ion cyclotron resonance heating

A radio-frequency electromagnetic wave launched from the low-field side of the tokamak propagates perpendicular to the field as a fast magnetosonic wave, with limited damping by the thermal electrons, until it reaches a location where the cyclotron frequency of one of the ion species present in the plasma matches the frequency of the wave. Strong absorption of the left-hand circularly polarised component of the wave occurs at this ‘resonance layer’, with the wave energy being converted to kinetic energy in the ions’ motion perpendicular to the magnetic field [38]. This technique for ion heating was first used on tokamaks in the 1970s [39], although heating via ion cyclotron rather than ion-ion hybrid resonance effects was not verified experimentally until the early 1980s [40]. Effective ion heating requires the wave to resonate with a minority ion species, present in a concentration of a few percent of the bulk ion density and ideally localised in the core of the plasma, in order to allow wave power to penetrate to the core rather than being absorbed at the edge. The parallel wavenumber should be small in order to maximise the amplitude of the left-hand circularly polarised component of the fast wave [38].

In cases in which a minority species is accelerated at its fundamental cyclotron frequency, a high-energy, anisotropic tail may be formed on the velocity distribution of the minority species [38]. Heating of minority FI produced either by NBI or by fusion reactions allows access to energies in the tail of the ion velocity distribution which may be even higher than the birth energy of the FI [38]. It was found in JET D-T experiments that one of the most promising candidate scenarios for increasing the ion temperature via ICRH is to use  $^3\text{He}$  minority heating, since the ICRH-accelerated  $^3\text{He}$  ions deposit much of their energy in the thermal D and T ions via collisional interactions [41]. Third-harmonic ICRH acceleration of  $^4\text{He}$ , injected into the plasma via the NBI system, has also been used on JET to simulate aspects of the physics of

fusion-born alpha particles with MeV energies [37].

### 2.2.3 Fusion reactions

As described in the previous chapter, fusion reactions between various combinations of D, T and  $^3\text{He}$  ions release several MeV of energy each; this energy is divided between the fusion products in inverse proportion to their mass, due to the requirement of momentum conservation. Energetic protons, tritons, helium-3 ions and helium-4 ions (fusion  $\alpha$ -particles) are produced in addition to energetic neutrons. Fusion reactions therefore constitute an additional source of FI. These ions are born with a fixed energy in the centre-of-mass frame which depends on the specific fusion reaction leading to their production. This source of FI, unlike NBI or ICRH, is inherently isotropic in velocity space.

## 2.3 Dynamics of fast ions in tokamak plasmas

### 2.3.1 Particle orbits in a tokamak

As they follow the magnetic field lines, the particles in a tokamak plasma are subject to the Lorentz force, given by

$$\mathbf{F} = Ze(\mathbf{E} + \mathbf{v} \times \mathbf{B})$$

where the charge of the particle is  $Ze$  and  $\mathbf{E}$ ,  $\mathbf{v}$  and  $\mathbf{B}$  represent the vectors of electric field, particle velocity and magnetic field. The  $\mathbf{v} \times \mathbf{B}$  component of this force, being perpendicular to both the particle velocity and the magnetic field, causes the particles to circle around the magnetic field lines with the cyclotron frequency  $\Omega_c$ , where

$$\Omega_c = \frac{ZeB}{m}.$$

The *Larmor radius*, or *gyro-radius*, of this motion is determined by the Lorentz force. It is given by

$$r_L = \frac{v_\perp}{\Omega_c} = \frac{mv_\perp}{ZeB},$$

where  $v_\perp$  is the particle's velocity perpendicular to the magnetic field. If the magnetic field were entirely homogeneous then, in the absence of any electric field, this circular motion superposed on uniform parallel motion at the speed  $v_\parallel$ , where  $|\mathbf{v}|^2 = v^2 = v_\parallel^2 + v_\perp^2$ , would completely describe the particle's trajectory. In a tokamak however, as shown in chapter 1, the field lines are helical and lie on toroidal flux surfaces. This geometry introduces several *drifts* into the particle motion. In the following discussion, the drift velocity should be understood as applying to the particle's *guiding centre*, which is the instantaneous position of the centre of the particle's gyro-orbit. The

trajectory of the guiding centre will be referred to as the *drift orbit*.

A charged particle in a magnetic field subjected to any force  $\mathbf{F}$  will experience a drift at the velocity

$$\mathbf{v}_d = \frac{\mathbf{F} \times \mathbf{B}}{ZeB^2}.$$

Crucially, this drift is perpendicular to both the imposed force and the magnetic field. The drifts which a particle experiences due to the toroidal geometry and the inhomogeneous magnetic field are the *curvature drift* and the *grad-B drift*. Neglecting currents [42], these combine to give

$$\mathbf{v}_B = \frac{m}{2Ze} (v_\perp^2 + 2v_\parallel^2) \frac{\mathbf{b} \times \nabla B}{B^2},$$

where  $\mathbf{b}$  is the unit vector in the direction of the magnetic field. The dominant component of the magnetic field is toroidal, and the gradient of this field is directed radially inward towards the centre column of the tokamak. The curvature and grad-B drifts are therefore vertical, and ions and electrons drift in opposite directions due to the charge dependence of  $\mathbf{v}_B$ . The resulting vertical charge separation is cancelled by a flow of electrons along the poloidal field, which allows the plasma to attain quasineutrality and hence remain in equilibrium. In reality, currents are present in the plasma and the field strength is not a function solely of major radius, so the above expression for  $\mathbf{v}_B$  is only approximate. Additional drifts also arise due to the radial electric field which accompanies plasma rotation in a tokamak. The  $\mathbf{E} \times \mathbf{B}$  drift velocity,

$$\mathbf{v}_E = \frac{\mathbf{E} \times \mathbf{B}}{B^2},$$

is independent of the charge and mass of the particles and hence acts equally on electrons and ions to generate a bulk flow.

In addition to drifts perpendicular to the magnetic field, a gyrating particle entering a region of increasing magnetic field strength is subject to a force parallel to the magnetic field at its guiding centre. Particles therefore decelerate in the parallel direction as they enter a region of increasing field strength, with the kinetic energy being transferred into their perpendicular motion. This situation pertains to the poloidal motion of particles around the flux surfaces in a tokamak, since the field strength is higher on the inboard side (close to the centre column) than on the outboard side. A simplified illustration of the geometry of such a ‘magnetic mirror’ is shown in fig. 2.1. Particles with  $(v_\parallel/v_\perp)^2 < B_{\max}/B_{\min} - 1$ , evaluated at the position of the magnetic field minimum, are unable to overcome the retarding force imposed by the gradient

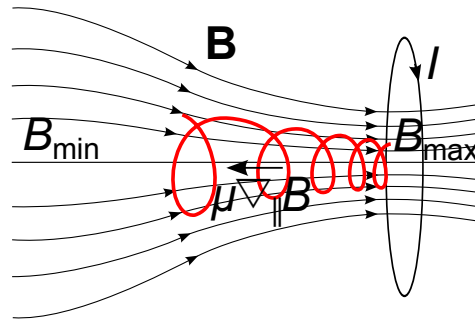


Figure 2.1: Sketch of a ‘magnetic mirror’ field configuration, in which the current in a circular coil causes an externally-imposed axial magnetic field to increase in strength from left to right. Part of the trajectory of a charged particle is shown in red; a force equal to  $-\mu\nabla_{\parallel}B$  acts on the particle in the axial direction, where the magnetic moment  $\mu = mv_{\perp}^2/(2B)$ .

of the magnetic field and are reflected by the mirror. Extending this analysis to the tokamak configuration, the drift orbits may be divided into two classes. *Passing orbits* have a sufficiently high value of *pitch*, defined as  $p = v_{\parallel}/v$ , to overcome the mirror force and are therefore able to traverse the full poloidal extent of a flux surface, circling the magnetic axis. *Trapped orbits* have values of  $p$  too low to overcome the mirror force, and their parallel velocity changes sign at a certain point on the flux surface; these orbits do not enclose the magnetic axis. The value of pitch which separates passing from trapped orbits, under the simplified assumption of a magnetic field which varies solely as a function of major radius according to  $B = B(R_0)(R_0/R)$ , is

$$p_0 = \left( \frac{2r}{R_0 + r} \right)^{1/2} \quad (2.3.1)$$

where  $p_0$  denotes the pitch evaluated at the outboard midplane where the field is weakest. The sign of  $p$  is further used to distinguish between *co-passing* ( $p > 0$ ) and *counter-passing* ( $p < 0$ ) orbits, where ‘co’ and ‘counter’ refer by convention to the direction of the toroidal motion with respect to the direction of the plasma current. The effect of curvature and grad-B drifts is to reduce the extent of co-passing orbits in minor radius and displace their centres outward in major radius, and to increase the extent of counter-passing orbits in minor radius and displace them inward in major radius. Examples of co-passing and trapped particle orbits are shown in fig. 2.2, along with a trapped beam ion trajectory in MAST. The shape of the poloidal projection of the trapped orbits means that these are also known as *banana orbits*. The ‘tips’ of the banana for a barely-trapped particle approach each other close to the midplane on the inboard side, while for a deeply-trapped particle the banana tips are located on opposite sides of the outboard midplane.

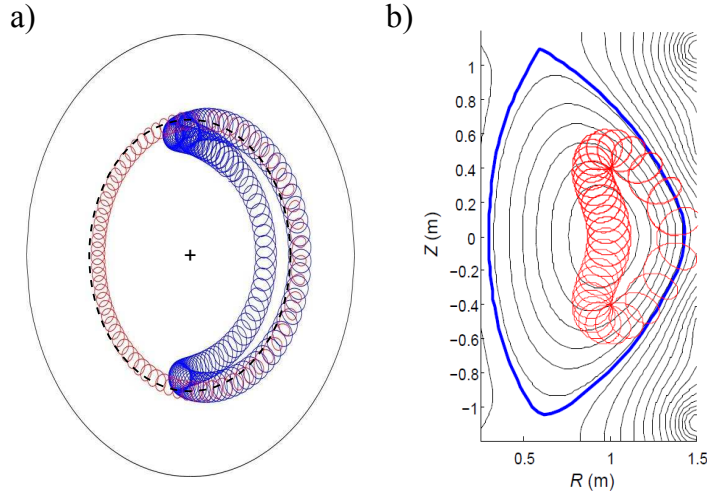


Figure 2.2: a) Poloidal projections of trapped and passing orbits in toroidal geometry with elliptical flux surfaces. The red orbit corresponds to a toroidally co-passing particle, and the blue orbit corresponds to a trapped particle. The dashed curve represents a flux surface, with the ‘+’ symbol indicating the position of the magnetic axis. The solid black curve marks the last closed flux surface (LCFS) at the edge of the plasma. Figure adapted from <http://iter.rma.ac.be/en/physics/tokamak>. b) A trapped 70 keV beam-ion orbit (red) calculated with the CUEBIT full-orbit code [43] for typical MAST equilibrium geometry. The ion is born on the midplane at  $R = 1.4$  m. Thin black curves represent flux surfaces, with the thick blue curve marking the LCFS. Figure provided by Dr. Ken McClements.

Neglecting collisions for the moment, which is a sensible zero-order approximation since the mean free path of FI in a tokamak is typically many times the circumference  $2\pi R_0$ , the kinetic energy  $E = mv^2/2$  of a particle is conserved. In addition to the kinetic energy, an additional constant of motion applies in the axisymmetric tokamak configuration. This is the *toroidal canonical momentum*, defined as

$$P_\phi = mRv_\phi + Ze\psi$$

where  $\psi$  is the poloidal flux discussed in chapter 1, and  $v_\phi$  is the velocity in the toroidal direction. This conservation is a direct consequence, via Noether’s Theorem, of the toroidal symmetry [44]. Any perturbations to the equilibrium which break this symmetry lead to non-conservation of  $P_\phi$ , which has important consequences for the confinement of FI in the presence of the non-axisymmetric perturbations which will be discussed in the next chapter. In the presence of time-varying electromagnetic fields, the symmetry leading to conservation of kinetic energy is broken. Collisions between particles also cause the values of  $E$  and  $P_\phi$  to change. Each of these processes is therefore responsible for an enhancement of particle transport.

### 2.3.2 Properties of fast-ion orbits in MAST

The expression given in eq. (2.3.1) for the pitch  $p_0$  which separates passing from trapped orbits is based on the assumption that the Larmor radius is much smaller than the magnetic field gradient scale length. In that case, the zero-order magnetic moment  $\mu_0 = mv_{\perp}^2/(2B)$  is an *adiabatic invariant*, the gyro-averaged value of which is a constant of motion [45]. It is important to distinguish such adiabatic invariants from the quantities  $E$  and  $P_{\phi}$ , which are true constants of the motion even on sub-cyclotron timescales. In a ST such as MAST, the magnetic field variation over a single gyro-orbit can be significant and the condition  $\langle \mu_0 \rangle_{\text{gyro}} = \text{constant}$  is often violated by FI [46]. Higher-order, energy-dependent corrections to  $\mu$  are required [47]. The pitch separating passing from trapped orbits is therefore a function of energy. Furthermore, the clear separation of confined orbits into the passing and trapped categories breaks down particularly strongly at low aspect ratio. Many beam ions in MAST follow *potato orbits*, which are reflected by the mirror force but which have sufficiently large orbit widths to encircle the magnetic axis, and *stagnation orbits*, which are aligned parallel to the magnetic axis but are displaced outward in major radius such that they never encircle the axis despite having a near-constant parallel velocity. Numerical calculations with a high-resolution computational grid are generally required to classify the orbits accurately.

NBI-generated FI in MAST, with the exception of those born very near the edge of the plasma, are deposited on co-passing orbits. The pitch of FI born close to the magnetic axis is approximately 0.7, which for a 70 keV deuteron in a magnetic field of 0.55 T implies a Larmor radius of  $r_L = 7$  cm. The drift orbit width of such an ion, which is the maximum distance by which the drift orbit is displaced from a flux surface, is also approximately 7 cm based on a minor radius  $r = 0.15$  m, major radius  $R = 0.95$  m and safety factor  $q = 1$  [42]. Both of these values are significantly smaller than the plasma minor radius of  $a \approx 0.5$  m, so the FI born in the core of MAST are well confined.

### 2.3.3 Collisional interactions with thermal species

As mentioned above, fast particles in a tokamak plasma collide only rarely with other (fast or thermal) particles. ‘Collisions’ in this case should be understood as referring to significant deviations from the trajectory prescribed by the equilibrium field; most interactions between particles in a plasma consist of Coulomb interactions



with a large impact parameter, which cause only small deviations from the initial trajectory. Collisions are therefore usually composed, on the microscopic scale, of the cumulative effect of many small-angle deviations. For thermal ions, the *normalised collisionality*  $\nu^* \propto \nu_{ii}/(\epsilon\omega_b)$ , where  $\nu_{ii}$  is the frequency of ion-ion collisions,  $\epsilon$  is the inverse aspect ratio  $r/R_0$ , and  $\omega_b$  is the poloidal *bounce frequency* of trapped ions, is generally in the range 0.001 to 1 [48]. This collisionality is sufficiently high to cause the thermal population to relax into a Maxwellian velocity distribution on a timescale shorter than that of the macroscopic plasma evolution. Populations of FI generated by NBI, ICRH or fusion reactions however deviate strongly from a Maxwellian velocity distribution. This is due to the low collisionality experienced by the FI, which allows them to remain out of equilibrium with the background plasma for many hundreds or thousands of transit periods.

One of the key parameters in the physics of FI in plasmas is the *critical energy*. This is the energy at which a slowing-down FI delivers equal power to the thermal ion and electron populations, and may be expressed as [33]

$$E_{\text{crit}} = 14.8 A_f T_e \left( \sum_j \frac{n_j Z_j^2}{n_e A_j} \right)^{2/3}$$

where the subscripts  $f$ ,  $e$  and  $j$  refer to the FI, the electrons, and the ion species present in the thermal plasma respectively.  $A$  and  $Z$  are the mass and charge numbers of the relevant species. An estimate using typical MAST parameters, with  $T_e = 1000$  eV and assuming a deuterium plasma containing carbon in the ratio  $n_C/n_e = 0.02$ , yields  $E_{\text{crit}} = 20$  keV.

Above  $E_{\text{crit}}$ , FI interact most strongly with the thermal electrons. Slowing down occurs due to electron drag, which reduces the energy of the FI without significantly affecting their pitch. The characteristic time over which a test particle slows down by drag on background particles was first derived by Spitzer [49]; for the case of FI slowing down by electron drag with  $v_{\text{th},e} \gg v_f$ , the expression may be written as [33]

$$t_s = 6.27 \times 10^{14} \frac{A_f T_e^{3/2}}{Z_f^2 n_e \ln \Lambda_e} \text{ s}$$

where  $T_e$  is expressed in eV.  $\ln \Lambda_e$  is the *Coulomb logarithm*, defined as the ratio of the largest impact parameter which causes a deflection of the particle trajectory to the classical distance of closest approach permitted by the electrostatic force. For Coulomb collisions between fast ions and warm electrons in a fully-ionised tokamak plasma,  $\ln \Lambda_e \approx 16$  [50]. In conditions typical of MAST plasmas, with  $T_e = 1000$  eV

and  $n_e = 3 \times 10^{19} \text{ m}^{-3}$ ,  $t_s$  is calculated from the above expression to be approximately 80 ms.  $t_s$  is commonly called the *slowing-down time on electrons*. The characteristic time on which the FI energy decays due to electron drag is  $t_s/2$  [49].

Below  $E_{\text{crit}}$ , Coulomb collisions with ions play the dominant role in the FI dynamics. In addition to reducing the energy of the FI, these collisions cause strong *pitch-angle scattering* of the FI such that the orientation of their velocity vectors with respect to the magnetic field may depart strongly from that with which they were born. The mean time taken for a particle of energy  $E$  to thermalise via interactions with the background plasma is given by Stix [33] as

$$\tau_{\text{th}} = \frac{t_s}{3} \ln \left[ 1 + \left( \frac{E}{E_{\text{crit}}} \right)^{3/2} \right]. \quad (2.3.2)$$

Once the energy of a FI has reached  $E_{\text{crit}}$ , it therefore thermalises in a time approximately equal to  $(t_s/3) \ln(2)$ , or  $0.23t_s$ . This is estimated from the above value for  $t_s$  as 20 ms in typical MAST conditions. When the FI birth energy is used in eq. (2.3.2),  $\tau_{\text{th}}$  is called the *thermalisation time* or *slowing-down time*. Typical values of  $\tau_{\text{th}}$  for beam ions in MAST range from 35 ms to 45 ms.

## 2.4 Steady-state fast-ion distributions

In most cases, the velocity distribution of thermal ions in a tokamak is adequately represented by a Maxwellian. The form of the distribution of particle speeds in the centre-of-mass frame is

$$f_0(v) = 4\pi n_i \left( \frac{m}{2\pi kT_i} \right)^{3/2} v^2 \exp \left( -\frac{m_i v^2}{2kT_i} \right).$$

Since the FI typically make up only a small minority of the total population of particles in the plasma, their distribution may be considered separately from that of the thermal ions. The full distribution of ion speeds including both fast and thermal ions will then be given as  $f(v) = C_n[f_0(v) + f_{\text{FI}}(v)]$ , where  $C_n$  is a normalisation factor. The expression for the steady-state velocity distribution of injected beam ions was first derived by Cordey and Core (1974) [51]. Under the simplifying assumptions of negligible self-interaction between the FI and negligible losses of FI from the plasma, the approximate pitch-averaged expression may be written as [52]

$$f_{\text{FI}}(v) = \begin{cases} S_0 t_s (v^3 + v_c^3)^{-1} & 2v_{\text{th},i} \lesssim v \leq v_b \\ S_0 t_s (v^3 + v_c^3)^{-1} \exp[-m_f(v^2 - v_b^2)/2T_e] & v > v_b \end{cases} \quad (2.4.3)$$

where  $v_b$  is the beam injection speed (or birth speed in the case of fusion products),  $v_c$  is the FI speed corresponding to  $E_{\text{crit}}$ ,  $m_f$  is the FI mass and  $S_0$  is the source term [32]. The exponential factor in the second expression relates to energy diffusion of the FI above their birth energy due to collisions with thermal electrons in the tail of the Maxwellian velocity distribution. The first expression is rendered inaccurate close to the ion thermal speed due to the neglect of energy diffusion caused by interactions between FI and the tail of the thermal ion velocity distribution, hence the lower bound.

The velocity distribution of ICRH-accelerated FI is significantly complicated by the fact that the fast-wave acceleration directly competes with the slowing-down process. Anisotropy in velocity space is introduced by the acceleration mechanism and is counteracted by pitch-angle scattering to different degrees depending on the ratio of the FI energy to the critical energy. An approximate expression for the isotropic part of  $f(E)$  in the case of a single-ion-species background plasma is given by Stix [38] as

$$f_{\text{FI}}(E) = \exp \left\{ -\frac{E}{T_e(1+\xi)} \left[ 1 + \frac{R_i(T_e - T_i + \xi T_e)}{T_i(1 + R_i + \xi)} H(E/E_i) \right] \right\}. \quad (2.4.4)$$

The following expressions are substituted:

$$R_i \equiv \frac{n_i Z_i^2}{n_e} \left( \frac{m_i T_e}{m_e T_i} \right)^{1/2}; \quad \xi \equiv \frac{m_f \langle P \rangle}{8\pi^{1/2} n_e n_f Z_f^2 e^4 \ln \Lambda_e} \left( \frac{2T_e}{m_e} \right)^{1/2}; \quad H(x) \equiv \frac{1}{x} \int_0^x \frac{du}{1+u^{3/2}};$$

$$E_i(\xi) \equiv \frac{m_f T_i}{m_i} \left[ \frac{3\pi^{1/2}(1 + R_i + \xi)}{4(1 + \xi)} \right]^{2/3} \leq E_i(0);$$

$$E_i(0) \equiv 14.8 A_f T_e^{1/3} \left( \frac{n_i Z_i^2 T_i}{n_e A_i} \right)^{2/3}.$$

$\langle P \rangle$  is the flux-surface averaged power density delivered to the minority ions which are subject to ICRH. Note that this expression applies only to cyclotron heating at the fundamental frequency of a minority species, not to the second harmonic heating which is commonly employed in experiments. Analytic expressions for  $f(E)$  in the presence of second harmonic ICRH can only be obtained in low or high-energy limits [53].

Figure 2.3 illustrates the forms of the FI distributions obtained with NBI and ICRH. The NBI-generated FI distribution falls off steeply above the injection energy, with very few ions diffusing to energies higher than  $E_b + T_e$ . The ICRH-driven FI distribution by contrast exhibits a long tail with a gradient which asymptotically approaches a fixed value determined by the balance between fast-wave acceleration and electron drag. Increasing  $\langle P \rangle$  leads to an increase in the tail temperature. It should be emphasised that the plot of the ICRH-driven distribution includes only the part of the distribution which is isotropic in velocity space; the preferential acceleration perpendicular to the

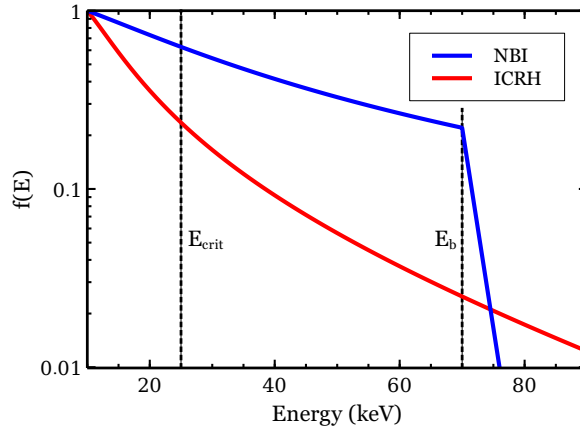


Figure 2.3: A sketch of the FI distributions driven by NBI (blue) and fundamental ICRH (red). For the purposes of determining the NBI-driven distribution based on eq. (2.4.3), the beam injection energy is 70 keV, the critical energy is 25 keV and the electron temperature is 2 keV. For the ICRH-driven distribution,  $E_i$  is taken to be 8 keV and a polynomial approximation to the integral in eq. (2.4.4) is used. The distributions are each normalised to their value at  $E = 10$  keV. Note the logarithmic vertical axis.

magnetic field introduces a strong velocity-space anisotropy, with a higher tail temperature in perpendicular velocity than in parallel velocity. Similarly, the NBI-driven distribution plotted here is averaged over pitch; the anisotropy in velocity space is determined by the beam injection angle to the magnetic field. NBI systems are often configured to inject nearly parallel to the field in the core of the plasma, since the FI thus produced drive a non-inductive current in the plasma which can help to sustain operation by reducing the flux consumption of the central solenoid.

Simulations of the evolving FI distribution in a real tokamak plasma can be carried out by tracking a large number of marker particles representing the FI, solving the equations of motion for the drift orbit of each marker and applying corrections for the finite Larmor radius. The experimentally-measured electron and ion density and temperature can be used to determine a collision operator to be applied to the FI in the simulation. The Monte Carlo NUBEAM module of the global 1.5-dimensional, time-dependent transport analysis code TRANSP is commonly used for this purpose. TRANSP and NUBEAM will be described in detail in chapter 6; for now, an example of such a distribution calculated for a typical MAST discharge is shown in fig. 2.4. The slowing-down part of the distribution below the primary beam injection energy of 60 keV is evident. As they slow down, because of the increasing level of interaction with thermal ions, the FI also spread out in pitch. This behaviour is particularly apparent below the critical energy, which in the core of the plasma in question was 21 keV.

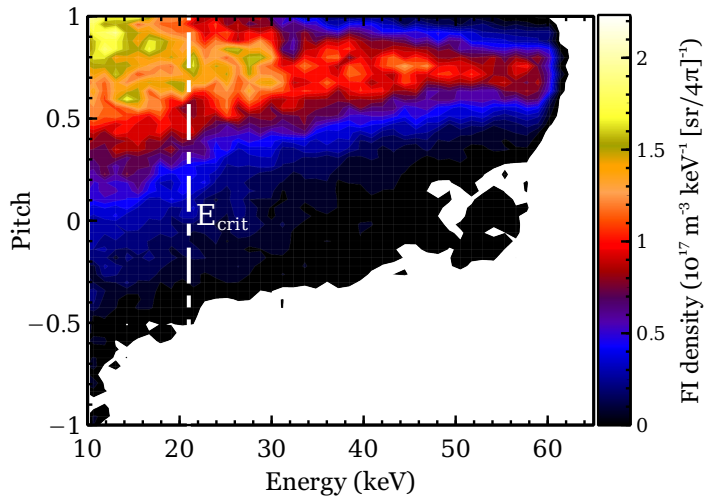


Figure 2.4: Synthetic FI distribution  $f_{\text{FI}}(E, p)$  in the core of MAST shot #29195, averaged over  $0.88 \text{ m} < R < 0.96 \text{ m}$ ,  $-0.04 \text{ m} < Z < 0.04 \text{ m}$ ,  $0.267 \text{ s} < t \leq 0.270 \text{ s}$ . The distribution is calculated with the NUBEAM particle-tracking module of the global time-dependent transport analysis code TRANSP.  $5 \times 10^4$  Monte Carlo marker particles are used in the simulation to represent the beam ions; statistical noise appears in the distribution caused by the use of a finite number of markers. The critical energy is marked by the dash-dotted white line, and the beam injection energy is 60 keV.

Superposed on the low-energy part of the distribution are additional FI born at one half and one third of the primary energy; these features arise due to the formation of  $\text{D}_2$  and  $\text{D}_3$  molecular ions in the beamline, which are then dissociated after acceleration across the 60 keV potential. The abrupt change in FI density at approximately 30 keV due to the appearance of the  $E_b/2$  component below this energy is particularly apparent.

FI produced by fusion reactions have a similar energy distribution to those produced by NBI, albeit with a spread close to the birth energy which is determined by the ion rather than the electron temperature; this spread arises due to the Maxwellian velocity distribution of the reactant ions. The occurrence of beam-thermal or beam-beam fusion reactions creates a tail on the fusion product velocity distribution which extends to even higher energies than that created by thermonuclear fusion reactions, since the range of relative energies in the case of reactions involving at least one beam ion is much larger than in the case of reactions involving only thermal ions. A further important point is that fusion products are born almost isotropically in velocity space, so the gradients in pitch above the critical energy are much smaller than those created by NBI-produced FI. This reduces the susceptibility of fusion products to kinetic instabilities driven by gradients in perpendicular velocity.

## 2.5 Loss mechanisms of fast ions

The foregoing discussion assumes that FI are redistributed in velocity space by collisions with thermal particles, but that they are confined within the plasma until thermalisation. In reality, several processes can cause losses of FI from the plasma:

- Collisions can scatter FI onto drift orbits which are no longer confined within the plasma, and which lead to the FI being lost to solid surfaces in the vacuum vessel [54].
- Even if they remain on confined orbits, the large Larmor radii of FI can allow them to approach or even to cross the LCFS on part of their gyro-orbit. These FI may be neutralised by CX reactions with neutrals at the edge of the plasma, and lost [55].
- The effects of finite aspect ratio and plasma shaping which cause  $\mu_0$  not to be a constant of the guiding centre motion can also cause non-adiabatic jumps in the value of  $\mu$ , which can lead to collisionless radial transport of FI [56].
- Fusion reactions constitute a sink term for the reactant species as well as a source term for the fusion products.
- MHD instabilities can change the topology of FI orbits, causing either a slow radial drift to the edge of the plasma [57] or a rapid transition to an unconfined orbit [58].
- Static magnetic field perturbations, including those produced by the ripple in the toroidal field arising from the use of discrete toroidal field coils [43] as well as those imposed to mitigate MHD instabilities [59], may also affect the orbit topology.

Losses of FI are an important topic of study for two reasons [60]. Firstly, the effectiveness of heating and current drive schemes which rely on FI is diminished by their loss, leading to reduced performance in terms of fusion reactivity. Secondly, escaping FI which impact the first wall could constitute an unacceptable heat load on the plasma-facing components in a fusion reactor, reducing the lifetime of these components. This is particularly critical if the spatial distribution of the FI losses is such that the enhanced particle flux to the first wall is strongly localised.

FI transport due to the last two mechanisms outlined above, namely dynamic and static MHD perturbations, will be the subject of the next chapter. This is a natural choice since the investigation of this ‘anomalous’ FI transport in MAST is the primary

subject of this thesis. Before commencing this discussion, the ongoing FI research on MAST should be placed in the wider context of FI research in support of ITER.

## 2.6 Fast-ion research on MAST

The effects of low aspect ratio, strong plasma shaping, high beta and large beam-ion orbits mean that ST pose a challenge to the validation of numerical models [61]. Nonetheless, the Larmor Orbit Code for Use in Spherical Tokamaks (LOCUST) was successfully applied to model beam-ion orbits in the spherical tokamak START [62], which was the forerunner to MAST. A new version of LOCUST, upgraded to run on graphics processing units, is currently being implemented to model FI physics in MAST and MAST-Upgrade [63]. This work is expected to result in high-resolution maps of enhanced particle fluxes to the first wall due to FI losses from MAST plasmas. The stability and effects of the *Alfvén eigenmodes* which will be discussed in the next chapter, including complex nonlinear interactions with the FI population, have been modelled in the case of MAST [64] using the MISHKA and HAGIS codes [65, 66]. Recent work by Pfefferlé and co-workers has explored the effects of rigid *internal kink* deformations on FI orbits in MAST plasmas [67]. Validation of these simulations in the ST operating regime as well as on conventional large-aspect-ratio tokamaks should allow the codes to be used with increased confidence to predict and model wave-particle interactions and FI physics in ITER [68].

In parallel with this numerical modelling effort, experimental studies have focused firstly on the stability and evolution of various FI-driven Alfvén eigenmodes in MAST [69, 70], and more recently on the exploitation of a range of diagnostics of the FI population [71, 72]. The diagnostics have been used to study the effects of *fishbones*, a type of FI-driven instability which is observed to be particularly virulent in ST and which will be described in the next chapter [73, 74]. Operating regimes have been identified in which these modes are suppressed [75]. During the experimental campaign over which the work described in this thesis was conducted, the enhanced diagnostic capability [76, 77] has also been used to examine the effects of sawteeth and frequency-chirping Alfvén eigenmodes [78]. Quantifying the effects of various plasma instabilities on the FI population should allow for verification of the results of associated numerical modelling. The ability to mitigate deleterious MHD activity by operating with off-axis NBI should also allow improved performance in MAST-Upgrade [79].

# Chapter 3

## Interactions between MHD instabilities and fast ions

### 3.1 Outline

The possibility of shear Alfvén waves being driven unstable by energetic particles in a fusion plasma was recognised in the mid-1970s [80, 81]. At around the same time, it was appreciated that such modes would flatten the radial density profile of fusion  $\alpha$ -particles [82]. A limited amount of this ‘anomalous’ transport of  $\alpha$ -particles would be beneficial in removing helium from the core of the plasma, but the transport could also be deleterious to fusion performance if the alpha particles were lost before giving up their energy to the thermal plasma. Initial theoretical work focused on turbulent transport caused by waves with high mode numbers  $n$  and  $m$ , which refer respectively to the number of wave periods in the toroidal and poloidal extent of a flux surface. This work was later extended to low- $n$  modes in more relevant cylindrical geometry [83].

The first observations of anomalous beam-ion transport caused by FI-driven MHD modes were made on the Poloidal Divertor Experiment (PDX) in 1983 [84]. These modes were identified as internal kink modes with principal mode numbers  $n = m = 1$ . Theoretical studies followed, and resonance with the toroidal precession of trapped FI was identified as a driving mechanism [85, 86]. These modes were dubbed ‘fishbones’ due to their appearance in the magnetic coil trace, shown in fig. 3.1. FI transport caused by modes related to shear Alfvén waves was later observed on the TFTR and DIII-D tokamaks [87].

Since these pioneering studies, the regime explored in both theory and experiment has expanded to include a wider range of modes [88], additional resonances [89, 90], spherical tokamaks [91–93], and modes without an accompanying rational surface [94]. The rapid nonlinear ‘frequency chirping’ characteristic of many strongly-driven modes



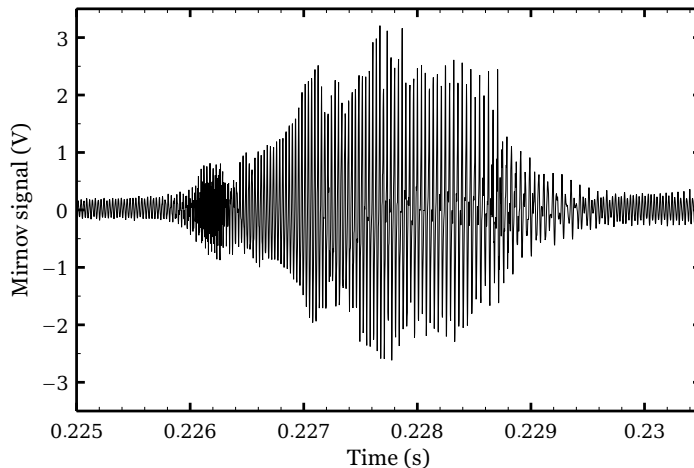


Figure 3.1: Time trace from a Mirnov coil located on the outboard midplane inside the MAST vessel, showing the perturbation caused by a ‘fishbone’. The Mirnov coil is oriented to detect perturbations in the vertical magnetic field,  $B_z$ , and the amplitude of the signal is proportional to the time derivative  $\dot{B}_z$  at the coil location. As well as growing and decaying in amplitude, the perturbation sweeps downward in frequency during its evolution from approximately 40 kHz to 20 kHz. The resemblance of the magnetic coil trace to the ribs of a fish skeleton gives the instability its name.

has also received attention [95, 96].

In this chapter, the shear Alfvén eigenmodes and internal kink modes which may appear in a tokamak plasma are first described. The possibility of a resonant interaction with energetic particles is explored, and various FI transport mechanisms are outlined. Non-resonant transport which occurs in the presence of internal kink modes and magnetic reconnection is also discussed, as this is relevant to the effects of *long-lived modes* and *sawteeth* which are investigated in chapter 8. It should be noted that many other instabilities which may affect the FI are not considered in this chapter, since their much weaker effects have proven difficult to isolate from those of the shear Alfvén eigenmodes, kink modes and sawteeth in MAST plasmas. These include tearing modes, edge-localised modes and compressional Alfvén eigenmodes.

## 3.2 MHD modes of a toroidal plasma

### 3.2.1 Ideal MHD modes of a cylinder

Consider firstly the case of a cylindrical flux tube of length  $L$ , periodic in the longitudinal direction, with a mass density  $\rho$  and an axial magnetic field of magnitude  $B$ . This situation is illustrated in fig. 3.2. An azimuthal perturbation to the magnetic field will propagate along the cylinder at the *Alfvén speed*,

$$v_A = \frac{B}{\sqrt{\mu_0 \rho}},$$

assuming  $a \ll L$  and  $v_A \ll c$ . This dependence arises from the fact that the magnetic field provides the tension which attempts to restore the initial state of the field, and the mass density provides the inertia. These transverse waves are therefore analogous to waves on a plucked string.

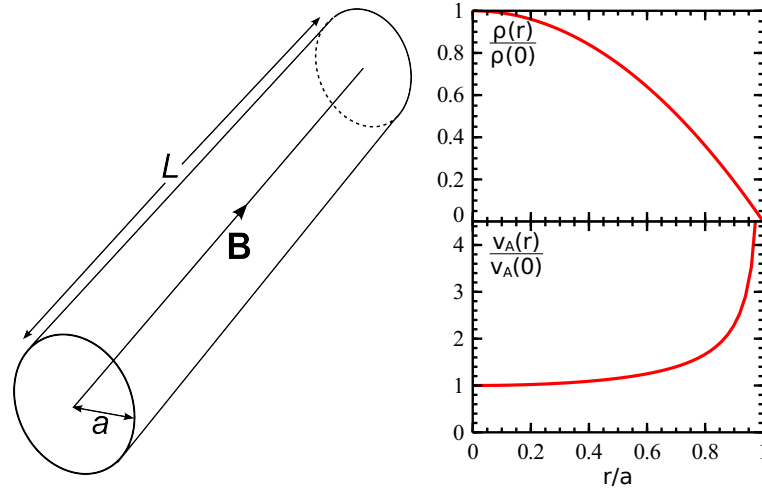


Figure 3.2: Sketch of a cylindrical flux tube of length  $L$  and minor radius  $a$ , with a uniform axial magnetic field  $\mathbf{B}$ . The top panel on the right shows a parabolic density profile as a function of minor radius, while the bottom panel shows the profile of the corresponding Alfvén speed. Both profiles are normalised to their value on the axis of the cylinder.

If both the density and magnetic field are uniform throughout the cylinder, the Alfvén speed is the same at all radii. A wave excited by rapidly twisting one end of the cylinder is supported as a normal mode of the system with a parallel wavenumber  $k_{\parallel} = 2\pi n/L$ ,  $n = 1, 2, 3, \dots$ . Such a mode is called a *torsional*, or *shear*, Alfvén eigenmode. A similar situation is obtained by rapidly displacing one end of the cylinder in the direction perpendicular to the magnetic field. The displacement propagates along the cylinder at the Alfvén speed (assuming the region outside the cylinder to be a vacuum), and discrete eigenmodes are again supported. This is the *kink mode*. Here, the amplitude of the displacement is assumed to be small relative to the minor radius of the cylinder so that the linearised ideal MHD equations may be used to describe the perturbation [97, 98].

In the example illustrated in fig. 3.2, the Alfvén speed varies as a function of minor radius; this variation is likely to be found in a real cylindrical flux tube due to the requirement for MHD pressure balance [99]. The dispersion relation for transverse waves is

$$\omega(r) = \pm k_{\parallel} v_A(r).$$

Shear Alfvén waves therefore dissipate through phase mixing between components at different minor radii [100]. A wave initially launched from one end of the cylinder is rapidly dispersed, and no coherent mode is supported. The damping of the wave arising due to this phase mixing is a direct consequence of the existence of the continuous frequency spectrum of Alfvén waves supported by the cylinder.

The situation illustrated above changes if an axial current flows in the cylinder, inducing an azimuthal (poloidal) component  $B_\theta$  to the magnetic field [99]. Now, the periodicity in the axial and poloidal directions restricts eigenmodes to particular *rational surfaces*. If the poloidal and axial mode numbers are  $m$  and  $n$ , this constraint may be written as  $k_\parallel = 2\pi(n - m/q)/L$ . Here,  $q = (2\pi r/L)(B_z/B_\theta)$  is analogous to the *safety factor* introduced in chapter 1. The positions of these rational surfaces depend on the radial profile of the current density, and correspond to  $q_r = m/n$ ; solutions of the wave equation describing the modes in ideal MHD are singular at these points [100], so the theory is no longer applicable. Although the magnetic field is sheared in the radial direction, phase mixing still occurs in the immediate vicinity of the rational surface and the Alfvén eigenmodes are strongly damped [101]. Physically, this damping arises from the mode conversion of ideal-MHD shear Alfvén waves into kinetic Alfvén waves when the effects of the finite ion Larmor radius become important at the singularity [102].

### 3.2.2 Alfvén gap modes

If the sheared cylindrical plasma column is bent into a torus by connecting the ends of the cylinder, an important change occurs in the nature of the Alfvén continuum [103]. To lowest order in the parameter  $\epsilon = r/R_0$ , where  $R_0$  is the major radius of the torus, a continuous spectrum exists with the same frequencies as discovered in the cylindrical case [104]. The foregoing discussion remains valid, with  $L$  being replaced by  $2\pi R_0$ . The equilibrium is no longer symmetric in the poloidal angle  $\theta$  however, since the toroidal field curvature varies periodically in  $\theta$ . First order corrections  $\sim\epsilon$  arise due to this periodicity, which perturbs the eigenfunctions of the modes such that they align with the equilibrium field on both the inboard and the outboard side. Modes with adjacent poloidal mode numbers  $m$  and  $m+1$ , the frequencies of which intersect on the rational surface  $q_r = (m+1/2)/n$ , become coupled due to this perturbation. The combined eigenfunction has two branches, one with its maximum amplitude on the outboard side, the other with its maximum amplitude on the inboard side. A frequency gap

$(\Delta\omega/\omega) \sim \epsilon$  appears in the spectrum at [105]

$$\omega \simeq \frac{v_A}{R_0} \left( n - \frac{m}{q_r} \right),$$

with the lower (upper) frequency of the gap corresponding to the mode localised on the outboard (inboard) side. Modes in the toroidicity-induced gap are no longer subject to the phase mixing which causes strong damping in the case of the cylinder, and may therefore be driven unstable more easily than continuum modes. These are called *toroidicity-induced Alfvén eigenmodes*, or sometimes toroidal Alfvén eigenmodes (TAE). It should be noted that TAE are not the only gap modes which may exist in tokamak plasmas. Elliptical shaping of flux surfaces introduces a periodicity of  $\pi$  in the  $\theta$ -variation of the poloidal curvature, which couples modes with poloidal mode numbers  $m$  and  $m \pm 2$ . This is called the *ellipticity-induced Alfvén eigenmode* (EAE). Higher-order shaping, for example triangularity, introduces the *non-circularity-induced Alfvén eigenmode* (NAE). These gaps appear at successively higher frequencies than the TAE gap and are also narrower,  $\sim \epsilon^2$  and  $\sim \epsilon^3$  respectively [106]. Figure 3.3 shows shear Alfvén continua and toroidicity/ellipticity-induced gaps in the case of a circular cross-section plasma (a) and in a JET plasma with vertical ellipticity  $\kappa = 1.68$ , horizontal triangularity  $\delta = 0.3$ ,  $\beta = 0.03$  and  $\epsilon = 0.423$  (b). Another gap appears at lower frequency than the TAE gap when the effects of finite plasma pressure and compressibility are included; this is the *beta-induced Alfvén eigenmode* (BAE) [107, 108].

### 3.2.3 Internal kink modes

A fundamental criterion for the global stability of a cylindrical or toroidal field configuration is that low-order ( $q_a = 1 - 3$ ) rational surfaces located close to the edge of the plasma should be avoided [110]. The reason for this is that a small radial displacement of the plasma under such conditions would lead to a rapidly-growing  $n = 1$  external kink instability with  $m = q_a$ ; once displaced, the plasma is driven away from equilibrium by the difference in poloidal magnetic field pressure between opposite sides of the perturbed plasma column. Tokamaks must therefore operate with  $q_a \gtrsim 3$ .

Unfortunately, although finite magnetic shear acts to stabilise the perturbations, kink modes with rational surfaces located *within* the plasma are still susceptible to instability in the presence of centrally peaked current density and pressure profiles [111]. The stability of the  $(m, n) = (1, 1)$  internal kink mode in a toroidal plasma is strongly dependent on the pressure profile and exhibits a threshold in the value of  $\beta_p$  which

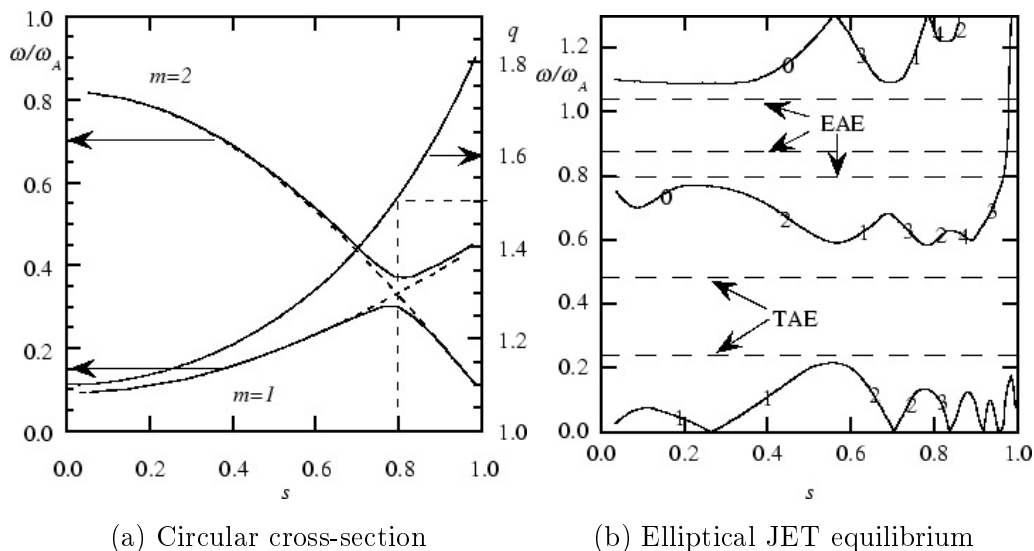


Figure 3.3: a) Frequency spectrum of  $m = 1$  and  $m = 2$  poloidal harmonics of the  $n = 1$  shear Alfvén wave in a uniform cylindrical plasma (dashed lines) and a toroidal plasma with  $\epsilon = 0.1$  (solid lines). The  $q$ -profile is indicated on the right-hand vertical axis. The toroidicity-induced gap appears at  $q \approx 3/2$ ,  $\omega/\omega_A \approx 1/3$ . b) Spectrum of the  $n = 1$  mode calculated with the MARS code based on a JET equilibrium [109]. Integer labels on the curves in the continuum indicate the poloidal mode existing at that frequency/position. The frequencies of TAE and EAE in the gaps are indicated by the dashed horizontal lines and labels. For both panels, an ideal, incompressible plasma is assumed. The radial coordinate  $s$  represents the square root of normalised poloidal flux,  $s = \sqrt{\psi(r)/\psi(a)}$ . Frequency is normalised to  $\omega_A = v_A/R_0$ . Images courtesy of ref. [109].

depends on the peaking of the current density. The most unstable configuration consists of a highly peaked profile of current density with a large pressure gradient at the  $q = 1$  surface [111]. Elliptical shaping of the flux surfaces has been found to destabilise the internal kink mode, while higher-order shaping such as triangularity is strongly stabilising [112]. These theoretical results have been reproduced numerically in an extensive parameter scan, which also included coupling between the internal kink and low- $n$  pressure-driven ballooning mode in the case  $q_{\min} \gtrsim 1$  [113]. It has also been found that instability persists, and can in fact be stronger than in the case of a monotonic  $q$ -profile, when the field exhibits reversed shear such that  $q_0 > q_{\min}$  [114].

The ideal-MHD internal kink is a purely growing mode [111]; the real part of its frequency is zero in the plasma frame. It may however be Doppler shifted by the toroidal rotation of the plasma such that the frequency in the lab frame matches the rotation frequency at the rational surface where the mode amplitude peaks. In the presence of a finite energetic-particle pressure, the kink mode develops a finite

frequency in the plasma frame [115]. The growth rate and frequency then become sensitive to both the FI pressure and the background plasma pressure; increasing FI pressure can act to stabilise or destabilise the kink mode depending on the proximity to ideal-MHD stability. This has important consequences for the interaction of such modes with FI, as will be discussed in the next section.

Figure 3.4 shows the structure of typical  $n = 1$  TAE and internal kink eigenmodes in MAST plasmas, calculated with the linear ideal-MHD code MISHKA-1 [65]. The broad structure of the global TAE, with multiple coupled poloidal harmonics peaking at successively larger radii, contrasts with the predominantly  $m = 1$  kink mode. The kink mode exhibits a ‘double layer’ due to the non-monotonic  $q$ -profile, with the internal region of negative displacement having  $q \gtrsim 1$  and the outer region of positive displacement having  $q \lesssim 1$ . Two  $q = 1$  rational surfaces are present, at  $s \approx 0.2$  and  $s \approx 0.6$ , which form the boundaries of the regions of opposite displacement. In the case of the TAE, by contrast, no  $q = 1$  surface exists within the plasma.

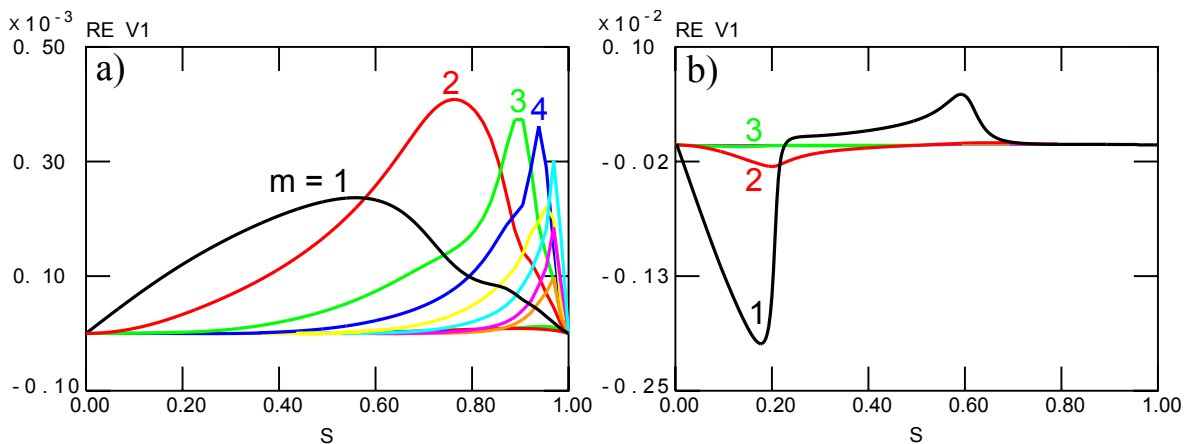


Figure 3.4: a) Structure of the  $n = 1$  TAE calculated with the linear ideal-MHD code MISHKA-1 for MAST shot #29210 at  $t = 0.165$  s. The abscissa  $s$  represents the square root of normalised poloidal flux, as in fig. 3.3, and the ordinate represents  $sv_r$ , where  $v_r$  is the radial velocity of the perturbation in arbitrary units. Integer labels indicate the poloidal mode number of the corresponding coloured line. b) As for panel (a), but for the  $n = 1$  internal kink mode in shot #29976 at  $t = 0.210$  s. Adapted from figures provided by Dr. Sergei Sharapov.

MISHKA-1 performs *normal mode analysis* of a given toroidal equilibrium configuration; in brief, this consists of finding solutions to the eigenvalue equation

$$-\omega^2 \rho_0 \boldsymbol{\xi} = \mathbf{F}(\boldsymbol{\xi})$$

for modes of each poloidal and toroidal mode number.  $\boldsymbol{\xi}$  represents a perturbation to the equilibrium field.  $\mathbf{F}(\boldsymbol{\xi})$  is the force operator arising from linearised ideal-MHD

momentum balance, in which only terms of first order in  $\xi$  are retained and perturbed quantities  $\tilde{q}(\mathbf{x}, t)$  are treated as the product of a spatial part  $\tilde{q}(\mathbf{x})$  and a time-dependent part  $e^{-i\omega t}$ . In general,  $\omega$  consists of a real part representing the oscillatory frequency and an imaginary part representing the linear growth rate of the mode. In ideal MHD however, the operator  $\mathbf{F}(\xi)$  is self-adjoint and so the eigenvalues are purely real. For the TAE, which necessarily has a finite real frequency, the eigenvalue is positive. For the internal kink the eigenvalue is negative and so only the imaginary part of the frequency, which is to say the growth rate, is known on the basis of ideal MHD. The ‘missing part’ of the complex frequency in each case must be determined empirically or estimated from simulations of the energetic-particle contribution to the growth rate or frequency.

### 3.2.4 Damping and dissipative processes

Whether or not an unstable MHD mode grows in amplitude over time is determined by the balance between *drive* and *damping*. Drive can be provided by gradients in the FI distribution, as discussed in the next section, while damping arises due to interactions between the mode and the background plasma, and between the mode and the non-resonant part of the FI population. The main processes in this regard are *continuum damping* and *Landau damping*.

Continuum damping is simply the aforementioned damping by phase mixing, which results in the generation of kinetic Alfvén waves, of that part of the mode structure which overlaps with the continuum [116]. For TAE, this is strongest near the edge of the plasma where the density gradient and the sheared magnetic field causes the continuum to span a wide range of frequencies over a small radial range, and negligible where the dominant poloidal harmonics peak inside the toroidicity-induced gap [117].

Landau damping arises from gradients in the electron, bulk or fast ion velocity distribution close to the phase velocity of the wave. Originally demonstrated theoretically in 1946 in the context of electrostatic plasma oscillations [118], it was applied rigorously in the early 1990s to the problem of damping of drift waves in slab geometry [119] and subsequently TAE in fusion plasmas [120]. Close to the phase speed, particles moving parallel to the wave are able to exchange energy with the wave through its electric field. Particles moving slower than the wave which gain energy move closer to phase speed, and their interaction with the wave becomes stronger. Slower particles which lose energy to the wave move further from the phase speed, and their interaction weak-

ens. There is therefore a net energy transfer from the wave to the slower particles. The converse is true of particles moving slightly faster than the phase speed; there is a net energy transfer from these particles to the wave. The particle velocity distribution may be written as  $f(v_{\parallel}, v_{\perp})$ , where  $v_{\parallel}$  and  $v_{\perp}$  in this case are the velocity components parallel and perpendicular to the wave vector  $\mathbf{k}$ . In the presence of a negative gradient  $\partial f/\partial v_{\parallel}$  close to the phase speed, which is always the case in the presence of a Maxwellian velocity distribution for example, more particles are found at slower speeds than at larger speeds. Damping of the wave therefore results from the interaction. Particles with a  $v_{\parallel}$  which differs substantially from the phase speed experience only a sinusoidally-varying electric field, and no overall energy transfer takes place.

### 3.3 Interactions with fast ions

#### 3.3.1 Resonant energetic-particle drive

Super-thermal particles in the plasma constitute a source of free energy which can excite instabilities. In particular, the negative radial gradient of the FI pressure profile has the potential to drive the mode until the wave-particle interaction reduces the gradient drive to match the damping of the mode on the thermal plasma [121]. This pressure gradient drive is exactly analogous to the Landau damping of the wave in the presence of negative gradients in the velocity distribution, and is therefore called *inverse Landau damping* [122]. In order for net energy transfer between the wave and the particles to occur, the particle orbits must satisfy a *resonance condition*. Typically, for low-frequency Alfvén waves such as TAE in a tokamak, this is given by [123]

$$n\omega_{\phi} - p\omega_{\theta} - \omega = 0 \quad (3.3.1)$$

where  $\omega_{\phi}$  and  $\omega_{\theta}$  are the toroidal and poloidal transit or bounce frequencies of the drift orbit,  $n$  is the toroidal mode number and  $p$  is an integer, and  $\omega$  is the mode frequency. If this condition is satisfied by FI close to the rational surface, the particles can exchange energy with the wave via the resonant interaction between their drift orbits and the electric field of the wave. In MAST, FI typically had  $v_{\parallel} \lesssim 2.5v_A$  with  $v_A \approx 1 \times 10^6 \text{ m s}^{-1}$ . Alfvén eigenmodes were therefore driven at the fundamental resonance with  $n = 1$ ,  $p \sim m$  in eq. (3.3.1). If the integer  $p$  is close to the poloidal mode number  $m$ , typically  $p \in [m - 1, m + 1]$ , net energy transfer is found to occur when the interaction is averaged over many orbital cycles [85]. Accompanying this transfer of energy is a radial transport of particles in resonance with the mode. Figure 3.5 shows



qualitatively the evolution of the FI density profile in the vicinity of a mode-particle resonance. A weak damping term due to the response of the background plasma to the perturbation is assumed. This results in the saturation of the mode amplitude once equilibrium has been reached between the drive and damping; the drive is sustained by FI slowing down and scattering into the region close to the resonance. The FI density gradient is reduced close to the resonance compared to the case in which no mode is excited [124].

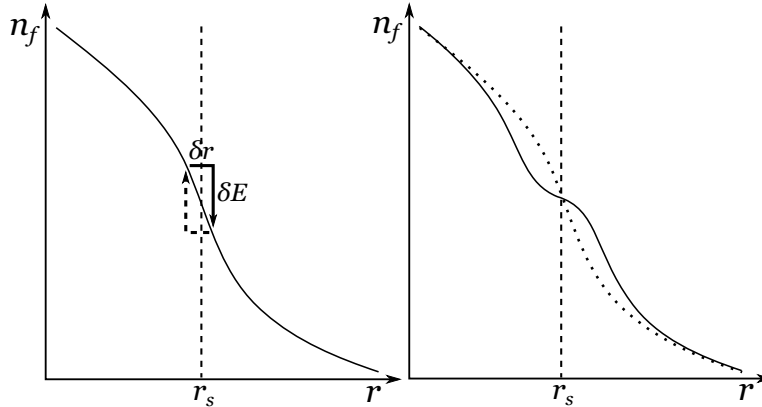


Figure 3.5: Sketch of the particle transport across a resonant surface located at  $r = r_s$  in the presence of a driving gradient in the FI distribution. Particles following the solid arrow in the left panel move outward in radius and lose energy to the wave. The wave can also transport particles radially inward and to higher energy (dashed arrow), but the sign of the FI density gradient means that there are fewer such particles. The right panel shows the relaxed FI density gradient once the drive has been reduced to balance the damping of the wave on the background plasma (solid line), with the original profile overlaid for comparison (dotted line).

It must be noted that, as well as causing time-dependent fluctuations which affect the energy of resonant particles, TAE and internal kink perturbations break the toroidal symmetry of the field.  $P_\phi$  is therefore no longer a constant of motion. In the presence of a mode of a single  $n$ , the symmetry violation in time and in toroidal angle is coupled through the toroidal periodicity. This implies that the change in particle energy and toroidal canonical momentum are related through [125]

$$\delta P_\phi = (n/\omega)\delta E.$$

Considering the relation  $P_\phi \sim \psi$  where the term  $Ze\psi$  dominates the expression for  $P_\phi$ , the radial transport is seen as a natural consequence of the resonant transport in phase space. Loss of energy, corresponding to negative  $\delta E$ , is associated with outward radial transport as  $\psi$  becomes more negative. A further consequence of the power transfer from the FI distribution to the wave is that, if the drive is strong enough to overcome

the resonance damping in the Alfvén continuum, modes can be excited in the continuum with frequencies determined by the drift motion of the resonant particles [86, 121]. The extent to which these *energetic-particle modes* (EPM) differ in structure and frequency from the ideal-MHD modes depends primarily on the strength of the energetic-particle drive, but is also affected by thermal pressure, plasma shaping, compressibility, and the finite Larmor radii and orbit widths of the FI [126, 127]. There is strong evidence that EPM arise due to a coupling between modes of the background plasma, including TAE, BAE and pressure-driven kinetic ballooning modes (KBM) [127–130]. The EPM branch of the internal kink manifests itself as the fishbone [86]. The frequency of a typical EPM tends to lie close to the bottom of the toroidicity-induced gap when the FI pressure constitutes only a small perturbation to the background plasma pressure, and to decrease as the energetic particle drive increases and the TAE couples to modes in the continuum. The mode frequency often approaches the bulk *ion diamagnetic drift* frequency when FI and thermal plasma beta become comparable [131]. Ion diamagnetic drift is an ‘effective drift’ arising from radial density or temperature gradients which mean that more ions exist on the part of their Larmor orbit with instantaneous perpendicular velocity in one particular direction (the ion diamagnetic direction) than in the opposite direction. It is given by [127]

$$\omega_{*i} = \frac{T_i}{ZeB^2} \mathbf{k} \times \mathbf{B} \cdot \nabla \ln P_i \simeq -\frac{1}{ZeBrn_i} \frac{dP_i}{dr},$$

where  $n_i$ ,  $T_i$  and  $P_i$  are the thermal ion density, temperature and pressure, and  $\mathbf{k}$  is the wave vector describing variations of equilibrium quantities. To lowest order, evaluated at a minor radius  $r$ ,  $\mathbf{k}_0 \times \mathbf{B}_0 \cdot \nabla \ln P_i \simeq (B/r)(1/P_i)dP_i/dr$  accounting for the second equality [131]. An estimate using parameters typical of the mid-radius of a MAST plasma yields  $\omega_{*i}/2\pi \approx 10$  kHz.

### 3.3.2 Nonlinear wave-particle interactions

The wave-particle interactions described above are relevant to isolated resonances close to *marginal stability* of the mode, in which the growth rate is small compared to the frequency ( $\gamma/\omega \ll 1$ ). In reality, the source of FI which generates the driving gradient in the FI distribution may be unable to maintain a steady-state distribution close to the resonance [132]. A further complication is that the finite width of magnetic field perturbations close to the resonance means that the resonances may effectively overlap and the particle orbits become chaotic [133]. If either of these conditions is satisfied, strong nonlinear interactions complicate the evolution of the beam-plasma

system. The envelope of the mode amplitude can exhibit pulsating, or ‘bursting’, behaviour on timescales determined by the balance between FI drive, slowing-down, and damping of the mode on the thermal plasma [132].

As well as changing the evolution of the mode amplitude, nonlinear interactions can have profound effects on FI transport. In the presence of an EPM resonance, rather than a localised flattening of the FI pressure profile, a collective ‘avalanche’-type behaviour can develop. This consists of an outward-propagating convective ‘front’ of particle transport, as the outward radial transport of particles at the initial resonance location causes steepening of the profile at larger radii and subsequent self-consistent evolution of the particle density and wave amplitude profiles. The transport can be viewed as advection of particles trapped in a ‘bucket’ in phase space [95, 134]; resonant particles are confined to closed orbits in a phase space region bounded by a separatrix, and stay in resonance until collisions scatter them out of the bucket or until the source of free energy is depleted and the mode decays. Commonly associated with this convective transport is the phenomenon of rapid frequency sweeping, or ‘chirping’ [135–137]. A significant downward shift of the mode frequency in the plasma frame accompanies the outward radial transport and energy loss of the resonant particles. A similar phenomenon arises for Alfvén eigenmodes if multiple closely-spaced resonances exist in the plasma. In the case where the mode amplitude is large enough that orbits become chaotic, stochastic transport leads to particle diffusion across the resonance [133]. Multiple closely-spaced resonances can cause these regions of diffusive transport to overlap, leading to large-scale particle transport and enhanced energy release from the FI distribution [132].

The most general way of expressing the interplay between MHD and kinetic effects in determining wave evolution is through the *generalised fishbone-like dispersion relation* (GFLDR) [138]. First derived in the context of trapped-particle induced fishbones [86], the general form is

$$i\Omega - \delta W_f - \delta W_k = 0.$$

Here,  $\delta W_f$  and  $\delta W_k$  are, respectively, the fluid (MHD) and kinetic contributions to the energy balance of the mode on scales where the inertia and finite Larmor radius of the thermal ions may be neglected.  $\Omega \propto S\omega/\omega_A$ , where  $S$  is the local magnetic shear [139] at the mode rational surface, represents the contribution of inertial and kinetic effects in a narrow layer close to the resonance. The form of each term is governed by the ordering

of various key parameters and by the specific instability under consideration. Generally,  $\delta W_f$  encapsulates the contributions of magnetic curvature and field line bending, kink instability drive through the current density, and ballooning instability drive through the pressure gradient.  $\delta W_k$  is often derived from the gyrokinetic equation relevant to the problem [121], and encapsulates the resonant FI motion including diamagnetic and guiding centre drifts, and gradients of the distribution.  $\Omega$  includes thermal ion diamagnetic and inertial effects, as well as FI kinetic effects in the long-wavelength limit. Depending on whether TAE or low-frequency instabilities are of interest,  $\Omega \sim 1$  or  $\Omega \sim \omega_{*i}/\omega_A \ll 1$  may apply. A comprehensive review of the application of the GFLDR in both linear and nonlinear regimes, published recently in two parts, is provided by Zonca and Chen [138,140]. The key message here is that the linear stability and nonlinear evolution of MHD and energetic-particle modes are determined by the principle of energy balance, including both fluid and kinetic contributions.

The basic mechanisms giving rise to Alfvén eigenmodes, EPM and internal kink modes in tokamaks have been described. It is now pertinent to examine the behaviour of such modes in MAST plasmas, since we will be concerned in later chapters with the effects of MHD modes on the FI distribution.

## 3.4 MHD activity observed in MAST

### 3.4.1 Classification of MHD modes

Figure 3.6 shows a spectrogram of the perturbations to the poloidal magnetic field in a typical beam-heated MAST discharge. This is derived from a magnetic pick-up coil located on the outboard midplane of the vessel, close to the interior wall. Neutral beam injection at  $E_{b1} = 71$  keV started at 0.05 s in this shot, injecting 2.0 MW of NBI power. A second beam at  $E_{b2} = 61$  keV was added at 0.18 s, providing an additional 1.5 MW of NBI power.

The period shown in fig. 3.6 exhibits closely spaced bursts of activity close to the core TAE frequency for approximately the first 20 ms. The frequency of this activity gradually decreases over the following 20 ms, and the bursts start to become more widely spaced in time. The low-frequency component of the well-separated bursts between 0.14 s and 0.18 s appears to span most of the frequency range from the core rotation frequency  $f_{\text{rot}}$  up to the TAE frequency  $f_{\text{TAE}}$ ; closer inspection of the signal reveals these to be *chirping modes*, which sweep down rapidly in frequency over approximately 1 ms. A clear transition occurs shortly before 0.19 s, when the duration of each

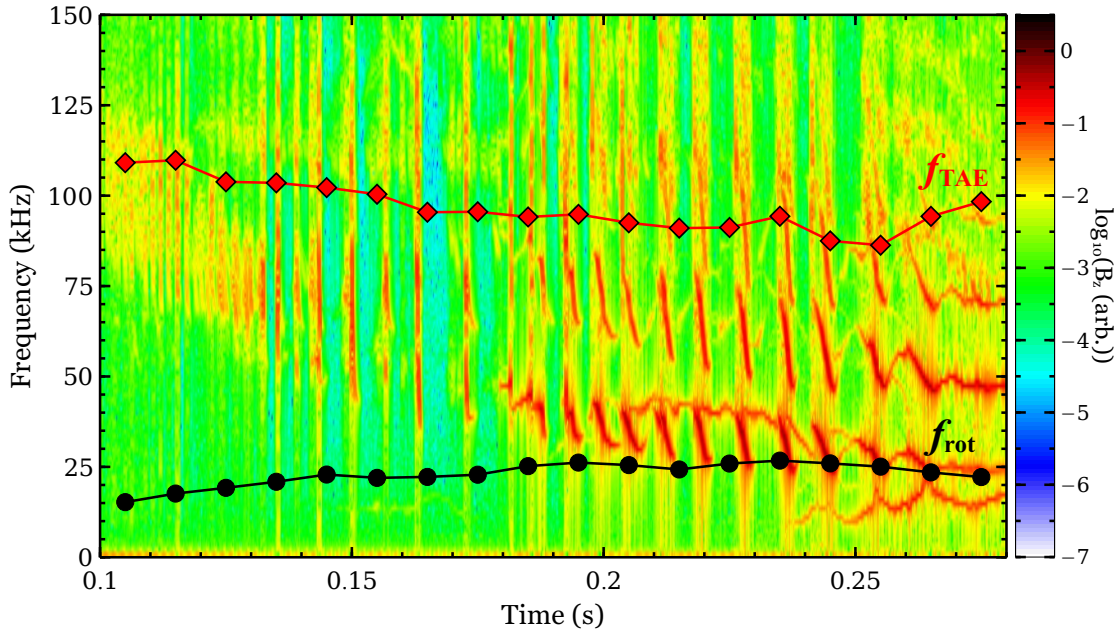


Figure 3.6: The temporal evolution of the spectrum of poloidal magnetic field perturbations on the outboard midplane of the MAST vessel during shot #29207. Black and red points show the on-axis toroidal rotation frequency and TAE gap frequency respectively. The parameters used to derive these values were obtained from charge-exchange measurements of the rotation velocity, Thomson scattering measurements of the electron density, and a reconstruction of the magnetic equilibrium with the EFIT equilibrium solver (see chapter 6).  $f_{\text{TAE}}$  plotted here is equal to the sum of the calculated core TAE frequency and the toroidal rotation frequency, accounting for the Doppler shift of the frequency observed in the lab frame.

burst lengthens substantially to approximately 3 ms and the amplitude of the bursts increases significantly. These large-amplitude bursts exhibit clear separation into a low-frequency fundamental component ( $n = 1$ ), chirping down from approximately 20 kHz above the core rotation frequency to match  $f_{\text{rot}}$  at the end of the burst, and a second harmonic ( $n = 2$ ) at twice the fundamental frequency in the lab frame. Higher harmonics are also observed, albeit at much lower amplitudes. Finally, the bursts undergo a transition to a continuous mode which tracks the core rotation frequency from 0.27 s until the end of the discharge.

The evolution of the bursts of MHD activity is seen clearly in a time trace of the Mirnov pick-up coil signal. Figure 3.7 shows the raw data from the coil used to generate the spectrogram shown above. There is no clearly-defined criterion to establish on the basis of the observed behaviour whether a given burst of MHD activity should be classed as a TAE or an EPM. The classification indicated in fig. 3.7 is based mainly on the frequency of the mode. As seen in fig. 3.6, the first set of weakly chirping MHD bursts is clustered close to the core TAE frequency, so these modes are identified as

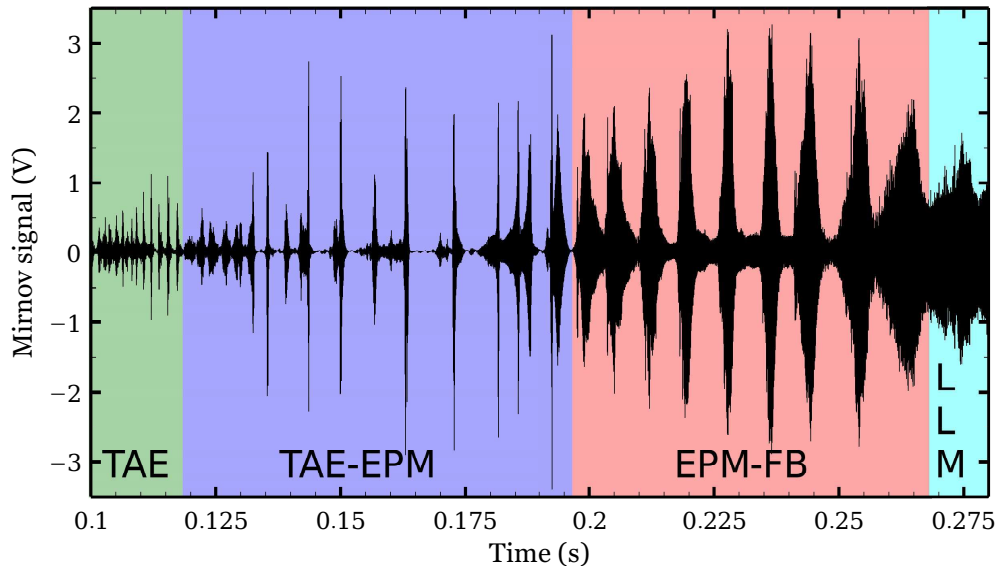


Figure 3.7: Time trace of the data acquired during shot #29207 by an outboard mid-plane magnetic pick-up coil. The coil is the same as that used to generate the spectrogram in fig. 3.6. Overlaid coloured regions show the qualitative classification of the different types of MHD activity as it evolves throughout the shot. The classification is based on the temporal evolution of the frequency and amplitude of the signal. TAE=toroidal Alfvén eigenmode; EPM=energetic particle mode; FB=fishbone; LLM=long-lived mode, which is the name commonly given to the saturated internal kink mode in MAST.

TAE. The modes in the blue region in fig. 3.7 exhibit much stronger frequency chirping and depart significantly from the TAE frequency, suggesting a strong energetic-particle drive which allows them to chirp down into the continuum. Features of these modes in the Mirnov coil trace include large ‘spikes’ in amplitude lasting for just one or two wave cycles; asymmetric evolution in time; highly variable spacing between bursts; and variable amplitude from one burst to the next. These are tentatively identified as TAE with nonlinear coupling to EPM, although they will be referred to simply as ‘chirping TAE’ hereafter. In the red region, although some of the features such as the temporal asymmetry of the TAE-EPM are still apparent in the first few bursts, the evolution of each burst is slower and more regular. The amplitude of successive bursts seems to follow a slowly evolving envelope, reaching a maximum at approximately 0.235s, and there is much less inter-event variability. In accordance with the nomenclature used for such MHD activity on other devices [84, 92, 136, 141], these are called fishbones. The term ‘chirping modes’ is taken throughout this work to include both chirping TAE and fishbones. A characteristic of the fishbones is that the frequency at the end of the burst coincides almost exactly with the core toroidal rotation frequency. Finally, the steady-state mode, which in MAST tends to evolve directly from the last of a

set of fishbones, tracks the core rotation frequency and exhibits no frequency chirping and only weak amplitude modulation. This behaviour suggests a saturated ideal-MHD mode. Analysis with soft X-ray detectors and a toroidal array of Mirnov coils shows the dominant structure of this mode to be that of a  $(m, n) = (1, 1)$  internal kink [142]. This is often called the *long-lived mode* (LLM) in MAST, due to its tendency to persist from the end of the fishbone period until the end of the discharge.

Each of the chirping modes described above was observed to affect the background plasma very weakly, if at all [26, 143]. The results presented in chapter 7 however show that the chirping modes had a strong effect on the FI population in MAST. This lends further support to their identification as EPM. Internal measurements of density fluctuations allow insight into the mode structure. Two arrays of SXR detectors were installed on MAST to measure internal fluctuations. One array viewed the plasma along chords lying in the poloidal plane, at a range of angles about the midplane, and the other array viewed the plasma on chords lying in the midplane at a range of tangency radii. The geometry of these lines of sight is shown in fig. 3.8.

The SXR system on MAST used a beryllium filter to block photons with an energy below approximately 1 keV. This allowed the line emission from the dominant impurities such as carbon to be excluded. The detected signal is therefore due primarily to *bremstrahlung*. Bremsstrahlung, or ‘braking radiation’, is emitted when a charged particle decelerates due to its Coulomb interaction with another charged particle. In a fully-ionised plasma, the emission from a given volume is related to the local electron density and temperature, and to the presence of ions of different charge states, through

$$\varepsilon \propto n_e^2 T_e^{1/2} Z_{\text{eff}} \exp(-E_0/T_e).$$

$E_0$  is the lower threshold on the integration in energy [144], corresponding in this case to the cut-off of the beryllium filter. The other parameters are as defined in chapter 1. The signal is therefore highly sensitive to local density fluctuations. Figure 3.9 shows time traces of SXR fluctuations on poloidal and equatorial chords with tangency radii close to the magnetic axis during the evolution of a fishbone in shot #29976. The amplitude of the fishbone in the magnetic coil trace peaks at approximately 0.2013 s, so the period shown in the figure includes the growth and decay phases of the instability.

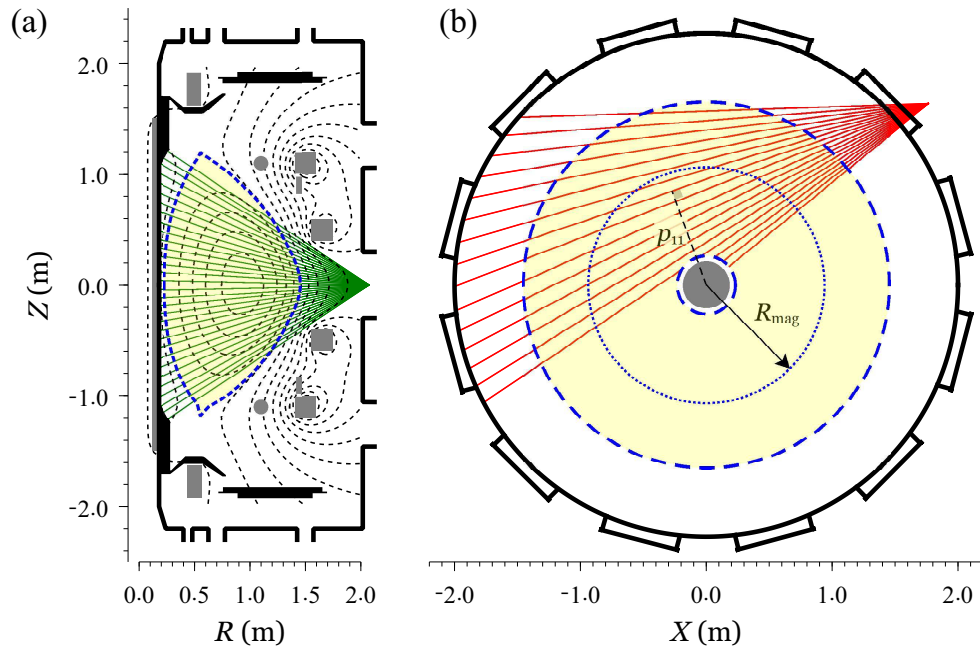
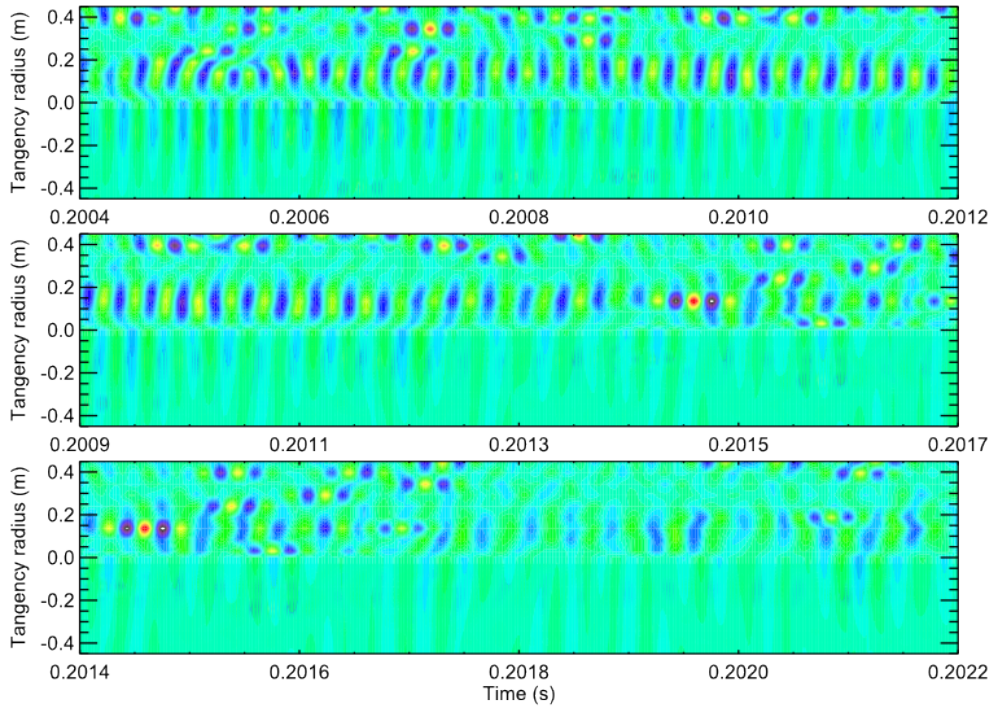
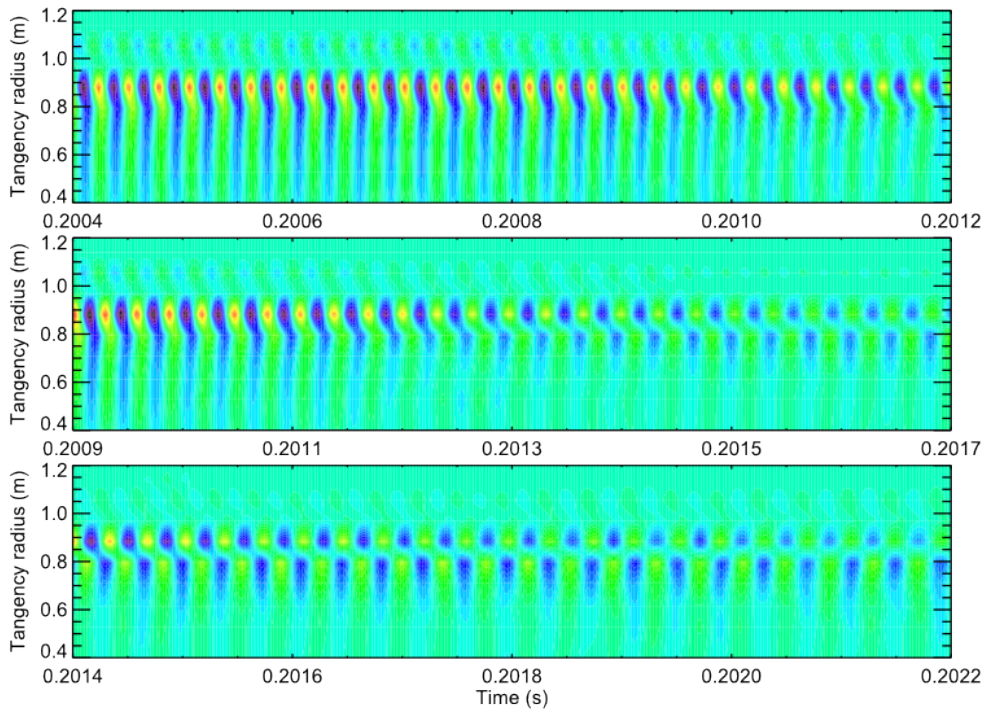


Figure 3.8: Geometry of the lines of sight (LOS) of the SXR detectors on MAST, projected onto the poloidal and equatorial planes. The array shown in green in panel (a) consists of a set of LOS spanning the poloidal cross-section of the plasma, with the central chord looking radially inward on the midplane. The red LOS in panel (b) lie on the midplane, and are identified by their tangency radii (the tangency radius of chord #11,  $p_{11}$  is labelled). Dashed lines represent flux surfaces, with the thick blue dashed line being the LCFS. Solid black structures are graphite armour on the divertor and centre column, and solid grey structures are the cross-sections of poloidal field coils. The dotted blue circle in panel (b) is the magnetic axis, at  $R_{\text{mag}} \approx 0.95$  m. Figure adapted from ref. [26].





(a) Poloidal SXR array



(b) Equatorial SXR array

Figure 3.9: Fluctuations in the [20:40] kHz bandpass-filtered SXR signal during a fishbone in shot #29976. The signal from the poloidally-viewing array of LOS is shown in panel (a), and that from the equatorially-viewing array of LOS is shown in panel (b). The tangency radius in (a) is defined as the height above the midplane at which the chord reaches major radius  $R = R_{\text{mag}}$ ; that in (b) is defined as indicated in fig. 3.8. Note that each panel overlaps with the preceding panel by 3 ms, and that the intensity scaling of each panel is arbitrary. The detector gain differs between channels, so the fluctuation amplitude is not directly comparable between channels.

Panel (a) of fig. 3.9 shows a clear antiphase relationship between the signals above and below the midplane; this identifies the fishbone as predominantly a  $m = 1$  mode. During the growth of the instability, the signal in each of the midplane channels is seen in panel (b) to be very nearly in phase. It appears however that the fluctuations in channels with tangency radii  $p_n \leq 0.8$  m gradually start to lead the outer channels in phase. By  $t = 0.2013$  s this phase ‘slippage’ has become very apparent, and by  $t = 0.2016$  s the channels either side of  $p_n = 0.8$  m are clearly in antiphase. At around the same time, the signals above and below the midplane in the poloidal array appear to suffer a breakdown in cross-correlation, losing the clear antiphase relationship which persists throughout the growth of the fishbone. Because the SXR detectors measure the emission integrated along the LOS, it is not straightforward to establish the cause of the change in phase between different signals. This behaviour is however observed in the majority of fishbones in this and other discharges, suggesting a fundamental role in the evolution of the mode. The LLM by contrast exhibits no such phase slippage and remains as a coherent  $(m, n) = (1, 1)$  mode throughout its evolution, implying that this behaviour is related to the nonlinear frequency chirping.

SXR signals associated with fishbones are shown here; the fluctuations in these signals are extremely weak in the case of the chirping TAE. This is likely due to their nature as predominantly shear Alfvén waves, which are incompressible and would not therefore be expected to perturb significantly the local  $n_e$  or  $T_e$ . Turning to consideration of the ideal-MHD kink mode, the LLM is observed to cause a flattening of the toroidal rotation profile in the core of the plasma. Moreover, the nonlinear evolution of the kink mode in the presence of finite plasma resistivity can lead to fast magnetic reconnection at the  $q = 1$  surface [145]. These reconnection events in turn cause a large reduction in core electron temperature due to mixing between warm plasma inside and cooler plasma outside the reconnection region [146]. This phenomenon is known as the *sawtooth*, for reasons which are apparent from fig. 3.10. The sawtooth is observed to flatten the electron temperature profile in the core of the plasma at minor radii less than the *mixing radius*, which coincides very nearly with the  $q = 1$  surface prior to the sawtooth crash. The growth of a kink, or fishbone, instability preceding the sawtooth is a result of the peaked current density inside the  $q = 1$  surface. Once the amplitude of the kink displacement becomes large enough, magnetic field lines with equal helicity on either side of the  $q = 1$  surface may rapidly reconnect in the region where the flux

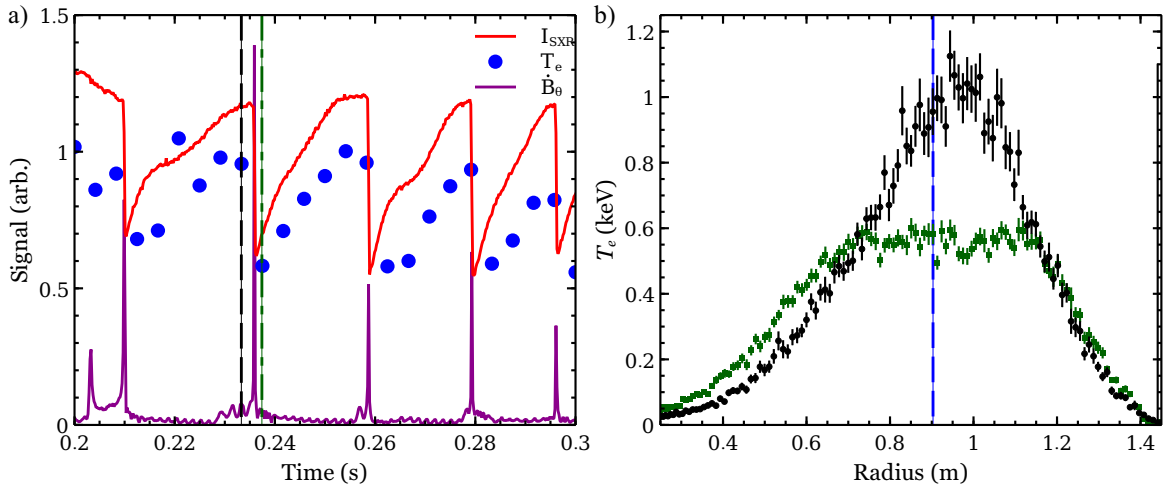


Figure 3.10: a) Time traces of data from an outboard midplane Mirnov coil (purple), a SXR detector with an equatorial LOS (red;  $p = 0.61$  m), and the  $T_e$  measurement from a central channel of the TS diagnostic (blue points;  $R = 0.90$  m) acquired during MAST shot #29880. Sawteeth are visible as a sudden collapse of the electron temperature and SXR emission from the core of the plasma, and as large spikes in the RMS-averaged magnetics signal following a low-amplitude fishbone-like precursor. SXR data are smoothed for clarity. b)  $T_e$  profiles acquired with the TS diagnostic before and after the second sawtooth at the time indicated by the dashed vertical lines in panel (a). The blue dashed vertical line at  $R = 0.90$  m marks the channel from which data are shown in panel (a). The radius within which the  $T_e$  profile is flattened is called the *mixing radius*.

surfaces are compressed by the kink. Helicity is defined as [147]

$$K = \int \mathbf{A} \cdot \mathbf{B} \, d^3\mathbf{r} \simeq \int \frac{2\rho}{q} \, d\rho$$

where  $\mathbf{A}$  is the magnetic vector potential, defined through  $\mathbf{B} = \nabla \times \mathbf{A}$ , and the approximate equality relates  $K$  to the toroidal flux  $\rho$  and the safety factor  $q$  in the presence of nested toroidal flux surfaces. The process of magnetic reconnection leads to the formation of a new set of flux surfaces with a flattened current density profile in the core of the plasma and a safety factor  $q \geq 1$  everywhere within the plasma [145]. Both trapped [148, 149] and co-passing [150] FI are found to affect sawtooth stability through their stabilising effects on the internal kink. This increased stability has been observed to lead to long sawtooth-free periods during ICRH-heated discharges in JET [151] and NBI-heated discharges in JT-60U [152]. Although these quiescent periods resulted in improved performance, the subsequent large sawteeth with mixing radii close to  $s = 0.5$  are of concern due to their degrading effect on global stability and confinement. It is therefore important to determine experimentally the effects of FI populations with different pressure profiles and velocity distributions on sawtooth stability.

### 3.4.2 Research background

MHD modes driven by FI in MAST have been investigated experimentally since 2002 [153], while the effects of these modes on the FI population first came under scrutiny in 2009 after the NBI system was upgraded to provide higher-power and longer-duration periods of NBI [154]. The observed MHD activity consisted of chirping modes at frequencies characteristic of gap modes and continuum EPM [69], while operation at high  $\beta$  was found to suppress the chirping modes [93]. MHD spectroscopy was used to determine the internal amplitudes of the chirping modes [64]. Neoclassical tearing modes associated with the formation of magnetic islands which flatten the local pressure profile, sawteeth and edge-localised modes were also routinely observed [25].

The installation of the collimated neutron flux monitor [71] and the fast-ion  $D_\alpha$  spectrometer [72] in 2010 and 2011 allowed a more detailed investigation into the effects of individual bursts of MHD activity on the confined FI population. Fishbones and the LLM were found to have a deleterious effect on FI confinement [73, 74]. At the same time, it was established that operating with off-axis NBI (obtained by shifting the plasma vertically downward within the vacuum vessel) led to a broadening of the FI pressure profile and consequent reduction of the EPM drive [75]. Improved FI confinement was found to result. The same improvement was recently achieved by operating at high density, which reduces the slowing-down time and hence the radial gradient of the FI distribution [79]. Modelling of FI deposition and transport with the axisymmetric, time-dependent global transport analysis code TRANSP [155] has been found to reproduce the global, and to some extent the local, neutron emission if ‘anomalous FI diffusion’ is introduced to represent the effects of MHD activity on the FI [156]. FI orbits have been calculated in the presence of a kinked core in a static MAST equilibrium [157], which is relevant to the effects of the LLM on FI. This modelling awaits further experimental verification [67]. The results and analysis presented in this thesis meanwhile form a continuation of the recent qualitative and quantitative assessment of the effects of a wide range of MHD modes on FI confinement in MAST [78].

The following three chapters describe the experimental and computational tools used in the course of this research project. We begin by presenting the FI diagnostics available on MAST during the last experimental campaign.

# Chapter 4

## Diagnosing the fast-ion distribution

### 4.1 Outline

Since the distribution of fast ions in velocity space generally cannot be represented by a Maxwellian, measurements of the properties of this distribution must be interpreted more carefully than measurements of properties of the thermal plasma. A particular diagnostic may be sensitive only to FI in a limited part of velocity space, or may have a sensitivity which varies continuously as a function of energy and pitch. Information about the FI distribution in velocity space derived from these diagnostics is therefore necessarily incomplete with regard to both the form of the distribution and also transient perturbations to this distribution caused by MHD activity.

In addition to the velocity-space distribution, it is desirable to measure the distribution of FI in real space. Doing so allows the profiles of heating and current drive to be constrained, and provides spatially-resolved measurements of the effects of MHD instabilities. The deployment of multiple FI diagnostics on a single tokamak is therefore beneficial in the sense that it allows several measurements, each of a different part of the real/velocity-space distribution of FI, to complement each other.

This chapter details the FI diagnostics installed on MAST, with a discussion of the sensitivity of each of these instruments in both real and velocity space. Alternative diagnostics deployed on other tokamaks are also briefly described.

### 4.2 Fast-ion diagnostics on MAST

#### 4.2.1 Description of the diagnostics

During the 2013 MAST experimental campaign, four FI diagnostics were available on the device; one of these, the *charged fusion product detector* (CFPD), is a

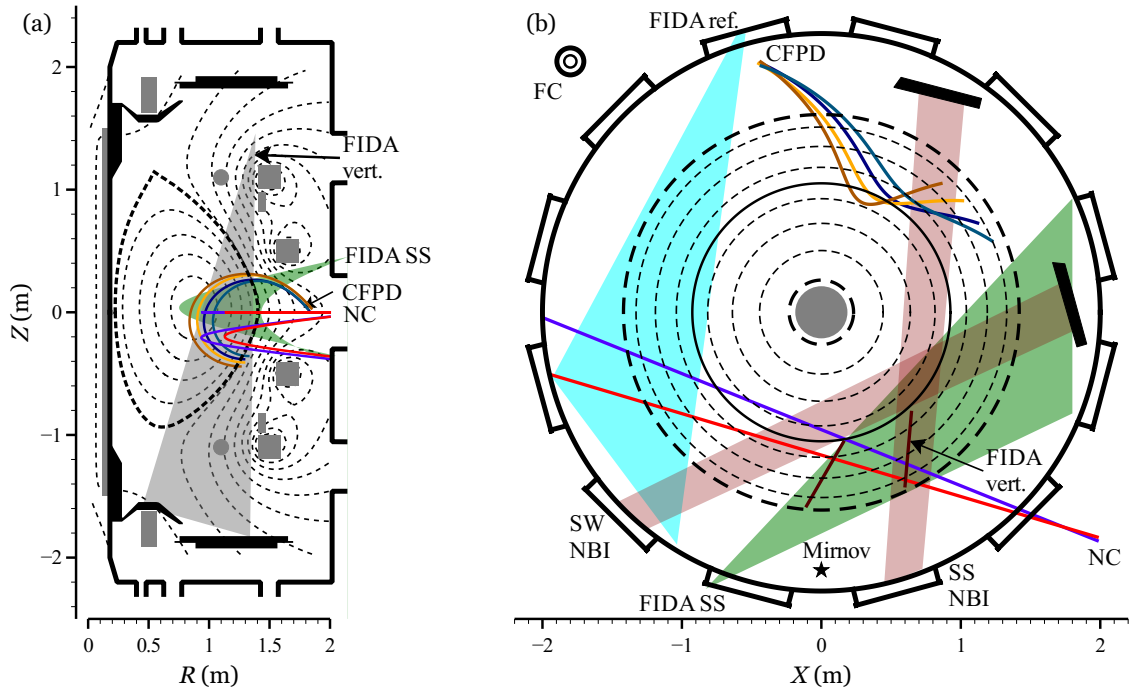


Figure 4.1: Poloidal (a) and equatorial (b) projections of the viewing geometry of each of the MAST FI diagnostics. Flux surfaces are superimposed as dashed lines; solid grey and black components respectively are cross-sections of poloidal field coils and graphite armour on the divertor and beam dumps. Green and grey shaded areas show the region spanned by toroidally- and vertically-oriented SS beam-viewing FIDA lines of sight (LOS) respectively. Red and blue lines show examples of NC LOS, both midplane and diagonally-oriented chords. Coloured, curved lines show fusion proton/triton trajectories from the plasma which reach the CFPD. NBI footprints are shown as red shaded regions. The cyan shaded area marks the region spanned by toroidal FIDA reference views, used for background subtraction. Also shown in (b) are the positions of the fission chamber (FC) and an outboard midplane Mirnov pick-up coil, used to detect MHD activity in the plasma. Midplane intersection radii of the active (SS beam-viewing) and reference (background subtraction) vertically-oriented FIDA chords are shown as dark brown lines in (b). Figure adapted from ref. [78].

novel prototype diagnostic which was installed for only a limited period during the campaign [77]. The other three diagnostics are: a uranium-235 fission chamber for volume-integrated neutron flux measurements [158]; a collimated, radially-scanning neutron detector (known as the neutron camera, or NC) [71]; and a dual-view fast-ion deuterium-alpha (FIDA) diagnostic [72]. Figure 4.1 shows the detector positions and lines of sight of each of these FI diagnostics projected onto the poloidal and equatorial planes of the MAST vessel.

It should be noted that although measurements of the neutron flux are not fundamentally restricted to fast-ion diagnostic applications, the relatively low ion tempera-

ture in MAST plasmas (typically  $T_i \lesssim 2$  keV in the core region of the plasma) resulted in a very low contribution of thermonuclear fusion reactions to the total neutron yield. Approximately 98% of D-D fusion reactions in MAST occurred either between a beam ion and a thermal ion ( $\sim 80\%$ ), or between two beam ions ( $\sim 20\%$ ). As a result, the flux of 2.45 MeV neutrons leaving the plasma provides information about the non-thermal, high-energy tail of the deuterium ion velocity distribution.

The two neutron diagnostics installed on MAST exploited the predominance of beam-thermal and beam-beam reactions in order to obtain information about the FI population in the plasma. The first to be installed was the  $^{235}\text{U}$  fission chamber, or FC [158], which was situated outside the tokamak at a distance of 0.7 m from the vessel and at a height of 0.6 m above the midplane. The diagnostic consisted of 1.34 g of  $^{235}\text{U}$  surrounded by an electrostatic shield, contained within a polythene moderator. Fusion neutrons entering the moderator are slowed down, increasing the probability of causing a neutron-capture fission reaction within the uranium sample; the ion current from the detector therefore provides a measure of the neutron flux. Absolute calibration of this diagnostic should be maintained by regular cross-calibration with an indium activation foil sample and concurrent Monte Carlo neutronics analysis, although this consistency check was last performed in 2008. Nonetheless, as will be shown in chapter 6, consistency of the measured neutron rate with the output of the TRANSP modelling code provides confidence in the robustness of the absolute calibration. The temporal resolution of the fission chamber is  $10 \mu\text{s}$ .

The second neutron diagnostic is the so-called *neutron camera* [71], which consisted of four liquid scintillator detectors coupled to photomultipliers, encased in polyethylene and lead shielding to block scattered neutrons and gamma rays. Four collimators passed through the shielding, providing LOS to the plasma via a thin stainless steel flange in the MAST vacuum vessel. Two of the LOS lay in the machine midplane, and the other two were oriented diagonally downward such that at the point of their tangency to the flux surfaces they lay approximately 20 cm below the midplane. The NC assembly was mounted on a curved rail such that the LOS could be scanned across the plasma between discharges; repeated discharges allowed a neutron emission profile, integrated within the NC fields of view, to be obtained as a function of viewing tangency radius. Post-processing allows the neutron and gamma flux to the detectors to be separated using digital pulse shape discrimination; pulses due to neutrons hitting the detectors

decay more slowly in amplitude than those of gamma rays, allowing the two to be separated to obtain the desired neutron flux measurement. Corrections for *pile-up* (two simultaneous events, which cannot be discerned using pulse shape discrimination) and dead time of the detectors are also applied in post-processing. Data are typically integrated over 1 ms, setting the temporal resolution of the measurements.

The charged fusion product detector was installed on MAST to provide a complementary measurement to that provided by the neutron camera [77]. Conventional solid-state silicon surface barrier detectors were used to measure the flux of 3.02 MeV protons and 1.01 MeV tritons (the gyro-radii, and hence paths to the detector, of these two fusion products being very nearly equal) produced by D-D fusion reactions. The diagnostic consisted of four detectors housed in a boron nitride casing. Collimators in the casing allowed fusion products to reach the detectors, and a 0.8  $\mu\text{m}$  thick aluminium foil prevented soft X-rays from hitting the detectors. The CFPD was mounted on the end of a linear reciprocating probe inserted into the MAST vessel at the midplane. This diagnostic technique is practical in small, low-field devices such as MAST because the large gyro-radii of the fusion products render them essentially unconfined by the magnetic field; they leave the plasma within a single gyro-orbit. With a suitable reconstruction of the magnetic equilibrium, orbits of these particles may be tracked ‘backward in time’ from the detector to determine the possible location of their emission. Retraction or insertion of the probe between repeated discharges allowed a spatial scan of the proton and triton emission profile. Protons and tritons are discriminated in post-processing via pulse height analysis. As in the case of the NC, the integration time of the data is typically set to 1 ms.

Finally, the FIDA diagnostic provided a more direct measurement of the FI density in the plasma, albeit in a bounded region of velocity space, by observing the Balmer-alpha ( $D_\alpha$ ) emission of reneutralised fast deuterons which had undergone charge exchange reactions with beam neutrals [72]. The light was coupled from lenses mounted on the MAST vessel via optical fibres to a spectrometer; spatial resolution was obtained by using individual fibres for each LOS through the plasma, and spectral resolution was provided by dispersion of a bandpass filtered portion of this light within the spectrometer. The spectrum of  $D_\alpha$  light provides information about the distribution of the FI LOS velocity at the point at which charge exchange occurred;  $D_\alpha$  light from reneutralised FI moving away from the lens is redshifted, while that from FI moving



toward the lens is blueshifted. Eleven channels could be connected to the spectrometer at any given time, allowing a radial profile of the FIDA emission to be acquired within a single discharge. Data were acquired with 0.3 ms temporal resolution using an electron-multiplying charge-coupled device (EMCCD) at the output of the spectrometer. Two sets of views were available: a near-toroidal set from a lens mounted 45 cm above the vessel midplane, and a near-vertical set from a lens mounted on a poloidal field coil support inside the vessel, looking vertically downward at the neutral beam. The toroidal views are predominantly sensitive to toroidally circulating fast ions, with a small angle between their velocity and the magnetic field, while the vertical views are more sensitive to magnetically trapped fast ions with a larger angle between their velocity and the magnetic field.

An example of the data from each of the diagnostics described in this section is shown in fig. 4.2. 2.0 MW of neutral beam heating power (at  $E_{b1} = 70$  keV) was applied from 0.051 s, with an additional 0.7 MW (at  $E_{b2} = 44$  keV) applied from 0.101 s. A series of large fishbones occurred from 0.20 s to 0.25 s; the time of the first of these bursts of MHD activity is indicated by the vertical dashed line. The effect of the fishbones is apparent as a significant drop in the magnitude of the signal in each time trace; this effect is particularly marked in the NC, FIDA and CFPD data, where drops in excess of 25% of the pre-fishbone signal are observed.

### 4.2.2 Real-space sensitivity

Interpretation of data such as those shown in fig. 4.2 requires an understanding of the spatial weighting of each measurement. This allows us to determine, for example, whether the effects of certain MHD instabilities on the FI population are restricted to a particular part of the plasma. The weighting which characterises each diagnostic depends on the geometry of the lenses or collimators which form part of the diagnostic apparatus, as well as on the emissivity profile of the particles or light to which the diagnostic is sensitive.

In the case of each of the fusion product diagnostics, i.e. the FC, NC and CFPD, the emissivity profile is almost identical (being simply the profile of the rate of neutron or proton-producing D-D fusion reactions per unit volume, per fast ion). The geometry of the diagnostics, the vessel hardware and, in the case of the CFPD, the magnetic field determine the spatial sensitivity of the diagnostics. The FC provides a volume-integrated measurement, and the sensitivity as a function of the location of neutron

emission is governed by the distance from the emitting volume to the diagnostic, and the presence of structures which scatter or absorb neutrons. The calibration of this sensitivity was performed shortly after installation with the use of a californium-252 source placed inside the vessel and moved systematically around the approximate location of the plasma axis; the FC signal was recorded with the source in each location in order to determine the sensitivity, and Monte Carlo neutronics analysis was used to extrapolate the response to that expected in the presence of an extended source

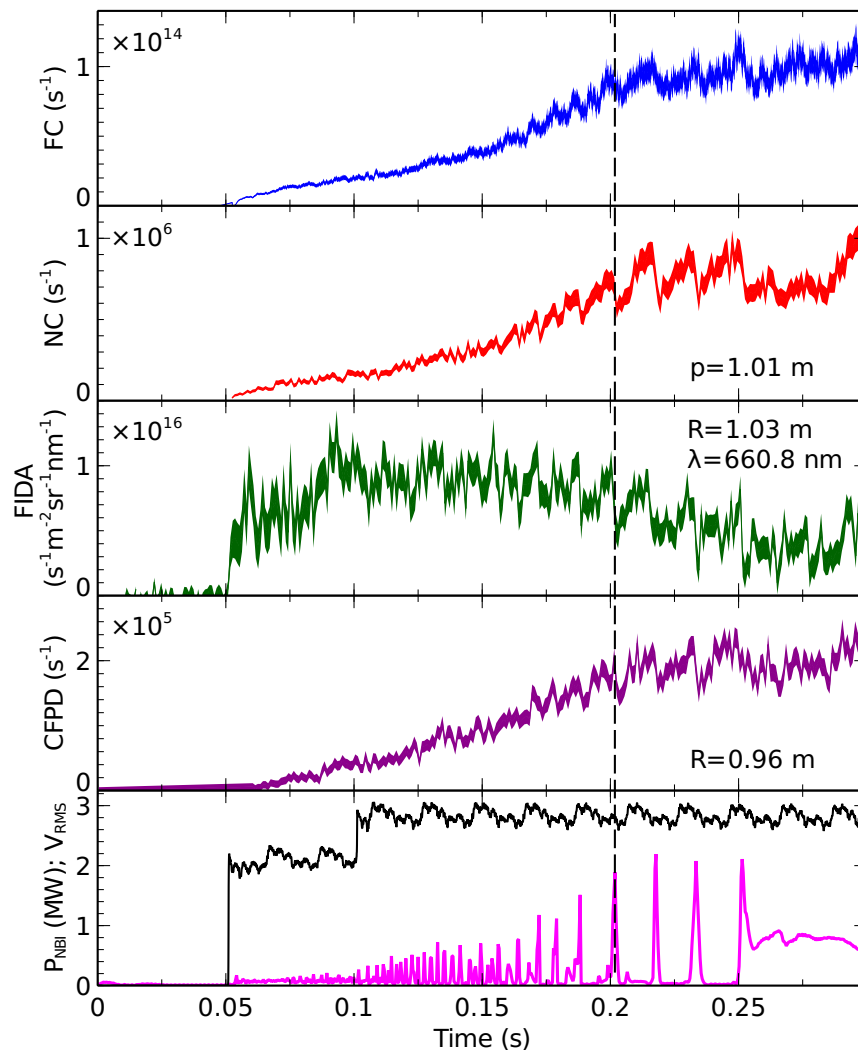


Figure 4.2: Time traces from single channels of the four MAST FI diagnostics, from shot #29980. The first four panels show, from top to bottom: fission chamber count rate; neutron camera count rate from a midplane chord with tangency radius  $p$ ; FIDA spectral radiance at wavelength  $\lambda$  from a chord intersecting the axis of the SS neutral beam at major radius  $R$ ; CFPD proton count rate from a channel with fusion proton trajectories intersecting the midplane at major radius  $R$  (where the values of  $p$ ,  $R$  and  $\lambda$  are given by the labels in each panel). The thickness of the lines shows the statistical uncertainty in the data. Shown in the bottom panel is the total NBI power and the RMS voltage in a vertically-oriented Mirnov coil on the outboard midplane.

of fusion neutrons [158]. Subsequent analysis and comparison with the output of the transport analysis code TRANSP has revealed this calibration to be robust, although a small correction factor of 0.91 must be applied to the measured neutron rate in double-null diverted (DND) discharges to obtain consistency with TRANSP modelling; this correction factor has been applied to the FC data in this thesis.

In contrast to the global nature of the FC measurement, the NC is sensitive only to neutrons which reach the detectors via the collimators. Monte Carlo neutronics analysis has shown that almost all the neutrons contributing to the signal, at least in the core of the plasma for views with tangency radius  $p \lesssim 1.15$  m, originate in the region of the plasma viewed through the collimators, although there is a small ‘background’ contribution ( $\sim 10\%$ ) from neutrons scattered by structures within the vessel into the collimators [76]. Part of the contribution of scattered neutrons to the total signal is eliminated by application of a lower threshold on the energy of recorded events. Determination of the volumetric contribution of each part of the plasma to the NC fields of view is carried out using the Monte Carlo solid-angle calculator LINE2 [76]. Synthetic neutron emission profiles are subsequently convolved with this volumetric contribution to determine profiles of count rate as a function of tangency radius. The finite solid angle of the collimators gives rise to the quoted uncertainty of  $\pm 2.1$  cm in tangency radius [76]. The NC is not absolutely calibrated, although the detector response has been estimated using a Monte Carlo code to model the interaction of neutrons with the liquid scintillator detectors. A parameter representing the detector efficiency is included in the fitting procedure to obtain a match between measured and synthetic count-rate profiles; values of this parameter are within 20% of the estimated detector efficiency based on Monte Carlo modelling.

The CFPD also relies on collimation of its LOS to restrict the viewing geometry to a well-defined region of the plasma, although in this case the trajectories of fusion products which reach the detectors vary throughout the discharge depending on the magnetic field strength and orientation. An additional modelling uncertainty is thereby introduced into the interpretation of CFPD data; the reconstruction of the magnetic equilibrium is subject to uncertainty, with the positions of flux surfaces typically varying by a centimetre or more depending on the weight given to various constraints in the equilibrium reconstruction. Furthermore, deviations from axisymmetry produced, for example, by a ‘ripple’ in the toroidal magnetic field resulting from the discrete nature

of the toroidal field coils are not taken into account in the reconstruction of particle orbits. The trajectories of the fusion protons or tritons also depend on their energy, so that two particles emitted from the same location in the same direction may follow slightly different trajectories; one may reach the detector via the collimator, while the other may not. The real-space and velocity-space sensitivity of the CFPD are therefore coupled, and full-orbit modelling of the fusion proton/triton trajectories is necessary in order to develop a fully consistent picture of the diagnostic's sensitivity. Such analysis has not yet been performed, so the paths to the detectors illustrated in fig. 4.1 for example are only approximate. At present, the uncertainty in the trajectories is represented by a quoted uncertainty of  $\pm 5 - 7$  cm in the radial location of the emission projected onto the midplane, in addition to an uncertainty of  $\pm 3$  cm arising due to the finite acceptance angle of the collimators [77].

For each of the fusion product diagnostics, the emissivity varies throughout the plasma. The D-D fusion reactivity must be averaged over the distribution of relative velocities between the reactant ions present in a given volume; dependence of emissivity on spatial location therefore arises via the ion temperature variation, which affects the beam-thermal reactivity averaged over the Maxwellian velocity distribution of thermal ions, and the variation of the FI distribution in real and velocity space, which affects the prevalence of beam-beam fusion reactions. In general, the higher ion temperature in the core of the plasma enhances the beam-thermal fusion reactivity, and the higher FI density enhances the beam-beam reactivity, so the fusion product diagnostics are particularly sensitive to fast ions in the core. One factor which mitigates this enhancement however is the toroidal rotation of the plasma. This is highest in the core where the beams inject the most torque, and reduces the relative velocity and hence the fusion reactivity between toroidally-passing FI and thermal ions in this region. These factors are taken into account by the Monte Carlo NUBEAM module of the TRANSP code [159]. NUBEAM tracks fast ions as they are deposited and slow down in the plasma, modelling their interactions with thermal and FI species to generate local FI distributions and neutron emission profiles. Figure 4.3 shows profiles of FI density (integrated over part of velocity space), and neutron emission divided by FI density, modelled by TRANSP for a particular MAST shot and time. The neutron emission profile is marginally more peaked in the core of the plasma than is the FI density, due mainly to the increased beam-beam neutron yield in this region (TRANSP output provides separate measures of the beam-beam and beam-thermal neutron emission rates; the ratio of beam-thermal

reactions to fast-ion density is largely constant throughout much of the plasma).

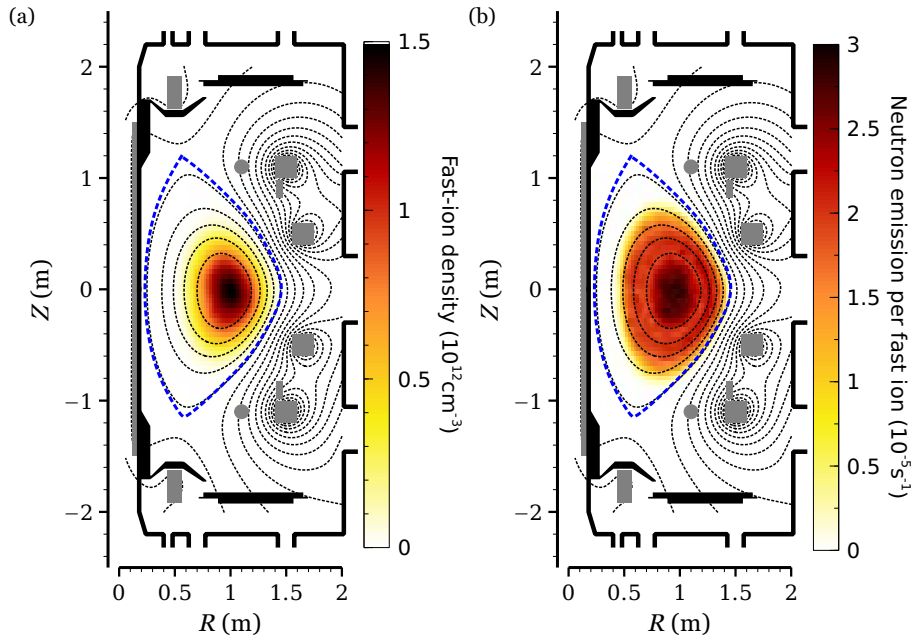


Figure 4.3: (a) TRANSP-calculated FI density as a function of  $(R, Z)$  for MAST shot #29976 at  $t = 0.2$  s. The FI distribution is integrated over values of pitch  $p \in [-1, 1]$ , and energy  $E \in [36, 72]$  keV (which excludes the half- and third-energy components of the injected beam ions). (b) TRANSP-calculated total neutron emission (beam-beam + beam-thermal) divided by the FI density shown in panel (a). The enhancement of this ratio in the core of the plasma indicates that the neutron emission is more peaked than the FI density. Dotted contours in each panel show surfaces of constant poloidal flux, with the LCFS shown in blue.

In contrast to the fusion products, the  $D_\alpha$  radiation contributing to the FIDA signal is spatially localised in origin owing to the requirement that neutral atoms be present as a source for CX reactions with the FI. Deuterium in the bulk plasma is fully ionised, meaning that the only ‘donors’ available for CX reactions are the injected beam neutrals, the so-called *halo* neutrals produced by CX between beam neutrals and thermal ions which form a cloud of ‘warm’ ( $T \approx T_i$ ) neutrals centred on the beam, and the ‘cold’ ( $T \sim 10$  eV) external neutrals which penetrate a short distance into the plasma edge before being ionised. The objective of the FIDA measurement is to provide information about the confined FI population in the core of the plasma; as such, the CX contribution from beam and halo neutrals is of primary interest. The CX contribution from edge neutrals constitutes a source of contamination of the spectrum, a so-called *passive FIDA* contribution, and should be subtracted. On MAST, this was achieved using ‘reference’ views which were positioned such that their geometry with respect to the plasma was similar to that of the active LOS. The reference views were toroidally

displaced so that their LOS did not intersect the neutral beams. Under the assumption that the passive FIDA emission is toroidally symmetric, the net (active–reference) FIDA signal contains only the contribution resulting from CX of FI with beam and halo neutrals. The FWHM of the beam neutral density profile perpendicular to the beam axis was approximately 12 cm to 15 cm; careful choice of the viewing geometry such that the LOS were close to being tangential to the flux surfaces where they intersected the beam allowed a radially-localised measurement of FIDA emission. The radial resolution of the measurement is governed by: the finite solid angle subtended by the LOS; the finite radial extent of the LOS path through the neutral beam; and the lifetime of the  $n = 3$  excited state of the reneutralised FI before they undergo the  $n = 3 \rightarrow 2$  transition. These factors limit the radial resolution to approximately  $\pm 2.5$  cm.

Since the FIDA emission is proportional to the product of FI density and neutral density, the measurement is most sensitive to FI in regions where the neutral density is large. Unlike the fusion product emission, which is strongest in the core of the plasma, the FIDA emission is strongest at the point on the outboard midplane ( $R \approx 1.1$  m) where the product of beam density (which is largest at the edge and decreases towards the core due to beam attenuation) and FI density (which is largest in the core, where most FI are deposited, and decreases towards the edge) is highest.

### 4.2.3 Velocity-space sensitivity

As mentioned earlier, each of the FI diagnostics has a sensitivity to FI which varies throughout velocity space as well as real space. This is most apparent in the case of the fusion product diagnostics, since the D-D fusion cross-section is a strong function of reactant energy. Figure 4.4 shows the cross-section of the two branches of the D-D fusion reaction as a function of centre-of-mass energy from 5 keV to 100 keV [160]. It is clear from the form of this curve that the sensitivity of fusion proton or neutron emission measurements is strongly weighted to the high-energy FI, especially given that the contribution of reactions at each energy to the total reactivity is proportional to  $\sigma v$  rather than simply to  $\sigma$ . The weighting of the measurements at each point in velocity space is determined by averaging the reactivity over the Maxwellian velocity distribution of thermal ions in the case of beam-thermal reactions and the (numerically-calculated) velocity distribution of beam ions, in the case of beam-beam reactions.

An illustrative example of the velocity-space sensitivity of the FIDA diagnostic is

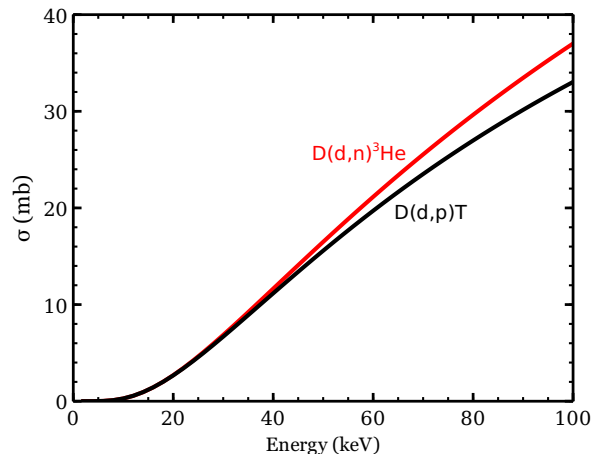


Figure 4.4: Cross-section of the two branches of the D-D fusion reaction as a function of the centre-of-mass energy of the reactants. The empirical formula of Bosch & Hale (1992) is used to obtain each of the curves [160].

shown in fig. 4.5. FIDA measurements are sensitive only to FI in a bounded region of velocity space; this region is shown in panels (b) and (d) of fig. 4.5 for two toroidally-viewing chords with different beam intersection radii. Variation of the sensitivity within this bounded region arises due to geometric factors, which determine the proportion of the gyro-orbit in which the LOS velocity of each FI renders it detectable in a particular viewing chord at a particular wavelength. Atomic physics factors also play a part, by determining the probability that interaction with beam or halo neutrals will give rise to the emission of a  $D_\alpha$  photon. This geometric part of this sensitivity function, known as a *weight function*, is determined by the geometry of the LOS, the magnetic field and the neutral beam. The CX probability depends on the electron temperature and density via their effect on the beam and halo neutral density and distribution of excited states. NBI energy and full, half and third-energy current fractions also affect the CX probability via their effect on the relative velocity between FI and beam neutrals. Observing FIDA light at a given wavelength corresponds to observing emission which is a product of the wavelength-dependent weight function and the FI distribution at the location of beam intersection. Stark splitting of the Balmer-alpha radiation also plays a part in determining the precise details of the weight function. Given the complexity of their construction, these weight functions must be calculated numerically in a similar manner to the fusion neutron or proton emissivity profiles. The general method for quantitative calculation of FIDA weight functions is detailed by Salewski *et al.* in ref. [161], while the Fortran version of the FIDASIM code developed by Geiger [162] calculates weight functions based on the contribution of Monte Carlo marker particles,

representing reneutralised FI, to the FIDA spectra. This code was used to generate the weight functions shown in fig. 4.5.

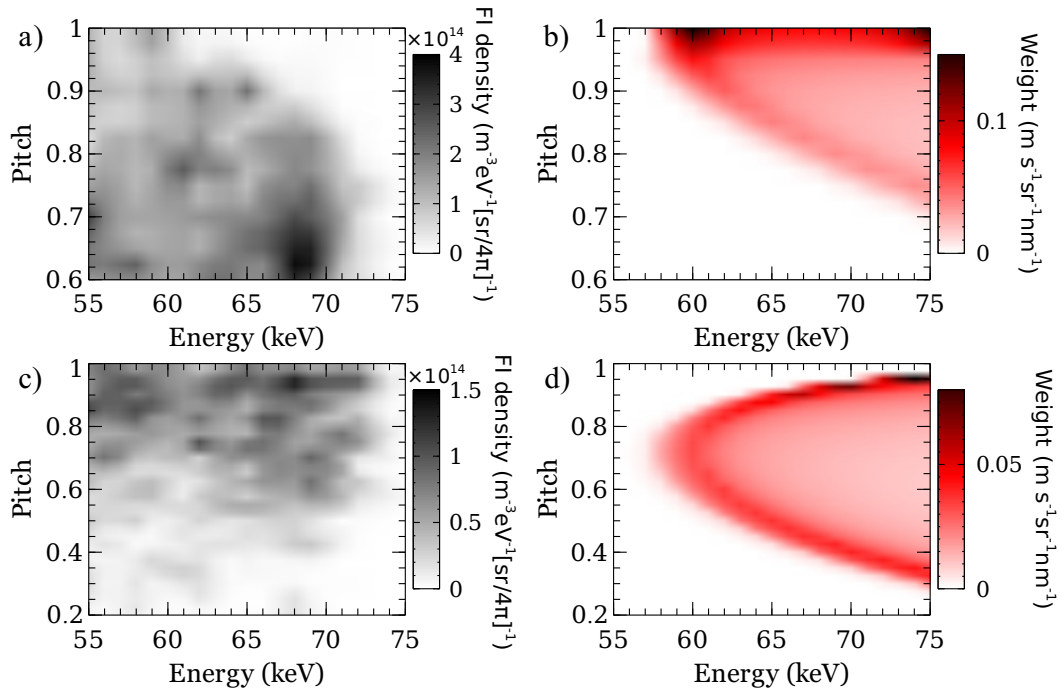


Figure 4.5: (a) High-energy part of the FI distribution from shot #29976 at  $t = 0.2$  s,  $R = 1.00$  m on the outboard midplane, modelled by TRANSP (based on the same TRANSP run as the FI density and neutron emission shown in fig. 4.3). (b) FIDA velocity-space sensitivity function (‘weight function’) at  $\lambda = 661.3$  nm for a toroidally-viewing chord intersecting the neutral beam at  $R = 1.00$  m. The spectral radiance is obtained by multiplying the FI distribution (panel (a)) by the weight function (panel (b)) and integrating over velocity space. (c) and (d) are similar to (a) and (b), but for a chord intersecting the neutral beam at  $R = 1.25$  m. Note the different ranges of pitch in (c) and (d) than in (a) and (b).

With the real-space and velocity-space sensitivity of each of the FI diagnostics being determined, diagnostic signals may be modelled based on synthetic FI distributions given measurements of the relevant profiles of plasma density and temperature, rotation velocity and impurity density. This modelling, as applied to MAST, is described in chapter 6. Apart from such modelling, knowledge of each diagnostic’s sensitivity is useful in interpreting time series and radial profiles as presented in chapters 7 and 8.

### 4.3 Alternative fast-ion diagnostics

Besides the FI diagnostics installed on MAST, diagnostics on other tokamaks include scintillator-based fast-ion loss detectors (FILDs) for spatially, temporally and energetically-resolved measurements of the flux of FI which are lost from the plasma [58], and neutral particle analysers which fulfil a similar role to the FIDA diagnostic by



providing measurements of the real-space and velocity-space distribution of FI which undergo CX with beam neutrals [163]. Measurements of the confined FI distribution with resolution in real and velocity space are also provided by collective Thomson scattering diagnostics [164], which utilise gyrotrons and waveguides for active diagnostic probing. Spectroscopic measurements of the neutron flux are performed on some tokamaks [165], providing information about the velocity distribution of the reactant isotopes.

The following chapter describes in greater detail the FIDA diagnostic on MAST, the calibration, operation and maintenance of which were the primary responsibilities of this author. Data from the NC and CFPD are used to extend the analysis in subsequent chapters, but the details of the implementation and exploitation of these instruments are deferred to publications authored by those responsible for the hardware [76, 77].

# Chapter 5

## The FIDA diagnostic on MAST

### 5.1 Outline

In order to motivate many of the choices made in the data analysis in subsequent chapters, an understanding of the limitations imposed by the diagnostic hardware is critical. This chapter details the criteria and constraints which influenced the design of the FIDA diagnostic, the choice of components and the compromises made in each of these areas. Set-up, calibration and alignment procedures are described. Finally, obstacles encountered during operation of the diagnostic, which have a bearing on the availability of data for subsequent analysis, and strategies adopted to overcome these obstacles are discussed.

### 5.2 Design considerations

FIDA measurements are challenging due to the weakness of the active CX signal compared to other features in the spectrum. Figure 5.1 shows an example of the spectrum, modelled using the FIDASIM code [162, 166], expected from one of the toroidally-viewing chords of the FIDA diagnostic on MAST. The figure shows the spectrum as emitted by Monte Carlo marker particles representing the beam neutrals and reneutralised fast/thermal ions; the diagnostic's instrument function is not taken into account at this point, as this will be discussed later. The beam and halo emission are at least two orders of magnitude brighter than the FIDA signal, which is similar in magnitude to the bremsstrahlung background. An added complication is caused by the passive FIDA signal mentioned in the previous chapter; this mandates the use of background subtraction techniques to obtain the uncontaminated active FIDA signal. Also present in this spectral region is the  $D_\alpha$  light from neutral deuterium at the edge of the plasma; although this light is emitted close to the rest wavelength of the

line, at 656.1 nm, its extreme brightness relative to the other components (typically three to four orders of magnitude brighter than the active FIDA signal) means that it must be removed from the spectrum to prevent scattered light in the spectrometer, or contamination due to frame-transfer smearing, from masking the FIDA signal.

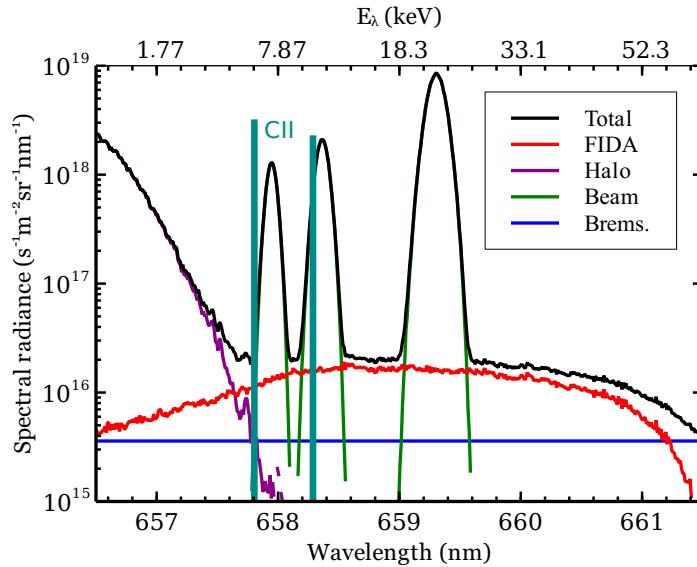


Figure 5.1: Modelled spectrum on the redshifted side of the  $D_\alpha$  line, which is centered at  $\lambda = 656.1$  nm, for a chord from the toroidally-viewing MAST FIDA system which intersects the SS neutral beam at  $R = 1.18$  m. The spectrum is modelled for shot #29034 at  $t = 0.25$  s. Features due to the halo emission, the emission from the full, half and third-energy components of the neutral beam, the active FIDA signal and the bremsstrahlung continuum radiation are shown separately, with the total spectral radiance being given by the black trace. The wavelengths of a pair of C II emission lines are also indicated; these are not included in the model, but are present in measured spectra at approximately the magnitude shown in the figure. Labels on the upper horizontal axis indicate the energy  $E_\lambda$  associated with the LOS velocity of a deuterium atom emitting  $D_\alpha$  light at the corresponding wavelength in the laboratory frame.

In each of the following subsections, the choice of components used in the diagnostic installed on MAST is justified based on these design considerations. It should be noted that the design and installation of the diagnostic were carried out prior to the work described in this thesis by a team of researchers including Dr. Clive Michael, Dr. Neil Conway and Dr. Brendan Crowley. Although many of the details of the diagnostic are described in ref. [72], the information is included in this document for completeness and to aid in understanding the challenges encountered by the present author during testing and operation of the diagnostic.

### 5.2.1 Optical components

The requirement for high light throughput in order to obtain an adequate signal-to-noise ratio (SNR) dictated a preference for fast (low  $f$ -number) optics, matched to the numerical aperture of the optical fibres used as an input to the spectrograph. Based on the design of the FIDA diagnostic installed on NSTX [167], it was decided to use a *HoloSpec*  $f/1.8$  spectrograph from Kaiser Optical Systems, Inc. This instrument features a  $2155 \text{ lines mm}^{-1}$  volume phase holographic (VPH) transmission grating, with a central wavelength of  $653 \text{ nm}$  and a reciprocal linear dispersion of  $6 \text{ nm mm}^{-1}$ . The focal length of the spectrograph is  $85 \text{ mm}$ . This focal length and  $f$ -number provide a close match to the numerical aperture of the optical fibres, which is given as  $0.37$  in the manufacturer's specification. As described by Bell [168], the use of such fast optics with a transmission grating introduces a curvature into the image such that a straight, vertical input slit would appear parabolic in the image plane. This is counteracted by using a curved input slit, with the array of fibres following the curvature of the slit. These components are shown in fig. 5.2; the dashed rectangle demarcates the *HoloSpec* spectrograph, although the slits and filter were produced separately by third parties to satisfy the specifications of the diagnostic.

As illustrated in fig. 4.1 in the previous chapter, both active (beam-viewing) and reference (background) views of the plasma are available. In order to subtract the background emission, spectra from active and reference channels with similar viewing geometry must be acquired simultaneously. This leads to the requirement that two sets of channels be used simultaneously within the spectrometer. As illustrated in the inset of fig. 5.2, three sets of eleven fibres are terminated within the fibre mounting block placed at the input of the spectrograph. Two of these are used at any given time, with one set of fibres feeding in light from the active views, and the other set feeding in light from the reference views. The columns of fibres are separated by a sufficient distance that, once the light has passed through the bandpass filter, the filtered active and reference spectra in the final image do not overlap. A *patch panel* allows the selection of fibres connected to the spectrometer to be changed between MAST discharges; the connections between fibres are made by means of ST connectors, so the process of changing the patched fibre layout is reasonably straightforward.

One of the most critical components of the system is the bandpass filter, which was manufactured by Barr Associates. The filter is required to attenuate the unshifted

$D_\alpha$  light from the edge of the plasma, while allowing the highest possible transmission in the FIDA region of the spectrum. Because of the orientation of the lines of sight in the MAST vessel with respect to the magnetic field, FIDA light from the toroidal views is predominantly redshifted while that from the vertical views is predominantly blueshifted. Two filters are therefore required, one passing the red wing of the  $D_\alpha$  spectrum, the other the blue wing. These are mounted in holders which allow red and blue filters to be swapped between discharges. The filter holders are able to rotate by a few degrees left or right of the optical axis; this flexibility allows the pass band to be precisely tuned to exclude the edge  $D_\alpha$  light while transmitting the halo emission. The halo emission contains useful information about the ion temperature at the location of beam intersection, and may be used to validate collisional-radiative models of the emission as discussed in chapter 6. The red trace in fig. 5.3 shows the spectrum obtained when illuminating the input fibres to the spectrometer with an integrating sphere, which provides a spatially and temporally uniform white light source of a known radiance and colour temperature. The shape of the filter function is apparent in the active (left) and reference (right) channels.

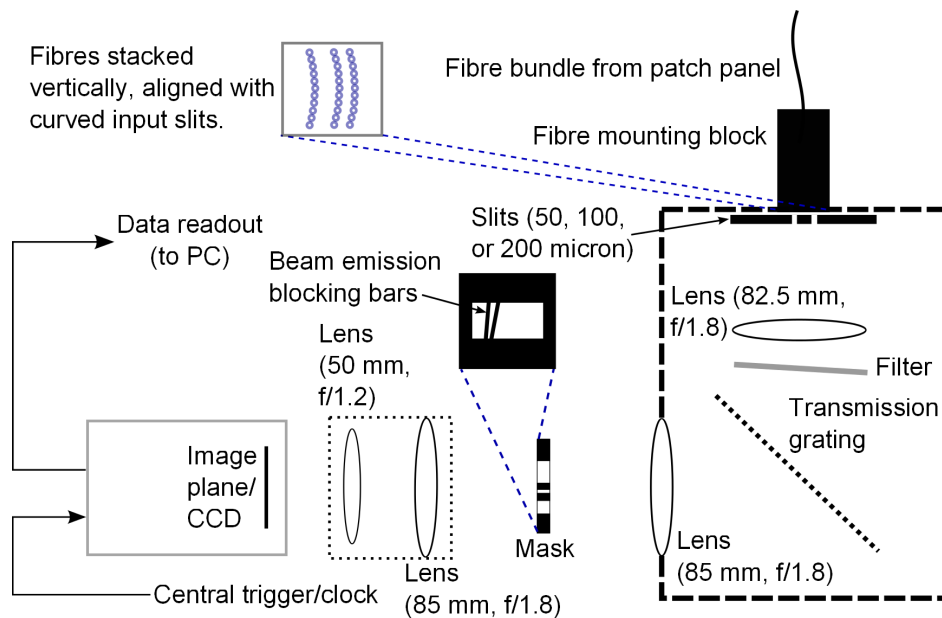


Figure 5.2: Schematic plan view of the FIDA spectrometer used at CCFE. The dashed rectangle shows the extent of the *HoloSpec* spectrograph. The bandpass filter is mounted in a rotating holder which allows it to be tilted left or right of the optical axis. A mask, consisting of a thin, blackened plate with an aperture cut into it, and narrow blocking bars occluding part of the aperture, may be placed in the image plane at the output of the spectrograph. A back-to-back lens pair demagnifies the image and projects it onto the CCD chip. Timing of the data acquisition and readout from the camera are controlled by a digital clock from the MAST control system.

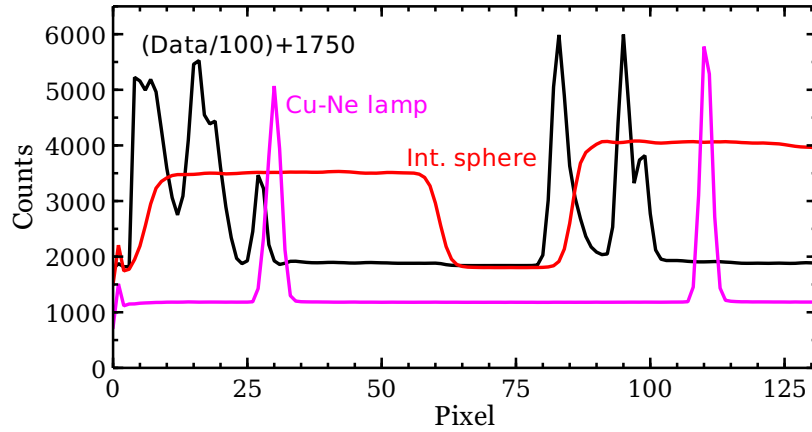


Figure 5.3: Spectra on the redshifted side of the  $D_\alpha$  line acquired during exposure to a uniform white light source (red line), a copper-neon spectral lamp (magenta line), and a beam-heated MAST plasma (black line). The spectrum on the left is from a channel connected to one of the active views (in the plasma exposure), while that on the right is connected to a reference view. The three prominent lines in the reference spectrum, with corresponding components in the active spectrum, are the edge  $D_\alpha$  emission, cut off on the left by the edge of the filter function, and the C II doublet. Note that in this case, during plasma exposure a mask in the intermediate image plane was used to block the beam emission components; the small peak present to the right of the C II lines in the active spectrum is the wing of the full-energy beam emission peak which is visible between two blocking bars of the mask.

Rather than focusing the image from the spectrograph directly onto the CCD chip, an intermediate stage was inserted allowing a mask to be placed in the intermediate image plane. The mask consists of a thin plate with a rectangular aperture, with narrow bars across the aperture oriented to block the beam emission peaks; blocking the beam emission reduces contamination of the FIDA spectrum by frame-transfer smearing on the CCD. A back-to-back 85 mm : 50 mm,  $f/1.8$  :  $f/1.2$  lens pair focuses a second, demagnified image onto the chip; reducing the magnification increases the number of channels and wavelength range that can be accommodated on the area of the chip.

### 5.2.2 EMCCD camera

A Photometrics *Cascade 128+* EMCCD camera records the image from the spectrograph after it has passed through the mask and been demagnified by the back-to-back lens pair. The camera is thermoelectrically cooled to  $-30^\circ\text{C}$  to minimise thermal noise on the dark current. The CCD chip has dimensions of  $3\text{ mm} \times 3\text{ mm}$ , with  $128 \times 128$  pixels; these pixels are binned in the vertical direction such that the spectrum from each of the 11 fibres is projected onto a binned row of 11 or 12 pixels. The camera is operated in frame-transfer mode, in which the charge collected on the exposed chip

is shifted to a covered readout area before being read, amplified and digitised in the analogue-to-digital converter (ADC) one row at a time. This reduces smearing of the spectrum compared to the alternative, parallel-clocking, mode of operation; transfer of each row from the exposed area to the readout area takes 83 ns, meaning that the difference between the exposure times of the first and last row to be transferred is  $127 \times 83 \text{ ns} = 10.5 \mu\text{s}$ . The maximum frame rate of the camera with the binning described above is 3.3 kHz, making the frame-transfer time 3.5% of the exposure time. Data are digitised at 16-bit resolution, with the ADC running at 12 MHz.

Because the FIDA signal is weak, adequate noise suppression requires the use of electron multiplication (EM) gain in a dedicated multiplication register adjacent to the readout register. Impact ionisation during transfer of electrons between adjacent, biased gates within the multiplication register multiplies the acquired charge by a specified gain factor, which scales exponentially with the bias voltage, in a low-noise cascade process [169]. For practical purposes, use of EM gain increases the FIDA signal by approximately an order of magnitude relative to the readout noise under normal operating conditions; the dominant contribution to the noise then becomes the photon, or shot, noise inherent in the signal. The penalty paid for this increased ratio of signal to readout noise is a reduced dynamic range; bright components of the spectrum such as the beam emission often saturate the detector, preventing simultaneous, quantitative measurements of beam emission signal and FIDA signal. Table 5.1 shows the relative contribution, in electrons ( $e^-$ ) per pixel per frame, of each component of the noise in a typical measured FIDA signal of  $100 e^-$  on a background (bremsstrahlung + passive FIDA) of  $100 e^-$ . It is clear from the values in this table that the use of EM gain effectively eliminates the contribution of readout noise to the uncertainty, leaving only the shot noise which scales with the square root of the signal. The noise floor is therefore effectively lowered, allowing detection of weaker FIDA signals.

### 5.2.3 Mechanical components

Each of the two bandpass filters requires a different alignment of the camera relative to the spectrograph, since the angles between the input fibres, the transmission grating and the lenses are fixed. The camera is mounted on a Vernier-controlled translating stage which allows its position in, and rotation around, three axes to be controlled precisely. The spectrograph is mounted on a translating stage which allows horizontal movement in each direction. During operation, the limited time available for alignment

	Read noise	Dark noise	Shot noise
Without EM gain	76	$\leq 1$	17
With EM gain	5	$\leq 1$	24

Table 5.1: Contributions to noise in FIDA measurements with the Photometrics *Cascade 128+* EMCCD. Values are calculated assuming a signal of 200 photo-electrons per pixel per frame in the active channel, and 100 photo-electrons per pixel per frame in the reference channel (values for each contribution are re-normalised in the case with EM gain, to facilitate comparison). The gain setting used in this case corresponds to a multiplication gain factor of 14.84. A frame rate of 3.3 kHz and a detector temperature of  $-30^\circ\text{C}$  are assumed.

during inter-shot setup and calibration meant that the orientation of the camera was not always optimal, giving rise to systematic errors such as those seen in fig. 5.4 in the following section.

The camera is realigned and focused each time the filter is changed, to optimise the position of the pass band imaged on the chip in active and reference channels. In the following section, the procedures used to calibrate the diagnostic after any change of filter, input slits, fibre patching, camera alignment or focus are described.

### 5.3 Calibration procedures

Quantitative analysis of the data requires absolute calibration, in order to convert measured count rates into photon fluxes, and spectral calibration, in order to determine an instrument function to allow comparisons between measured and modelled spectra.

Absolute calibration is performed with the use of an integrating sphere; this provides a steady, spatially-uniform source of white light with a pre-calibrated spectral radiance as a function of wavelength. The spectrometer input fibres may be connected, between plasma shots, to dedicated calibration fibres via the patch panel. Routine calibration is therefore carried out each time the diagnostic configuration is altered. It has been found that sufficiently reliable calibration data may be obtained by connecting only four calibration fibres to the spectrometer, one at each corner of the chip. Relative transmission values of each of the tokamak, spectrometer and calibration fibres were measured during installation of the diagnostic; these typically vary by up to 15% between individual fibres in each set, but the variation is taken into account as a separate coefficient for the transmission of each channel in determining the calibrated spectral radiance. Uncertainties are however introduced by the imperfect reproducibility of the patching between fibres; slight misalignments between connectors in the patch panel,



as well as the presence of dust or scratches on the ends of the fibres, introduce a reproducibility error of  $\lesssim 10\%$ .

Spectral calibration data are also recorded each time the diagnostic configuration is altered. A spectral lamp with a neon buffer gas provides suitably distinct Ne I lines in each of the filter pass bands. Figure 5.3 shows an example of the calibration spectrum recorded using this source. The natural widths of the lines emitted by the spectral lamp are negligible compared to the spectral resolution of the diagnostic, so the recorded spectrum as a function of pixel number provides a direct measurement of the diagnostic's instrument function, albeit coarsely discretised due to the limited number of pixels spanned by each line. The FWHM of the line on the CCD chip is approximately 2 pixels, corresponding to 0.3 nm, when using 50  $\mu\text{m}$  input slits. Aberrations introduced by the fast optics cause the instrument function to exhibit low-amplitude 'wings' which are much broader than the FWHM however; these wings span approximately 14 pixels, or 1.9 nm, at the 0.1% intensity level, and care must be taken when analysing the FIDA signal in the region of the spectrum close to the beam emission peaks.

Figure 5.4 shows typical (time-averaged) frames from the CCD camera associated with white light and spectral calibration. Note that, due to a breakage in one of the spectrometer fibres, the first and tenth rows are patched. The breakage occurred early during the 2013 experimental campaign, rendering only ten channels usable throughout the campaign rather than the original eleven channels. Contamination of row 2 with light from row 1 due to imperfect alignment of the camera is evident; the maximum level of this contamination is approximately 7% of the signal intensity in row 1.

The spectrometer transmission derived from a chi-square minimisation fit to the white light calibration data is typically in the range 0.36 to 0.42. Combined with the tokamak fibre transmission of approximately  $0.52 \pm 0.06$  for fibres from the toroidally-viewing lens and  $0.65 \pm 0.02$  for fibres from the vertically-viewing lens, and the typical spectrometer fibre transmission of  $0.75 \pm 0.05$ , the overall efficiency of light throughput is estimated to be  $0.15 \pm 0.02$  for the toroidal views and  $0.19 \pm 0.02$  for the vertical views. One factor which is not taken into account in this analysis however is that the transmission of light from the vertically-viewing lens inside the vessel to the ex-vessel feedthrough relies on imaging fibre to fibre. The core of the fibres is 400  $\mu\text{m}$  in diameter, which renders the light throughput extremely sensitive to slight misalignments of the ex-vessel feedthrough assembly. An additional complication is that, unlike the vacuum

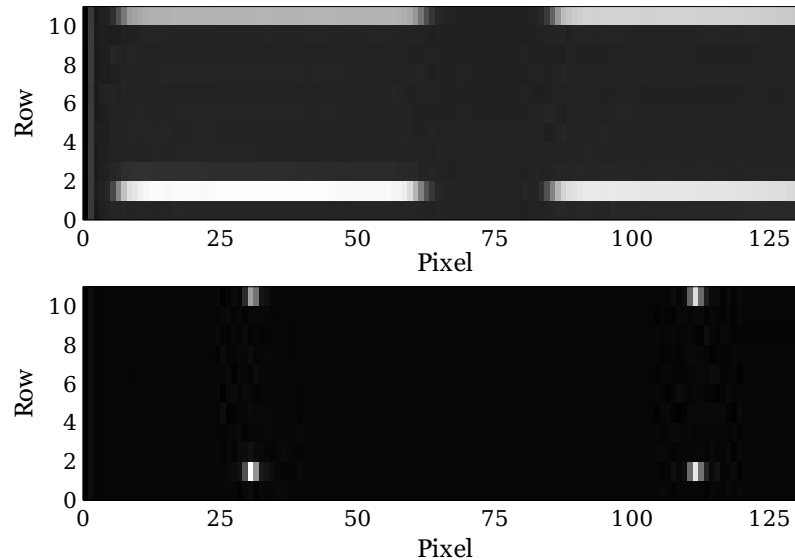


Figure 5.4: Time-averaged CCD frames acquired with four input fibres exposed to an integrating sphere (top panel) and a copper-neon spectral lamp (bottom panel). In the top panel, the illuminated region shows the pass-band of the filter. The FWHM of the filter spans approximately 60 pixels; one end of the pass-band on the right of the frame is truncated due to the limited size of the CCD chip. In the bottom panel, the FWHM of the spectral line is approximately 2.5 pixels. This represents the resolution of the diagnostic, determined by the instrument function of the spectrograph.

window through which the toroidally-viewing lenses observe the plasma, the vertically-viewing lenses cannot be protected by a mechanical shutter. The lenses may therefore become coated with contaminants such as carbon released during glow-discharge cleaning of the plasma-facing components. These factors give rise to significant additional losses in the vertically-viewing system. The factor by which the throughput of the vertically-viewing system must be multiplied to account for these factors was estimated from beam emission measurements made during beam-into-gas discharges during the 2011 experimental campaign to be 0.13. There is some evidence, presented in later chapters, that the transmission deteriorated further during the 2013 campaign. As a result, very little information can be extracted from data taken using the vertical views, accounting for the paucity of such data in this work.

Installation of the diagnostic hardware was carried out in 2011, and the software required to analyse the calibration data and apply absolute and spectral calibration was developed throughout 2011 and 2012. The following section gives an overview of the process by which raw data are converted to calibrated spectra, and presents some of the limitations encountered during operation of the diagnostic.

## 5.4 Preliminary data

Acquisition software is run on a dedicated data acquisition (datac) PC connected to the camera. An XML settings file read by the datac software allows the EM gain, exposure time, ADC offset and vertical binning of the chip to be configured manually by the user. Eleven raw data files are generated per discharge, one for each binned row of pixels on the CCD chip. These files store count rates as a function of pixel and time, as well as a structure of metadata including camera gain and exposure settings, ADC offset and detector temperature. Labels indicating the patching configuration, filter, slits and calibration data files associated with each shot are stored in a log file in CSV format for use by post-processing scripts, which are written in Interactive Data Language (IDL). One of the first tasks carried out as part of this research project was to gather together and document the IDL scripts essential for basic data processing; the removal of redundant and vestigial code, correction of errors, and application of consistent formatting and comments in each of these scripts now renders them suitable for use by third parties. The purpose of these scripts is to automate the full chain of processing from raw data files to a structure of calibrated spectral radiance and uncertainty as a function of wavelength and time. User-defined variables set the degree of smoothing in wavelength and time, allowing a trade-off between resolution and SNR of the processed data. Figure 5.5 shows the raw and processed data from one of the earliest shots in the 2013 campaign; active and reference spectra for this pair of viewing chords were acquired on one side of the chip in two adjacent rows.

The first step in processing the raw data is to subtract the ADC offset from the data at each time point. This is achieved by subtracting from each row the value of the signal in a pixel between the active and reference pass bands, in the middle of the row. These signals, in counts per pixel per frame, are divided by the user-set EM gain factor and the factory-set gain, in counts per photo-electron, of the detector. The active and reference spectra for each channel are then paired based on the known fibre patching layout, and aligned in wavelength using the calculated dispersion based on the chi-square fit to spectral calibration data. At this stage, the absolute calibration is applied accounting for the exposure time, wavelength range of each pixel, étendue (based on the design geometry of the diagnostic) and overall transmission. The signal in photo-electrons/pixel/frame is thereby converted to a spectral radiance in photons/s/m<sup>2</sup>/sr/nm. A scaling factor required to match the baseline level of the

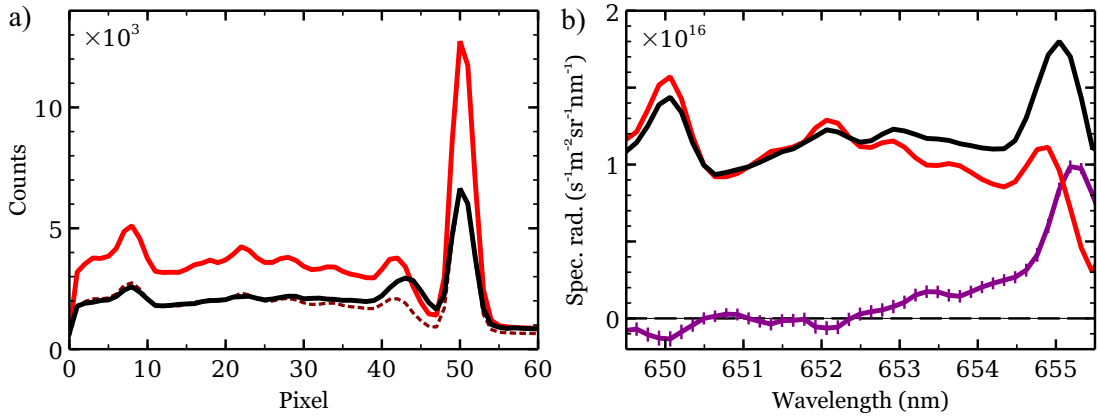


Figure 5.5: a) Raw FIDA data from an active, vertically-viewing channel intersecting the neutral beam at  $R = 1.09$  m (black), and from the corresponding reference channel (red), from MAST shot #28824. The dotted line shows the reference signal scaled and offset to match the level of the active signal, for comparison with the processed active and reference spectra. b) The same data, processed to provide calibrated spectral radiance as a function of wavelength and smoothed over 3 pixels in wavelength. An O V line, centred at 650 nm, is clearly visible. The purple trace shows the net (active – reference) spectrum, with error bars representing the shot noise uncertainty. Note that panel (b) shows a restricted wavelength range; the large peak due to the (strongly attenuated) edge  $D_\alpha$  light, evident in panel (a), is not shown in panel (b). Data are time-averaged over the period 0.32 s to 0.34 s, which is a period between two sawteeth with a near-constant density and slowly evolving electron and ion temperature.

active spectrum is then applied to the reference spectrum, to account for the difference in transmission between the active and reference channels. This factor is obtained by matching the signal level at a time during the shot at which neither of the beams is operating, and hence the active and reference signals are expected to be identical. Finally, the difference between active and reference signals at a wavelength at which no FIDA signal is present is subtracted from the active signal at each time point throughout the shot. This offset accounts for the difference in path length through the plasma caused by the slight difference in viewing geometry between the active and reference channels, which gives rise to different levels of line-integrated bremsstrahlung, and also for the presence of blackbody sources and reflections inside the vessel.

An example of the conversion of an acquired signal of 100 photo-electrons to a calibrated spectral radiance is given in table 5.2. Values given in the table are typical of the toroidally-viewing FIDA system with  $50\ \mu\text{m}$  input slits; these narrow slits are used with the toroidal views in order to prevent the wings of the beam emission peaks from contaminating the FIDA spectrum.

Since the absolute calibration procedure makes no distinction between active and

Parameter	Value	Units
Acquired charge	100	photo-electrons
Exposure time	$3.0 \times 10^{-4}$	s
Pixel width ( $\lambda$ )	0.14	nm
Transmission	0.15	—
Étendue	$4.5 \times 10^{-9}$	$\text{m}^2 \text{sr}$
Spectral radiance	$3.5 \times 10^{15}$	$\text{s}^{-1} \text{m}^{-2} \text{sr}^{-1} \text{nm}^{-1}$

Table 5.2: Typical values of the parameters required to convert an acquired FIDA signal of  $100 e^-$  into spectral radiance when using  $50 \mu\text{m}$  input slits with the toroidally-viewing system.

reference channels, and the transmission of individual tokamak fibres is taken into account when applying the calibration, the use of a scaling factor applied solely to the reference signal represents a source of systematic error. The reason for applying this factor to the signal in the reference channel is that the absolute calibration may in principle be validated by comparison between measured and modelled beam emission in the active channels; any channel-to-channel scaling factor applied to the active signal on an *ad hoc* basis would affect the measured beam emission, whereas a comparison of this component of the spectrum to the modelled emission requires a stable calibration in order to be practically applicable. Scaling factors derived from comparison of the active and reference baseline are unstable on a shot-to-shot basis even when the diagnostic configuration remains unchanged, as shown in panel (a) of fig. 5.6.

Given a scaling factor  $\alpha_i$  in channel  $i$ , the fractional uncertainty in the net signal introduced by applying this scaling factor to the reference signal  $S_R$  (or, equivalently, applying a scaling factor of  $1/\alpha_i$  to the active signal  $S_A$ ) is  $(1 - \alpha_i)/(1 + \alpha_i)$ . A nominal 7% uncertainty in  $S_{A,R}$  is added to account for cross-contamination between channels such as that seen in fig. 5.4. Taking these systematic contributions to the uncertainty into account, the total uncertainty in the net signal in channel  $i$  is then given by

$$\epsilon_i = \left[ \sigma_A^2 + \sigma_R^2 + \left( \frac{1 - \alpha_i}{1 + \alpha_i} \right)^2 (S_A - S_R)^2 + 0.07^2 (S_A^2 + S_R^2) \right]^{\frac{1}{2}},$$

where  $\sigma_{A,R}$  represent the standard (statistical) uncertainty in the active and reference signals. Error bars calculated using both the random and systematic uncertainty are shown in panel (b) of fig. 5.6; it is apparent that the systematic uncertainty makes a large contribution to the total uncertainty. Many of the results presented in this thesis depend only on the analysis of relative changes in time series or spectra based on data from a single channel, and in such cases the absolute value of the spectral radiance is

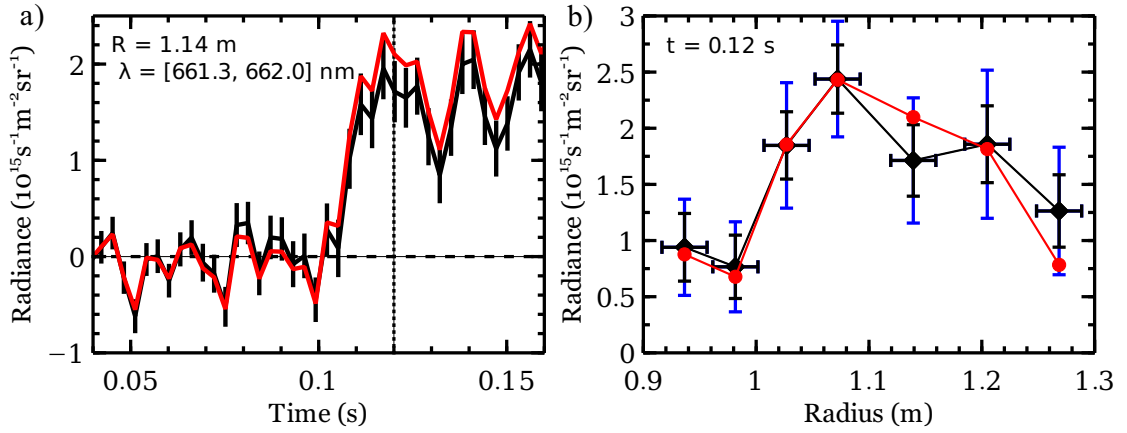


Figure 5.6: a) Comparison of FIDA time traces from shot #29160 based on two different scaling factors applied to bring the reference signal into line with the active signal during a period with no NBI. The black trace shows the net signal when a scaling factor of 1.04, derived from shot #29156, is applied to the reference signal. Error bars represent the uncertainty due to shot noise and readout noise. A scaling factor of 0.834, derived from shot #29160, is applied to the reference signal to obtain the red trace; these two scaling factors were obtained with identical spectrometer configuration and alignment. b) Radial profiles of FIDA signal from shot #29160 at the time indicated by the dotted line in panel (a). Black diamonds show data obtained with the set of reference scaling factors derived from shot #29156. Red circles show data obtained with reference scaling factors derived from shot #29160. Black  $y$ -error bars represent random noise, while blue  $y$ -error bars include both the random uncertainty and the systematic uncertainty calculated according to the expression given in the text. Spectral radiance has been integrated over the wavelength range indicated in the label of panel (a) to obtain the radiance shown in each panel.

unimportant. In these cases, it is sufficient to consider only the random uncertainty in determining whether the observed changes in signal are significant. In comparing the absolute values of measured and modelled signals however, and in plotting radial profiles of signal at a given wavelength, it is important to account for sources of systematic error.

One further complication in analysing FIDA spectra arises from the presence of numerous contaminant features in the spectral region of interest. Figure 5.7 illustrates this point; the spectrum from a core channel, with a beam intersection radius of  $R = 0.91 \text{ m}$ , is strongly contaminated with  $D_\alpha$  emission from the SW neutral beam which overlaps with the SS neutral beam in the core of the plasma. The smaller angle between the LOS and the SW beamline than between the LOS and SS beamline causes the SW beam emission to be observed at a larger redshift than the SS emission for a given injection energy. In the outer channel, at  $R = 1.25 \text{ m}$ , a similar problem arises

due to the presence of trace quantities of  $^1\text{H}$  in the beam. The hydrogen beam emission appears at approximately  $\sqrt{2}$  times the redshift of the deuterium beam emission, resulting in spectral contamination which is most apparent in the outer channels where the beam density is largest. Both the SW  $\text{D}_\alpha$  and the SS  $\text{H}_\alpha$  emission fluctuate on timescales similar to the changes in the FI distribution which are of interest. Channels which are contaminated with SW beam emission clearly cannot provide usable FIDA spectra, since the SW beam emission peak completely dominates the spectral region of interest. In the case of the  $\text{H}_\alpha$  beam emission from the SS beam however, it is possible to obtain a reasonable estimate of the FIDA signal by interpolating the spectrum across the affected region. The blue trace in fig. 5.7 shows the result of such interpolation; data points in a 0.55 nm (approximately 4 pixel) band centred on the contaminant beam emission are replaced by their linear interpolates based on the data points either side of this band. Such interpolation improves the agreement between measured and modelled FIDA radiance.

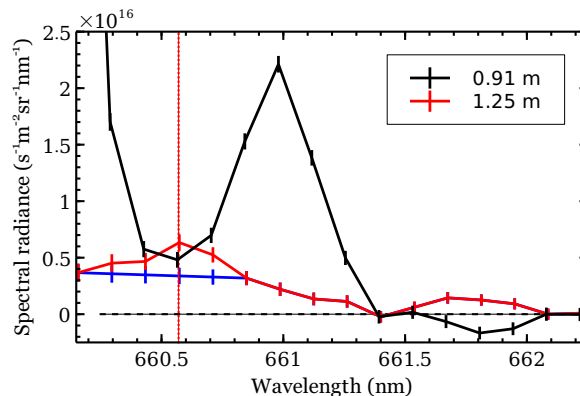


Figure 5.7: Spectra from two channels of the toroidally-viewing FIDA system acquired during shot #29036 at  $t = 0.26$  s. The spectrum from the core channel, shown in black, is clearly dominated by a large peak due to emission from the SW neutral beam. The spectrum from the outer channel, shown in red, is contaminated with  $\text{H}_\alpha$  beam emission from the small amount of hydrogen in the SS beam. This contamination is less apparent than the SW beam emission; the central wavelength of the  $\text{H}_\alpha$  beam emission is marked by the red, dotted vertical line. The blue trace is obtained by linear interpolation of the red trace across values 0.275 nm either side of the  $\text{H}_\alpha$  beam emission peak. Error bars represent random uncertainty.

In the next chapter, the numerical modelling tools used throughout this project to support the analysis of experimental data are described. These include codes used to model the behaviour of FI in MAST, as well as synthetic diagnostics which allow comparisons to be made between modelled and experimentally-realised FI distributions.

# Chapter 6

## Modelling for fast-ion diagnostics

### 6.1 Outline

In order to integrate the information about the fast-ion distribution derived from advanced FI diagnostics into the broader understanding of plasma performance and stability, numerical modelling is generally required. Integrated plasma scenario and transport modelling has received widespread attention due partly to the necessity of predicting plasma performance in ITER [170–172]. Many of the tools which are used for interpretative modelling of present-day experiments may, if their internal models are validated over a sufficiently wide range of parameter space, be used for predictive modelling of ITER scenarios [173].

The time-dependent transport analysis code TRANSP [155] has been used to analyse MAST plasmas for many years [174]. Development of TRANSP is carried out at the Princeton Plasma Physics Laboratory, and the code has a large user base at many fusion research laboratories worldwide; published references to many of the models applied within TRANSP are listed on the project website [155]. The code is described as 1.5-dimensional, since 1D profiles of plasma parameters as a function of normalised minor radius are mapped onto a 2D magnetic equilibrium.

This chapter briefly outlines the process employed to generate magnetic equilibria and prepare TRANSP input profiles for MAST, and to initialise TRANSP runs, and presents some of the basic output, relevant to FI physics, from the author’s own runs. Synthetic diagnostics used to derive expected FI diagnostic signals from TRANSP-calculated FI distributions are described, and preliminary comparisons between measured and modelled FC, NC and FIDA signals are presented.



## 6.2 TRANSP simulations of MAST plasmas

In order to model the transport of heat and particles in the plasma, the input data must faithfully represent the experimental conditions. The inputs to TRANSP may be divided into two key parts, each of which is described separately in this section. Firstly, the magnetic geometry of the plasma must be reconstructed to provide a background magnetic equilibrium onto which other plasma parameters may be mapped. Secondly, measured profiles of these plasma parameters must be mapped onto a common grid covering the minor radius of the plasma, with spatial or temporal interpolation between measurements if necessary. Required input data to TRANSP includes time traces of plasma current and auxiliary (NBI) heating power, and time-dependent profiles of electron density, electron and ion temperature, toroidal rotation, effective charge, and neutral hydrogen density at the plasma edge. Given these experimental constraints, TRANSP applies internal physics models to calculate, for example, heat transport coefficients, electron and ion power balance, FI distributions, neutron emission, plasma resistivity, and self-generated ‘bootstrap’ current.

### 6.2.1 Equilibrium reconstruction

Magnetic equilibria are reconstructed using EFIT, which iteratively solves the Grad-Shafranov equation given certain experimental constraints with specified weights on each constraint. Iterations are performed until the value of chi-squared falls below a pre-defined threshold, which constitutes successful convergence on a physical solution, or until a set number of iterations is reached, implying a failure to find a valid solution for this timeslice. The minimal set of constraints which must be provided includes signals from magnetic flux loops inside the vacuum vessel, as well as currents in each of the coils used to control the position and shape of the plasma. Often it is also desirable to constrain the profile of current density within the plasma itself, and for this purpose internal measurements are required. These include motional Stark effect (MSE) measurements of the magnetic field pitch  $B_Z/B_\phi$ , where the  $Z$  and  $\phi$  subscripts denote vertical and toroidal field components, and TS measurements of electron density and temperature. The current density may then be derived from ideal-MHD force balance which requires that, neglecting flows,  $\nabla p = \mathbf{j} \times \mathbf{B}$ . An additional constraint is provided by measurements of the position of the edge of the plasma obtained using a  $D_\alpha$  filtered camera. Figure 6.1 shows an example of the flux surfaces, pressure and current profiles reconstructed by EFIT for shot #29976 at  $t = 0.2$  s, along with the

fits to MSE and TS data used to constrain these profiles. Note that the pressure profile is unconstrained in the core of the plasma, since the TS data account only for the thermal electron pressure. Leaving the pressure unconstrained in the core allows EFIT to account for kinetic pressure due to fast ions and toroidal rotation, both of which are significant in the core and negligible at the edge of the plasma. The thermal ion pressure, which is not measured, is assumed to be equal to the thermal electron pressure.

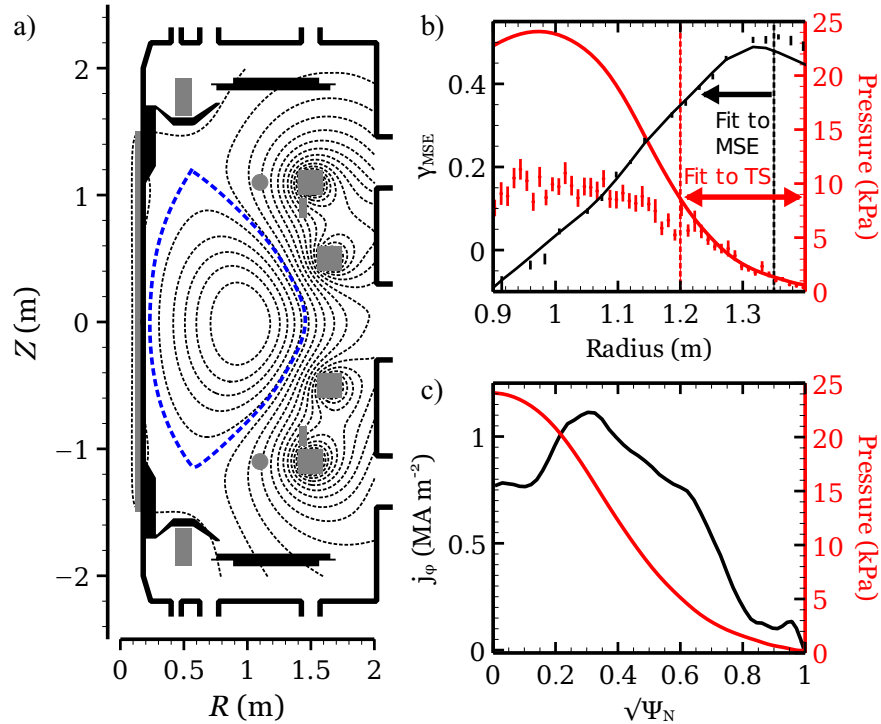


Figure 6.1: a) Surfaces of constant poloidal flux,  $\Psi$ , calculated with EFIT for MAST shot #29976 at  $t = 0.2$  s. The dashed blue line shows the LCFS. Surfaces are uniformly spaced in  $\sqrt{\Psi}$ . b) The fit to motional Stark effect data (black;  $\gamma_{\text{MSE}} = B_Z/B_\phi$ ) and Thomson scattering pressure data (red) obtained in the final iteration of the same EFIT calculation. The radial range in which each of the measured profiles was used as a constraint is indicated by dotted vertical lines and arrows. c) Kinetic pressure and toroidal current density profiles from the same EFIT calculation as a function of  $\sqrt{\Psi_N}$ , where the subscript N indicates normalization to the poloidal flux at the LCFS.

Rather than providing the full magnetic equilibrium as an input to TRANSP, the approach more commonly adopted is to provide only the vacuum toroidal field and plasma boundary from EFIT, and to allow TRANSP to use an internal equilibrium solver to generate flux surfaces given an internally-calculated pressure profile and an initial estimate of the  $q$ -profile based on the EFIT output. The total plasma current is used as a global constraint, and the  $q$ -profile is modified until force balance is satisfied given the imposed pressure profile, boundary and vacuum toroidal field at the edge of the plasma.

The advantage of this approach is that the equilibrium thus obtained is self-consistent, with the total pressure being given by the sum of thermal pressure and TRANSP-calculated FI pressure related via the internal power balance calculation. This self-consistency comes at the cost of the inability to resolve detailed structure in the current density profile which would be included if the  $q$ -profile from EFIT were imposed. MAST plasmas typically exhibit weakly reversed shear in the core, corresponding to hollow current profiles as shown in panel (c) of fig. 6.1, whereas the  $q$ -profile computed within TRANSP is usually monotonic, corresponding to a centrally-peaked current density profile. The equilibrium solver used in the TRANSP runs described in this work is the TEQ solver, extracted from the CORSICA transport code for inclusion in TRANSP [175].

Equilibria computed by TEQ within TRANSP cannot account for poloidal asymmetries in the pressure profile caused by toroidal rotation, or for unequal parallel and perpendicular pressure caused by the directed NBI, and therefore can only approximately represent the true equilibrium. Inclusion of pressure anisotropy and toroidal flow into equilibrium reconstruction is the subject of ongoing research [176], and is beyond the scope of this work.

### 6.2.2 Profile mapping

Once the EFIT equilibrium has been obtained, profiles of bulk plasma parameters such as density and temperature are mapped onto normalised minor radius  $r/a$ . The data processing tool MC<sup>3</sup>, which was developed in-house at CCFE by Dr. Rob Akers, is used for this purpose. Often, the mapping is straightforward; analysed data from the TS and CXRS systems are provided as a function of major radius on the machine midplane, and must simply be interpolated onto a specified grid in  $r/a$ . Outlying data points may be excluded manually to improve the fit to the profile, and the degree of regularisation is adjusted to obtain fits which represent the data as faithfully as possible while avoiding spikes or oscillations which occur as artefacts of the cubic spline fitting procedure. Profiles of deuterium neutral density and  $Z_{\text{eff}}$ , which must be inferred from Abel inversion of  $D_\alpha$  and bremsstrahlung emission profiles respectively, and which also rely on accurate profiles of electron density and temperature for their calculation, are subject to significant uncertainty. Although the uncertainty in neutral density has very little effect on the calculation of the FI population, since the edge neutrals serve only to reduce by a few percent the NBI power delivered to the plasma, the uncertainty in  $Z_{\text{eff}}$  has a potentially significant impact on calculations of the FI

distribution and the beam-thermal neutron emission. Moreover, residual helium from inter-shot glow-discharge cleaning of the vessel is now known to be responsible for significant dilution of the deuterium ion population, and hence for a reduction in D-D neutron emission, while  $Z_{\text{eff}}$  is rather insensitive to the presence of helium. Future prospects for the diagnosis of impurity ion content are promising however, since data from the RGB filtered visible imaging camera are now routinely available and allow profiles of the density of the dominant impurity ion species, namely helium and carbon, to be derived from measurements of their emission after CX with beam neutrals [177]. An example of such a profile measurement is shown in fig. 6.2, where the density of each species is expressed as a relative concentration in terms of its contribution to the electron density. Such measurements should allow TRANSP runs to be set up with multiple impurity species, rather than the single impurity species (carbon) assumed in simulations to date.

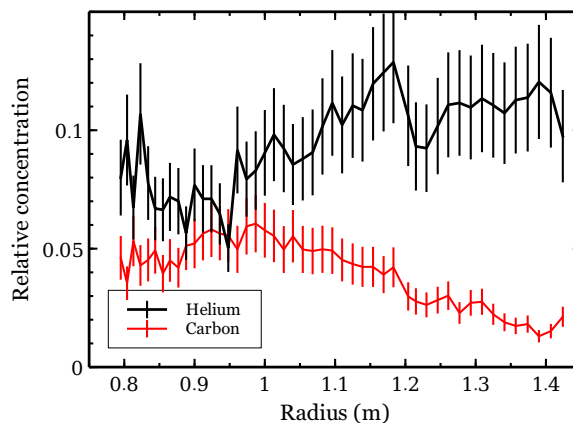


Figure 6.2: The effect of helium and carbon impurity ions on deuterium fuel dilution in MAST shot #29976 at  $t = 0.2$ s. Relative concentration is defined as the ion number density multiplied by the ion charge, divided by the electron density, i.e.  $r = Z_i n_i / n_e$ , and is therefore a measure of the fraction of deuterium which is displaced by each impurity species at a given electron density. Data provided by Dr. Stuart Henderson.

### 6.2.3 Calculation of the fast-ion distribution

The equilibrium geometry and profiles of plasma parameters allow NBI deposition to be calculated given the beam geometry, voltage and the current in each energy component, and provide a background on which the deposited fast ions may be tracked as they undergo collisional interactions with electrons, ions and neutrals. The NUBEAM module of TRANSP [159] applies Monte Carlo techniques to model the beam deposition and to track a number of markers, each representing a collection of beam ions, which is held constant at each time step. These marker particles are followed until

thermalisation or loss from the plasma; the guiding centre drift orbit equation is integrated numerically to update the marker position at each time step, and the position is corrected to account for the finite Larmor radius of the beam ions before a collision operator is applied. Markers representing thermalised or lost ions are replaced by markers representing newly born fast ions, to maintain a constant ‘census’ number of marker particles. The markers are defined as being thermalised when their energy falls below  $3T_i/2$ , and the thermalisation source term is passed back to the main TRANSP code for inclusion in power balance and particle transport calculations. Potential loss mechanisms for the beam ions prior to thermalisation include collisional scattering onto lost orbits, charge exchange reactions with beam or thermal neutrals, fusion reactions, loss due to ‘ripple’ in the toroidal field, and optionally loss due to fishbones, a model for which is available within NUBEAM. In addition to the neoclassical dynamics determined by drifts and collisional processes, FI in NUBEAM may be affected by ‘anomalous’ diffusion and convection mechanisms. These mechanisms, which are applied with user-specified coefficients prescribing the magnitude of their effects as functions of time and radial position, cause enhanced radial fluxes of FI proportional to the radial FI density gradient in the case of diffusion and to the FI density in the case of convection. Chapter 7 includes many examples of TRANSP runs in which anomalous diffusion and advection have been applied to obtain agreement between synthetic and measured FI diagnostic signals; although these *ad hoc* mechanisms do not represent the underlying physics of anomalous transport in any first-principles sense, they provide useful tools to study the nature and magnitude of the effects of various MHD instabilities on FI.

Examples of FI distributions generated by NUBEAM were shown in chapter 4. In addition to the four-dimensional FI distribution  $f_{\text{FI}}(R, Z, E, p)$  and corresponding beam-beam and beam-thermal neutron emission, the output from the code includes instantaneous FI torque, angular momentum, parallel and perpendicular pressure, and current density. Time traces of these quantities from a TRANSP run modelling MAST shot #29195 are shown in fig. 6.3; although the beam-driven current is small compared to the total plasma current of 800 kA, the contribution of FI to the instantaneous angular momentum (20% – 90%) and kinetic pressure (20% – 40%) of the plasma is significant. The contribution integrated over time is even higher; the angular momentum imparted by the beam ions is responsible for almost all of the toroidal rotation in beam-heated MAST plasmas.

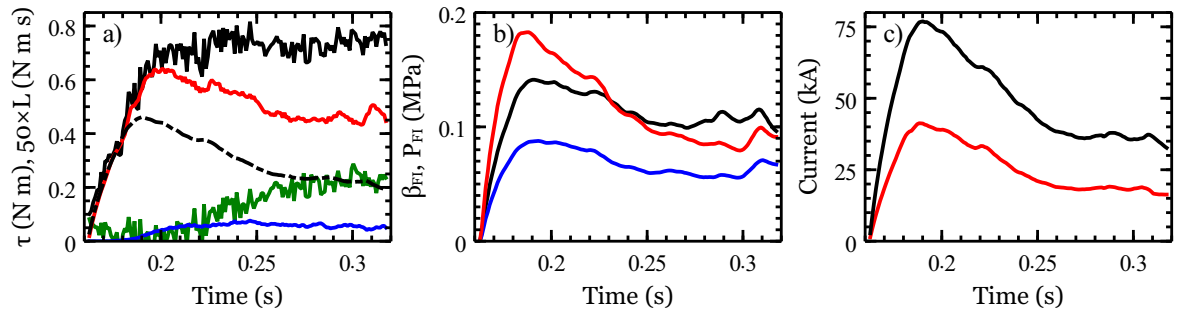


Figure 6.3: Global properties of the FI population as modelled with TRANSP for shot #29195. a) Collisional torque exerted by FI on the bulk plasma (red);  $\mathbf{j} \times \mathbf{B}$  torque due to FI (green); torque due to thermalising FI (blue); and total FI torque (solid black). The dash-dotted black trace shows the angular momentum of the FI population, scaled by a factor of 50 for clarity. b) Poloidal beta due to parallel motion (red) and due to perpendicular motion (blue) of the FI, and total FI pressure (black). c) Toroidal current due to FI without (black) and with (red) the effect of an electron current acting to screen the FI current.

First-principles physical models or empirical scaling laws which depend on various properties of the FI population may therefore be indirectly constrained and validated by FI diagnostic measurements, provided that these measurements are themselves able to constrain the form of the FI distribution. The intermediate step comes in the form of *synthetic diagnostics*, which are the subject of the next section.

### 6.3 Synthetic fast-ion diagnostics

NUBEAM FI distributions are provided as functions of energy and pitch in each of 840 zones which span the poloidal cross-section of the plasma. Given relevant properties of the detector, beam, and background plasma, it is possible to model the expected FI diagnostic signals based on these synthetic distributions. Codes which perform such forward-modelling calculations are referred to as ‘synthetic diagnostics’. The term ‘forward-modelling’ is used to distinguish this procedure from the solution of the inverse problem, in which tomography or Abel inversion is used to infer properties of the FI distribution from the diagnostic measurements. It should be noted that both the forward and inverse approaches to diagnostic modelling are subject to uncertainty caused by the possibility of degenerate solutions; since only a limited part of both real space and velocity space is probed by each diagnostic, there are in general many different FI distributions which will give rise to the same detected signal. This section discusses the synthetic diagnostics used to attempt to replicate the data of each of the FI diagnostics installed on MAST.

### 6.3.1 Fission chamber

Since one of the outputs of the TRANSP code is the predicted total neutron emission from the plasma, and the FC is calibrated to provide a measurement of this quantity, no post-processing of the TRANSP output is required for comparison with the FC data. A comparison between the measured and modelled neutron rates for shot #29270 is shown in fig. 6.4. In the early part of the discharge, up to  $t = 0.26$  s, the neutron rate is well reproduced by the TRANSP model. The relatively high electron density in this discharge leads to a short slowing-down time and rapid thermalisation of the FI. As a result, the FI radial pressure gradient remains low and few MHD modes are excited; this can clearly be seen in the purple trace, which shows the root-mean-square (RMS) value of an outboard midplane magnetic pick-up coil signal (scaled for clarity). The MHD-quiescent period lasting from 0.24 s to 0.27 s allows a comparison between the NUBEAM-modelled FI distribution and that obtained experimentally in the absence of MHD-induced redistribution.

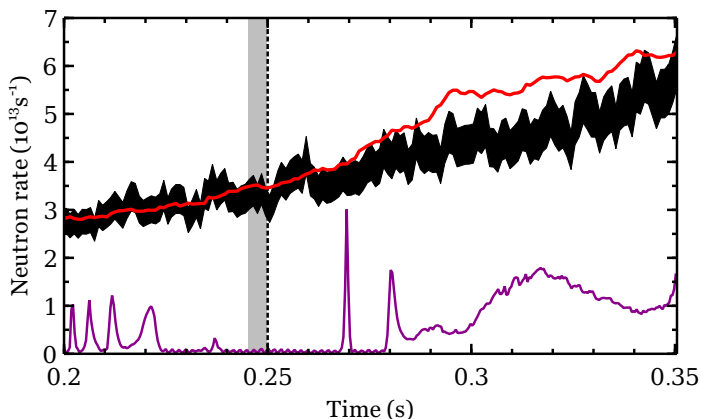


Figure 6.4: Comparison between measured (black) and TRANSP-modelled (red) neutron rates for MAST shot #29270. The scaling factor 0.91, mentioned in chapter 4, has been applied to the measured neutron rate. Also shown (purple) is the RMS amplitude of a Mirnov coil signal, which measures the rate of change of poloidal magnetic field,  $\dot{B}_\theta$ , at the coil location on the outboard midplane of the vessel. The rapid bursts in magnetic activity indicate frequency-chirping TAE and EPM, while the continuous perturbation which persists from 0.285 s onward indicates the presence of a saturated internal kink mode. The grey shaded region, from 0.247 s to 0.250 s, is the time over which the synthetic FI distribution and FIDA data are averaged to obtain the spectrum shown in fig. 6.5.

A comparison of the measured global neutron rate with TRANSP predictions provides a constraint on the FI density integrated over real and velocity space, but a more detailed examination of the degree to which the synthetic FI distribution reproduces

the real distribution requires comparison with data from the FIDA and NC systems.

### 6.3.2 FIDA diagnostic

Forward-modelling of the FIDA signal is much more challenging than modelling of the neutron rate due to the interplay between FI physics and atomic physics involved in determining the FIDA spectrum. NUBEAM models the FI physics from beam deposition to thermalisation, and includes CX with beam and thermal neutrals as a loss process for the fast ions, but does not provide detailed information about the trajectories or the distribution among atomic levels, and hence the  $D_\alpha$  emission, of the reneutralised FI. While TRANSP input parameters allow the geometry of neutral particle analyser chords to be specified, and the emission rate and velocity distribution of fast and thermal neutrals generated by CX reactions and directed toward the detector are calculated for each chord, FIDA spectra depend on the velocity distribution of FI close to the point of neutralisation rather than the velocity distribution of only those neutrals which reach the detector. For this reason, a dedicated code is required to determine the rate at which FI are reneutralised at each point along the FIDA LOS and to model the processes of excitation, ionisation and radiative decay affecting each of the neutral species which contribute to the  $D_\alpha$  spectrum. Such a code was first developed by Prof. William Heidbrink and others at the University of California, Irvine, under the name FIDASIM [166]. The original version of FIDASIM was written in IDL. A recent Fortran 90 rewrite of the main body of the code by Dr. Benedikt Geiger at IPP Garching [162], followed by work by Luke Stagner at UC Irvine to render the code suitable for application to other tokamaks via the development of a configurable set of input routines, has reduced the run-time by a factor of at least 10. Part of the work carried out during this research project was to develop MAST-specific input routines for the Fortran version of the code, and to benchmark this version against the IDL version. At first, the output of the two versions exhibited significant disagreement. This author subsequently identified the disagreement as being due to an error in the Fortran source code which led to reneutralised FI being tracked from their guiding centre location rather than the location of the particle on the gyro-orbit. The source code maintained at <https://github.com/D3DEnergetic/FIDASIM> has now been amended to remove this error. Figure 6.5 shows a comparison between the spectrum modelled by FIDASIM and that obtained experimentally during shot #29270 at the time indicated by the dotted vertical line in fig. 6.4.



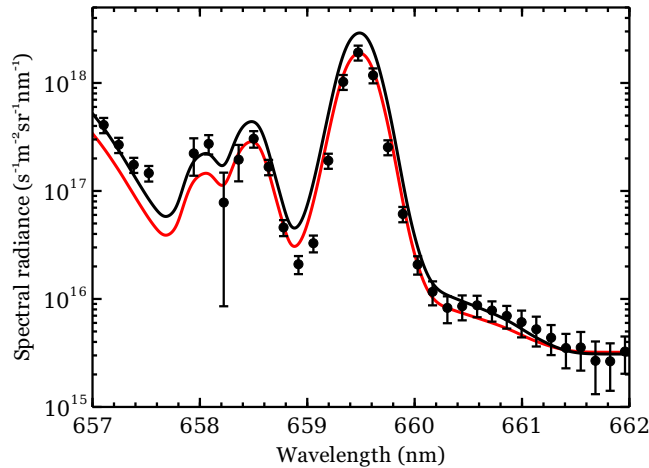


Figure 6.5: A spectrum modelled by the Fortran version of the FIDASIM code for MAST shot #29270 at  $t = 0.25$  s,  $R = 1.07$  m (black trace), and the relevant data points with error bars accounting for both random and systematic uncertainty. Note that the net measured spectrum has been offset to match the bremsstrahlung baseline level of the modelled spectrum at  $3 \times 10^{15} \text{ s}^{-1} \text{ m}^{-2} \text{ sr}^{-1} \text{ nm}^{-1}$ . Also shown, in red, is the modelled spectrum multiplied by 0.6 to illustrate the discrepancy between measured and modelled beam emission which is discussed in the text of this section. The modelled spectrum includes FIDA, beam and halo emission components, hence the logarithmic vertical axis. The two missing data points between 657.5 nm and 658.0 nm are due to imperfect background subtraction of one of the C II lines, resulting in a negative net signal at these wavelengths; the other C II line is responsible for the very large error bar on the point at 658.3 nm.

FIDASIM adopts a Monte Carlo approach to the collisional-radiative modelling of neutral particles; a three-dimensional rectangular grid surrounding the active neutral beam is specified, and profiles of electron and ion density and temperature, magnetic field vectors, toroidal rotation and the FI distribution are mapped from TRANSP output onto this grid. Marker particles representing beam neutrals are tracked within the grid, and the probability of interactions with fast and thermal ions leading to the production of fast and halo neutrals in each atomic level is evaluated in each grid cell. These neutrals are themselves tracked, with excitation, radiative decay and ionisation rates calculated in each grid cell; the rate at which the population decays from  $n = 3$  to  $n = 2$  determines the FI and halo  $D_\alpha$  radiance. Diagnostic lines of sight are modelled as cylindrical chords, and the number of photons emitted toward the viewing lens, per unit LOS velocity per unit time, determines the spectral radiance at each specified wavelength in each LOS. The simulation grid must be large enough in the directions perpendicular to the beam axis that the full beam neutral density profile and a sufficient part of the halo neutral population are contained within the grid to allow the

interactions between neutrals and FI to be modelled accurately. Discretisation must be sufficiently fine that plasma parameters, beam neutral density and FI density may be assumed to take a single value in each grid cell. The grid chosen for MAST spans 88 cm perpendicular to the neutral beam in each direction, and a 144 cm-long portion of the beam is modelled. Grid cells are 4 cm on each side. This grid is sufficiently wide and deep compared to the beam neutral density profile, which has a FWHM of between 12 cm and 15 cm, to allow almost all FI to be tracked from their point of neutralisation by beam or halo neutrals to the point at which they emit  $D_\alpha$  light. The size of the grid cells represents a compromise, allowing the grid to span a suitable spatial range in all three dimensions while avoiding prohibitive memory consumption. Poloidal and equatorial projections of the grid and the toroidally-viewing FIDA LOS, along with the beam and halo neutral density, are shown in fig. 6.6.

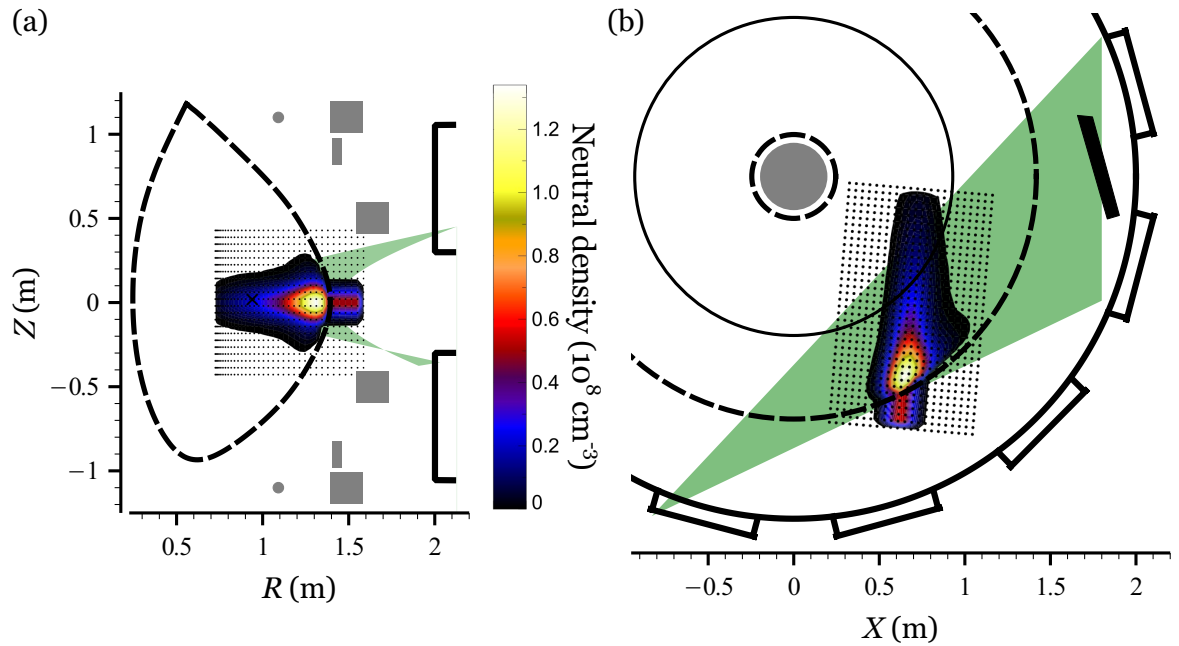


Figure 6.6: Poloidal (a) and equatorial (b) projections of 2D slices of the grid used in FIDASIM as installed for MAST. Points mark the centre of each grid cell. Filled contours show the sum of beam and halo neutral densities, including full, half and third-energy beam components, and all atomic levels up to  $n = 5$ ; the shot being simulated is #29270 at  $t = 0.25$  s. Thick, dashed contours mark the LCFS, and the solid circle in panel (b) marks the magnetic axis. The green, shaded area shows the projection of the maximum extent of the FIDA lines of sight. The colour bar pertains to both panels.

Simulations supporting the analysis described in this thesis were carried out with  $2.5 \times 10^6$  Monte Carlo marker particles representing the reneutralised FI,  $5 \times 10^4$  markers representing the injected beam neutrals, and  $5 \times 10^5$  markers representing the halo

neutrals. These numbers provide for sufficiently low statistical variation for a reliable measure of the spectral radiance due to each population of neutrals. Running as a serial job on the servers at CCFE, the code takes 10 to 20 minutes to simulate a full spectrum in eleven channels for a single time-slice, and requires up to 420 MB of memory. In addition to the calculation of the spectra, a significant contribution to the run-time arises from the calculation of weight functions for a range of wavelengths in each LOS; this calculation can optionally be omitted, since it is not required for the generation of synthetic spectra.

Although the modelled FIDA radiance usually agrees well with the measured signal in MHD-quiescent cases or in cases where anomalous diffusion has been used within NUBEAM to obtain agreement between the modelled and measured global neutron rate, a significant discrepancy is observed between measured and modelled beam emission. A similar discrepancy is observed between the predictions of the NEBULA beam modelling code, developed by Stuart Henderson as part of his Ph.D. project [177] and based on an older code developed by Dr. Mikhail Turnyanskiy, and the measured signal in the beam emission channel of the RGB filtered imaging camera, which is calibrated entirely independently of the FIDA diagnostic. In both cases, the modelled emission overestimates the measured emission by  $\sim 60\%$ . The observation of this discrepancy using two independent pairs of modelling codes and calibrated diagnostics indicates a problem underlying each of the models. FIDASIM uses Monte Carlo markers to represent beam neutrals, whereas NEBULA calculates beam attenuation and beam emission rates from look-up tables of atomic rate coefficients and applies these at sequential steps along the beam path. The computational scheme is therefore unlikely to be in error; it seems most likely that the fundamental atomic data on which both codes rely, which are extracted from the Atomic Data and Analysis Structure (ADAS) [178] and are based on the empirical expressions of Janev et al. [179], are responsible for the discrepancy. The particular dataset which falls under suspicion is that of the ion impact excitation rate coefficients, since ion impact excitation is primarily responsible for determining the beam emission but has very little effect on the halo or FIDA emission. Both the modelled halo and modelled FIDA emission are seen from fig. 6.5 to be in agreement with the data without the need for any correction factor.

Experiments are planned for MAST-Upgrade and for future JET campaigns to study the beam emission across a wide range of plasma densities, temperatures and

beam energies; preliminary observations on JET by Dr. Ephrem Delabie suggest that a  $\sim 40\%$  overestimate of the measured beam emission may also affect modelling of JET data. At present, it cannot be said with certainty whether erroneous atomic data are responsible for the beam emission discrepancy. Nonetheless, FIDA data and FIDASIM modelling provided by this author have played a part in highlighting this issue as being of real concern for the analysis of spectroscopic data from fusion plasmas.

### 6.3.3 Neutron camera

Forward-modelling of the NC data from the poloidal profile of neutron emission generated by TRANSP requires detailed knowledge of the detector and collimator geometry. Given this geometry, the volumetric contribution to each field of view (FOV) as a function of  $R$ ,  $Z$  and  $\phi$  may be calculated. The Monte Carlo 3D ray-tracing code LINE2 is used for this purpose [76]. LINE2 adopts a scheme whereby the plasma volume is divided into  $1\text{ cm}^3$  grid cells, and  $\sim 10^4$  points are selected at random within each of these cells. The code then calculates whether a straight line from each point passes through the  $2\text{ cm} \times 5\text{ cm}$  planes coincident with the plasma-facing and detector-facing ends of the NC collimator. Each grid cell in the plasma is weighted according to the number of points within that cell which satisfy this criterion, and the contribution of the cell to the NC spatial sensitivity in a given FOV is given by the number of qualifying points, the volume of the cell and the solid angle subtended by the cell as viewed from the detector. The code also calculates poloidal and equatorial projections of these volumetric contributions to each FOV; fig. 6.7 shows some examples of these projections. It is apparent from the poloidal projection shown in panel (a) that the NC is most sensitive to neutron emission close to the tangency radius of the LOS.

Count rates in each of the NC channels are estimated as the product of the neutron emission rate per unit volume from TRANSP, the poloidal projection of the FOV volumetric weighting from LINE2, and the overall detector efficiency included as a scaling parameter; this efficiency, including the attenuation of the neutron flux due to the steel flange in the vacuum vessel as well as the response of the liquid scintillator detectors, is approximately 9%. Profiles of measured and modelled count rate from a NC radial scan during a set of repeated high-density discharges, in which the MHD activity was weak and the global neutron rate modelled by TRANSP matches that measured by the FC to within a few percent, are shown in fig. 6.8. LINE2 simulations providing the synthetic profiles of NC count rates shown throughout this work were performed by

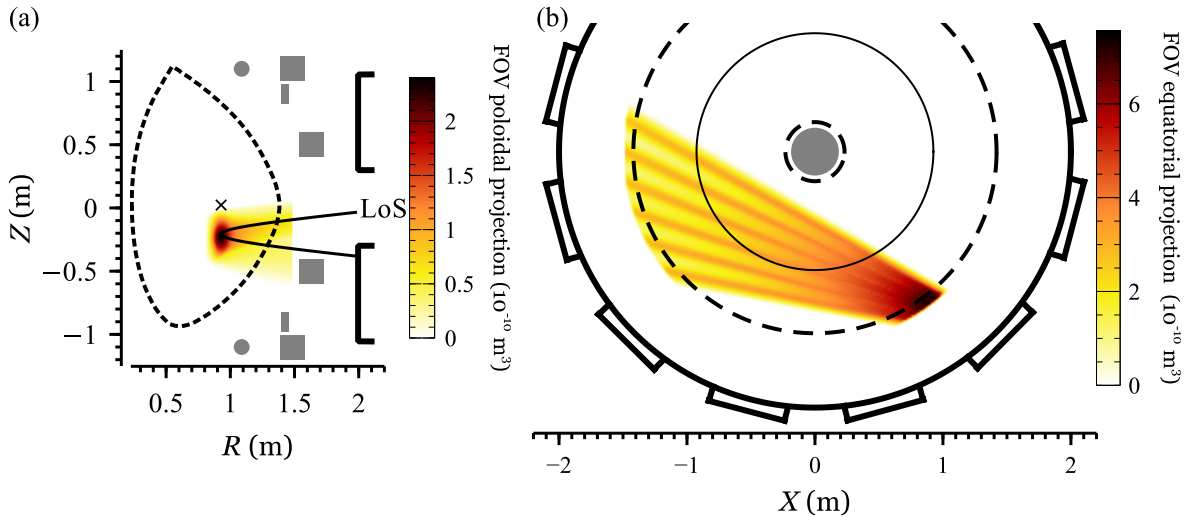


Figure 6.7: Poloidal (a) and equatorial (b) projections of a set of NC fields of view (FOV). (a) shows the volumetric contribution, projected onto the poloidal plane, of each part of the plasma to the FOV of a single diagonally-oriented chord with tangency radius  $p = 0.93 \text{ m}$ . (b) shows the contribution, projected onto the equatorial plane, to horizontal FOV at six equally-spaced viewing angles. Figure adapted from ref. [76].

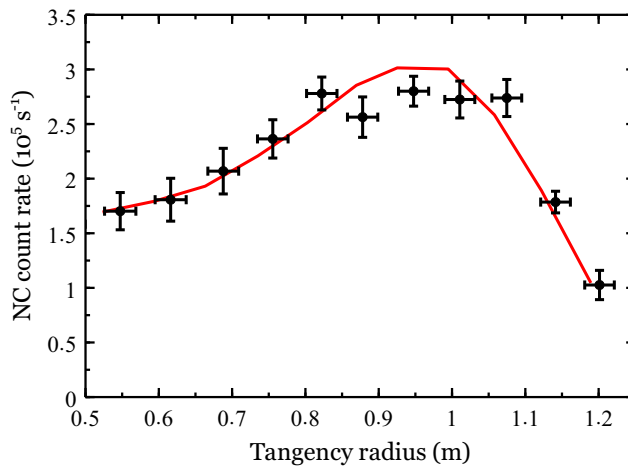


Figure 6.8: Profile of NC count rate as a function of midplane LOS tangency radius averaged over the MHD-quiescent period  $t = 0.255 \text{ s} - 0.260 \text{ s}$  in repeated high-density, low-NBI power discharges #29904 – #29910 (excluding shot #29907, which was a poor repeat). Shown in red is the profile generated using the LINE2 solid-angle calculator based on the neutron emission modelled using TRANSP/NUBEAM for one of the shots in the series. The overall system efficiency, which has been calculated to minimise the sum of the squared residuals between the measured and modelled profile, is 0.0875. Note the asymmetry of the profile about the magnetic axis, located at  $R = 0.93 \text{ m}$ ; this arises due to the line-integrated nature of the NC measurements. LINE2 simulations performed by Iwona Klimek.

Iwona Klimek at Uppsala University, Sweden.

In future, it is hoped that a version of LOCUST which has been upgraded by Dr. Rob Akers to run on graphics processing units (GPU) [63] will be able to take the place

of NUBEAM in modelling FI distributions in MAST. The principal advantages of this GPU-based code are: the ability to simulate many more particles than NUBEAM in a given time on the available hardware (by a factor of approximately 100); the ability to track full gyro-orbits rather than just the guiding-centre orbit with a first-order correction for finite Larmor radius; an internal calculation of  $n$ -resolved (beam, halo and FI) neutral deuterium distributions; and the inclusion of 3D geometry to account for non-axisymmetric perturbations to the magnetic field. The synthetic diagnostics developed for use with NUBEAM FI distributions could easily be adapted for use with LOCUST-GPU distributions.

Development of a synthetic diagnostic for the CFPD is ongoing, and is proving challenging due to the difficulty of accurately reconstructing fusion proton and triton orbits. The present discussion of synthetic FI diagnostics on MAST therefore ends here. In future, with the installation of a scintillator-based FILD and the possibility of upgrades to the NC and CFPD, continued development of synthetic diagnostics will be a vital part of the MAST-Upgrade FI research programme. In the next chapter, we move from description of the research methodology used in this project to presentation of experimental results which give an insight into anomalous FI transport mechanisms due to instabilities driven by energetic-particle resonances.

# Chapter 7

## Effects of resonant MHD instabilities

### 7.1 Outline

Resonant MHD instabilities observed in MAST, as discussed in chapter 3, include toroidicity-induced Alfvén eigenmodes (TAE) and fishbones. In this chapter, observations of changes in the FI diagnostic signals correlated with each of these instabilities are presented, and the interpretation of these observations is discussed. The results of TRANSP modelling in which anomalous FI transport or loss processes are invoked to try to match the observations are presented and compared with the measurements. Four main conclusions are supported by the results presented in this chapter:

- Drops in both FIDA and NC signals are correlated with chirping TAE and fishbones at a statistically significant level, indicating a reduction of the confined FI density.
- Chirping TAE and fishbones cause enhanced losses of FI from the plasma.
- The profiles of NC and FIDA signals in quiescent periods between bursts of MHD activity are well modelled by applying anomalous diffusion to the FI in NUBEAM.
- Fishbones strongly affect the high-energy, passing FI population in a manner which may be reproduced with some success using the fishbone model in NUBEAM.

Of these points, the latter two in particular represent the value of the multi-diagnostic approach adopted in this work. Previous studies on MAST have focused mainly on the effects of particular instabilities on the signal from a single diagnostic [73, 74], or on the agreement between modelled and measured signals from a subset of the available diagnostics [75]. Multiple diagnostics have been used simultaneously, along with associated transport modelling and synthetic diagnostics, to study FI transport

induced by Alfvén eigenmodes in DIII-D [180] and by sawteeth in ASDEX-Upgrade [181]. This work represents the first application of such methods to study fishbone-induced FI transport. It is also the first time that both global and local fusion product measurements have been combined with FIDA observations to draw inferences about the FI transport.

## 7.2 Plasma scenarios

Two sets of discharges were selected for the analysis of the effects of fishbones and TAE on the FI population. Both sets consist of discharges with high NBI power and high electron density, the combination of which provides a reasonable SNR in the FI diagnostic signals along with large-amplitude bursts of TAE and fishbones separated in time by approximately 5 ms to 10 ms. These points are important in allowing the effects of individual bursts of MHD activity on the FI population to be resolved by each of the diagnostics. A further reason for choosing these sets of discharges for analysis is the fact that the NC was scanned in tangency radius between repeated shots, allowing composite NC count-rate profiles to be derived. Figure 7.1 shows time traces of key parameters related to the FI population and MHD activity in a representative discharge from each set.

Each set of discharges featured periods with well-separated bursts of MHD activity, with the typical evolution of the magnetic spectrogram exhibited by beam-heated MAST plasmas in which chirping energetic-particle modes grow in amplitude and decrease in frequency as the  $q$ -profile evolves; this behaviour was illustrated in chapter 3. Spectrograms from the periods of interest in each of these scenarios are shown in fig. 7.2. Shot #29207 *et seq.* included a period with a single neutral beam injecting 2.0 MW of power with a primary energy of 71 keV, throughout which chirping TAE persisted, followed by a period with both neutral beams injecting a total of 3.5 MW of power with the primary energy of the second beam set at 61 keV. In this latter period, large quasi-periodic fishbones were observed to merge into the LLM. The second set of discharges, commencing with #29975, exhibited very strong fishbones occurring with semi-regular spacing between bursts; the TAE are less distinct, and the early stages of the three discharges less similar to each other, than those in the first set, so the analysis of the second set focuses on the large fishbones occurring late in the discharge. The total NBI power in the second set was 3.0 MW, and the primary beam energies were 70 keV and 44 keV.



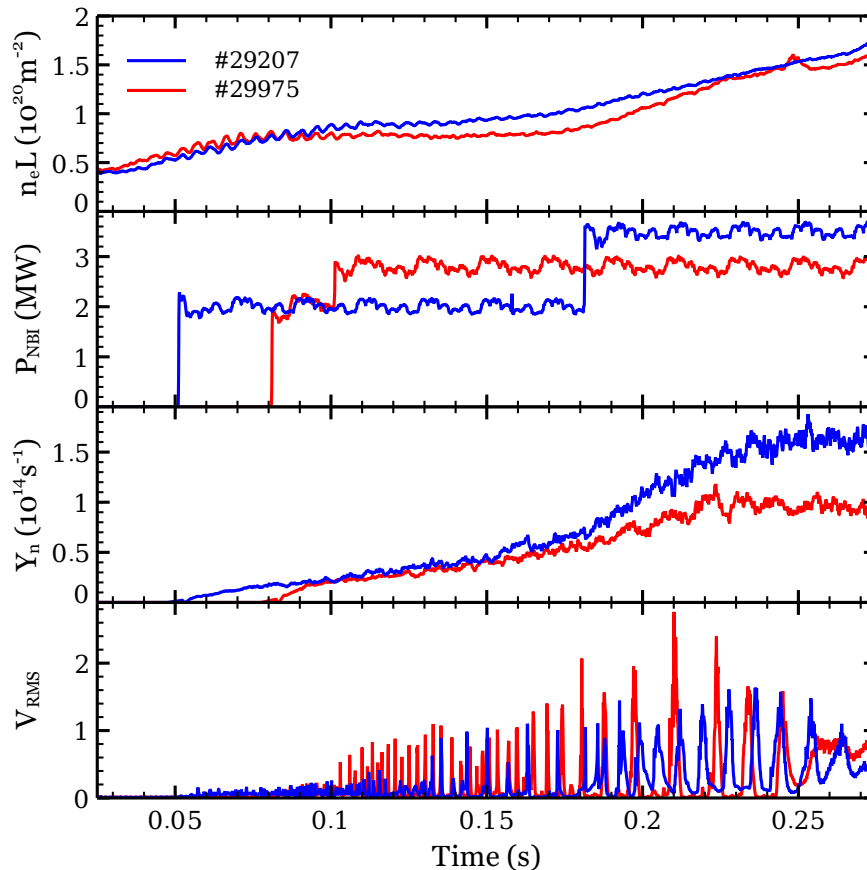


Figure 7.1: Global parameters of representative discharges from the two sets selected for analysis of the effects of TAE and fishbones. The first set consists of shots #29207 – #29210, and the second set includes shots #29975, #29976 and #29980. The panels show, from top to bottom: line-integrated electron density measured with a CO<sub>2</sub> laser interferometer; total injected NBI power; global neutron rate measured with the fission chamber; and RMS amplitude of an outboard-midplane Mirnov coil signal sensitive to changes in the poloidal field.

Preliminary results from the investigation into the effects of TAE, fishbones and the LLM on FI using data from the second set of discharges have been published in a special issue of the journal *Plasma Physics and Controlled Fusion*, in a paper to which this author contributed substantially (M Ceconello *et al.* 2015, 57(1):014006). The continuation of this analysis and the novel analysis of the first set of discharges, which are the subjects of this chapter, form the basis of a manuscript recently submitted by this author to *PP&CF*.

## 7.3 Effects of chirping modes on confined fast ions

### 7.3.1 TAE

As shown in fig. 7.3, a significant reduction in the NC count rate and FIDA radiance is observed to coincide with many TAE bursts. The timing of these drops in signal

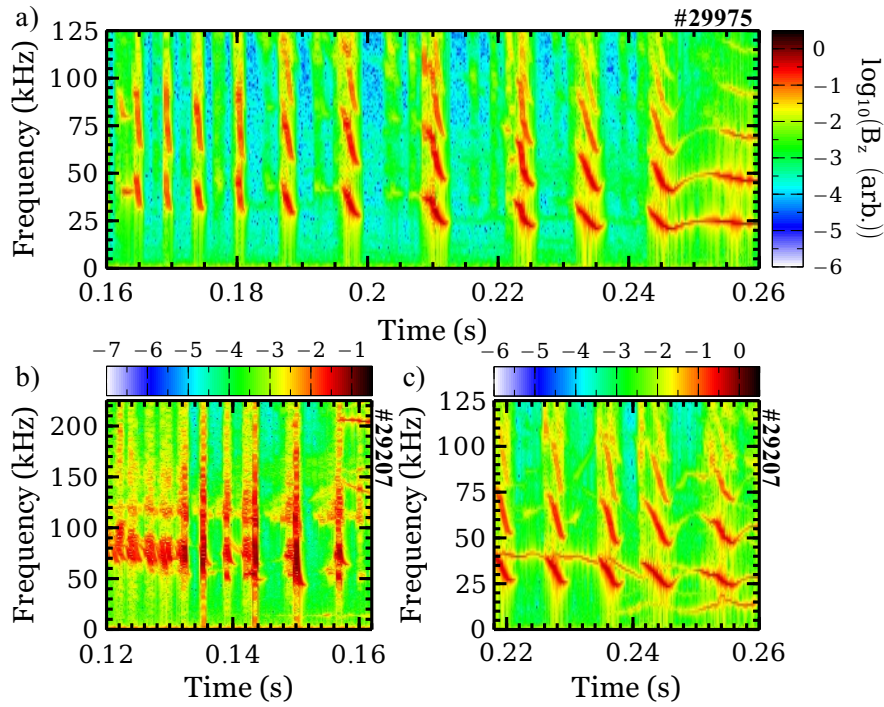


Figure 7.2: Spectrograms from an outboard-midplane Mirnov coil signal measuring the poloidal component of the perturbed magnetic field. (a) shows a period during shot #29975 in which chirping TAE evolve into large-amplitude fishbones. (b) and (c) show two separate periods during shot #29207 in which chirping TAE and large-amplitude fishbones respectively dominate the low-frequency magnetic activity. Note the extended vertical axis in (b) compared to (a) and (c). In neither of these shots are there any signs of high-frequency energetic-particle modes, which would appear at around 1 MHz; the absence of high-frequency EPM in the presence of low-frequency EPM is a characteristic feature of MAST plasmas.

relative to the amplitude of the envelope of the Mirnov coil signal varies substantially between events. Not all drops in the diagnostic signals are associated with prominent chirping modes, neither are all bursts of magnetic activity correlated with significant changes in the diagnostic signals. This variation is likely due to the fact that the bursts of MHD activity are not mutually independent; the period between successive bursts is considerably shorter than the FI slowing-down time, hence the modification of the FI distribution by one burst may affect the susceptibility of the distribution to modification by subsequent bursts. In light of this variability, a quantitative approach must be adopted to determine the degree to which the reduction in FI confinement indicated by the NC and FIDA signals is correlated with chirping TAE. No CFPD data are available for this set of discharges, since the diagnostic had not been installed at the time.

The first stage in identifying the correlation between TAE and FI diagnostic signals

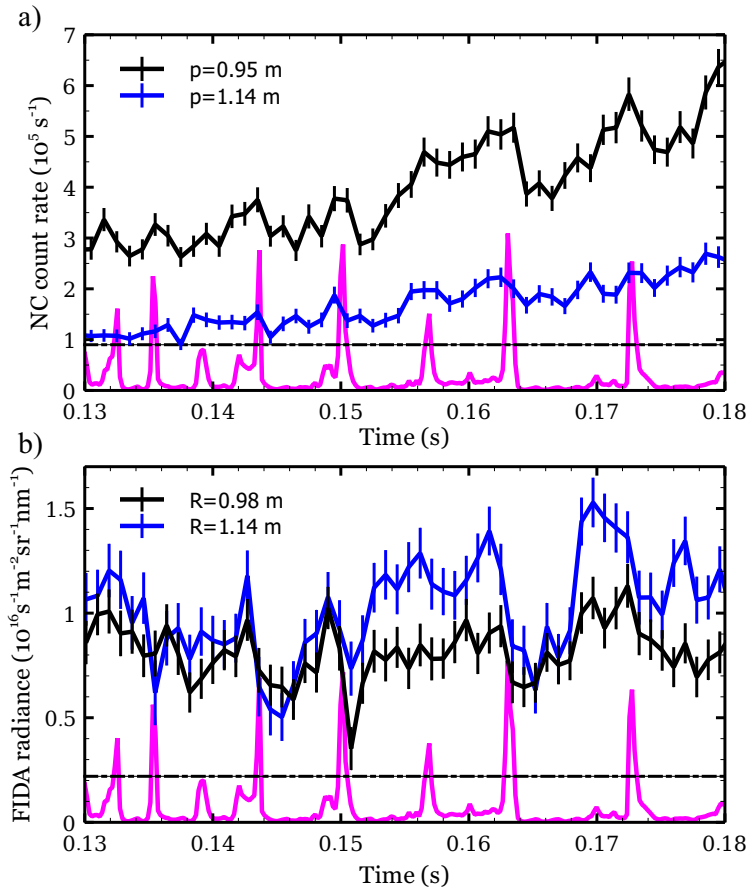


Figure 7.3: a) Traces of NC count rates from the two midplane chords during a period in shot #29207 in which chirping TAE were active. The tangency radii of the two chords are labelled, and the magenta trace shows the RMS amplitude of an outboard-midplane Mirnov coil signal in arbitrary units. b) Traces from two channels of the toroidally-viewing FIDA system during the same discharge, with the beam intersection radii labelled. Data are averaged over wavelengths 660.7 nm to 661.3 nm, and therefore include FIDA emission from passing FI with energy  $E > 46$  keV. Error bars on each trace represent random uncertainty.

is to establish criteria for the identification of an ‘event’ in each case. Inspection of time traces such as those shown in fig. 7.3 suggests that strong effects on the diagnostic signals are associated with TAE bursts with a large amplitude in the RMS Mirnov coil trace. Any increase in magnetic activity which exceeds a threshold RMS amplitude is therefore chosen to constitute an ‘event’ in the magnetics signal; this threshold is indicated by the dot-dashed horizontal lines in fig. 7.3. In order to exclude drops in the NC and FIDA signals which occur due to noise, or spurious drops in the net FIDA signal caused by rapid, transient spikes in passive FIDA correlated with TAE bursts, the condition imposed on these signals is that an ‘event’ constitutes a drop in signal which does not recover to the pre-event level within four time steps. With the integration time of the FIDA data set at 0.9 ms and that of the NC data set at

1.0 ms, this provides sufficient temporal resolution to allow each of the TAE bursts to be separated while ensuring that most of the ‘events’ represent true reductions in the part of the FI population to which the diagnostics are sensitive. Examples of qualifying events in the NC and FIDA signals are shown in fig. 7.4. Note that a quadratic trend is removed from each of the time traces prior to analysis; this ensures that significant drops in diagnostic signals are not masked by the trend of the signal throughout the analysis period, which extends from 0.13 s to 0.18 s in each of the four discharges analysed in this work.

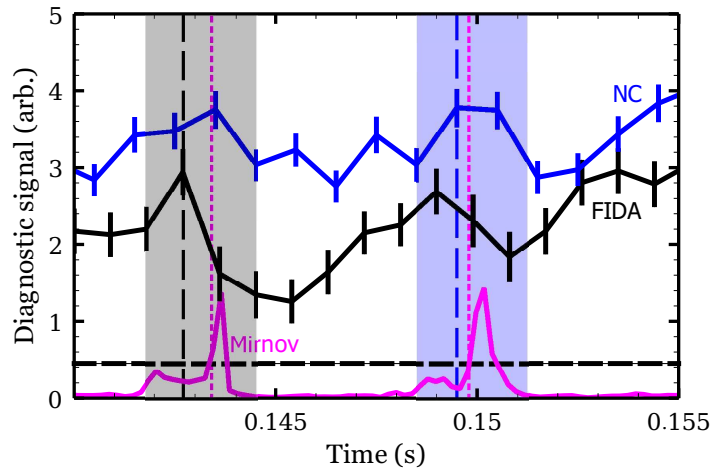


Figure 7.4: Drops in NC and FIDA signals which qualify as ‘events’ for the purposes of determining the correlation with chirping TAE. The dashed vertical black and blue lines mark the onset times of events in the FIDA and NC signals respectively. Dotted magenta lines mark the onset times of events in the RMS Mirnov coil signal, in which the Mirnov coil trace exceeds the threshold shown by the dashed horizontal line. The shaded regions indicate the period within which the magnetics event must occur in order to be counted towards successful identification. Both of the events highlighted here clearly satisfy this criterion.

Proceeding from the strict definition of an ‘event’ in the magnetics and FI diagnostic time traces, the criterion chosen to determine whether events coincide is that the onset time of the magnetics event must lie within a period extending from one time step before to two time steps after the start of the drop in FIDA or NC signal. This period is indicated by the shaded regions in fig. 7.4. The natural variation between events, arising due to the variable levels of drive and damping of the TAE, is thereby taken into account. For each FI diagnostic time trace, and for the analysis period during each discharge, an ‘identification factor’ may be defined to quantify the correlation between events in the diagnostic signals and the occurrence of TAE bursts. This factor

is defined as

$$Q_{\text{ID}} = \frac{\text{identified events}}{\text{total TAE events} + \text{false positives}}. \quad (7.3.1)$$

The top panel of fig. 7.5 shows the results of the TAE identification analysis for all four discharges in this set. In each case, the FI diagnostics are best able to identify the effects of TAE bursts in the radial range where the signal is strongest; in the case of the NC this corresponds to the region close to the magnetic axis, and in the case of the FIDA diagnostic this corresponds to mid-radius on the outboard side. This observation suggests that the limiting factor in the ability of the diagnostics to resolve the effects of chirping TAE on FI, at least in this set of discharges, is the SNR.

Note that only seven FIDA channels were included in this analysis since strong bursts of passive FIDA emission contaminate the signal from two channels with beam intersection radii larger than  $R = 1.3$  m, and the fibre feeding light from the innermost channel into the spectrometer is partially blocked by the end of the input slit. Signals from these channels are too unreliable to provide usable data in this instance.

A meaningful assessment of the significance of these identification factors requires confidence intervals to be determined. The process adopted here was to randomly permute the data points in each time series, and to establish an identification factor  $Q_{\text{ID}}^*$  based on the new, randomised time series. Repeating this process many times allows confidence levels to be quantified as percentiles of all  $Q_{\text{ID}}^*$ . If the  $Q_{\text{ID}}$  of the original time series lies above, say, the  $n\%$  confidence level, then the probability of the observed value of  $Q_{\text{ID}}$  arising purely by chance is less than  $(100 - n)\%$ . Dashed, horizontal lines in fig. 7.4 mark the 90<sup>th</sup> percentile of 10,000 values of  $Q_{\text{ID}}^*$ , which is to say the 90% confidence level. The advantage of this procedure is that it is insensitive to the distribution of data points in the time series as long as the properties of this distribution are constant throughout the analysis period. To ensure that this was the case, the time series (with least-squares fitted quadratic trends removed) were subjected to the Dickey-Fuller test for the presence of unit root [182]. In all cases, the null hypothesis (that a unit root is present in the time series) was rejected at the 1% level, allowing the time series to be treated as stationary. It can therefore be said with confidence that chirping TAE cause a significant reduction of the confined FI density in these plasmas.

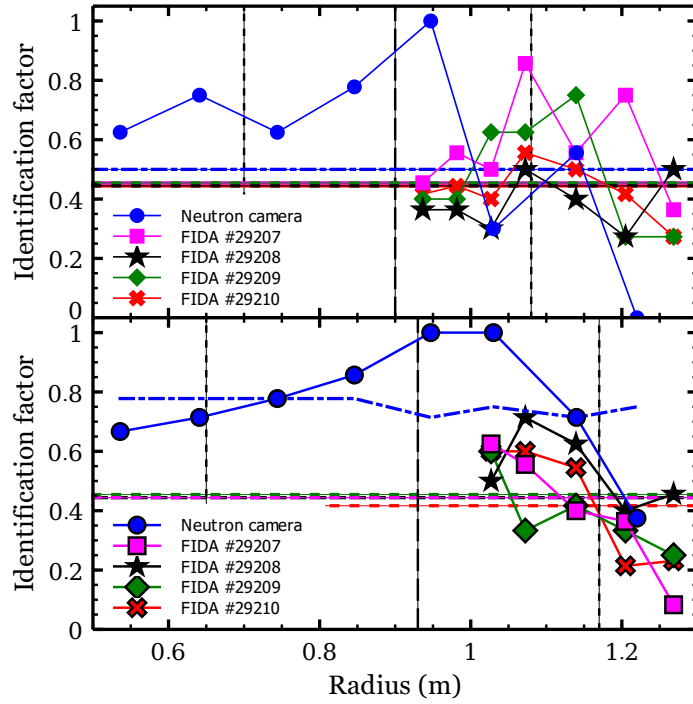


Figure 7.5: Top panel: TAE identification factors, defined according to eq. (7.3.1), for the NC and FIDA diagnostics during the period 0.13s to 0.18s in shots #29207 – #29210. Vertical dashed and dotted lines mark the approximate positions of the magnetic axis and  $q_{\min}$  surfaces respectively. Dashed horizontal lines of various colours mark the 90% confidence level for event identification in the corresponding FI diagnostic signal; data points have less than a 10% chance of lying above these lines assuming random time series. Bottom panel: as above but for fishbones occurring in the period 0.208s to 0.258s during the same set of discharges. The two innermost FIDA channels are excluded from this panel due to the contamination of the spectra with SW beam emission.

### 7.3.2 Fishbones

Each of the discharges in the set analysed above also exhibited well-spaced, quasi-periodic fishbones as seen in panel (c) of fig. 7.2. The method described in the previous subsection was applied to the NC and FIDA signals to establish the correlation between these signals and the fishbones. In this analysis, the threshold applied to the RMS Mirnov coil signal was increased to account for the larger amplitude of the fishbone bursts compared to the TAE bursts. Dashed horizontal lines in each panel of fig. 7.6 indicate the chosen threshold. The width of the time window which was searched for a burst in Mirnov coil signal corresponding to each drop in NC or FIDA signal was also widened compared to that used in the TAE analysis. This widening accounts for the fact that the fishbones evolve more slowly than the TAE and therefore take longer to have a significant effect on the FI population. The window was extended by half a time

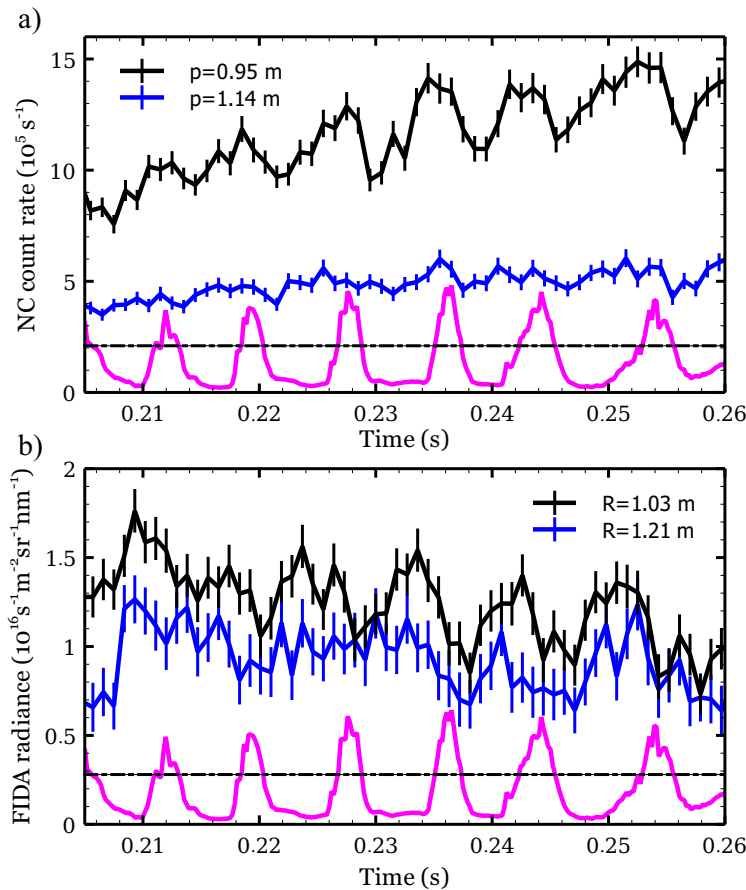


Figure 7.6: a) Traces of NC count rates from the two midplane chords during a period in shot #29207 in which fishbones were active. The tangency radii of the two chords are labelled, and the magenta trace shows the RMS amplitude of an outboard-midplane Mirnov coil signal in arbitrary units. b) Traces from two channels of the toroidally-viewing FIDA system during the same discharge, with the beam intersection radii labelled. Data are averaged over wavelengths 660.7 nm to 661.3 nm, and therefore include FIDA emission from passing FI with energy  $E > 46$  keV. Error bars on each trace represent random uncertainty.

step in each direction, thus covering the period from 1.5 time steps before to 2.5 time steps after the commencement of the drop in FI diagnostic signal. Significant drops in NC and FIDA signals are clearly seen to accompany the fishbone bursts in fig. 7.6. The results of the analysis described above are shown in the bottom panel of fig. 7.5. As in the case of the TAE, both diagnostics see significant drops in signal correlated with the fishbones. In many of the channels the confidence in the correlation exceeds 90%. Note that the two innermost channels of the FIDA system cannot be included in this analysis since the spectra are strongly contaminated with SW beam emission.

In previous studies of MAST FIDA data by this author [74], it was found that the relative change in core FIDA signal due to the fishbones was correlated strongly with the maximum RMS amplitude of the Mirnov coil signal and only weakly with

the amplitude of the perturbation. This analysis was repeated for the data from the recent set of discharges (#29207 *et seq.*). Figure 7.7 shows the scaling of the drops in

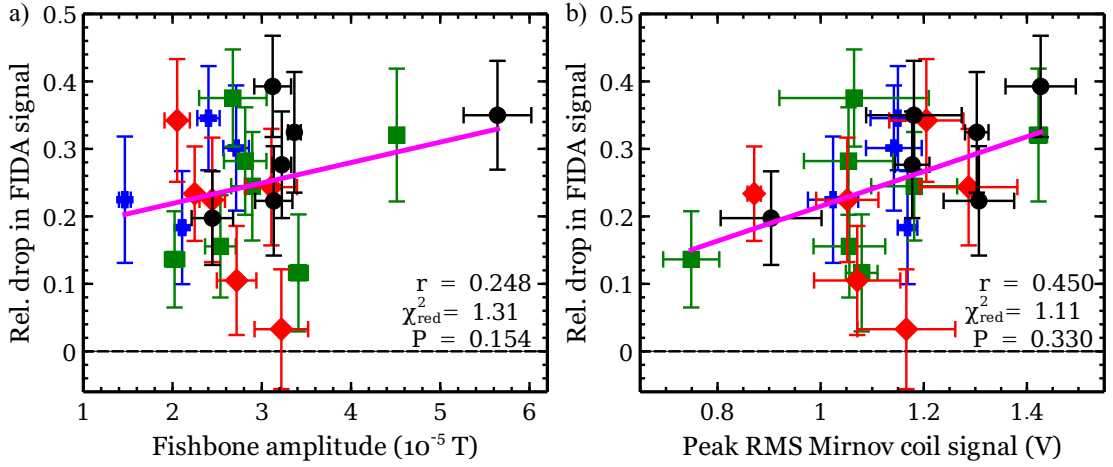


Figure 7.7: Relative change in FIDA signal plotted against (a) the amplitude of the fishbone perturbation and (b) the maximum RMS amplitude of the Mirnov coil signal for a set of 23 fishbones in shots #29207 – #29210. Each data point corresponds to a single fishbone, and different symbols are used for each discharge. The relative drop in signal is defined as  $(S_i - S_f)/S_i$  where  $S_i$  and  $S_f$  are the signal before and after the fishbone respectively. The correlation coefficient  $r$ , reduced  $\chi^2$  and cumulative chi-squared probability  $P = \Pr(X^2 \geq \chi^2)$  are shown in each panel. Data are averaged over  $R = 1.03$  m to 1.14 m at  $\lambda = 660.7$  nm.

FIDA signal with the amplitude of the fishbones and with the RMS amplitude of the perturbation in the Mirnov coil signal. The wavelength used in fig. 7.7 corresponds to a minimum FI energy of 46 keV. The data are averaged over three channels with beam intersection radii 1.03 m, 1.07 m and 1.14 m. A different symbol is used for each shot, but the regression analysis takes into account the whole data set. As in the earlier study [74], the drops in FIDA signal are correlated much more strongly with the RMS Mirnov coil signal than with the fishbone amplitude. This suggests that the strength of the interaction between the fishbones and the FI is sensitive to the frequency of the perturbation as well as to its amplitude, since  $\dot{B}_\theta \approx \omega \tilde{B}_\theta$ . Here,  $\dot{B}_\theta$  is the time derivative of the poloidal magnetic field, to which the Mirnov coil signal is proportional assuming a fixed mode location, and  $\omega$  and  $\tilde{B}_\theta$  are the frequency and amplitude of the mode. Such a relationship was previously found between drops in the global neutron rate and  $\langle \dot{B}_\theta \rangle_{\text{RMS}}$  during TAE bursts in DIII-D [87], while no linear dependence on  $\langle \dot{B}_\theta \rangle_{\text{RMS}}$  was seen in the case of fishbone bursts. A linear correlation was later found, albeit in a smaller data set, between drops in the neutron rate and the amplitude  $\tilde{B}_\theta$  of chirping modes in the fishbone-EPM frequency range [137]. In NSTX meanwhile, a



very weak linear scaling was identified between FI losses and mode amplitude  $\tilde{B}_\theta/B$  in the case of both EPM and TAE, with TAE having a stronger effect for a given mode amplitude [183]. Fishbones were not included in that data set, and the correlation with  $\dot{B}_\theta$  was not examined. For the changes in FIDA signal associated with the chirping TAE discussed in the previous subsection, no significant correlation was found with either  $\langle \dot{B}_\theta \rangle_{\text{RMS}}$  or with  $\tilde{B}_\theta$ . The present result therefore raises the question of which quantity is the better proxy for the ability of chirping modes to redistribute FI, particularly in the presence of mixed low and high-frequency modes.

Since the tangency radius of the NC was scanned between discharges in this set, the correlation analysis presented in fig. 7.7 unfortunately cannot be extended to this diagnostic. Furthermore, the drops in global neutron rate due to these fishbones are small and difficult to distinguish from noise or from perturbations caused by changes in bulk plasma parameters or non-resonant MHD modes. We therefore move on to consideration of the possibility that as well as causing real-space or velocity-space transport of resonant FI as suggested by the results in this section, the TAE and fishbones may also cause losses of FI from the plasma.

## 7.4 Fast-ion losses due to resonant MHD instabilities

Spikes in the  $D_\alpha$  radiation from the edge of the plasma and from the divertor are observed to coincide with many chirping modes. Figures 7.8 and 7.9 show examples of this behaviour from shot #29207. Bursts in the Mirnov coil trace coincide with a significant reduction in FIDA and neutron emission from the core of the plasma, as well as with pronounced spikes in the signal from a filtered  $D_\alpha$  monitor viewing the edge of the plasma close to the midplane. These spikes in  $D_\alpha$  light were hypothesised to be the result of CX reactions between FI ejected from the plasma by the modes, and neutrals close to the plasma boundary. The open divertor in MAST meant that deuterium recycled from the plasma at the divertor plates was able to circulate freely in the vacuum vessel, forming a dense ‘blanket’ of neutrals at the edge of the plasma.

To test this assertion about the origin of the  $D_\alpha$  spikes, the passive FIDA emission provides useful information. By inspecting the time trace of passive FIDA during a time window in which edge  $D_\alpha$  spikes are observed, the mechanism giving rise to these spikes is firmly established as being related to the FI. The top panel of fig. 7.10 shows time traces of passive FIDA from a reference channel ( $R = 1.33$  m) during the period in which large-amplitude TAE and  $D_\alpha$  spikes are observed in fig. 7.8. The spikes in

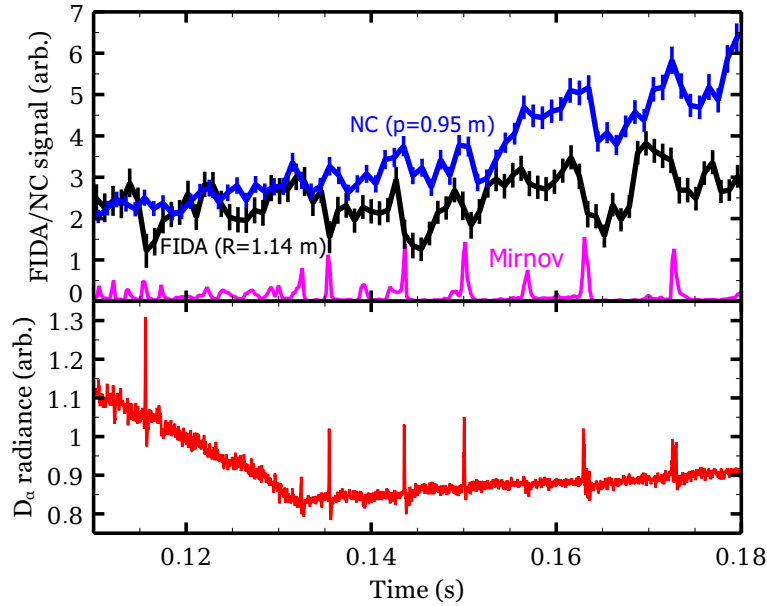


Figure 7.8: Chirping TAE during shot #29207 are observed to cause large drops in core NC and FIDA signals which in most cases take several milliseconds to recover to the pre-event level (top panel). Coincident with the largest of these bursts, spikes in  $D_\alpha$  radiation from the edge of the plasma are observed (bottom panel). A large drop in FIDA signal and a spike in edge  $D_\alpha$  are also observed at around 0.115s, despite the fact that only a small TAE, and no drop in NC signal, is observed at this time. The nature of this event is unknown, but the observations suggest an ejection of fast ions from the plasma in a narrow region of real space or velocity space.

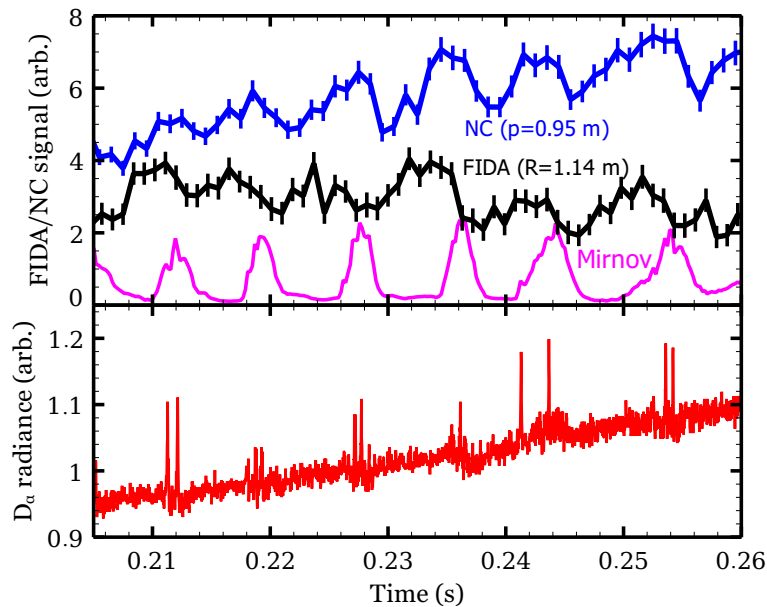


Figure 7.9: Fishbones during shot #29207 are observed to cause large drops in core NC and FIDA signals which in most cases take several milliseconds to recover to the pre-event level (top panel). Coincident with these bursts, spikes in  $D_\alpha$  radiation from the edge of the plasma are observed (bottom panel). The  $D_\alpha$  spikes in this case exhibit more structure, last longer, but have a smaller amplitude than in the case of the TAE.

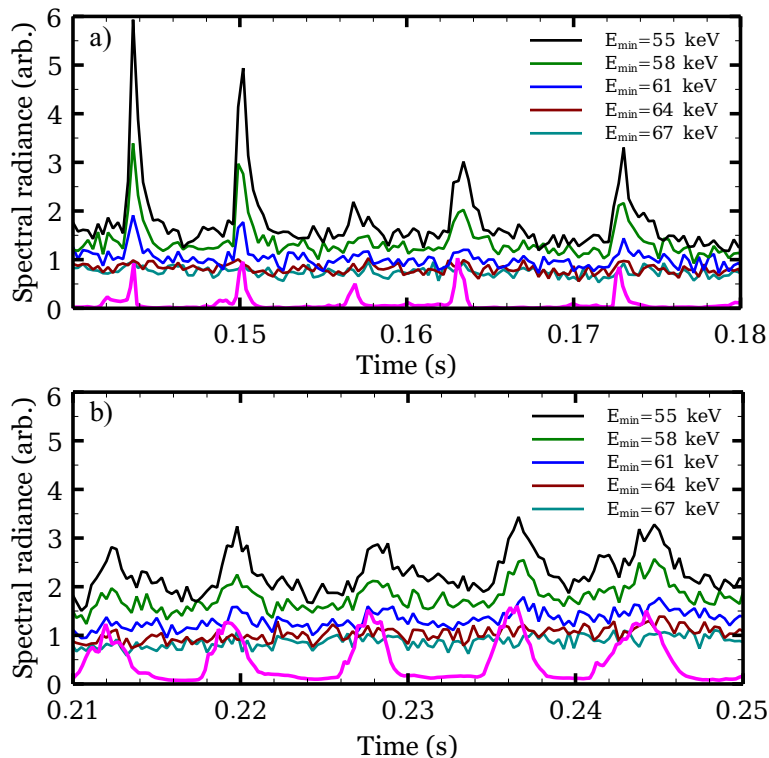


Figure 7.10: Passive FIDA emission at five wavelengths, with the corresponding minimum FI energy indicated by the labels, during two separate periods in shot #29207. The RMS amplitude of the Mirnov coil signal is shown in magenta. Chirping TAE are visible in panel (a), and fishbones in panel (b). The FIDA chord views tangentially with a midplane intersection radius of 1.33 m. The primary beam energy is 71 keV.

passive FIDA emission are clearly seen to be suppressed close to the beam injection energy, which was 71 keV during this shot. This observation demonstrates conclusively that the  $D_\alpha$  spikes are at least partially caused by reneutralised FI rather than by thermal neutrals or perturbations to bremsstrahlung radiation. The same conclusion applies to the  $D_\alpha$  spikes in fig. 7.9 and in the bottom panel of fig. 7.10, which are observed to coincide with the fishbones. This implies that both TAE and fishbones cause losses of FI from these plasmas.

Analysis and interpretation of the FIDA and NC observations reveals that both TAE and fishbones cause FI to be transported from the core of the plasma and even lost through the plasma boundary. The next step in this analysis is to attempt to model the effects of the modes on FI using the *ad hoc* models available within TRANSP.

## 7.5 TRANSP modelling of fast-ion redistribution

### 7.5.1 Anomalous transport models

Two mechanisms are available within NUBEAM to allow the effects of TAE and fishbones on the FI to be modelled. The redistribution may be modelled as a combination

of diffusive and convective transport, with user-specified diffusion and convection coefficients  $D_{\text{an}}$  and  $V_{\text{an}}$  specified as a function of radial position, time and energy. Without first-principles modelling of the underlying physics to guide the choices of these coefficients however, only the simplest models are practically applicable. In the modelling described in this chapter, anomalous diffusion was varied as a function of time but was taken to be radially uniform throughout the plasma. Convective transport was not applied, since diffusive transport was found to reproduce the observations reasonably well. The effect of diffusion is to cause radial transport of FI at a rate proportional to the gradient of the FI density. The radial flux resulting from a combination of convective and diffusive transport is

$$\Gamma_{\text{FI}} = V_{\text{an}} n_f - D_{\text{an}} \nabla_r n_f.$$

The second FI transport mechanism available within NUBEAM is an *ad hoc* fishbone loss model. This model takes as input parameters: the time of the first fishbone and the time at which the model is switched off; the duration of the fishbone burst and the characteristic loss time of the FI while the fishbone is active; the time between fishbone bursts; the minimum and maximum values of energy and pitch of the affected FI; and an optional trapping-depth parameter to override the chosen range of pitch. This model was successfully used to reproduce global and local neutron emission from MAST plasmas as described by Klimek *et al.* [156]. In the present work however, FIDA observations are used as an additional constraint on the parameters of the model.

In the following subsections the results of TRANSP modelling using anomalous diffusion and the fishbone model are presented. Each of these models is confronted with the FI diagnostic observations. These observations are used to refine the implementation of the fishbone model and to reveal its shortcomings. The main strength of this approach lies in its capacity to discriminate between different transport models using a ‘hierarchy’ of diagnostics; in going from the global fission chamber measurement to the local FIDA measurement, increasingly stringent constraints are placed on each implementation of the *ad hoc* transport models. It is found that the models currently available within TRANSP have only a limited ability to reproduce the effects of fishbones on the FI population.

### 7.5.2 Modelling with anomalous diffusion

The series of discharges #29207 *et seq.*, with chirping TAE and quasi-periodic fishbones, provided an opportunity to test the diffusive NUBEAM modelling in the

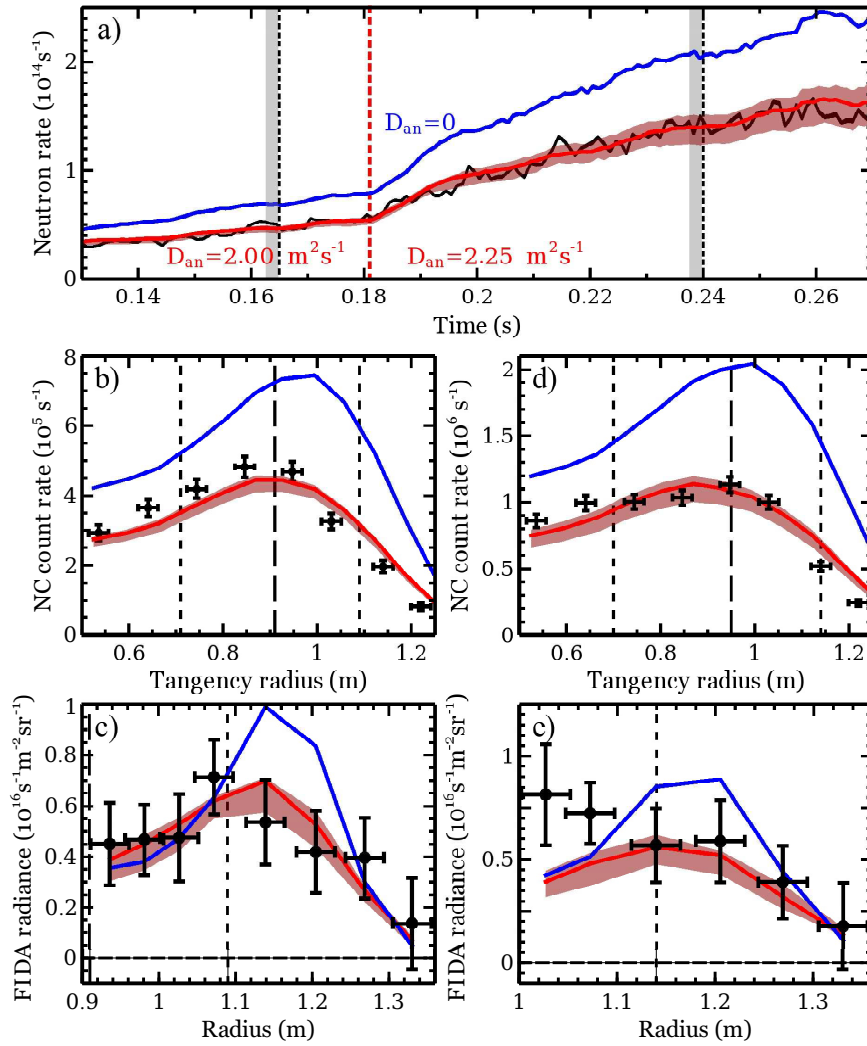


Figure 7.11: Comparisons between measured and NUBEAM-modelled FI diagnostic time traces and radial profiles in the presence of chirping TAE and fishbones. Panel (a) shows the global neutron rate measured in shot #29210 (black) compared to that modelled with (red) and without (blue) spatially-uniform anomalous FI diffusion in TRANSP. The values of anomalous diffusivity used in these simulations are given in the labels. The forward-modelled NC and FIDA profiles are compared to the measured profiles in panels (b) and (c) for  $t = 0.165$  s and in panels (d) and (e) for  $t = 0.240$  s. Contamination of the core FIDA signal with SW beam emission at the later time means that the two channels between 0.9 m and 1.0 m cannot be included, and the signal in the two channels between 1.0 m and 1.1 m is artificially elevated. Vertical dashed and dotted lines in panels (b) to (e) indicate the approximate radial positions of the magnetic axis and minimum- $q$  surfaces.  $\lambda = [660.9 - 661.9]$  nm for FIDA data. Shaded regions around the red traces indicate the nominal uncertainty in the TRANSP-simulated profiles, as discussed in the text.

presence of resonant MHD activity. Time slices averaged over 3 ms, from 0.162 s to 0.165 s during the chirping TAE phase and from 0.237 s to 0.240 s during the fishbone phase, were used for a comparison between NUBEAM modelling and FI diagnostic

signals under the assumption of spatially-uniform anomalous diffusion. The results of this comparison are shown in fig. 7.11.

TRANSP simulations are subject to uncertainties in the input data. To capture this effect, profiles of electron density, electron and ion temperature and  $Z_{\text{eff}}$  were modified to a degree corresponding approximately to the uncertainties in the measured profiles of these quantities. In one simulation, the density was increased by 5% while electron and ion temperature were reduced by 10% compared to the values in the original simulation. This increased the collisionality, reducing the modelled neutron rate and FIDA signal. A third simulation was run in which the sign of these changes was reversed. The measured value of  $Z_{\text{eff}}$  in this series of shots was  $\sim 1.1$  across most of the plasma, so a significant reduction in  $Z_{\text{eff}}$  was not realisable. The uncertainty in  $Z_{\text{eff}}$  therefore introduces a one-sided uncertainty in the neutron rate and FIDA signal. A realistic increase of 50% in  $Z_{\text{eff}}$  was found to have a similar impact to a reduction in temperature of 10% and a corresponding increase in density of 5%. Shaded regions around the simulated signals in fig. 7.11, from the TRANSP run with anomalous FI diffusion, show the margin of error due to these uncertainties in the input data.

Clearly the introduction of anomalous diffusion is sufficient in this case to model the effects of both chirping TAE and fishbones on the FI distribution, at least to the extent that the distribution may be constrained by the available diagnostics. It is worth noting that at the two times shown in fig. 7.11 the measured profiles are averaged over periods during which a significant MHD perturbation occurred; profiles during selected MHD-quiescent windows shortly before a TAE or fishbone burst exhibit increased signal levels, although the signal still does not reach the level modelled in the absence of anomalous FI diffusion. The coarse assumption of spatially-uniform diffusivity, held constant over a long period, cannot capture the dynamics of individual bursts of MHD and the interaction of these bursts with the FI.

### 7.5.3 Inclusion of the fishbone model

Figure 7.12 shows that spatially-uniform anomalous diffusion models well the early part of shot #29975 *et seq.* during which chirping TAE were active. The forward-modelled NC and FIDA profiles show good agreement with the measured profiles at  $t = 0.160$  s, when a diffusivity of  $D_{\text{an}} = 3.0 \text{ m}^2 \text{ s}^{-1}$  allows the TRANSP modelling to match the measured global neutron rate to within 10%.

Later in each of the discharges from this set, a series of large fishbones caused

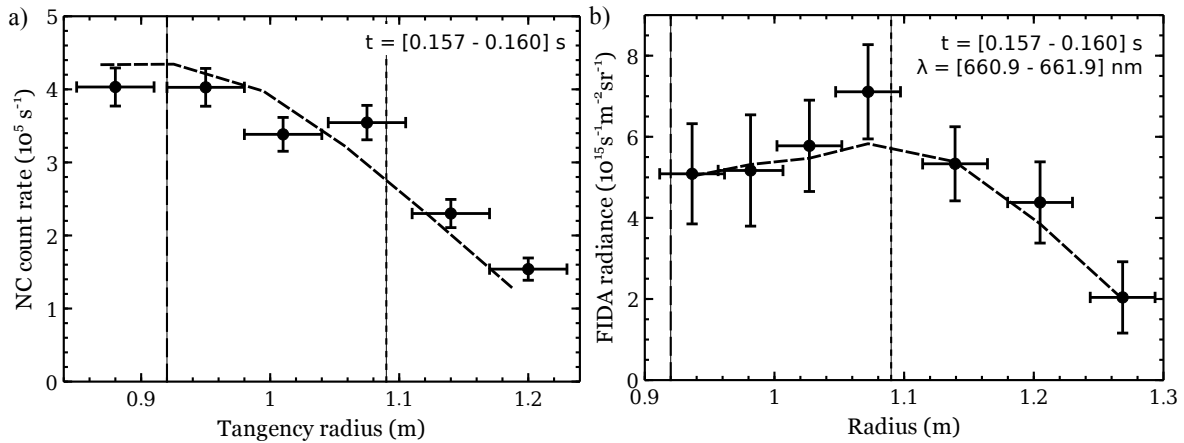


Figure 7.12: Profiles of measured and modelled NC and FIDA signals averaged over the period 0.157 s to 0.160 s during shot #29976 (with the measured NC profile including data from similar discharges #29975 and #29980). The modelled profile is based on a simulation with an anomalous diffusivity of  $3.0 \text{ m}^2 \text{ s}^{-1}$  at this time during the discharge. Vertical dashed and dotted lines mark the approximate radial positions of the magnetic axis and minimum- $q$  surface.

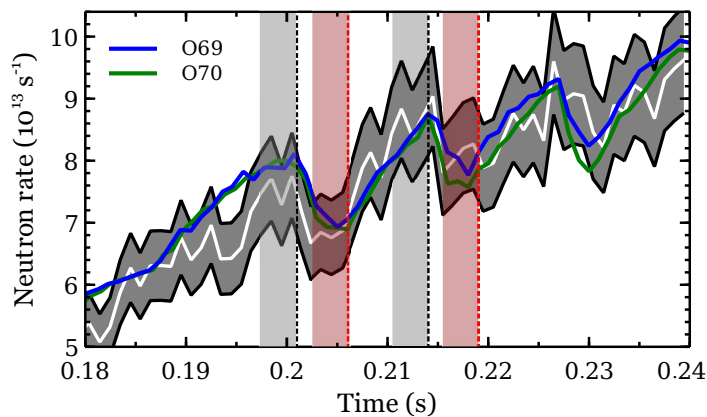


Figure 7.13: A comparison between the measured (white trace, with shaded region indicating statistical uncertainty) and modelled (green and blue traces) global neutron rates for shot #29976 with the fishbone model applied within NUBEAM. The fishbones were specified to occur from 0.201 s to 0.230 s with a period of 12.8 ms. Other parameters of the model are given in table 7.1. In addition to the fishbone model, a small anomalous diffusivity of  $0.15 \text{ m}^2 \text{ s}^{-1}$  was applied to FI with  $E \leq 45 \text{ keV}$  during the fishbone phase in both simulations;  $D_{\text{an}}$  decreased linearly with energy from  $0.150 \text{ m}^2 \text{ s}^{-1}$  to  $0.105 \text{ m}^2 \text{ s}^{-1}$  between 45 keV and 75 keV. Grey and red shaded rectangles indicate the periods, before and after the first two fishbones, over which synthetic FI distributions and measured NC and FIDA signals were averaged to produce the subsequent figures in this section.

transient FI redistribution which the simple diffusive transport model is unable to capture. This redistribution resulted in drops of  $\sim 10\%$  in the global neutron rate, as seen in fig. 7.13. As mentioned earlier, NUBEAM contains a fishbone model which allows FI to be expelled from the plasma within a specified part of velocity space,

with a chosen periodicity and characteristic loss time. This model was previously used to reproduce changes in global and local neutron emission in another series of MAST discharges [156], but FIDA data from the toroidally-viewing system are unavailable for those shots.

In the series of discharges studied here, the fishbone model was initially used with settings similar to those applied in the previous study. FI with  $E \geq 50$  keV and with  $-0.5 \leq p \leq 0.5$  were removed from the plasma at the time of each fishbone burst. It was found however that despite the relatively successful match to the global neutron rate and the changes in NC count rate profiles achieved using these settings, the observed changes in the toroidally-viewing FIDA signal were not reproduced. This may be understood by referring to the geometric weight functions of the FIDA system discussed in chapter 5. The toroidal FIDA views are insensitive to ions with such a small pitch, since the LOS are almost tangential to the magnetic field at the point of beam intersection in the core of the plasma. By contrast, the large fishbones in these shots are observed to cause significant drops in toroidal FIDA signal at all radii from the magnetic axis to the plasma boundary. This observation, which clearly implies the redistribution of co-passing FI from the core of the plasma, informed the choice of energy and pitch boundaries used within the fishbone model in this work.

An iterative process was adopted by which the simulation parameters were at first coarsely modified to converge on the global neutron rate, then modified more precisely to converge on the relative changes in NC and FIDA radial profiles. The neutron rate comparisons from the two most successful simulation runs are shown in fig. 7.13. Parameters of the fishbone model used in each of these runs are outlined in table 7.1.

	O69	O70
Burst duration (ms)	4.0	4.0
FI loss time (ms)	3.0	1.0
Energy range (keV)	50–75	60–70
Pitch range	0.69–0.93	0.00–0.70

Table 7.1: Parameters used in the TRANSP fishbone-loss model for the two simulations in this study which most successfully reproduced the diagnostic observations.

Figure 7.14 shows that TRANSP run O70, in which high-energy FI with  $0 \leq p \leq 0.7$  are removed by the fishbones, produces a good match to the relative size of the observed changes in NC signal across the plasma radius as well as to the shape of the NC profile. Run O69 produces a similar match to the profile shape, but significantly underestimates



the magnitude of the transient reduction in signal caused by the fishbones.

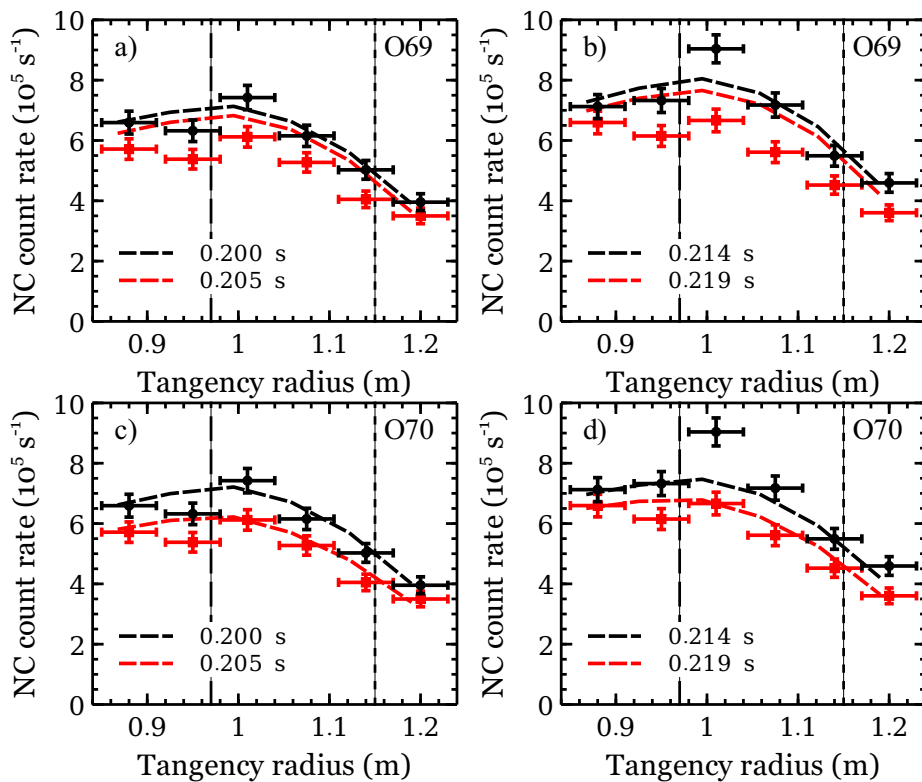


Figure 7.14: Profiles of NC count rate before (black points) and after (red points) the first two fishbones in shots #29975, #29976 and #29980. Panels (a) and (b) compare the measured profiles to those forward-modelled from the neutron emission profiles generated in TRANSP run O69 for shot #29976 (dashed lines), while panels (c) and (d) show a comparison with TRANSP run O70 for the same shot. The calibration scaling factor applied to all profiles is 0.083. Vertical dashed and dotted lines mark the radial positions of the magnetic axis and minimum- $q$  surface.

The same pair of TRANSP runs was used to generate synthetic FIDA profiles. Although the absolute match between the modelled and measured signal levels was slightly better for run O70 than for run O69, the simulated fishbones with these settings failed to cause the observed reduction in core FIDA signal. Figure 7.15 shows that run O69, by contrast, matches the relative change in signal fairly well and also matches the profile shape well, at least at mid-high energies (top panels), even though it underestimates the magnitude of the signal. The comparison between the two runs in terms of their match to the relative change in FIDA signal is quantified in fig. 7.16. Clearly the removal of high-energy passing ions reproduces the FIDA observations. The resonant interaction of passing FI with fishbones finds a precedent in results from the PBX tokamak [184], and was explained theoretically by Betti and Freidberg [89].

The fact that run O69 systematically slightly overestimates the magnitude of the changes in FIDA signal across the plasma radius, while run O70 underestimates these

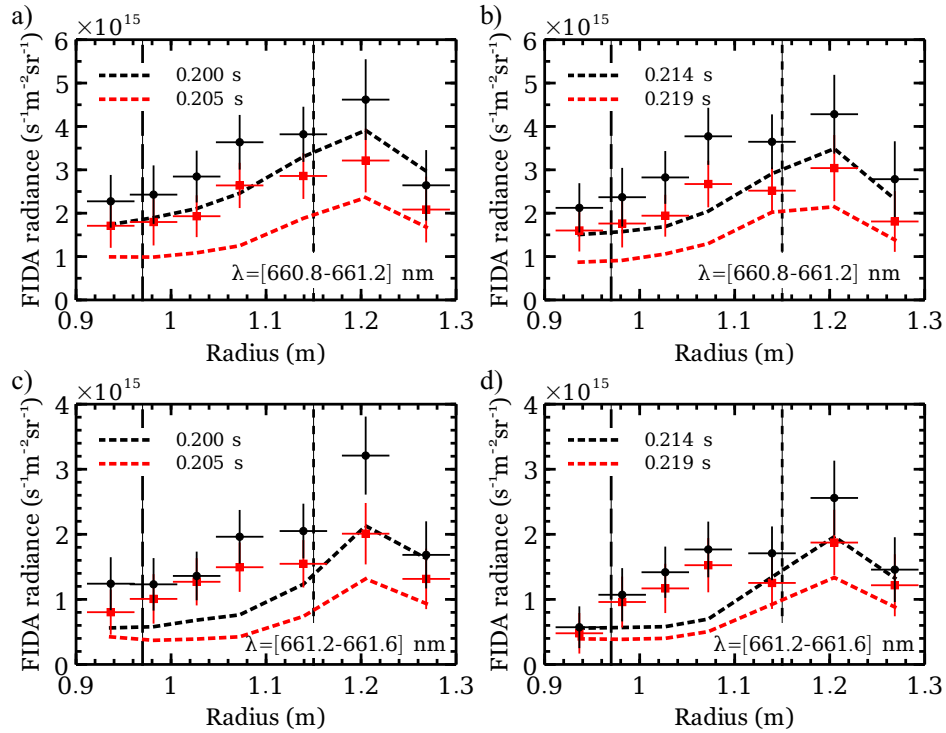


Figure 7.15: Profiles of FIDA radiance before (black points) and after (red points) the first two fishbones in shot #29976. Panels (a) and (b) compare the measured profiles to those forward-modelled with FIDASIM from the FI distributions generated in TRANSP run O69, in a wavelength range corresponding to a minimum FI energy of 48 keV (dashed lines). Panels (c) and (d) show a comparison at higher wavelengths, with  $E_{\min} = 57$  keV. Vertical dashed and dotted lines mark the radial positions of the magnetic axis and minimum- $q$  surface.

changes in the core but matches them well at the edge, suggests that the real effect of the fishbones is best represented by a combination of these models. It is reasonable to suppose that the properties which allow FI to resonate with the mode, and hence to be strongly redistributed, are a function of radial position in the plasma. This dependence cannot be captured with the simple *ad hoc* model available in NUBEAM. More realistic simulations must await the inclusion of a first-principles model of resonant transport in the global transport simulations.

In the set of shots commencing with #29975, the radial position of the reciprocating probe carrying the CFPD was scanned between discharges. This allowed the effects of the large fishbones on the CFPD count rate to be determined as a function of midplane intersection radius; the data from each channel are shown in fig. 7.17. It is apparent that the strongest effect of the fishbones on the CFPD count rate is observed on trajectories which intersect the midplane close to the magnetic axis. Channels with midplane intersection radii from 0.86 m to 0.96 m see a strong depletion in the count rate coinciding with each of the large fishbones, while those at 0.79 m and 0.81 m see only

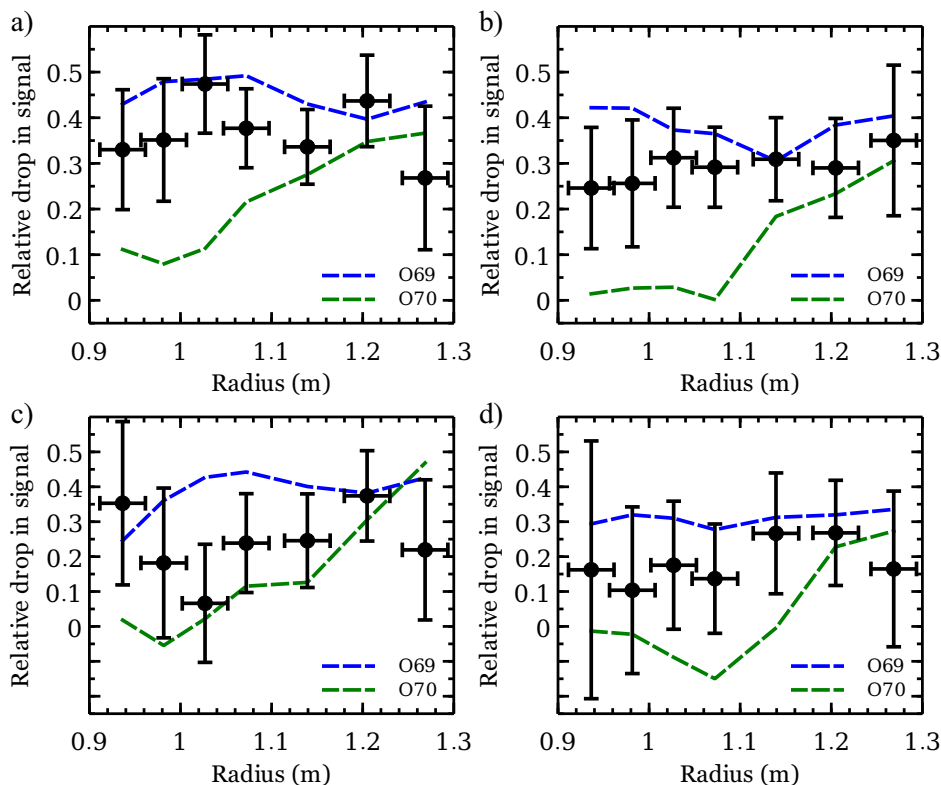


Figure 7.16: Profiles of the relative reduction in FIDA radiance, defined as  $(S_i - S_f)/S_i$ , where  $S_i$  and  $S_f$  are the pre and post-fishbone signals, caused by two fishbones in shot #29976. The measured relative changes are compared to those derived from the FIDASIM profiles based on TRANSP run O69 (blue dashed lines) and O70 (green dashed lines). Wavelengths are the same as those in the corresponding panels of fig. 7.15.

a weak effect. Without a reliable synthetic diagnostic, the fishbone modelling carried out with TRANSP and NUBEAM cannot be validated against the CFPD measurements. Nonetheless, the observation of fishbone-induced drops in signal in *all* of the traces in fig. 7.17 is broadly consistent with the NC and FIDA measurements, which show a significant reduction in signal throughout the core of the plasma.

## 7.6 Summary

The results presented in this chapter demonstrate the advantages of employing several complementary diagnostics to study the behaviour of the FI population. A systematic analysis of NC and FIDA data has allowed the deleterious effects of chirping modes on the confined FI population to be identified with confidence. The velocity-space sensitivity of the FIDA measurements permits losses of FI to be identified unambiguously, and these losses are seen to be strongly correlated with the MHD activity.

Radial profiles of neutron and FIDA emission have been used to constrain transport modelling and to establish the effects of fishbones on the FI distribution. A simultaneous comparison of the modelling results to measurements made with the FC, NC

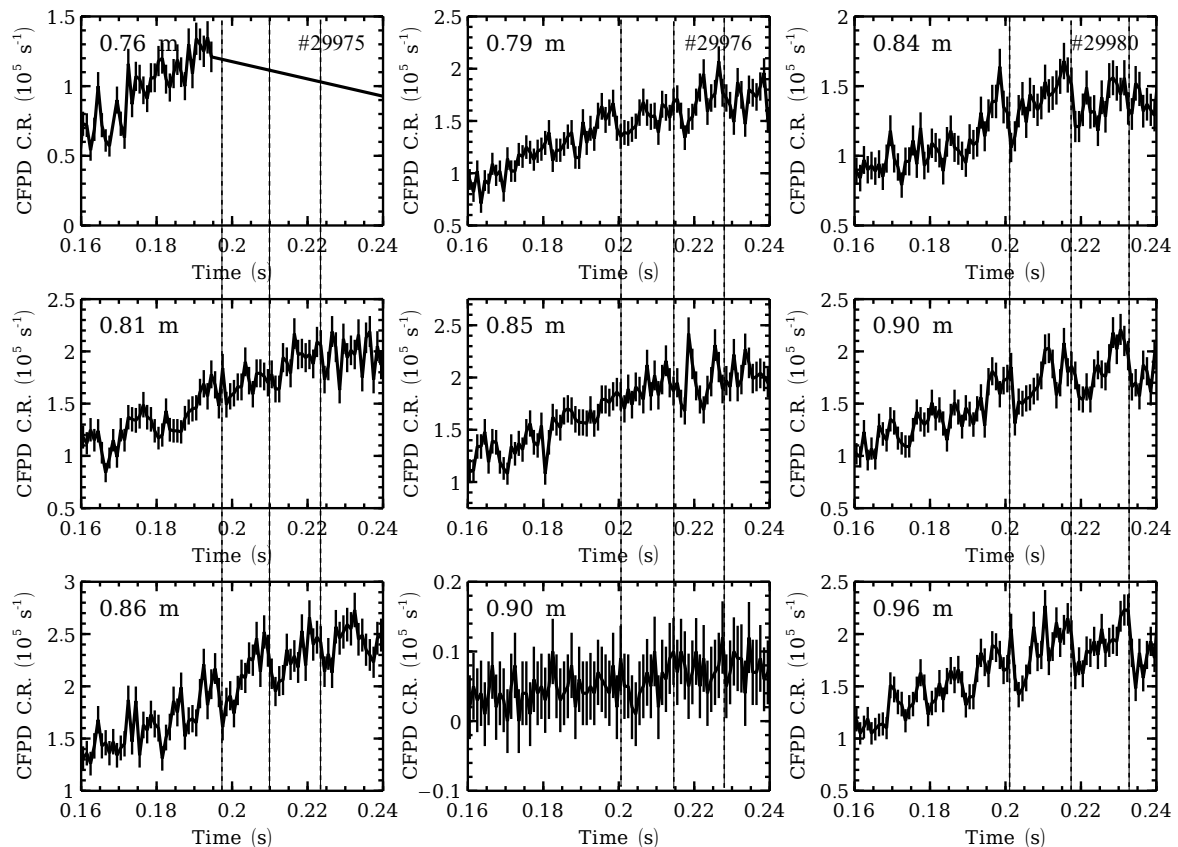


Figure 7.17: Time traces of data from the three operational channels of the CFPD during the large fishbones in shot #29975 *et seq.*. Each column includes data from a single shot, with dotted vertical lines marking the time at which the amplitude of each of the three largest fishbones reaches a maximum. The label in each panel indicates the midplane intersection radius of the centre of the bundle of fusion proton trajectories which reaches the detector. The magnetic axis is located at approximately  $R = 0.97$  m. The top-left and bottom-middle traces are affected by hardware failures which mean that no information can be derived from these data.

and FIDA diagnostic has allowed constraints to be placed on the effects of fishbones on the velocity-space distribution of FI; these modes are seen to affect high-energy, passing particles in the core of the plasma. Data from the prototype CFPD support the conclusion that fishbones have a strong impact on core FI confinement.

The following chapter presents results pertinent to *non-resonant* transport of FI in MAST. The focus is primarily on sawtooth reconnection events and on the LLM, but the effects of edge-localised modes (ELMs) and resonant magnetic perturbations (RMP) used to mitigate ELMs are also briefly considered.

# Chapter 8

## Effects of non-resonant MHD instabilities

### 8.1 Outline

Even when their drift orbits do not satisfy a resonance condition, FI can affect the stability of MHD modes as outlined in chapter 3. The current density and pressure profiles within the plasma are determined in part by the energetic-particle population, hence these particles can affect the stability of internal kink modes and ballooning modes. In this chapter, the effects of the LLM and the sawtooth crash on FI in MAST plasmas are investigated. TRANSP modelling is once again used to attempt to reproduce the FI diagnostic signals, providing additional insight beyond that derived from straightforward data analysis. The current status of an ongoing investigation into the effects of edge-localised modes (ELMs) and resonant magnetic perturbations (RMP) on FI is briefly summarised towards the end of the chapter. The main conclusions of this chapter are as follows:

- The LLM causes persistent radial redistribution of FI from the core towards the edge of the plasma for as long as the mode remains active.
- Sawteeth cause a rapid redistribution of FI across a broad region of the plasma extending beyond the sawtooth mixing radius.
- Experimental evidence, supported by transport modelling, suggests that sawteeth affect the passing FI in MAST more strongly than the trapped FI.
- No direct evidence has been found for FI redistribution caused by ELMs.
- In some cases, the application of RMP has a negative effect on FI confinement.

The novelty of the present analysis, compared to previous studies, lies once again in the hierarchical application of diagnostic constraints to the TRANSP modelling.

Several distinct models of LLM and sawtooth-induced FI redistribution are capable of reproducing the global neutron rate. In this chapter, shortcomings of each model are revealed when the transport modelling is confronted with NC and FIDA data. Some progress is made towards agreement between synthetic and measured data. It is the residual disagreement however which, by mandating further improvements in the modelling, demonstrates the strength of the multi-diagnostic approach.

We begin, as in the previous chapter, by presenting the sets of discharges selected for analysis.

## 8.2 Plasma Scenarios

The two sets of discharges studied in this chapter were both heated with a single neutral beam, in contrast to the high-NBI-power discharges analysed in the previous chapter. The FI population, and hence the neutron rate and FIDA signal, was much lower in each of these sets of discharges than in those studied in the previous chapter. The set analysed for the effects of the LLM consisted of shots #29924, #29928, #29929 and #29931. Each of these shots exhibited weak chirping mode activity during the early part of the discharge, with the transition to the LLM occurring at approximately  $t = 0.3$ s. Obtaining pronounced sawtooth oscillations in the absence of energetic-particle-driven MHD required a higher density and lower plasma current, reducing the FI population even further. Sawteeth were identified in shots #29879 – #29885. The evolution of several key variables during a representative discharge from each set is shown in fig. 8.1. The RMS Mirnov coil signal indicates a significant level of MHD activity in shot #29924, while very little such activity apart from the sawteeth is present in shot #29879. A spectrogram of the magnetic activity in the former discharge shows the characteristic series of fishbones leading into a saturated LLM at approximately  $t = 0.3$ s, as seen in fig. 8.2. Also shown in fig. 8.2 is the significant reduction in toroidal rotation frequency which was observed to accompany large-amplitude LLM in MAST.

As in the case of the chirping modes investigated in the previous chapter, the effects of sawteeth and the LLM on FI confinement in MAST were examined qualitatively in the recent *PP&CF* article by Ceconello *et al.* [78]. The present work serves to extend that study with additional transport modelling in which a wider range of models of enhanced FI transport have been explored. The extent to which these models have led to improvements in the agreement between synthetic and measured diagnostic signals is shown in the following two sections.

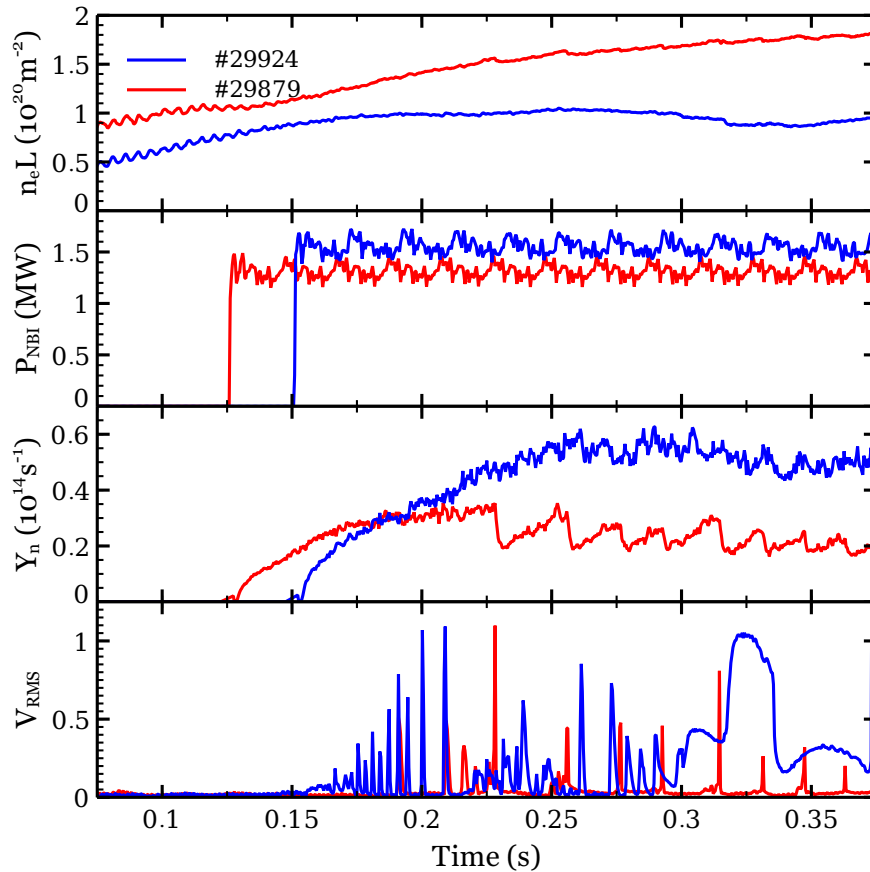


Figure 8.1: Global parameters of representative discharges from the two sets selected for analysis of the effects of the LLM and sawteeth. The first set consists of shots #29924, #29928, #29929 and #29931, and the second set includes shots #29879 – #29885. The panels show, from top to bottom: line-integrated electron density measured with a CO<sub>2</sub> laser interferometer; total injected NBI power; global neutron rate measured with the fission chamber; and RMS amplitude of an outboard-midplane Mirnov coil signal sensitive to changes in the poloidal field.

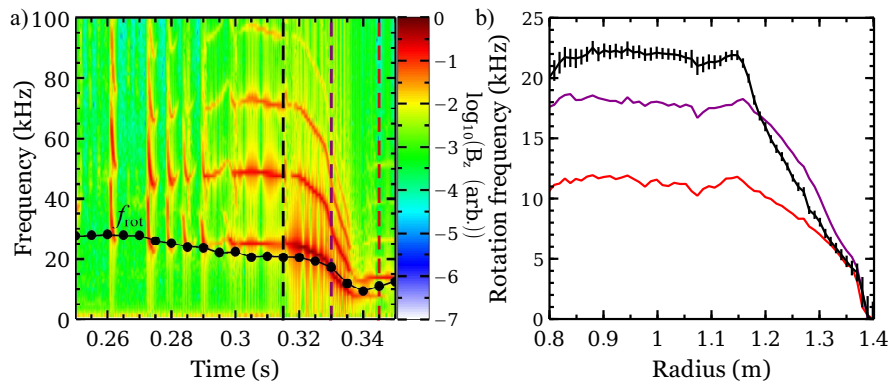


Figure 8.2: a) Spectrogram of an outboard-midplane Mirnov coil signal acquired during shot #29924. Black points mark the on-axis toroidal rotation frequency measured with the CXRS diagnostic. b) Profiles of toroidal rotation frequency measured with CXRS at the three times indicated by dashed vertical lines in panel (a).

## 8.3 LLM-induced redistribution

Discerning the effects of the LLM on the FI diagnostic signals is non-trivial due to the lack of a ‘reference’ time window with similar profiles of plasma parameters to those found during mode activity, but in the absence of the mode. The approach adopted in this analysis was to run a TRANSP simulation for the majority of the length of a discharge featuring a LLM, and to compare the match between synthetic and measured FI diagnostic signals obtained prior to LLM onset and during the LLM. Finding good agreement with the measured profiles at the former time but not at the latter allows the effects of the LLM to be isolated.

It was shown in the previous chapter that the effects of multiple chirping modes are well-represented on average by applying spatially-uniform anomalous diffusion to the FI in NUBEAM. The initial TRANSP simulation of shot #29924 was therefore carried out with spatially-uniform anomalous diffusion applied with a time-varying strength to match the global neutron rate. Figure 8.3 illustrates the good agreement between the modelled and measured global neutron rate, and between the profiles of NC and FIDA signals, during the early part of the discharge in which weak chirping TAE were active. While the agreement with the global neutron rate is preserved later in the discharge, during LLM activity, the agreement with the shape of the NC and FIDA profiles is seen to be significantly worse. Particularly notable is the significant

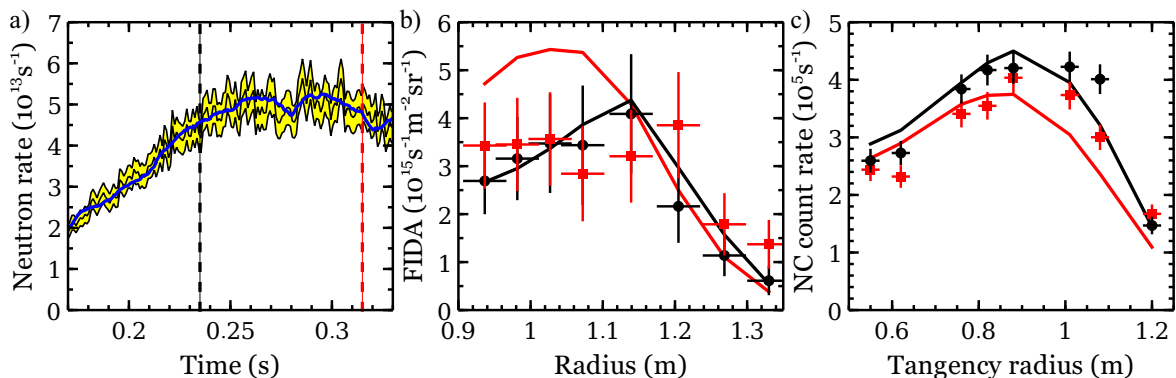


Figure 8.3: a) Time trace of the global neutron rate from shot #29924 (yellow shaded region indicating statistical uncertainty) and simulated rate using time-varying, spatially-uniform anomalous FI diffusion in TRANSP (blue trace). b) The signal from the toroidally-viewing FIDA chords, integrated in wavelength from 660.8 nm to 661.7 nm, acquired during shot #29924 at the two times indicated by the correspondingly-coloured dashed lines in panel (a). The FIDASIM-calculated profiles based on the associated NUBEAM FI distributions are overlaid. c) Measured profiles of the NC count rate obtained during the series of discharges #29924 *et seq.* at the two times indicated in panel (a). The LINE2-calculated profiles are overlaid.



overestimate of the FIDA signal in the core of the plasma during the LLM, with a corresponding underestimate at larger radii. This behaviour is less apparent in the NC count rate, possibly due to the line-integrated nature of the signal. One striking observation however is that the efficiency which must be assumed in order to minimise the sum of the squared residuals between measured and modelled NC profiles is much lower during the LLM than prior to the LLM. The efficiency factor used in plotting the red trace in panel (c) of fig. 8.3 is 0.81, whereas that used in plotting the red trace is 0.92. This 13% difference is close to the  $\sim 15\%$  limit in the uncertainty in the calculation caused by measurement uncertainties in the plasma parameters used as input to TRANSP [156]. Since the global neutron rate is reproduced equally well in the simulation at both timeslices, it therefore seems likely that some FI are redistributed from inside to outside the radial range covered by the NC scan performed during these discharges (0.55 m to 1.20 m). This is commensurate with the change observed in the FIDA profile, where the signal is depleted at  $R \lesssim 1.18$  m and enhanced at  $R \gtrsim 1.18$  m relative to the simulated profile.

As mentioned in the previous chapter, TRANSP allows spatially-varying anomalous diffusion and convection coefficients to be applied to the FI. It was previously found that using a ‘top hat’ diffusivity profile localised inside  $r/a \approx 0.5$  more accurately reproduced the effects of the LLM on the FIDA signal than did a spatially-uniform profile [72]. Although such a diffusivity profile was found in this case to provide a better match to the magnitude of the core FIDA signal than the uniform profile, a better match still was obtained by applying a radial convection to the FI in the region where the diffusivity gradient is steepest. The profiles of diffusivity and convection velocity which provided the best match between the modelled and measured profiles of FIDA radiance are shown in fig. 8.4. The magenta curve in panel (b) is seen clearly to provide a better match than the blue curve to the shape and magnitude of the measured profile. The same cannot however be said of the modelled NC count rate profile. No systematic improvement in agreement is obtained by applying radially-varying transport coefficients in this case. On the contrary, the magenta curve in panel (c) is seen to be flattened and shifted inward compared to the blue curve, whereas a higher degree of peakedness and an outward shift would improve the fit to the measured profile. This discrepancy between the indications of the two diagnostics suggests that substantial further work is needed to understand the nature of the FI transport caused by the LLM. First-principles physical models would aid in this regard.

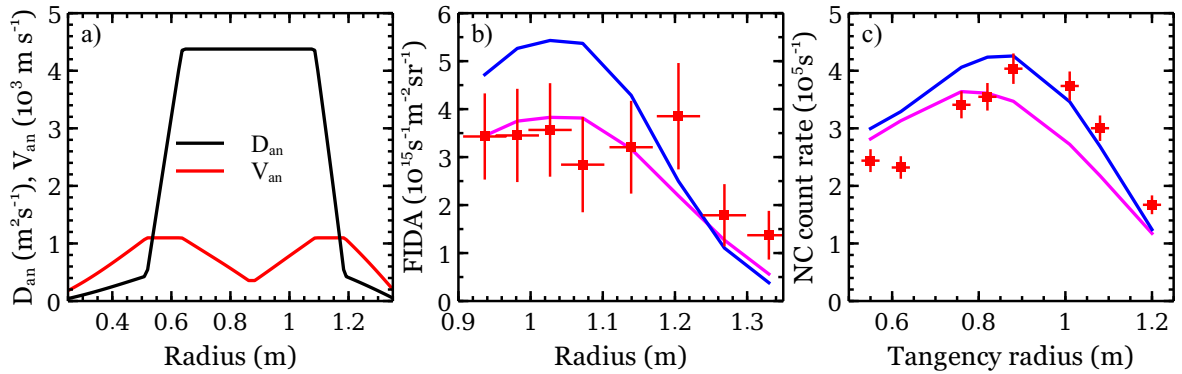


Figure 8.4: a) Profiles of anomalous diffusivity  $D_{an}$  and convection velocity  $V_{an}$  used during a TRANSP simulation of shot #29924 at  $t = 0.315$  s. These profiles were obtained by running TRANSP iteratively to provide agreement with the measured neutron rate and FIDA signal. The total neutron rate modelled using these profiles is within 5% of that modelled using spatially-uniform diffusivity. b) Profiles of FIDA radiance measured during shot #29924 at  $t = 0.315$  s compared to those modelled with spatially-uniform diffusivity (blue) and with the radially-varying profiles of  $D_{an}$  and  $V_{an}$  shown in panel (a) (magenta). Wavelength integration is as in panel (b) of fig. 8.3. c) Corresponding profiles of measured and modelled NC count rate, with an efficiency factor of 0.092 applied to the modelled profiles in both cases.

Orbit-following simulations with a non-axisymmetric MAST background equilibrium have been conducted by Pfefferlé and co-workers [67]. Profiles of FI density in the presence of a kink deformation were found to be depleted in the core and elevated towards the edge compared to those found in the axisymmetric case. These findings are consistent with the NC and FIDA observations shown here. The causes of the flattened FI density profile are found to be twofold [67]. Firstly, in the presence of a helical core, the magnetic axis is displaced outward in minor radius from its position in the axisymmetric equilibrium. This results in significant off-axis neutral beam deposition, since the beams are designed to deposit FI mostly on-axis in the axisymmetric case. Secondly, the deformed magnetic field leads to radial drifts which serve to reduce radial gradients in the FI distribution.

The results shown in this section illustrate the benefit of applying multiple diagnostics to the study of FI transport. Models of increasing complexity are challenged by FI diagnostics with resolution in real space and velocity space. Although consistency with the measured profiles from two of the diagnostics may readily be obtained, the modelling is revealed to be inadequate when confronted with data from a third diagnostic. A similar outcome applies in the case of sawtooth-induced FI redistribution, as discussed in the following section.

## 8.4 Sawtooth-induced redistribution

The profile of electron temperature is observed to be flattened across the core of the plasma after a sawtooth crash, as shown in chapter 3. Figure 8.5 shows that a significant reduction in CFPD and NC count rate, and in FIDA signal in the toroidally-viewing channels, also accompanies these events. The NC profiles show however that the reduction in neutron emission extends beyond the outermost radius at which the electron temperature is reduced by the sawteeth, implying that a redistribution of FI in real space, or a significant reduction in FI energy, occurs even at  $R > 1.2$  m. Similarly, the toroidally-viewing FIDA profiles suggest a redistribution of the passing FI as far out as  $R > 1.3$  m on the midplane. The electron temperature by contrast is reduced only at  $R < 1.2$  m on the outboard midplane and  $R > 0.7$  m on the inboard midplane. There is no strong evidence for a reduction in core FIDA signal in the vertically-viewing channels, suggesting a much weaker effect on the trapped and barely-passing FI than on the strongly-passing FI.

In panel (c) of fig. 8.5, two data points are seen to lie significantly below the others. This is indicative of a partial hardware failure in the CFPD; such a localised suppression of the fusion product emission is unphysical, given that it represents a fall-off in the emission with a radial scale length smaller than the typical FI Larmor radius. Both of these data points originate from a single discharge, #29884, suggesting that the hardware was not operating correctly during this shot. Data points from the other discharges however are fairly consistent with each other, showing a largely uniform emission profile over the radial range covered by the CFPD. The high density and low beam power in this set of discharges renders the FIDA signal subject to large statistical uncertainties, reflected by the size of the error bars in panels (e) and (f) of fig. 8.5. The effect of individual sawteeth on the FIDA signal cannot readily be seen in time traces of the signal from an individual shot; conditional averaging over many events, relying on the reproducibility of MAST discharges, is necessary in order to extract useful information from the FIDA data. Sixteen separate events from four discharges were used to obtain the average profiles in panel (e), while eight events from two discharges were used to generate the profiles in panel (f).

TRANSP was run for shot #29881 using an implementation of the Kadomtsev sawtooth model [185]. Initially developed to explain the occurrence of disruptive instabilities in plasma columns, whereby a part of the poloidal flux and stored energy are

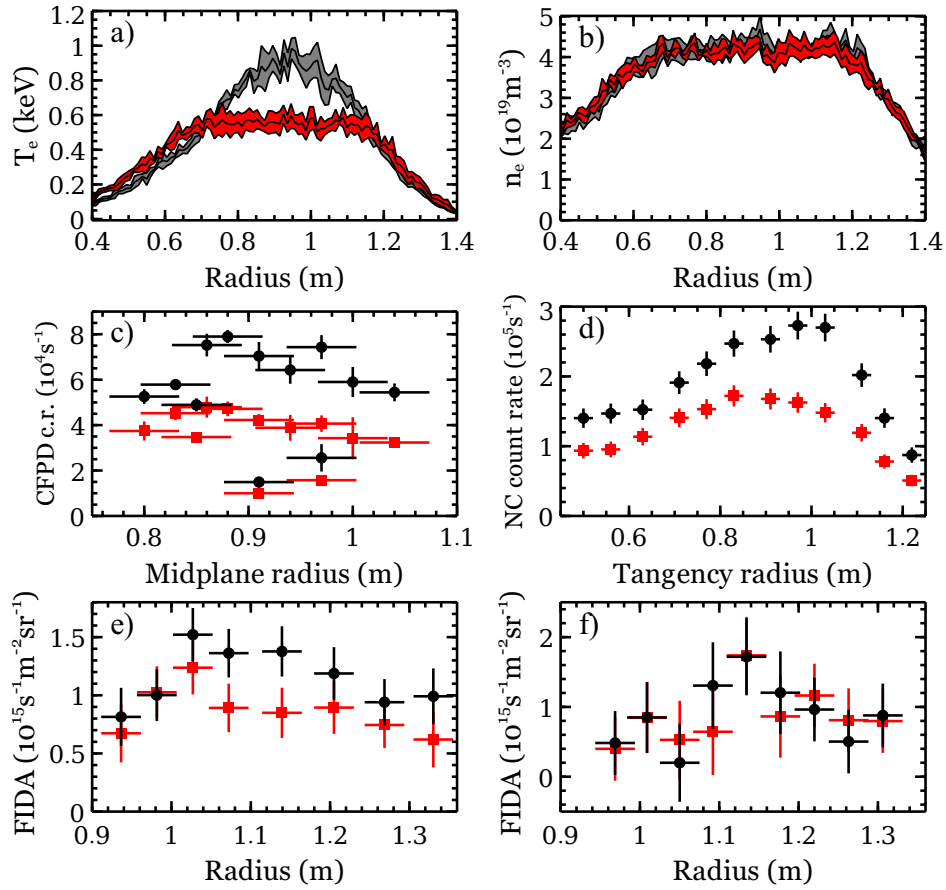


Figure 8.5: a) Averaged profiles of electron temperature before and after four sawteeth occurring during shot #29884. b) Averaged profiles of electron density before and after the same four sawteeth. c) Profiles of CFPD count rate as a function of the midplane intersection radius of the central orbit reaching the detector. The profiles are obtained by averaging over four sawteeth during three shots (#29879, #29884 and #29885); each point corresponds to data from a single CFPD channel acquired during a single shot. Black points show the pre-sawtooth profile, and red points show the post-sawtooth profile. d) Profiles of midplane NC signal averaged before and after four sawteeth from shots #29879 – #29885. e) FIDA radiance integrated from 660.6 nm to 661.7 nm acquired with the toroidally-viewing system during shots #29879 – #29882. Profiles are obtained by taking the average of the signal before and after four sawteeth in each shot. f) As panel (e), but for data acquired with the vertically-viewing FIDA system during shots #29884 and #29885 and integrated from 652.1 nm to 654.0 nm. Error bars on each profile represent statistical uncertainty. CFPD, NC and FIDA profiles are averaged over 3 ms in each case.

expelled from the plasma on a fast timescale, this model treats the sawtooth as an ‘internal disruption’ resulting from the nonlinear growth of the  $n = 1$  kink instability. The underlying mechanism behind the sawtooth is the reconnection of magnetic field lines of equal helicity on opposite sides of the  $q = 1$  surface. This leads to a relaxation of the current profile within the so-called *mixing radius* such that after the sawtooth,

$q \geq 1$  everywhere within the plasma. The mixing radius corresponds to the outermost flux surface at  $r_{\text{mix}} > r(q = 1)$  which, prior to the sawtooth, is matched by a flux surface with corresponding helicity at  $r < r(q = 1)$ . Typically this is a few centimetres outside the  $q = 1$  surface in MAST.

The sawtooth model within TRANSP allows the times of sawteeth to be specified in an input file. The internally-calculated equilibrium is adjusted at these times in order to flatten the current and pressure profiles within the mixing radius. FI are also redistributed such that their density within the mixing radius is spatially uniform after the sawtooth. Since FI-driven MHD activity was almost entirely absent from shot #29881, no additional anomalous FI diffusion was needed to obtain agreement with the measured global neutron rate. The results of the TRANSP and NUBEAM analysis are shown in fig. 8.6. Satisfactory agreement is obtained between the modelled and

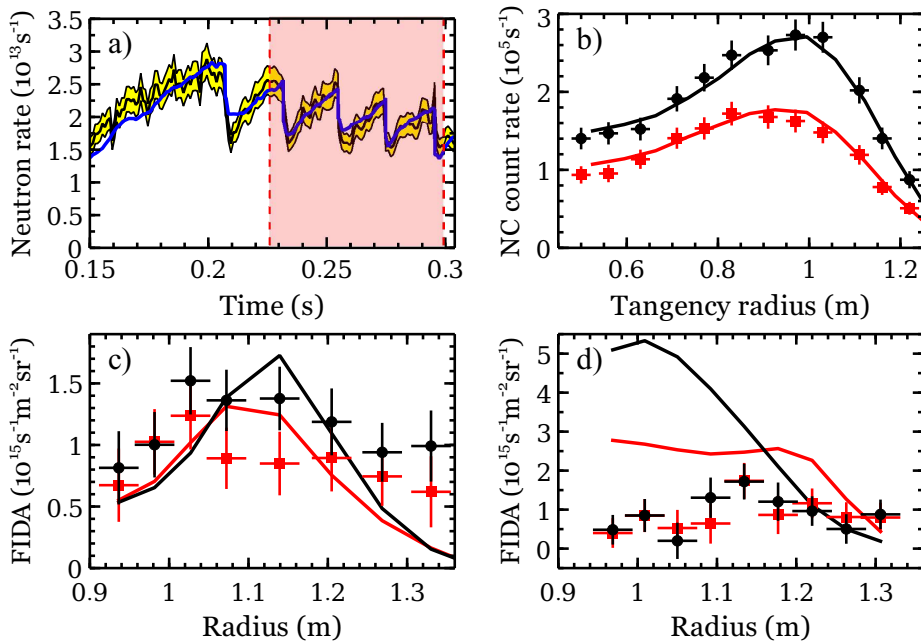


Figure 8.6: a) TRANSP-calculated global neutron rate (blue trace) compared to the measured neutron rate (yellow shaded region representing statistical uncertainty) during MAST shot #29881. Five sawteeth are seen to occur during the simulated time window. b) Average pre- and post-sawtooth NC count rate profiles calculated with the LINE2 code based on synthetic FI distributions before and after the four sawteeth occurring in the shaded region in panel (a). These are compared to the measured profiles averaged over four sawteeth per discharge from shots #29879 – #29885; the measured profiles are the same as those shown in fig. 8.5. c) Average profiles of pre- and post-sawtooth FIDA signal in the toroidally-viewing chords calculated with FIDASIM based on the same synthetic FI distributions as used in panel (b). These profiles are compared to the conditionally-averaged measured profiles which were shown in fig. 8.5. d) As panel (c), but for the vertically-viewing FIDA chords.

measured global neutron rate, local neutron emission and toroidal FIDA signal. The vertical FIDA signal shown in panel (d) however is overestimated by a factor of 4 in the core of the plasma. A possible reason for this discrepancy is the misalignment of in-vessel and ex-vessel fibres in the feedthrough from the vertically-viewing lenses. This source of systematic uncertainty was discussed in chapter 5; the removal and re-installation of the ex-vessel fibre assembly prior to the last experimental campaign may have significantly worsened the light throughput. Coating of the in-vessel lenses with contaminants during operations represents another possible source of deterioration. A failure of the CCD camera after the experimental campaign meant that no in-vessel calibration could be carried out for the vertically-viewing lenses, so this reduction in transmission cannot be quantified. Comparison of the measured bremsstrahlung to that calculated with FIDASIM supports the conclusion that the throughput of the vertical views had deteriorated significantly since the original calibration; the calculated line-integrated bremsstrahlung is approximately three times higher than the baseline of the measured spectrum in the core of the plasma, whereas that calculated for the toroidal views is in good agreement with the measurements. The bremsstrahlung calculation within FIDASIM has not been extensively validated however, so this finding is by no means conclusive. Despite the discrepancy in the absolute magnitude of the signal, information can still be drawn from the relative change in the signal caused by the sawteeth. The measured FIDA signal in the toroidal views is depleted across a larger radial range than predicted by the model, whereas no significant changes are observed in the FIDA signal in the vertical views. This suggests that the redistribution of passing FI is underestimated, and that of trapped FI is overestimated, by the Kadomtsev sawtooth model within TRANSP.

A strong effect of sawteeth on passing FI and a negligible effect on trapped FI was previously found in studies on the TEXTOR tokamak using the collective Thomson scattering diagnostic [164]. Measurements on DIII-D [186] and on ASDEX-Upgrade (AUG) [187] showed a stronger effect of sawteeth on toroidally-viewing than on vertically-viewing FIDA signals. In both cases, the simulated changes in signal using the Kadomtsev model within TRANSP underestimated the observed changes in both toroidal and vertical views. In contrast to the observations from MAST presented here however, a finite effect on the vertically-viewing FIDA signal was observed in DIII-D and AUG. This suggests that the effects of sawteeth on trapped FI in DIII-D and in AUG are stronger than in MAST or TEXTOR. The reason for this difference is unclear; certainly the

toroidal drift of trapped FI, which decouples them from the flux surfaces and renders them less susceptible to redistribution by MHD instabilities, is not solely responsible. TEXTOR had a stronger magnetic field than either AUG or DIII-D, whereas MAST had a much weaker field than those devices. TEXTOR and MAST operated with beam voltages only slightly lower than those in DIII-D and AUG. If the toroidal drift were responsible for decoupling trapped FI orbits from the helical flux surfaces created during the sawtooth evolution, this effect should be weaker in TEXTOR than in any of the other devices. It is not surprising however that the effect of sawteeth on trapped FI in MAST is seen to be so weak; an estimate of the critical energy above which the toroidal drift motion decouples trapped FI from the evolving flux surfaces, based on an expression given in the literature [188], yields  $E_c \lesssim 10$  keV. The minimum FI energy to which the measurements shown in panel (d) of fig. 8.6 is sensitive is approximately 9.6 keV. The Kadomtsev model in TRANSP cannot account for this energy threshold, and treats all FI equally as being mixed by the sawtooth. The effect of sawteeth on trapped FI is therefore expected to be significantly overestimated by this model.

## 8.5 Effects of RMP and ELMs

Data acquired during the 2013 experimental campaign formed the basis of an investigation into the effects of resonant magnetic perturbations (RMP) on FI in MAST [189]. RMP in MAST were applied with two sets of coils situated close to the outer edge of the plasma. The lower set consisted of twelve coils equally spaced toroidally, while the upper set consisted of six coils also with equal spacing between them. Each coil was oriented so as to perturb the edge of the plasma with a radial magnetic field, and the power supplies to each coil were configured to apply static perturbations with toroidal mode numbers  $n = 2, 3, 4$  or  $6$ . The coil configuration is illustrated in fig. 8.7. Application of RMP was found to be effective in mitigating the explosive growth of MHD instabilities known as edge-localised modes (ELMs) in MAST, in common with many other tokamaks [190].

It was found that, in at least two cases, RMP with a toroidal mode number  $n = 3$  caused a strong redistribution of FI from the core of the plasma. The plasma current in the pulses in question was 400 kA, so the confinement would be expected to be worse than in the other discharges studied in this and in the previous chapter. The pulses were run with a SND configuration, meaning that the beam deposition profile was relatively broad since the magnetic axis and midplane in this configuration are

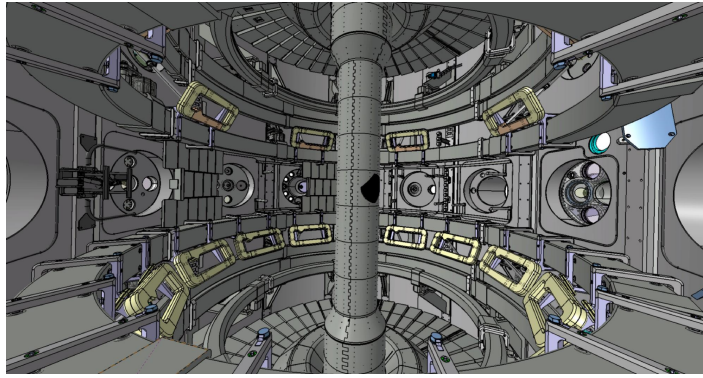


Figure 8.7: Rendering of the interior of the MAST vessel showing the ELM control coils (light yellow) used to apply RMP. Image credit: CCFE Drawing Office

displaced vertically from the neutral beam path. The edge of the plasma is closer to the lower ELM control coils in SND than in DND pulses, so the amplitude of the magnetic perturbation within the plasma should also be higher in this configuration. If RMP affected FI confinement, the effects would therefore be expected to be most noticeable in such discharges. A summary of a few key observations is shown in fig. 8.8. Very few pairs of shots were identified in which a ‘coils on’ discharge is matched with a similar ‘coils off’ discharge to allow a direct comparison of the effects of RMP on FI confinement. RMP usually cause a substantial reduction in bulk plasma confinement such that the electron density is lower, and the beam deposition profile consequently is different, from that obtained in the absence of RMP. This was not the case in shot #30086 however, which allowed the direct effects of the magnetic perturbations on FI confinement to be isolated. The neutron rate and core FIDA signal are seen to be substantially reduced during application of RMP until a back-transition from H-mode to L-mode causes the neutron rate and FIDA signal to recover due to the increased beam penetration in L-mode. Measurements with the CFPD, and with the NC in another pair of shots for which NC data are available, revealed similar behaviour. CFPD and NC traces are not shown here since the time evolution of those signals is very similar to that of the global neutron rate shown in panel (b) of fig. 8.8. The interested reader is referred to the recent publication of McClements *et al.* for further details [189].

No clear evidence has yet been found for an effect of unmitigated ELMs on FI confinement in MAST. Some ELMs in MAST were correlated with small sawtooth crashes, and the effects of sawteeth on FI confinement were identified in such cases. These combined sawtooth-ELM events seem moreover to be no more damaging to FI confinement than sawteeth alone, as seen in fig. 8.9. The main difficulty with



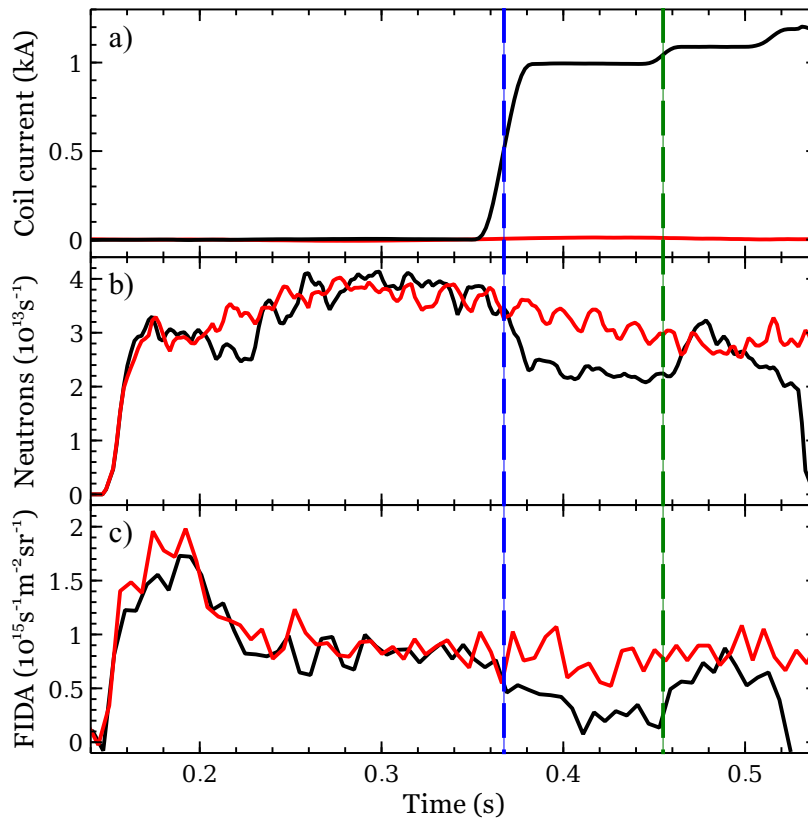


Figure 8.8: a) Time trace of the current in three of the lower ELM control coils in the MAST vessel during shots #30086 (black) and #30090 (red). The polarity of the coils was arranged to produce a  $n = 3$  perturbation in shot #30086. b) Global neutron rate measured during the same shots. The apparent dip in the neutron rate from 0.22 s to 0.24 s during shot #30086 arises because the second beam was switched on slightly later in that shot than in #30090. c) FIDA spectral radiance integrated from 661.3 nm to 661.6 nm in a channel with a beam intersection radius of 1.13 m. The corresponding  $E_{\min} = 58$  keV. The dashed blue line marks the midpoint of the ELM control coil ramp, while the dashed green line marks the time of a H-L back-transition in shot #30086.

attempting to isolate the effect of ELMs on FI confinement is that in all discharges with NBI in which ELMs were present, MHD activity was observed which was not necessarily correlated with the ELMs but which was observed to cause drops in the neutron rate and FIDA signal.

The apparent lack of an enhancement in FI transport when ELMs are correlated with sawteeth is in contrast to behaviour observed in DIII-D [191]. In that study, losses of FI were measured with thin-foil Faraday collectors at the outboard edge of the plasma. Losses were correlated primarily with ELMs but were observed to be larger when these ELMs coincided with core fishbone activity. Discharges were however identified in which ELMs did not cause a significant increase in FI losses, consistent with the observations on MAST reported here. It is moreover unclear whether the FI

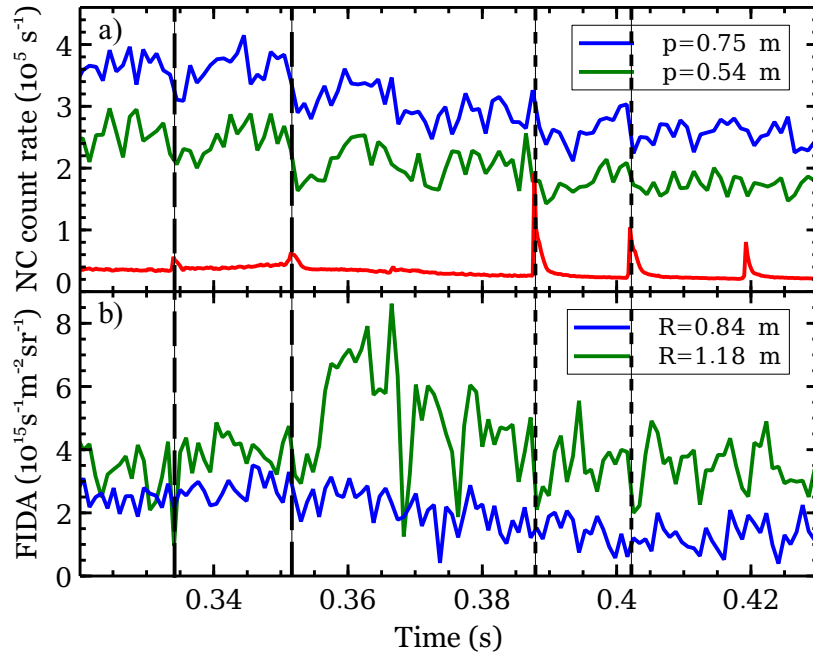


Figure 8.9: Time traces of data from several FI diagnostic channels during shot #30147 in which sawteeth, marked by dashed vertical lines, were observed in L-mode and sawtooth-triggered ELMs, marked by dotted vertical lines, were observed in H-mode. a) NC data from the two midplane channels. Also shown in red, in arbitrary units, is the trace from a  $D_\alpha$  monitor viewing the outboard edge of the plasma. b) Data from two channels of the toroidally-viewing FIDA system. Data are integrated from 660.8 nm to 661.3 nm. Note that this shot is in lower single-null (SND) configuration, so the FI observed here are approximately 21 cm to 24 cm above the midplane of the equilibrium.

losses associated with ELMs in DIII-D constituted a significant fraction of the total FI population, and hence whether such losses would be detectable with diagnostics of the confined FI population such as those used on MAST. FI losses correlated with ELMs were also observed in AUG, but again these losses were not quantified in terms of the proportion of the total FI population and no data from diagnostics of the confined FI were presented [192]. It seems, based on the observations from MAST, DIII-D and AUG, that FI losses caused by ELMs may be of concern in the context of the localised heat loads on structures in the vessel but that they are insignificant in the context of global confinement and heating.

## 8.6 Summary

Data from the fission chamber, neutron camera, CFPD and FIDA diagnostic have once again shown that MHD instabilities in MAST cause redistribution of FI. Transport modelling has been confronted with data from the suite of FI diagnostics on MAST. The models have been refined and some of their shortcomings have been revealed in

each case.

The long-lived internal kink mode causes a depletion of the FI density in the core of the plasma and an enhancement at the edge relative to the purely axisymmetric case. Attempts to reproduce this behaviour using spatially and temporally-varying anomalous transport coefficients in TRANSP modelling have so far been unsuccessful, matching the global neutron rate and the FIDA emission profile reasonably well while failing to account for the observed changes in the neutron emission profile.

Sawteeth are seen to have a strong effect on the FI confinement, with a collapse in FI density accompanying each sawtooth crash. FIDA data suggest that the effect on passing FI is stronger than on trapped FI, which is consistent with observations on other tokamaks. The Kadomtsev sawtooth model within TRANSP reproduces the changes in the neutron emission profile and accounts for the significant changes in toroidal FIDA signal, but significantly overestimates the changes in the vertical FIDA signal. This is likely due to the fact that this model does not account for the ‘critical energy’ above which trapped FI are decoupled from the evolving flux surfaces.

A recent investigation has uncovered strong evidence for the anomalous transport of FI in the presence of resonant magnetic perturbations, at least in cases where the FI confinement is expected to be particularly susceptible to such perturbations. No significant effect of ELMs on FI confinement has been found in MAST or in any other tokamak, although some FI losses have been found to be correlated with ELMs in DIII-D and AUG.

The following chapter concludes this thesis by summarising the strengths, shortcomings and possible future improvements of the experimental techniques and analysis tools used in this work. A final summary of the relevance of the main results to the ongoing development of experimental fusion devices is provided.

# Chapter 9

## Summary and conclusions

### 9.1 Outline

This chapter provides an assessment of the experimental techniques and analysis tools used in this research project. The contribution of each of these utilities to the study of FI transport is summarised, and limitations encountered during data acquisition and subsequent analysis are discussed. Improvements which could be implemented as part of the MAST-Upgrade project are suggested.

The main results are summarised, and the chapter concludes by placing these results in the context of the fusion research programme and exploring their implications for ITER.

### 9.2 Experimental techniques

#### 9.2.1 Fusion product diagnostics

The FC, NC and CFPD each provided insight into the temporal evolution of the FI population in MAST. The simplicity of the FC in providing a single, global measure of the neutron emission renders it extremely valuable as a tool with which to assess large-scale changes in the FI distribution. A reduction in the global neutron rate implies either a reduction in the mean FI energy, a redistribution of FI to regions of lower electron temperature or higher impurity concentration, or a loss of FI from the plasma. Examining the temporal correlation of such changes with the MHD activity allows various instabilities to be identified as being deleterious to FI confinement, although no information about the mechanism of FI redistribution in real space or velocity space may be obtained. The FC provides a useful constraint on transport modelling, since any model which fails to reproduce the measured global neutron rate can simply

be rejected from further consideration. We have seen in chapters 7 and 8 how the neutron rate can guide the choice of transport coefficients in modelling. The lack of any spatial sensitivity however means that the FC can only ever provide the lowest-order constraint on the validity of various transport models. Full calibration of the FC should nonetheless be a priority upon completion of MAST-Upgrade.

Although the NC installed on MAST had only two midplane channels and two channels looking below the midplane (one of which was not operational during the 2013 campaign), the repeatability of MAST discharges allowed neutron emission profiles to be obtained in any given scenario. Neutron emission profiles, integrated over the collimated fields of view of the detectors, provide a higher-order constraint than global neutron rate measurements on transport modelling. Improvements in absolute calibration of the diagnostic would however be advantageous. The dimensions of the collimators meant that the SNR was good, with statistical uncertainty contributing to a typical error bar of 10% of the count rate in each channel. Scattered neutrons, which added a spurious background signal to the measurements, were only problematic at tangency radii  $p \gtrsim 1.15$  m. The fast response of the liquid scintillator detectors was advantageous in minimising the pile-up and dead time for which the signal had to be compensated in post-processing. The NC designed for MAST-Upgrade will have at least eight LOS lying in the midplane, with the possibility of a similar number of diagonally-oriented LOS [76]. Improved detection efficiency would be desirable as it would allow neutron spectroscopy to be performed with reasonable temporal resolution, which could not be realised with the system on MAST.

As a prototype diagnostic, first results from the CFPD were fairly encouraging. Such diagnostics clearly have the potential to supplement the data provided by the NC, especially if the detector efficiency can be improved to allow shorter integration times. The principal difficulty confronting the use of the CFPD is the challenge of accurately reconstructing the orbits of fusion products to determine the possible location of their emission. Development of a synthetic diagnostic for use with TRANSP-calculated fusion product emission profiles should be prioritised. The system installed on MAST suffered from problems of reliability, with faults rendering the data from some channels unusable in several discharges. A further disadvantage of the system as used on MAST was the requirement that it be mounted on the reciprocating probe. This reduced the availability of the probe for its use with Langmuir probes for edge electron temperature

and plasma potential measurements. A dedicated CFPD, with more lines of sight, is being considered for NSTX-Upgrade and would also be a valuable addition to the suite of diagnostics on MAST-Upgrade.

### 9.2.2 The FIDA diagnostic

Reviewing the performance of the FIDA diagnostic on MAST, it must be concluded that such diagnostics are largely unsuitable for use on spherical tokamaks. The large drift orbit widths and Larmor radii of the FI, coupled with the high edge neutral density resulting from the open divertor and graphite plasma-facing components, meant that passive FIDA emission severely contaminated the signal in almost all cases. This contamination significantly reduced the radial range over which the measurements were usable, with passive FIDA often dominating the signal at  $R \gtrsim 1.25$  m. The detection of redistributed FI during transient MHD perturbations was significantly complicated by this contamination, with ‘spikes’ in passive FIDA masking the small changes in the active signal during such events. The use of a closed, cryo-pumped divertor on MAST-Upgrade will almost certainly mitigate this problem, but the large orbit widths will still render passive FIDA contamination a significant concern near the edge of the plasma. An improved choice of reference LOS would be beneficial.

Despite the limitations imposed by passive FIDA contamination, the analysis performed in this work has revealed changes in the FI distribution resulting from MHD instabilities in a wide range of operating scenarios. Assessment of the validity of FIDA data on a case-by-case basis has allowed the diagnostic to contribute to this study on an equal footing with the NC, which suffers from no such contamination. This approach is however labour-intensive, severely limiting the number of discharges which can be studied. The choice to focus primarily on fishbones, TAE, sawteeth and the LLM was made because, of all the instabilities observed in MAST, their effects are strongest and easiest to isolate.

The hardware employed in the FIDA diagnostic on MAST represented a reasonable compromise between performance requirements and budgetary constraints. In hindsight, the 0.3 ms readout time of the existing camera and the fast optics in the existing spectrometer are not strictly necessary for the effective exploitation of the diagnostic. All data analysed in this work were averaged over 0.9 ms or longer. Relaxing the requirement for fast readout would allow a larger CCD chip to be used, allowing the diagnostic to accommodate more channels and to monitor the toroidal and vertical

views simultaneously with full radial coverage. The priority before any such modification however would be to improve the light throughput from the vertically-viewing lenses. This could be achieved with the insertion of a periscope into the vessel, which would transmit the light through a vacuum window to an ex-vessel lens of a similar type to that used with the toroidally-viewing system. Such a development was envisaged for MAST-Upgrade, and two new ports were drilled in the vacuum vessel to accommodate these periscopes, but it is uncertain whether the precarious budgetary situation currently affecting the upgrade will allow them to be installed.

### 9.2.3 The MAST device

The increased discharge duration on MAST-Upgrade will provide a welcome opportunity to study phenomena in fully steady-state conditions, which were unattainable on MAST. Various components of the NBI system will be reconditioned and replaced to increase the available beam power and beam pulse length. The SW beam will be raised to an off-axis position, which will allow the FI distribution to be tailored to create either peaked, hollow or flat FI density profiles. Each of these changes promises to support a full FI-physics research programme once the Upgrade becomes operational. One capability which would significantly increase the usefulness of the NBI system is that of *beam notching*. Used on many other tokamaks, this would entail modulation of the beam voltage with a square wave on a timescale much shorter than the FI slowing-down time. Such a capacity would lend itself to improved background subtraction for beam-viewing diagnostics such as FIDA, and would also allow beam ions to be injected into the plasma as ‘test particles’ to establish the effects of non-FI-driven instabilities on these ions.

The main factor limiting the effective exploitation of MAST was a lack of manpower, and this looks set to affect the operation of MAST-Upgrade. In order to obtain the best possible results in any investigation, each diagnostic and each software tool should have a dedicated Responsible Officer with the time and the expertise to support its maintenance, operation, and the analysis of the data. Collaborations with researchers at external institutions will prove essential in maximising the output of the research programme. The FI-physics studies described in this work provide a model for such collaboration, with invaluable contributions from researchers at Uppsala University, Florida International University, the Max Planck Institute for Plasma Physics in Garching and the University of California, Irvine.

## 9.3 Analysis tools

Much of the analysis in this thesis has relied on EFIT equilibrium reconstruction, data mapping in MC<sup>3</sup>, and TRANSP simulation. Each of these processes is subject to uncertainties in several free parameters, and the effects of systematic errors in each process are strongly coupled.

### 9.3.1 Data preparation

The weights on different constraints and the parameters guiding spline fitting can make a significant difference to the results of equilibrium reconstruction. In one case, run as a sensitivity study, EFIT was found to converge on a solution within a wide range of values of many of these fitting parameters. The value of  $q_{\min}$  in the full range of such solutions varied by as much as  $\pm 0.1$  about the median value. While different equilibria were found not to affect the FI modelling in TRANSP to a measurable degree, such uncertainties may be problematic for MHD stability modelling. The stability and structure of Alfvén eigenmodes depends on the precise shape of the  $q$ -profile. A strong effort should be made to settle on a ‘canonical’ set of weights and constraints for EFIT. Bayesian models have previously been used to eliminate faulty or unreliable diagnostic measurements from the set of constraints [193]; further refinement and implementation of this technique would be advantageous.

Profiles of plasma parameters including  $n_e$ ,  $T_e$ ,  $T_i$  and  $\Omega_\phi$  are mapped onto the normalised minor radius of the plasma with the processing tool MC<sup>3</sup>. The data are fitted with splines to produce smooth profiles covering the radial range from the magnetic axis to the plasma boundary. Often, these profiles represent a compromise between smooth, physically realistic profiles and the fit to noisy TS or CXRS data. In addition, the choice to run TRANSP with a fixed, prescribed EFIT boundary means that the position of the boundary used in TRANSP does not always coincide with that inferred from density gradients measured with the TS diagnostic. This is particularly problematic in H-mode, where the density gradient at the edge of the plasma is large and an error of a few centimetres in the position of the boundary is significant. While the discharges analysed in this work did not present such difficulties, others require more care in the selection of a suitable equilibrium to allow self-consistent mapping of plasma profiles.

### 9.3.2 TRANSP modelling

The number of free parameters which may be adjusted in both TRANSP and NUBEAM is very large. In the context of the physical models used, choices must be



made regarding the plasma resistivity, the degree of electron-ion coupling, the impurity species, the neutral density external to the plasma, the bootstrap current fraction, the excited-states distribution of beam neutrals and the degree of current profile relaxation occurring at a sawtooth crash, to name but a few. Many of these choices are poorly constrained by experimental data, and the values of the parameters governing the models are based largely on historical consensus. A full study of the sensitivity of bulk plasma and FI transport to these parameters is far beyond the scope of this work. The success with which FI diagnostic data have been reproduced in many of the cases presented here suggests that the most important models have been used appropriately. The limited sensitivity studies which have been conducted as part of this project suggest that the values of several parameters relevant to FI physics do not strongly affect the observed outcome of the experiments. To cite two examples, the choice of excited-states beam deposition model was found to affect the global neutron rate and NC and FIDA profiles by less than 5%, and the degree of current mixing occurring at a sawtooth crash was found to make no difference to the global neutron emission.

A further source of uncertainty in the modelling is that derived from passing incorrect profiles of plasma parameters to TRANSP. A sensitivity study to changes in these profiles within the measurement uncertainty, performed by Klimek et al. [156], has shown clearly that such uncertainties cannot account for all of the observed discrepancies between measured and modelled neutron emission. The results of that study therefore support the conclusion that a significant degree of MHD-induced FI transport occurred in many MAST discharges. The uncertainties in modelled neutron and FIDA emission resulting from plasma profile measurement errors are nonetheless significant, as shown in this work and also in recent modelling of AUG discharges [194].

One of the most promising recent developments in the modelling of FI transport with NUBEAM concerns a ‘reduced’ model for the effects of resonant MHD modes [195]. Such a model depends upon calculations from first principles of the changes in constants of motion due to the wave-particle interaction. The probability density function of the magnitude of these ‘kicks’ in  $E$ ,  $P_\phi$  and  $\mu$  is used to derive transport coefficients which may be applied within NUBEAM. Because the changes in these constants of motion are found to scale almost linearly with the mode amplitude, a proxy for the mode amplitude as a function of time may be used to scale the magnitude of the transport coefficients. Preliminary tests of this model for the case of NSTX have shown encouraging results.

## 9.4 Conclusions and contextual discussion

The results presented in this work are divided into those pertaining to TAE and fishbones, considered as instabilities which engage in a resonant interaction with the FI, and those pertaining to sawteeth, the LLM, RMP and ELMs, which cause non-resonant FI redistribution. The main conclusions about the resonant redistribution, supported by the analysis in chapter 7, are as follows:

- Drops in both FIDA and NC signals are correlated with chirping TAE and fishbones at a statistically significant level, indicating a reduction of the confined FI density.
- Chirping TAE and fishbones cause enhanced losses of FI from the plasma.
- The profiles of NC and FIDA signals in quiescent periods between bursts of MHD activity are well modelled by applying anomalous diffusion to the FI in NUBEAM.
- Fishbones strongly affect the high-energy, passing FI population in a manner which may be reproduced with some success using the fishbone model in NUBEAM.

Chapter 8 presented analysis of the effects of non-resonant instabilities. This analysis supports the following main conclusions:

- The LLM causes persistent radial redistribution of FI from the core toward the edge of the plasma for as long as the mode remains active.
- Sawteeth cause a rapid redistribution of FI across a broad region of the plasma extending beyond the sawtooth mixing radius.
- Experimental evidence, supported by transport modelling, suggests that sawteeth affect the passing FI in MAST more strongly than the trapped FI.
- No direct evidence has been found for FI redistribution caused by ELMs.
- In some cases, the application of RMP has a negative effect on FI confinement.

Predictive modelling of the linear and quasilinear MHD stability of ITER plasmas is now well-advanced [196]. The implications for transport of FI, including both beam ions and fusion  $\alpha$ -particles, appear at this stage to be favourable. No global modes have been found which are expected to jeopardise FI confinement significantly. The possibility that in some scenarios the overlapping of multiple resonances could lead to TAE ‘avalanches’ similar to those observed in present-day experiments has not however been excluded. On the basis of the modelling performed in this study, we would then expect the FI distribution to relax to that obtained in the presence of spatially-uniform

anomalous diffusion.

A further concern is that EPM could be driven unstable by the FI pressure in ITER. No first-principles kinetic modelling of the stability of ITER plasmas to these modes has yet been conducted. This is in spite of extensive theoretical exploration of the relevant physics [197], and some recent progress towards the development of the required computational tools [198]. Being a conventional large-aspect-ratio tokamak, ITER would be expected to exhibit fairly weak trapped-particle-driven fishbones similar to those observed in JET [199] and AUG [181]. The virulent passing-particle-driven EPM observed in MAST and NSTX should not present a problem for ITER. This study nonetheless illustrates the importance of considering all possible resonant instabilities, including those such as passing-particle fishbones and off-axis fishbones [200] which do not often receive attention.

Observations of FI redistribution during the LLM offer the chance to validate the latest 3D orbit-following models [67]. The fact that the structure of the perturbation remains static, and the mode changes in amplitude very little over a fast-ion thermalisation time, significantly reduces the complexity of the modelling. The same can be said of promising recent developments in simulating the effects of RMP on FI in MAST [201], with the distinction that this modelling may be directly relevant to ITER since ITER will use ELM control coils. In both cases, the integration of synthetic FI diagnostics into these simulations should be a priority.

The limitations of the naive mixing model applied to FI within NUBEAM to represent the effects of sawteeth have been shown. Understanding the effects of these modes requires the decoupling between trapped FI orbits and perturbed flux surfaces to be taken into account. In a similar vein to the modelling of the effects of the LLM, orbit-following codes should be able to reproduce the effects of the evolving magnetic topology on the confinement of FI. The key difference in the case of the sawtooth is the fundamentally time-varying nature of the perturbation, which imposes stricter requirements on the resolution of the model than apply in the case of a static internal kink. Following the theoretical background laid down by Kolesnichenko *et al.* [188], significant progress in modelling these effects has been made by Jaulmes and co-workers [202].

Finally, we note that fast ions produced by auxiliary heating systems can offer only a fairly poor simulacrum of fusion  $\alpha$ -particles. Energetic-particle physics promises to remain at the fore as fusion research enters the burning plasma regime.

# Bibliography

- [1] International Energy Agency. World Energy Outlook 2014.
- [2] Rajendra K Pachauri et al. IPCC Climate Change 2014: Synthesis Report.
- [3] Frank Umbach. <http://www.nato.int/docu/review/2014/nato-energy-security-running-on-empty/Ukrainian-conflict-Russia-annexation-of-Crimea/EN/index.htm>, accessed 06/05/2015.
- [4] N Chapman and C McCombie. *Principles and Standards for the Disposal of Long-lived Radioactive Wastes*. Elsevier Science Ltd., Oxford, 2003.
- [5] L T Cox, Jr, F B Mead and C K Choi. Thermonuclear reaction listing with cross-section data for four advanced reactions. *Fusion Technol.*, 18:325–339, 1990.
- [6] B Nayak. Reactivities of neutronic and aneutronic fusion fuels. *Ann. Nucl. Energy*, 60:73–77, 2013.
- [7] J D Lawson. Some Criteria for a Power Producing Thermonuclear Reactor. *Proc. Phys. Soc. B*, 70(1):6–10, 1957.
- [8] E Rebhan and G Van Oost. Thermonuclear burn criteria. *Fusion Sci. Technol.*, 45:15–23, 2004.
- [9] D Maisonnier et al. Power plant conceptual studies in Europe. *Nucl. Fusion*, 47(11):1524–1532, 2007.
- [10] <https://www.iter.org/proj/iterandbeyond>, accessed 10/04/2015.
- [11] B B Kadomtsev and V D Shafranov. Magnetic plasma confinement. *Sov. Phys. Uspekhi*, 26(3):207–227, 1983.
- [12] Jeffrey P Freidberg. *Ideal MHD*. Cambridge University Press, Cambridge, 2014.
- [13] H Grad and H Rubin. Hydromagnetic Equilibria and Force-Free Fields. In *Proc. 2nd UN Intl. Conf. Peac. Uses At. Energy* P/386, 1958.
- [14] F Najmabadi et al. The ARIES-AT advanced tokamak, Advanced technology fusion power plant. *Fusion Eng. Des.*, 80:3–23, 2006.
- [15] K Tobita et al. SlimCS—compact low aspect ratio DEMO reactor with reduced-size central solenoid. *Nucl. Fusion*, 47(8):892–899, 2007.
- [16] V P Smirnov. Tokamak foundation in USSR/Russia 1950–1990. *Nucl. Fusion*, 50:014003, 2010.
- [17] A Sykes. Physics of spherical tokamaks. *Tech. Phys.*, 44(9):1047–1053, 1999.

- 
- [18] B Lloyd et al. MAST and the impact of low aspect ratio on tokamak physics. *Plasma Phys. Control. Fusion*, 46(12B):B477–B494, 2004.
- [19] F Wagner et al. Regime of Improved Confinement and High Beta in Neutral-Beam-Heated Divertor Discharges of the ASDEX Tokamak. *Phys. Rev. Lett.*, 49(19):1408–1412, 1982.
- [20] [http://www.ipp.mpg.de/3850444/w7x\\_15](http://www.ipp.mpg.de/3850444/w7x_15), accessed 15/04/2015.
- [21] R Lorenzini et al. Self-organized helical equilibria as a new paradigm for ohmically heated fusion plasmas. *Nat. Phys.*, 5(8):570–574, 2009.
- [22] J S Sarff et al. Overview of results from the MST reversed field pinch experiment. *Nucl. Fusion*, 53:104017, 2013.
- [23] F C Jahoda, E M Little, W E Quinn, G A Sawyer and T F Stratton. Continuum Radiation in the X Ray and Visible Regions from a Magnetically Compressed Plasma (Scylla). *Phys. Rev.*, 119(3):843–860, 1960.
- [24] R A Dandl, A C England, W B Ard, H O Eason, M C Becker and G M Haas. Properties of a high-beta plasma produced by electron-cyclotron heating. *Nucl. Fusion*, 4:344–353, 1964.
- [25] R J Buttery et al. Stability at high performance in the MAST spherical tokamak. *Nucl. Fusion*, 44(9):1027–1035, September 2004.
- [26] M Cecconello et al. Impurity transport driven by fishbones in MAST. *Nucl. Fusion*, 55:032002, 2015.
- [27] S V Mirnov. A probe method for measuring the displacement of the current channel in cylindrical and toroidal discharge vessels. *J. Nucl. Energy Part C*, 7:325–334, 1965.
- [28] M J Hole, L C Appel and R Martin. A high resolution Mirnov array for the mega ampere spherical tokamak. *Rev. Sci. Instrum.*, 80(12):123507, 2009.
- [29] T H Stix. Radiation and absorption via mode conversion in an inhomogeneous collision-free plasma. *Phys. Rev. Lett.*, 15(23):878–882, 1965.
- [30] M Porkolab, S Bernabei, W M Hooke and R W Motley. Observation of Parametric Instabilities in Lower-Hybrid Radio-Frequency Heating of Tokamaks. *Phys. Rev. Lett.*, 38(5):230–234, 1977.
- [31] V N Budnikov and M A Irzak. Mechanism of ion and electron LH heating on the FT-2 tokamak. *Plasma Phys. Control. Fusion*, 38:A135–A147, 1996.
- [32] J G Cordey et al. Neutral injection heating of a tokamak plasma: Theory and experiment. *Nucl. Fusion*, 15:441–451, 1975.
- [33] T H Stix. Heating of toroidal plasmas by neutral injection. *Plasma Phys.*, 14:367–384, 1972.
- [34] J D Strachan et al. Fusion neutron production during deuterium neutral-beam injection into the PLT tokamak. *Nucl. Fusion*, 21(1):67–81, 1981.

- [35] JET Team. Fusion energy production from a deuterium-tritium plasma in the JET tokamak. *Nucl. Fusion*, 32(2):187–203, 1992.
- [36] H Nakamura et al. Helium Ash Exhaust Studies with Core Fueling by a Helium Beam: L-Mode Divertor Discharges with Neutral-Beam Heating in the JT-60 Tokamak. *Phys. Rev. Lett.*, 67(19):2658–2661, 1991.
- [37] M Mantsinen et al. Alpha-Tail Production with Ion-Cyclotron-Resonance Heating of  $^4\text{He}$ -Beam Ions in JET Plasmas. *Phys. Rev. Lett.*, 88(10):105002, February 2002.
- [38] T H Stix. Fast-wave heating of a two-component plasma. *Nucl. Fusion*, 15(5):737–754, October 1975.
- [39] H Takahashi et al. Ion Heating in ATC Tokamak in the Ion-Cyclotron Range of Frequencies. *Phys. Rev. Lett.*, 39(1):31–34, 1977.
- [40] D Q Hwang et al. Heating of Plasma Ions in a Tokamak by the Second-Harmonic Ion-Cyclotron Resonance Interaction with Radio-Frequency Waves. *Phys. Rev. Lett.*, 51(20):1865–1868, 1983.
- [41] D F H Start et al. Bulk ion heating with ICRH in JET DT plasmas. *Nucl. Fusion*, 39(3):321–336, March 1999.
- [42] John Wesson. *Tokamaks*. Oxford University Press, Oxford, 3rd edition, 2004.
- [43] K G McClements. Full orbit computations of ripple-induced fusion  $\alpha$ -particle losses from burning tokamak plasmas. *Phys. Plasmas*, 12(7):072510, 2005.
- [44] R G Littlejohn. Variational principles of guiding centre motion. *J. Plasma Phys.*, 29(1):111–125, 1983.
- [45] Weston M. Stacey. *Fusion Plasma Physics*. Wiley-VCH, Berlin, 2nd edition, 2012.
- [46] J Carlsson. Breakdown of adiabatic invariance in spherical tokamaks. *Phys. Plasmas*, 8:4725, 2001.
- [47] E V Belova, N N Gorelenkov and C Z Cheng. Self-consistent equilibrium model of low aspect-ratio toroidal plasma with energetic beam ions. *Phys. Plasmas*, 10(8):3240, 2003.
- [48] D Boucher et al. The International Multi-Tokamak Profile Database. *Nucl. Fusion*, 40(12):1955–1981, 2000.
- [49] L Spitzer. *Physics of Fully Ionized Gases*. Interscience Publishers, University of Michigan, 2nd edition, 1962.
- [50] J D Huba. *NRL Plasma Formulary*. Naval Research Laboratory, Washington, D.C., 2011.
- [51] J G Cordey and W G F Core. Energetic particle distribution in a toroidal plasma with neutral injection heating. *Phys. Fluids*, 17(8):1626–1630, 1974.
- [52] D L Jassby. Neutral-beam-driven tokamak fusion reactors. *Nucl. Fusion*, 17(2):309–365, 1977.

- 
- [53] D Anderson, L G Eriksson and M Lisak. Analytical treatment of the distortion of velocity distributions in the presence of ICRH. *Nucl. Fusion*, 25(12):1751–1760, 1985.
- [54] J A Rome, D G McAlees, J D Callen and R H Fowler. Particle-orbit loss regions and their effects on neutral-injection heating in axisymmetric tokamaks. *Nucl. Fusion*, 16(1):55–66, 1976.
- [55] M R Tournianski, R J Akers, P G Carolan and D L Keeling. Anisotropic fast neutral particle spectra in the MAST spherical tokamak. *Plasma Phys. Control. Fusion*, 47(5):671–684, May 2005.
- [56] V A Yavorskij, D Darrow, V Ya Goloborod'ko, S N Reznik, U Holzmueller-Steinacker, N Gorelenkov and K Schoepf. Fast ion non-adiabaticity in spherical tokamaks. *Nucl. Fusion*, 42:1210–1215, 2002.
- [57] M Garcia-Muñoz et al. Fast-ion transport induced by Alfvén eigenmodes in the ASDEX Upgrade tokamak. *Nucl. Fusion*, 51(10):103013, October 2011.
- [58] X Chen et al. Prompt non-resonant neutral beam-ion loss induced by Alfvén eigenmodes in the DIII-D tokamak. *Nucl. Fusion*, 53(12):123019, December 2013.
- [59] A Bortolon, W W Heidbrink, G J Kramer, J K Park, E D Fredrickson, J D Lore and M Podestà. Mitigation of Alfvén Activity in a Tokamak by Externally Applied Static 3D Fields. *Phys. Rev. Lett.*, 110(26):265008, June 2013.
- [60] S D Pinches et al. The role of energetic particles in fusion plasmas. *Plasma Phys. Control. Fusion*, 46:B187–B200, 2004.
- [61] A W Morris et al. The role of the spherical tokamak in clarifying tokamak physics. *Plasma Phys. Control. Fusion*, 41:B191–B207, 1999.
- [62] R J Akers et al. Neutral beam heating in the START spherical tokamak. *Nucl. Fusion*, 42:122–135, 2002.
- [63] R J Akers, E Verwichte, T J Martin, S D Pinches and R Lake. GPGPU Monte Carlo Calculation of Gyro-Phase Resolved Fast Ion and n-State Resolved Neutral Deuterium Distributions. In *Proc. 39th Eur. Phys. Soc. Conf. Plasma Phys.* P5.088, 2012.
- [64] S D Pinches, H L Berk, M P Gryaznevich and S E Sharapov. Spectroscopic determination of the internal amplitude of frequency sweeping TAE. *Plasma Phys. Control. Fusion*, 46:S47–S57, 2004.
- [65] A B Mikhailovskii, G T A Huysmans, W O K Kerner and S E Sharapov. Optimisation of computational MHD normal-mode analysis in tokamaks. *Plasma Phys. Reports*, 27:844, 1997.
- [66] S D Pinches et al. The HAGIS self-consistent nonlinear wave-particle interaction model. *Comput. Phys. Commun.*, 111(1-3):133–149, June 1998.
- [67] D Pfefferlé, J P Graves, W A Cooper, C Misev, I T Chapman, M Turnyanskiy and S Sangaroon. NBI fast ion confinement in the helical core of MAST hybrid-like plasmas. *Nucl. Fusion*, 54(6):064020, June 2014.

- [68] S D Pinches et al. TH/P3-34: Development of a Predictive Capability for Fast Ion Behaviour in MAST. In *Proc. 24th IAEA Fusion Energy Conf. TH/P3-34*, 2012.
- [69] M P Gryaznevich and S E Sharapov. Perturbative and non-perturbative modes in START and MAST. *Nucl. Fusion*, 46(10):S942–S950, October 2006.
- [70] L C Appel, T Fülöp, M J Hole, H M Smith, S D Pinches and R G L Vann. Compressional Alfvén Eigenmodes on MAST. *Plasma Phys. Control. Fusion*, 50(11):115011, November 2008.
- [71] M Cecconello et al. A neutron camera system for MAST. *Rev. Sci. Instrum.*, 81(10):10D315, October 2010.
- [72] C A Michael et al. Dual view FIDA measurements on MAST. *Plasma Phys. Control. Fusion*, 55(9):095007, September 2013.
- [73] M Cecconello, S Sangaroon, M Turnyanskiy, S Conroy, I Wodniak, R J Akers and G Ericsson. Observation of fast ion behaviour with a neutron emission profile monitor in MAST. *Nucl. Fusion*, 52(9):094015, September 2012.
- [74] O M Jones et al. Fast-ion deuterium alpha spectroscopic observations of the effects of fishbones in the Mega-Ampere Spherical Tokamak. *Plasma Phys. Control. Fusion*, 55(8):085009, August 2013.
- [75] M. Turnyanskiy et al. Measurement and control of the fast ion redistribution on MAST. *Nucl. Fusion*, 53(5):053016, May 2013.
- [76] M Cecconello et al. The 2.5MeV neutron flux monitor for MAST. *Nucl. Instruments Methods Phys. Res. Sect. A Accel. Spectrometers, Detect. Assoc. Equip.*, 753:72–83, July 2014.
- [77] R V Perez et al. Investigating fusion plasma instabilities in the Mega Amp Spherical Tokamak using mega electron volt proton emissions (invited). *Rev. Sci. Instrum.*, 85(11):11D701, November 2014.
- [78] M Cecconello et al. Energetic ion behaviour in MAST. *Plasma Phys. Control. Fusion*, 57(1):014006, January 2015.
- [79] D L Keeling et al. Mitigation of MHD induced fast-ion redistribution in MAST and implications for MAST-Upgrade design. *Nucl. Fusion*, 55(1):013021, 2015.
- [80] A B Mikhailovskii. Thermonuclear "drift" instabilities. *Sov. Phys. JETP*, 41(5):890–894, 1975.
- [81] M N Rosenbluth and P H Rutherford. Excitation of Alfvén waves by high-energy ions in a tokamak. *Phys. Rev. Lett.*, 34(23):1428–1431, 1975.
- [82] D J Sigmar and H C Chan. Anomalous alpha-particle transport in thermonuclear tokamak plasma. *Nucl. Fusion*, 18(11):1569–1581, 1978.
- [83] K T Tsang, D J Sigmar and J C Whitson. Destabilization of low mode number Alfvén modes in a tokamak by energetic or alpha particles. *Phys. Fluids*, 24(8):1508–1516, 1981.



- 
- [84] K McGuire et al. Study of high-beta magnetohydrodynamic modes and fast-ion losses in PDX. *Phys. Rev. Lett.*, 50(12):891–895, 1983.
- [85] R B White, R J Goldston, K McGuire, A H Boozer and D A Monticello. Theory of mode-induced beam particle loss in tokamaks. *Phys. Fluids*, 26(10):2958–2965, 1983.
- [86] L Chen, R B White and M N Rosenbluth. Excitation of Internal Kink Modes by Trapped Energetic Beam Ions. *Phys. Rev. Lett.*, 52(13):1122–1125, 1984.
- [87] H H Duong, W W Heidbrink, E J Strait, T W Petrie, R Lee, R A Moyer and J G Watkins. Loss of energetic beam ions during TAE instabilities. *Nucl. Fusion*, 33(5):749–765, 1993.
- [88] W W Heidbrink. Basic physics of Alfvén instabilities driven by energetic particles in toroidally confined plasmas. *Phys. Plasmas*, 15(5):055501, 2008.
- [89] R Betti and J P Freidberg. Destabilization of the internal kink by energetic circulating ions. *Phys. Rev. Lett.*, 70(22):3428–3430, 1993.
- [90] E Fredrickson, L Chen and R White. Bounce precession fishbones in the national spherical torus experiment. *Nucl. Fusion*, 43(10):1258–1264, October 2003.
- [91] Ya I Kolesnichenko, V V Lutsenko and V S Marchenko. Fishbone Mode in Spherical Tokamaks. *Phys. Rev. Lett.*, 82(16):3260–3263, April 1999.
- [92] E D Fredrickson et al. Wave driven fast ion loss in the National Spherical Torus Experiment. *Phys. Plasmas*, 10(7):2852, 2003.
- [93] M P Gryaznevich and S E Sharapov. Beta-dependence of energetic particle-driven instabilities in spherical tokamaks. *Plasma Phys. Control. Fusion*, 46(7):S15–S29, July 2004.
- [94] X Q Wang, R B Zhang, L Qin and X G Wang. Non-resonant fishbone instabilities of  $q \min \gtrsim 1$  in tokamak plasmas with weakly reversed magnetic shear. *Plasma Phys. Control. Fusion*, 56(9):095013, September 2014.
- [95] C T Hsu, C Z Cheng, P Helander, D J Sigmar and R White. Particle Dynamics in Chirped-Frequency Fluctuations. *Phys. Rev. Lett.*, 72(16):2503–2507, 1994.
- [96] R Vann, H Berk and A Soto-Chavez. Strongly Driven Frequency-Sweeping Events in Plasmas. *Phys. Rev. Lett.*, 99(2):025003, July 2007.
- [97] R Gajewski. Magnetohydrodynamic Waves in Wave Guides. *Phys. Fluids*, 2(6):633–641, 1959.
- [98] C Uberoi. Alfvén waves in inhomogeneous magnetic fields. *Phys. Fluids*, 15(9):1673–1675, 1972.
- [99] K Appert, R Gruber and J Vaclavik. Continuous spectra of a cylindrical magnetohydrodynamic equilibrium. *Phys. Fluids*, 17(7):1471–1472, 1974.
- [100] J Tataronis and W Grossmann. Decay of MHD waves by phase mixing. *Zeitschrift fur Phys.*, 261:203–216, 1973.

- [101] L Chen and A Hasegawa. Plasma heating by spatial resonance of Alfvén wave. *Phys. Fluids*, 17(7):1399–1403, 1974.
- [102] A Hasegawa and L Chen. Kinetic Process of Plasma Heating Due to Alfvén Wave Excitation. *Phys. Rev. Lett.*, 35(6):370–373, 1975.
- [103] D A D’Ippolito and J P Goedbloed. Mode coupling in a toroidal, sharp-boundary plasma. I. Weak-coupling limit. *Plasma Phys.*, 22(12):1091–1107, 1980.
- [104] J P Goedbloed. Spectrum of ideal magnetohydrodynamics of axisymmetric toroidal systems. *Phys. Fluids*, 18(10):1258–1268, 1975.
- [105] C E Kieras and J A Tataronis. The shear Alfvén continuous spectrum of axisymmetric toroidal equilibria in the large aspect ratio limit. *J. Plasma Phys.*, 28(3):395–414, 1982.
- [106] L Chen and F Zonca. Theory of Shear Alfvén Waves in Toroidal Plasmas. *Phys. Scr.*, T60:81–90, 1995.
- [107] M S Chu, J M Greene, L L Lao, A D Turnbull and M S Chance. A numerical study of the high- $n$  shear Alfvén spectrum gap and the high- $n$  gap mode. *Phys. Fluids B*, 4(11):3713–3721, 1992.
- [108] A D Turnbull et al. Global Alfvén modes: Theory and experiment. *Phys. Fluids B*, 5(7):2546–2553, 1993.
- [109] G Vlad, F Zonca and S Briguglio. Dynamics of Alfvén waves in tokamaks. *Riv. del Nuovo Cim.*, 22(7), 1999.
- [110] J A Wesson. Hydromagnetic stability of tokamaks. *Nucl. Fusion*, 18(1):87–132, 1978.
- [111] M N Bussac, R Pellat, D Edery and J L Soulé. Internal Kink Modes in Toroidal Plasmas with Circular Cross Sections. *Phys. Rev. Lett.*, 35(24):1638–1641, 1975.
- [112] D Edery, G Laval, R Pellat and J L Soulé. Current-driven internal kink modes in cylindrical and helicoidal discharges. *Phys. Fluids*, 19(2):260–265, 1976.
- [113] J Manickam. Stability of  $n = 1$  internal modes in tokamaks. *Nucl. Fusion*, 24(5):595–608, 1984.
- [114] T Ozeki, M Azumi, S Tokuda and S Ishida. Effects of a hollow current profile on the ideal MHD stability of high  $\beta_p$  plasmas in a tokamak. *Nucl. Fusion*, 33(7):1025–1035, 1993.
- [115] Y Z Zhang, H L Berk and S M Mahajan. Effect of energetic trapped particles on the ‘ideal’ internal kink mode. *Nucl. Fusion*, 29(5):848–853, 1989.
- [116] S Poedts, W Kerner, J P Goedbloed, B Keegan, G T A Huysmans and E Schwarz. Damping of global Alfvén waves in tokamaks due to resonant absorption. *Plasma Phys. Control. Fusion*, 34(8):1397–1422, 1992.
- [117] H L Berk, J W Van Dam, Z Guo and D M Lindberg. Continuum damping of low- $n$  toroidicity-induced shear Alfvén eigenmodes. *Phys. Fluids B*, 4(7):1806–1835, 1992.

- [118] L D Landau. On the vibration of the electronic plasma. *J. Exp. Theor. Phys.*, 16:574, 1946.
- [119] G W Hammett, W Dorland and F W Perkins. Fluid models of phase mixing, Landau damping, and nonlinear gyrokinetic dynamics. *Phys. Fluids B*, 4(7):2052–2061, 1992.
- [120] C L Hedrick, J-N Leboeuf and D A Spong. Alpha-Alfvén local dispersion relation and solutions. *Phys. Fluids B*, 4(12):3869–3882, 1992.
- [121] L Chen. Theory of magnetohydrodynamic instabilities excited by energetic particles in tokamaks. *Phys. Plasmas*, 1(5):1519–1522, 1994.
- [122] G Y Fu and C Z Cheng. Excitation of high- $n$  toroidicity-induced shear Alfvén eigenmodes by energetic particles and fusion alpha particles in tokamaks. *Phys. Fluids B*, 4(11):3722–3734, 1992.
- [123] T D Kaladze and A B Mikhajlovskij. Excitation of Alfvén waves by trapped alpha particles in a tokamak reactor. *Nucl. Fusion*, 17(3):411–418, 1977.
- [124] G Y Fu and W Park. Nonlinear Hybrid Simulation of the Toroidicity-Induced Alfvén Eigenmode. *Phys. Rev. Lett.*, 74(9):1594–1596, 1995.
- [125] L Chen, J Vaclavik and G W Hammett. Ion radial transport induced by ICRF waves in tokamaks. *Nucl. Fusion*, 28(3):389–398, 1988.
- [126] C Z Cheng. Energetic particle effects on global magnetohydrodynamic modes. *Phys. Fluids B*, 2(6):1427–1434, 1990.
- [127] F Zonca, L Chen and R A Santoro. Kinetic theory of low-frequency Alfvén modes in tokamaks. *Plasma Phys. Control. Fusion*, 38:2011–2028, 1996.
- [128] H Biglari and L Chen. Unified theory of resonant excitation of kinetic ballooning modes by energetic ions and alpha particles in tokamaks. *Phys. Rev. Lett.*, 67(26):3681–3684, 1991.
- [129] C Z Cheng, N N Gorelenkov and C T Hsu. Fast particle destabilization of toroidal Alfvén eigenmodes. *Nucl. Fusion*, 35(12):1639–1650, 1995.
- [130] W W Heidbrink, E Ruskov, E M Carolipio, J Fang, M A van Zeeland and R A James. What is the “beta-induced Alfvén eigenmode?”. *Phys. Plasmas*, 6(4):1147, 1999.
- [131] B Coppi and F Porcelli. Theoretical model of fishbone oscillations in magnetically confined plasmas. *Phys. Rev. Lett.*, 57(18):2272–2275, 1986.
- [132] B N Breizman, H L Berk and H Ye. Collective transport of alpha particles due to Alfvén wave instability. *Phys. Fluids B*, 5(9):3217–3226, 1993.
- [133] C T Hsu and D J Sigmar. Alpha-particle losses from toroidicity-induced Alfvén eigenmodes. Part I: Phase-space topology of energetic particle orbits in tokamak plasma. *Phys. Fluids B*, 4(6):1492–1505, 1992.
- [134] H E Mynick and N Pomphrey. Frequency sweeping: a new technique for energy-selective transport. *Nucl. Fusion*, 34(9):1277–1282, 1994.

- [135] J D Strachan et al. Studies of energetic ion confinement during fishbone events in PDX. *Nucl. Fusion*, 25(8):863–880, 1985.
- [136] W W Heidbrink and G Sager. The fishbone instability in the DIII-D tokamak. *Nucl. Fusion*, 30(6):1015–1025, 1990.
- [137] W W Heidbrink. Beam-driven chirping instability in DIII-D. *Plasma Phys. Control. Fusion*, 37:937–949, 1999.
- [138] F Zonca and L Chen. Theory on excitations of drift Alfvén waves by energetic particles. I. Variational formulation. *Phys. Plasmas*, 21(7):072120, July 2014.
- [139] J L V Lewandowski and M Persson. Local magnetic shear in tokamak plasmas. *Plasma Phys. Control. Fusion*, 37:1199–1205, 1995.
- [140] F Zonca and L Chen. Theory on excitations of drift Alfvén waves by energetic particles. II. The general fishbone-like dispersion relation. *Phys. Plasmas*, 21(7):072121, July 2014.
- [141] M F F Nave, D J Campbell, E Joffrin, F B Marcus, G Sadler, P Smeulders and K Thomsen. Fishbone activity in JET. *Nucl. Fusion*, 31(4):697–710, 2011.
- [142] I T Chapman et al. Saturated ideal modes in advanced tokamak regimes in MAST. *Nucl. Fusion*, 50(4):045007, April 2010.
- [143] S Günter, A Gude, K Lackner, M Maraschek, S Pinches, S Sesnic and R Wolf. The influence of fishbones on the background plasma. *Nucl. Fusion*, 39(11):1535–1539, 1999.
- [144] I H Hutchinson. *Principles of Plasma Diagnostics*. Cambridge University Press, Cambridge, second edition, 2002.
- [145] B V Waddell, M N Rosenbluth, D A Monticello and R B White. Non-linear growth of the  $m = 1$  tearing mode. *Nucl. Fusion*, 16(3):528–532, 1976.
- [146] S Von Goeler, W Stodiek and N Sauthoff. Studies of internal disruptions and  $m = 1$  oscillations in tokamak discharges with soft-X-ray techniques. *Phys. Rev. Lett.*, 33(20):1201–1203, 1974.
- [147] M A Berger. Introduction to magnetic helicity. *Plasma Phys. Control. Fusion*, 41:B167–B175, 1999.
- [148] R B White, P H Rutherford, P Colestock and M N Bussac. Sawtooth stabilization by energetic trapped particles. *Phys. Rev. Lett.*, 60(20):2038–2041, 1988.
- [149] F Porcelli. Fast particle stabilisation. *Plasma Phys. Control. Fusion*, 33(13):1601–1620, 1991.
- [150] J P Graves. Influence of asymmetric energetic ion distributions on sawtooth stabilization. *Phys. Rev. Lett.*, 92(18):185003, 2004.
- [151] D J Campbell et al. Stabilization of Sawteeth with Additional Heating in the JET Tokamak. *Phys. Rev. Lett.*, 60(21):2148–2151, 1988.
- [152] G J Kramer et al. Fast particle experiments in JT-60U. *Nucl. Fusion*, 40(7):1383–1396, 2000.

- 
- [153] M J Hole et al. Stability at high performance in the MAST spherical tokamak. In *Proc. 29th Eur. Phys. Soc. Conf. Plasma Phys. Control. Fusion O-2.02*, 2002.
- [154] M Turnyanskiy et al. Study of the fast ion confinement and current profile control on MAST. *Nucl. Fusion*, 49(6):065002, June 2009.
- [155] <http://w3.ppp1.gov/transp>, accessed 04/11/2014.
- [156] I Klimek et al. TRANSP modelling of total and local neutron emission on MAST. *Nucl. Fusion*, 55(2):023003, 2015.
- [157] D Pfefferlé, J P Graves and W a Cooper. Exploitation of a general-coordinate guiding centre code for the redistribution of fast ions in deformed hybrid tokamak equilibria. *J. Phys. Conf. Ser.*, 401:012020, December 2012.
- [158] K Stammers and M J Loughlin. The calibration of the MAST neutron yield monitors. *Nucl. Instruments Methods Phys. Res. Sect. A Accel. Spectrometers, Detect. Assoc. Equip.*, 562(1):521–530, June 2006.
- [159] A Pankin, D McCune, R Andre, G Bateman and A Kritz. The tokamak Monte Carlo fast ion module NUBEAM in the National Transport Code Collaboration library. *Comput. Phys. Commun.*, 159(3):157–184, June 2004.
- [160] H S Bosch and G M Hale. Improved formulas for fusion cross-sections and thermal reactivities. *Nucl. Fusion*, 32(4):611–631, April 1992.
- [161] M Salewski et al. On velocity-space sensitivity of fast-ion D-alpha spectroscopy. *Plasma Phys. Control. Fusion*, 56(10):105005, October 2014.
- [162] Benedikt Geiger. *Fast-ion transport studies using FIDA spectroscopy at the AS-DEX Upgrade tokamak*. PhD thesis, Ludwig-Maximilians-Universität, 2012.
- [163] A N Karpushov, B P Duval, C Schlatter, V I Afanasyev and F V Chernyshev. Neutral particle analyzer diagnostics on the TCV tokamak. *Rev. Sci. Instrum.*, 77(3):033504, 2006.
- [164] S K Nielsen et al. Dynamics of fast ions during sawtooth oscillations in the TEXTOR tokamak measured by collective Thomson scattering. *Nucl. Fusion*, 51(6):063014, June 2011.
- [165] M Nocente et al. Neutron spectroscopy measurements of tritium beam transport at JET. *Nucl. Fusion*, 54(10):104010, October 2014.
- [166] W W Heidbrink, D Liu, Y Luo and E Ruskov. A Code that Simulates Fast-ion  $D_\alpha$  and Neutral Particle Measurements. *Commun. Comput. Phys.*, 10(3):716–741, 2011.
- [167] M Podestà, W W Heidbrink, R E Bell and R Feder. The NSTX fast-ion D-alpha diagnostic. *Rev. Sci. Instrum.*, 79(10):10E521, October 2008.
- [168] R E Bell. Exploiting a transmission grating spectrometer. *Rev. Sci. Instrum.*, 75(10):4158–4161, 2004.
- [169] M S Robbins and B J Hadwen. The Noise Performance of Electron Multiplying Charge-Coupled Devices. *IEEE Trans. Electron Devices*, 50(5):1227–1232, 2003.

- [170] J D Callen, J P Christiansen, J G Cordey, P R Thomas and K Thomsen. Modelling of temperature profiles and transport scaling in auxiliary heated tokamaks. *Nucl. Fusion*, 27(11):1857–1875, 1987.
- [171] G Bateman, T Onjun and A H Kritz. Integrated predictive modelling simulations of burning plasma experiment designs. *Plasma Phys. Control. Fusion*, 45(11):1939–1960, November 2003.
- [172] H Nuga and A Fukuyama. Kinetic Integrated Modeling of Plasma Heating in Tokamaks. *Prog. Nucl. Sci. Technol.*, 2:78–84, 2011.
- [173] A H Kritz, T Rafiq, C Kessel, G Bateman, D C McCune, R V Budny and A Y Pankin. Integrated modelling for prediction of optimized ITER performance. *Nucl. Fusion*, 51(12):123009, December 2011.
- [174] R J Akers et al. Transport and confinement in the Mega Ampère Spherical Tokamak (MAST) plasma. *Plasma Phys. Control. Fusion*, 45(12A):A175, 2003.
- [175] A H Kritz et al. The National Transport Code Collaboration Module Library. *Comput. Phys. Commun.*, 164(1-3):108–113, December 2004.
- [176] Z S Qu, M Fitzgerald and M J Hole. Analysing the impact of anisotropy pressure on tokamak equilibria. *Plasma Phys. Control. Fusion*, 56:075007, 2014.
- [177] Stuart Henderson. *Impurity transport studies on MAST*. PhD thesis, University of Strathclyde, 2014.
- [178] <http://www.adas.ac.uk>, accessed 22/11/2014.
- [179] R K Janev, D Reiter and U Samm. *Collision processes in low-temperature hydrogen plasmas*. 2003.
- [180] W W Heidbrink et al. Confinement degradation by Alfvén-eigenmode induced fast-ion transport in steady-state scenario discharges. *Plasma Phys. Control. Fusion*, 56(9):095030, September 2014.
- [181] B Geiger. Quantification of the impact of large and small scale instabilities on the fast-ion confinement in ASDEX Upgrade. *Plasma Phys. Control. Fusion*, 57(1):014018, 2015.
- [182] D A Dickey and W A Fuller. Distribution of the Estimators for Autoregressive Time Series With a Unit Root. *J. Am. Stat. Assoc.*, 74(366):427–431, 1979.
- [183] E D Fredrickson et al. Collective fast ion instability-induced losses in National Spherical Tokamak Experiment. *Phys. Plasmas*, 13(5):056109, 2006.
- [184] W W Heidbrink et al. Tangential Neutral-Beam-Driven Instabilities in the Princeton Beta Experiment. *Phys. Rev. Lett.*, 57(7):838, 1986.
- [185] B B Kadomtsev. Disruptive instability in Tokamaks. *Sov. J. Plasma Phys.*, 1:389–391, 1975.
- [186] C M Muscatello, W W Heidbrink, Ya I Kolesnichenko, V V Lutsenko, M A Van Zeeland and Yu V Yakovenko. Velocity-space studies of fast-ion transport at a sawtooth crash in neutral-beam heated plasmas. *Plasma Phys. Control. Fusion*, 54(2):025006, February 2012.

- 
- [187] B. Geiger et al. Fast-ion transport in the presence of magnetic reconnection induced by sawtooth oscillations in ASDEX Upgrade. *Nucl. Fusion*, 54(2):022005, February 2014.
- [188] Ya I Kolesnichenko, V V Lutsenko, R B White and Yu V Yakovenko. Effect of sawtooth oscillations on energetic ions. *Nucl. Fusion*, 40(7):1325–1341, 2000.
- [189] K G McClements et al. The effects of resonant magnetic perturbations on fast ion confinement in the Mega Amp Spherical Tokamak. *Plasma Phys. Control. Fusion*, 57:075003, 2015.
- [190] A Kirk et al. Magnetic perturbation experiments on MAST L- and H-mode plasmas using internal coils. *Plasma Phys. Control. Fusion*, 53:065011, 2011.
- [191] Y B Zhu, W W Heidbrink and L D Pickering. Phenomenology of energetic-ion loss from the DIII-D tokamak. *Nucl. Fusion*, 50:084024, 2010.
- [192] M Garcia-Muñoz, H-U Fahrback and H Zohm. Scintillator based detector for fast-ion losses induced by magnetohydrodynamic instabilities in the ASDEX upgrade tokamak. *Rev. Sci. Instrum.*, 80(5):053503, 2009.
- [193] L C Appel, M J Hole, J Svensson and G von Nessi. Bayesian Inference applied to Magnetic Equilibrium on MAST. In *Proc. 37th Eur. Phys. Soc. Conf. Plasma Phys.* P4.103, 2010.
- [194] J Rasmussen et al. Comparing real and synthetic fast-ion measurements at ASDEX Upgrade. *Plasma Phys. Control. Fusion*, 57:075014, 2015.
- [195] M Podestà, M Gorelenkova and R B White. A reduced fast ion transport model for the tokamak transport code TRANSP. *Plasma Phys. Control. Fusion*, 56(5):055003, 2014.
- [196] S D Pinches, I T Chapman, Ph W Lauber, H J C Oliver, S E Sharapov, K Shinohara and K Tani. Energetic ions in ITER plasmas. *Phys. Plasmas*, 22(2):021807, 2015.
- [197] F Zonca, S Briguglio, L Chen, G Fogaccia and G Vlad. Transition from weak to strong energetic ion transport in burning plasmas. *Nucl. Fusion*, 45(6):477–484, 2005.
- [198] A Bierwage et al. Nonlinear simulation of energetic particle modes in JT-60U. In *Proc. 24th IAEA Fusion Energy Conf.* TH/P6–17, 2012.
- [199] C Perez von Thun et al. Study of fast-ion transport induced by fishbones on JET. *Nucl. Fusion*, 52(9):094010, September 2012.
- [200] W W Heidbrink et al. Characterization of off-axis fishbones. *Plasma Phys. Control. Fusion*, 53:085028, August 2011.
- [201] D Pfefferlé, C Misev, W A Cooper and J P Graves. Impact of RMP magnetic field simulation models on fast ion losses. *Nucl. Fusion*, 55(1):012001, 2015.
- [202] F Jaulmes, E Westerhof and H J de Blank. Redistribution of fast ions during sawtooth reconnection. *Nucl. Fusion*, 54:104013, 2014.